Dissertation zur Erlangung des Doktorgrades
der Fakultät für Chemie und Pharmazie
der Ludwig-Maximilians-Universität München

Diffusion in a Crowded Adsorbate Layer

A Video-Rate Scanning Tunneling Microscopy Study

Ann-Kathrin Henß

aus

Ehringshausen, Deutschland

2019

Erklärung

Diese Dissertation wurde im Sinne von § 7 der Promotionsordnung vom 28. November 2011 von Herrn Prof. Dr. Joost Wintterlin betreut.

Eidesstattliche Versicherung

Diese Dissertation wurde eigenständig und ohne unerlaubte Hilfe erarbeitet.

München, den 03.09.2019

____

Ann-Kathrin Henß

Dissertation eingereicht am:	03.09.2019
Erstgutachter:	Prof. Dr. Joost Wintterlin
Zweitgutachter:	Prof. Dr. Axel Groß
Mündliche Prüfung am:	24.10.2019

"…expliquer du visible compliqué par de l'invisible simple…"

"To explain that which is visible but complicated
by that which is invisible but simple…"

Jean Perrin
in preface to *Les Atomes*
(1913)

Table of Contents

1. Introduction

The diffusion of atoms, molecules, and clusters on surfaces plays a vital role in surface and interface processes. This is because it governs mass transport, which is the basis for many surface phenomena, like the growth of crystals or thin films,[1, 2] surface restructuring,[3, 4] self-assembly processes,[5] or dissolution processes.[6, 7] These structural changes of the surface are also of technical importance for coating processes or thin film fabrication, e.g., for solar cells or LED applications.[8, 9]

In addition, surface diffusion plays a major role in various chemical reactions. More than 70% of the industrially relevant reactions require the use of a solid catalyst to enhance the yield and selectivity.[10-12] In surface reactions, the particles from the gas or liquid phase adsorb on the surface of the solid catalyst. However, for the reaction to occur these particles must be able to move on the catalyst surface to meet reaction partners or to reach specific active sites. Diffusion therefore determines the mixing and spreading of the reactants on the surface and thus their ability to react. A detailed comprehension of the underlying principles and mechanisms of diffusion on surfaces is therefore essential to understand and control macroscopic surface processes and phenomena.[13] Furthermore, it holds the promise to improve existing processes, such as in heterogeneously catalyzed reactions or in other technical applications. Consequently, great efforts have been undertaken in the past to investigate and understand surface dynamics and adsorbate diffusion on metals,[6, 9, 14-20] semiconductors,[14, 20-23] and oxides.[24, 25]

With the invention of the field-ion microscope (FIM) by Erwin Müller in 1951,[26] imaging of surfaces with atomic resolution became possible, which laid the basis for a new level of understanding in surface science. The first observation of the motion of individual adsorbed atoms on surfaces was achieved in 1966 by Ehrlich and Hudda,[27] who followed the diffusion of single tungsten adatoms on the surface of a sharp tungsten tip. However, the necessity of a strong electric field and a sharp metal tip as sample for FIM imaging strongly limit the number of adsorbate/support systems that are suitable for investigation.[15]

In the early 1980s, the development of the scanning tunneling microscope by Binnig and Rohrer[28] opened up new possibilities to study surface processes. It allows for real-space imaging with (sub-)atomic resolution of a wide variety of samples[24, 29-32] and in different environments.[33-37] The inventors were awarded with the *Nobel Prize* in Physics in 1986. Since then scanning tunneling microscopy (STM) has become one of the major analysis methods in surface science and led to a more detailed comprehension of many surface processes, such as adsorption, reconstruction or reactions on surfaces.[38-42]

When investigating dynamic processes, such as surface diffusion, a major drawback of STM is its comparatively long image recording time that typically lies in the range of several tens of seconds to minutes. Surface processes that take place on the same timescale or faster than the imaging rates will appear blurred or not even be visible at all in STM measurements. The great benefit of the high spatial resolution of STM, is thus diminished by its low temporal resolution.

Meanwhile other methods have been developed to study diffusion on surfaces with better temporal resolution than STM but on a more macroscopic scale. Most of these techniques are based on the evolution of concentration profiles in time, such as the observation of surface dynamics with low energy electron microscopy,[43] photoemission electron microscopy,[44] laser-induced thermal desorption,[45-49] or optical grating techniques.[50, 51] Yet, these macroscopic techniques have major disadvantages when aiming at a deeper understanding of diffusion processes: Diffusion is treated by a mean-field approach that averages over all particles adsorbed on the surface. In this way, local binding geometries, which may be quite different along a surface even for the same type of particles, and interaction with surface steps and defects are not resolved but averaged out. To achieve atomic-scale understanding of diffusion processes and elucidate the role of defects, steps, and adsorbate-adsorbate interactions, an atomically resolved method with high temporal resolution is needed.

To exploit the outstanding spatial resolution of STM, but improve its temporal resolution, Swartzentruber developed a so-called *atom-tracking* STM in 1996.[52, 53] In this technique, the STM tip is positioned above a selected atom or molecule on the surface. Two-dimensional lateral feedback is then used to lock the tip over the moving atom. In this way the tip follows the migrating particle over the surface. The motion of the tip is identical to the particle trace. As the tip is no longer used for imaging, but just for following the motion of a specific particle, the temporal resolution for diffusion studies can be increased by up to three orders of magnitude in comparison to conventional STM imaging.

Another approach to studying diffusion with STM on a shorter time scale was developed by Wang *et al.* in 2005: the tunneling current fluctuation measurement.[54-56] They positioned the STM tip over a fixed point of the sample, e.g., an adsorption site, and recorded the tunneling current over time at constant tunneling voltage. The diffusion of an atom or a molecule to or away from the monitored adsorption site leads to a change in the current signal. By this method, residence times of atoms on the specific adsorption site can be directly extracted from the measured tunneling current fluctuations. As a feedback loop was abandoned in this technique, the temporal resolution was further increased by two to three orders of magnitude.[54] In contrast to the presented macroscopic methods the STM techniques by Swartzentruber and Wang *et al.* in fact monitor single particle diffusion events. However, they do not provide information on the local adsorption geometries, since the surface is not imaged. The influence of defects or interactions with other adsorbates, exactly those effects that make atomic-scale diffusion so complicated, are thus not accessible by these techniques.

Therefore, attempts have been made to speed up conventional STM imaging by developing a so-called video-rate STM (Video-STM) technique, decreasing the required time for imaging from several tens of seconds or minutes per image to the millisecond range. [4, 34, 41, 57-59] Here, video rate means that at least ten to twelve images per second can be acquired. At these imaging rates the human eye starts to perceive the sequences of images as continuous movies.[60] The first dynamic STM study that revealed insights into atomic surface processes at imaging rates of up to 20 images per second was realized by Wintterlin *et al.* in 1997.[41] They observed equilibrium fluctuations in an adsorbate layer of O atoms on a Ru(0001) surface at room temperature. These processes are not observable with conventional STM as the single O atoms move too fast to be captured at conventional scan rates. Since then, several working groups put effort into the design of new STM setups to improve mechanical stability during high-speed scanning as well as into the development of faster STM electronics.[58, 59] By now, imaging rates have been pushed to around 100 Hz. However, setups that are especially tailored for video-rate imaging, mostly only allow for measurements at room temperature. The investigation of surface processes with strongly different rates, however, requires the possibility to vary the sample temperature. Furthermore, for the extraction of kinetic parameters by means of the Arrhenius equation one has to vary the temperature. The temperature range should be as wide as possible, so that these measurements provide meaningful values.

Thus, within this thesis two operational capabilities of the STM technique were combined: a variable temperature STM (VT-STM) and a Video-STM. By this combination, the study of surface processes at different temperatures and with high temporal resolution is made possible. For this purpose, a VT-STM setup, consisting of the mechanical part of the STM in an ultra-high vacuum (UHV) chamber and the STM electronics for scan control and data acquisition, was upgraded to enable video-rate imaging. Whereas there are several groups in the world that perform VT-STM[61, 62] or Video-STM,[35, 58, 63] the combination of these two capabilities is unique and provides the experimental basis to study diffusion processes, and moreover all kinds of dynamic processes on surfaces, over a much broader temperature range than before. In this way, kinetic parameters, namely activation energies and pre-exponential factors, can be determined more precisely, which contributes to the elucidation of the underlying atomic processes.

As diffusion is based on the stochastic movement of single particles, a sufficiently large sample of observations is required for a meaningful analysis. The developed video-rate VT-STM technique provides the opportunity to acquire a statistically significant number of images in a reasonable time. In turn, this fact implies the necessity to evaluate a large number of STM images, so as to extract the relevant information on the atomic processes. The analysis of these data could not be performed manually, since one video-rate STM movie of a few minutes already contains several thousand individual images. A manual evaluation of these large numbers of images would be too time consuming. Therefore, a series of image processing routines have been developed in the course of this work.

A central step of this data evaluation process is the automated detection and localization of particles of interest and their tracking through consecutive STM images. In a cooperation with Philipp Messer, M.Sc. and Prof. Dr. Don Lamb of the *Ludwig-Maximilians-Universität* (*LMU*) Munich, this step was realized by adapting a *Wavelet Transform* (WT)-based algorithm originally developed for the detection of fluorescent-labelled particles in biological environments.[64] By this method, the motion of individual particles on a surface can be identified. As a result, trajectories can be obtained that precisely show the dynamics on the surface through thousands of consecutive STM images.

Within this thesis, the developed combined video-rate VT-STM setup has been used for studying the diffusion of single oxygen atoms coadsorbed with carbon monoxide on a Ru(0001) surface. The system of a mixed adsorbate layer of O and CO on Ru is an important model system in heterogeneous catalysis, as their reaction to CO_2 on the surface of the Pt group metals is one of the most extensively studied catalyzed reactions.[65-68] The role of surface diffusion in catalytic reactions is, however, in general neglected when considering the reaction kinetics. Yet, rapid diffusion is essential for the mixing and spreading of the reactants on the catalyst surface, because the particles must meet each other for a reaction to occur or might also have to reach active sites on the surface.

Moreover, under the conditions of an industrial catalytic reaction, which is usually carried out at high pressures,[69] it can be assumed that the surface of the catalyst is highly covered with adsorbed particles. In addition to the reactants also reaction intermediates and byproducts can be present on the surface. It is not yet understood how atoms or molecules can move when the surface is densely occupied by adsorbates. There simply seems to be no room for motion, as the particles block each other's way. Therefore, the main focus of the present investigations was the question how an increasing CO coverage affects the diffusion of the O atoms.

For diffusion of single O atoms in the $(\sqrt{3} \times \sqrt{3})R30°$ structure of CO on Ru(0001), which is the densest ordered CO structure achieved in UHV and at temperatures above 200 K, O atoms are completely surrounded by CO molecules and trapped in what could be called a "CO cage." Activation barriers were extracted from temperature dependent measurements over a range of 70 K and interpreted with the help of complimentary density functional theory (DFT) calculations performed by Dr. Sung Sakong and Prof. Dr. Axel Groß of *Ulm University*. Contradicting expectations, the O atoms were found to move in this full layer of CO molecules almost as fast as on the clean Ru(0001) surface. A previously unknown diffusion mechanism was identified in which density fluctuations in the ordered CO layer allow the O atoms to move over the highly occupied surface. As the CO molecules intermittently leave their most stable position and thus make way for the O atoms to move out of a CO cage, the mechanism was named *door-opening* mechanism.

Chapter 2 of this thesis deals with the development of the combined video-rate variable temperature STM. The VT-STM setup that served as a starting point in this project is introduced and the design criteria for the new combined setup are defined. The modifications of the STM electronics and software are presented.

Chapter 3 focuses on the data evaluation process. The designed custom-made image processing algorithms as well as the particle tracking algorithm are discussed in detail in this section.

Chapter 4 provides a description of the UHV system which houses the mechanical part of the STM setup. The chapter also describes the employed analysis techniques and the sample setup.

The diffusion experiments with the newly established Video-VT-STM are presented in chapter 5. A detailed description of the data analysis procedure is given and the obtained kinetic parameters for the diffusion process are discussed with the help of DFT calculations. The results are also qualitatively compared to STM observations of the O diffusion on an only partially CO-covered Ru(0001) surface. Furthermore, first results on the diffusion of single O atoms at domain boundaries of the $(\sqrt{3} \text{ x } \sqrt{3})$R30° structure are presented.

This thesis concludes with a summary of the main achievements and an outlook on future work in chapter 6.

2. Video-Rate Scanning Tunneling Microscopy

2.1 Introduction

Already in the early days of STM, scientists started working on the development of video-rate or high-speed STM techniques in order to make up for the disadvantage of conventional STM, its rather long image recording times.[57] In principle, there are two main problems that have to be addressed when speeding up STM imaging. The first is the speed of the STM electronics, which include the STM control and the signal acquisition system. All components need to have sufficiently high bandwidths and sampling rates to allow for a fast-enough positioning of the tip, as well as fast signal processing, and handling of large amounts of data. Especially speed-critical is the amplifier for the tunneling current signal. Whereas its bandwidth must be in the high kHz range for Video-STM, its noise level still needs to be low enough to detect the small current signals that are in the nA regime.

STM imaging with line frequencies greater than 1 kHz, that translate into image frequencies according to the number of lines, was realized for the first time by Bryant *et al.* already in 1986.[57] By scanning in *constant-height* mode, they avoided the bandwidth limitation of the feedback circuit and received atomically resolved images of a flat graphite surface. In 1991 Besenbacher *et al.* were able to study the oxygen-induced restructuring of a Cu(110) surface with an STM image rate of 1 Hz.[4] The use of a 20 MHz CPU allowed for recording, displaying, and saving of a 128 x 128 pixel image within one second and thus enabled acquisition of longer STM movies.

The second challenge of high-speed STM is the mechanical stability of the STM setup as scanning with the STM tip at very high frequencies results in the excitation of mechanical vibrations, especially when coming close to the eigenfrequencies of the STM setup. These vibrations deteriorate the imaging or prevent it completely. Wintterlin *et al.* were the first to push the imaging rates of a conventional *pocket-size* STM[70] to up to 20 frames per second, in this way reaching video rate.[41] These rates were achieved by introducing sine-shaped scan ramps instead of the typically-used triangular wave forms. In this way the excitation of resonant modes of the STM by an interference with the tip motion could be reduced, and driving the STM at higher scan frequencies became possible. In 2005 researchers of the Frenken group at the *University of Leiden* designed an STM scan head specifically for Video-STM applications.[58] The more compact and stiffer design showed much higher resonance frequencies than the conventionally-used STMs and thus allowed for faster scanning without interference of tip motion and mechanical response of the system. With this setup image rates of up to 80 Hz were realized. However, the stiffer scanner design also implicated a much smaller accessible scan range, which limited its practical use.

In recent years Esch *et al.* presented a one-piece electronic add-on module that combined several technical solutions previously proposed by other groups to overcome the speed limitations of STM control and data acquisition systems. This electronic module can be combined with all types of conventionally-used STMs to enable video-rate scanning if the mechanical stability of the respective STM permits it. The use of commercially available 8 bit *digital-to-analog-converter* (DAC) and 12 bit *analog-to-digital-converter* (ADC) units allows for data sampling rates of up to 10 MHz, which corresponds to a maximum frame rate of 100 Hz for 100 x 100 pixel images. In turn, the use of an 8 bit DAC unit strictly limits the maximum image size to 256 x 256 pixels.[59] This size is sufficient for most Video-STM applications, but reduces the capabilities for conventional scanning.

The aim of this work was to upgrade a VT-STM of the working group of Prof. Dr. Joost Wintterlin at *LMU* Munich to enable STM imaging at video rate (>10 images/s). As a VT-STM is especially designed to study surface dynamics at different temperatures, the combination with video-rate acquisition promised the ability to investigate dynamic processes on surfaces over a broader temperature range than possible before. Furthermore, dynamics over a wider range of activation energies become observable.

Some groups have already attempted to build a combined high-speed VT-STM setup, however, not achieved imaging rates greater than 1 Hz.[71-74] What is special in this work is that an already existing system that had been optimized for measurements at variable temperatures is modified in such a way that it additionally allows for measurements at video-rate. At the same time the properties of the original setup, such as scan range, resolution, and image sizes, should remain unrestricted. To maintain full control over hardware and software components and preserve the possibility of modifications for future applications, it was refrained from buying a commercial control system, e.g., the *LPM Video Rate SPM Control Electronics* including the acquisition and analysis software *CAMERA* by *Leiden Probe Microscopy B.V.*[75] or the *FAST* add-on unit[59] by Esch and coworkers.

This chapter describes the development of the Video-VT-STM setup that was performed in this work. After a brief explanation of the basic concepts of an STM measurement (section 2.2), the original VT-STM setup that served as a starting configuration for the development of the video-rate system is introduced (section 2.3). The design criteria for the Video-VT-STM setup are defined in section 2.4. Based on the given VT-STM setup, speed-critical hardware components were modified or completely replaced. The software for video-rate scan control and data acquisition was developed and extended on the basis of a version for conventional STM developed by Prof. Dr. Rolf Schuster of the *Karlsruhe Institute of Technology* (*KIT*). The modifications to hard- and software are presented in section 2.5. The appearance and quality of the acquired STM data is discussed in section 2.6. Section 2.7 reviews the final setup of the combined Video-VT-STM and the performance that is achieved with it.

2.2 Scanning Tunneling Microscopy

In an STM measurement, a sharp metal tip is scanned across a conducting or semiconducting sample surface at a distance of around 1 nm. A constant voltage that is applied between tip and sample results in a small current in the nA range, the so-called tunneling current I_t, which is based on the quantum mechanical tunneling effect.

The tunneling current exponentially depends on the tip-sample distance s. A variation of the distance by 1 Å results in a change of the tunneling current I_t of around one order of magnitude. Thus, when moving the tip over the sample each slight height variation causes a huge response in the tunneling current and in this way implicates a high spatial resolution in vertical and lateral direction. The tunneling current is, however, not only dependent on the topography of the sample, but also on the local density of states of the sample at the Fermi level $LDOS(E_F)$. The resulting image is therefore a superposition of electronic structure and topography. For low tunneling voltages V_t ($eV_t \ll \varphi_{eff}$) the dependencies of I_t are described by equation 2.1 and 2.2.[76, 77]

$$I_t \propto V_t \cdot LDOS(E_F) \cdot e^{-2\kappa s} \tag{2.1}$$

$$\text{with the decay length } \kappa = \sqrt{\frac{2m_e\varphi_{eff}}{\hbar^2}} \tag{2.2}$$

Here m_e is the electron mass, $\varphi_{eff} \approx \frac{1}{2}(\varphi_{tip} + \varphi_{sample})$ the effective tunneling barrier, as indicated in Figure 2.1, and $\hbar$ the reduced Planck constant. The bias of the tunneling voltage determines the sign of the tunneling current. A positive voltage applied to the sample leads to tunneling of electrons from the tip into empty states of the sample, giving a so-called *empty state* image. The reverse process at negative bias voltage produces a *filled state* image, in which electrons tunnel from the sample to the tip. The energy diagram for this *filled state* process is illustrated in Figure 2.1. The applied tunneling voltage V_t leads to an upward shift of the Fermi energy of the sample with respect to the Fermi level of the tip.

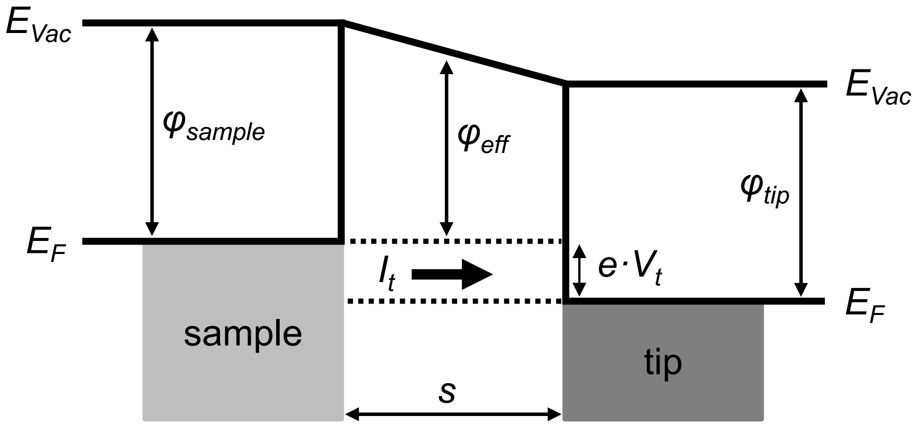

Figure 2.1: Energy diagram of the tunneling process for a *filled state* STM image. A negative bias voltage V_t is applied to the sample, shifting its Fermi energy (E_F) upwards by $e \cdot V_t$ with respect to E_F of the tip. In this configuration electrons can tunnel from filled states in the sample into empty states of the tip.

There are two different measurement modes for STM. One is the so-called *constant-current* mode, in which I_t is kept constant at a preset value while the vertical position of the tip is controlled and altered by a feedback loop throughout the measurement. This mode is the standard mode as the height (electronic or topographic) of a surface feature is directly obtained in Å. Moreover the distance between tip and sample is kept (nearly) constant and thus even very rough samples can be imaged. Also slight tilts of the sample with respect to the tip or thermal drift towards or away from the tip do not affect imaging. With a *constant-current* measurement the STM image visualizes the height variation Δz of the tip.

The second mode is the *constant-height* mode. In this technique the tip is scanned at a constant height (i.e., a constant z value), over the sample. In this mode, the STM image depicts the tunneling current. As the distance between tip and sample is not controlled in this mode, large height variations of the sample entail the risk of tip crashes with the sample or in the opposite case a loss of tunneling contact during the measurement. Usually, the feedback controller is not completely switched off in this mode but set to a low frequency, so that slow vertical changes, e.g., by thermal drift, are still compensated.

An image is build up pixel by pixel by moving the tip sequentially in x and y direction over the sample surface while recording the height variation Δz of the tip or the tunneling current I_t for each point. Usually this is done line-wise with x being defined as the fast scanning direction. The movements in all three directions require Ångström precision and are realized by using piezoelectric positioners.[78]

2.3 Start Configuration: The VT-STM Setup

In this work, the VT-STM setup of the Wintterlin group at *LMU* Munich was modified to enable video-rate STM measurements. A photograph of the mechanical part of the VT-STM, which was designed and built by Rolf Schuster and Joost Wintterlin, is shown in Figure 2.2. The central part of the setup is a *beetle-type* STM according to the concept of Besocke[78] and Frohn *et al.*[79]. For a measurement a sample is clamped onto the indicated copper block and the *beetle-type* STM is set up onto the sample holder with the vertical manipulator. A schematic representation of the *beetle-type* STM is depicted in Figure 2.3. It consists of an anodized aluminum disc, onto which four piezoelectric tubes are mounted. Each piezoelectric tube consists of one inner electrode and four sections of electrodes on its outside. By applying appropriate voltages between outer and inner electrodes, a stretching, shrinking, or bending of the tubes can be induced.[78]

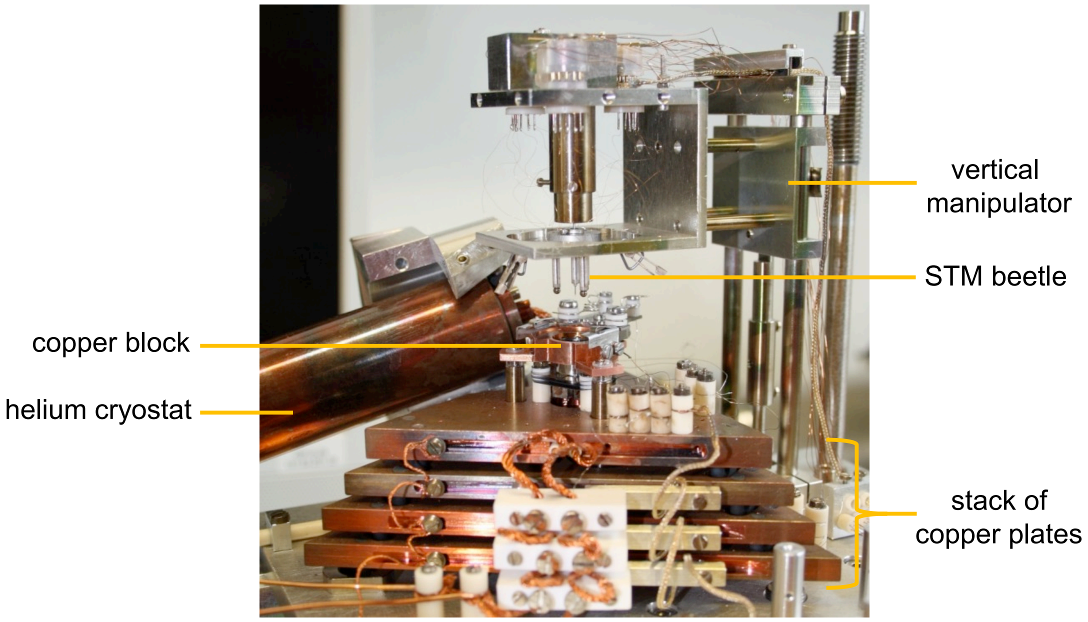

Figure 2.2: The VT-STM setup of the Wintterlin group. For measurements a sample is clamped onto the copper block and the *beetle-type* STM is set up onto the sample holder by the vertical manipulator.

Stainless steel balls are attached to the bottom of the three outer piezo tubes that act as legs of the STM head. The central piezo tube carries the STM tip that is positioned over the sample. The tip was obtained by electrochemical etching of a tungsten wire (ø = 0.25 mm).[80] The sample holder features a segmented helical ramp that operates as platform for the STM. The STM head is put on the sample holder by moving the vertical manipulator downward until the stainless steel balls touch the surface of the segmented helical ramps. By further lowering the vertical manipulator the STM head is mechanically decoupled from the manipulator. Thin copper wires remain the only connection, through which the electric supply of the piezo tubes is realized. By a collective movement of all three leg piezos, the STM head can either be translated in x or y direction, or rotated with respect to the ramp. In this way the tip can be approached to or retracted from the sample very precisely. In preparation for a measurement, the tip-sample approach by a clockwise motion of the STM head down the ramp is realized by an electronic circuit that automatically stops the movement when the tip arrives within tunneling distance to the sample. The scanning motion of the tip in a *beetle-type* STM is realized by a bending motion of the central piezo.

The VT-STM allows for measurements at different temperatures by a combination of liquid helium cooling and radiative heating. During a measurement the sample holder is clamped onto the copper block, which is cooled by a copper braid connected to a liquid helium cryostat, see Figure 2.2. In this way, minimum sample temperatures of around -220 °C are achieved. Counterheating with a tungsten filament located inside the copper block, underneath the sample, allows for a continuous adjustment of the sample temperature up to +230 °C. *Beetle-type* STMs are specifically well-suited for temperature variations. Vertical thermal drift is internally compensated for, as temperature-induced length changes of the three outer piezo legs will automatically result in the same change of the tip-carrying piezo, when a uniform heat transfer is assumed. Owing to their quasi-cylindrical symmetry, *beetle-type* STMs do also not exhibit significant lateral drift.

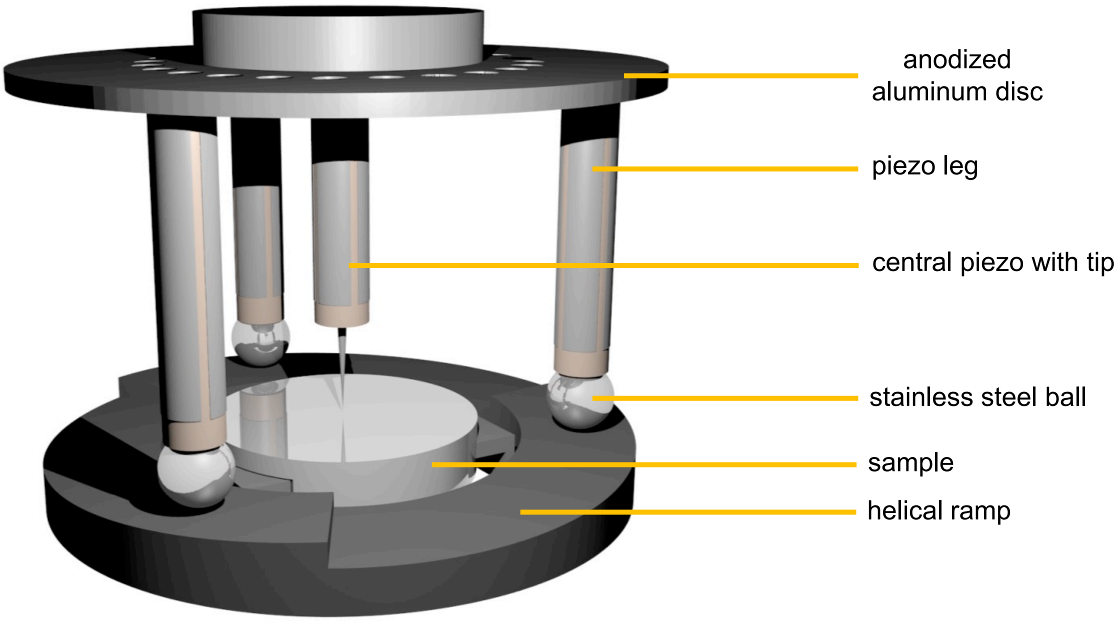

Figure 2.3: Schematic representation of the *beetle-type* STM on the helical ramps of the sample holder. The tip is approached to (retracted from) the sample by a clockwise (counter-clockwise) motion of the three outer piezo legs on the ramps.

In order to damp the setup from mechanical vibrations of its surroundings, it is mounted on top of a stack of copper plates (compare Figure 2.2) that are separated from each other by *Viton* loops. However, the VT-STM cannot be completely decoupled from the rest of the UHV chamber as a connection to the He cryostat is always required. This problem is solved by means of air-damped legs on which the UHV chamber is mounted.

A block diagram of the previous electronic part of the STM control and the data acquisition system is given in Figure 2.4. The scan parameters for an experiment were set on a personal computer (PC) via a *JAVA* user interface. The digital scan ramps for x and y motion were generated by a real-time computer hosting a field programmable gate array (FPGA) and subsequently converted to analog signals by two DACs (2 MHz, 16 bit, ± 10 V). The scan signals were enhanced by voltage amplifiers in the 40V-Unit before being applied to the scan piezo.

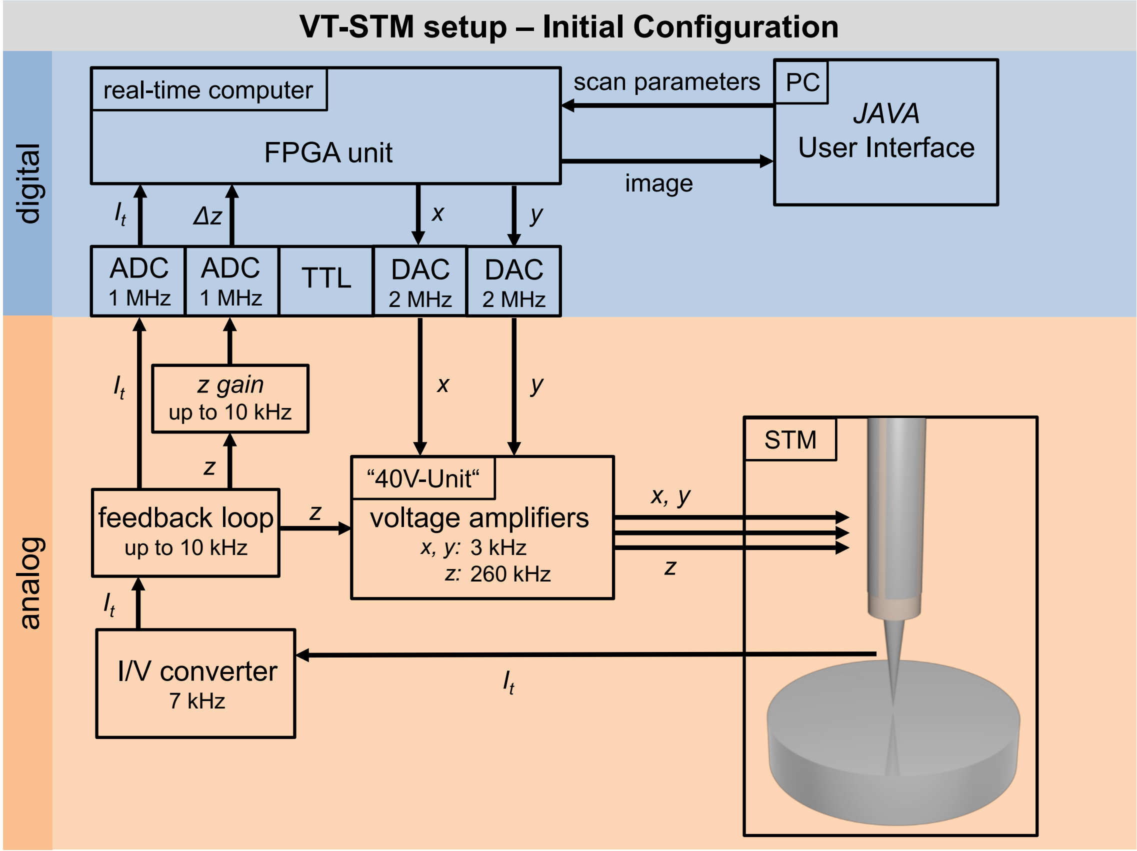

Figure 2.4: Block diagram of the electronic setup of the VT-STM in its initial configuration. The blue shading marks the digital scan control and data acquisition system based on a real-time computer hosting a FPGA unit. The analog part of the setup is highlighted in orange and includes the voltage amplifiers in the "40V-Unit," the STM itself, the current amplifier, and the electronics of the feedback loop. Separate ADC and DAC units realize the crossover between analog and digital signals. Bandwidths of the individual components are indicated, respectively.

The measured tunneling current signal was preamplified by a factor of 10^8 V/A by a commercial I/V-converter (*FEMTO DLPCA-200*) with a cutoff-frequency of 7 kHz (low-noise mode). The signal was then fed into the feedback control of the STM and the z signal was determined. The nominal values for I_t in the feedback loop could be set between 3 pA and 30 nA. The tunneling voltage V_t could be adjusted up to ± 10 V and is given with respect to the polarity at the sample. Typically the cutoff-frequency of the feedback loop was tuned to ∼ 2.3 kHz. After amplification, the feedback signal z was applied to the scan piezo to adjust its vertical position. I_t and z signals were simultaneously passed on to the real-time computer via ADCs (1 MHz, 16 bit, ± 10 V). A variable gain (*z gain*) could be applied to the z signal prior to conversion in order to enhance the vertical resolution. The resulting image was eventually displayed in the user interface. A transistor-transistor logic (TTL) was used for timing of the scan and acquisition process.

The *JAVA* interface and the real-time computer/ FPGA system were designed by H. Junkes of the *PP&B IT Department* of the *Fritz-Haber-Institute* (*FHI*) Berlin. The *FHI* electronics workshop developed and built the TTL, DACs and ADCs. The feedback electronic and the “40V-Unit” were developed by Dr. Joachim Wiechers.[81, 82]

2.4 Design Criteria

For the development of the video-rate STM the following design criteria were formulated.

a) **Acquisition of 200 x 200 pixel images with at least 20 images/s**

The setup should be capable of acquiring 200 x 200 pixel images with a rate of 20 images per second. Since for every scan from left to right (forward scan) there has to be a scan from right to left (backward scan), an image consists of 80000 data points (2 x 200 x 200). This leads to a required minimum sampling rate of the acquisition system of around 1.6 MHz (80000 data points/image x 20 images/s) and a required tip scan frequency (line frequency) of 4 kHz (200 lines/image x 20 images/s).

b) **Atomic resolution**

has to be maintained during video-rate scanning.

c) **Full transparency of the new scan control and data acquisition system**

All output and input signals should be accessible to allow for future modifications and extensions of the setup. It is thus refrained from buying a commercially available system.

d) **Full integration of the video mode into the existing STM electronics**

The resulting setup should allow for operation in both, video and conventional slow STM mode. Implementation of the video mode should not affect or restrict the properties of the conventional one. Switching between the two measuring modes should be easy and fast and should not make hardware changes necessary.

2.5 Realization of the Video Mode

As a consequence of the defined demands for the video-rate VT-STM system, the following components of the initial VT-STM setup had to be checked for their compatibility for video-rate scanning and, if necessary, modified or exchanged.

a) **Scan control and data acquisition system**
   - **DAC units for tip positioning: output rate and resolution**
   - **ADC units for signal readout: sampling rates and resolution**

b) **Bandwidth of the voltage amplifiers for tip positioning ("40V-Unit")**

c) **Bandwidth & signal-to-noise ratio of the current preamplifier**

d) **Bandwidth of the feedback control**

e) **Mechanical eigenfrequencies of the STM head**

f) **Software**
   - real-time processing of the acquired data (displaying of the images, background correction, saving of large data volumes)

2.5.1 STM Electronics

2.5.1.1 Scan Control and Data Acquisition System

One major point that had to be addressed during the development was the question how the scan control and the data acquisition system (blue shading in Figure 2.4) could be changed in order to fulfill the above requirements. Concerning speed demands at least the ADC system had to be upgraded, as its conversion rate of 1 MHz was below the required 1.6 MHz. A yet more important issue was the lack of modifiability of the whole system. The key component is an FPGA unit that was configured and programmed at the *PP&B IT Department* of the *FHI*. This system was the result of extensive development work during which, in particular, difficult timing problems had to be solved and could not be changed at an acceptable expense.

For these reasons it was decided to develop a new scan control and data acquisition system based on a commercially available *multifunctional data acquisition device* (DAQ device) by *National Instruments*. These devices can perform analog-to-digital as well as digital-to-analog signal conversion and are equipped with timers to synchronize different processes. The functionality of such a device can be set and controlled as required by the on-site integrated development environment *LabVIEW* (*National Instruments*) or also by the add-on *NIDAQ Tools MX* for the *IGOR Pro* software by *Wavemetrics*, a convenient feature as *IGOR Pro* is the default analysis tool in the Wintterlin group. The scan control and data display software developed within this thesis is described in section 2.5.3.

The selected DAQ device was a *PCIe 6361*, hosting two DAC units with an analog output (AO) rate of 2.86 MHz and eight ADC units with a maximum sampling rate of 2 MHz (analog input, AI). Both rates are higher than the demanded 1.6 MHz required for the fast positioning of the tip and data readout. All ADC and DAC units have a maximum input/output voltage range of ± 10 V and a resolution of 16 bit, identical to the properties of the previously-used ADC and DAC units, providing a lateral resolution of ~0.15 Å/bit and a vertical resolution of ~0.017 Å/bit (in the *constant-current* mode). In principle, DAQ devices with higher conversion rates are also available, but an increase in speed would result in a decrease of resolution. At the time of purchase, there was no suitable off-the-shelf 16 bit DAQ device available with higher conversion rates. In order to maintain the same lateral and spatial resolution, a decrease of the bit number would also reduce the maximum voltage ranges and thus the achievable scan ranges. The *constant-height* mode could be operated with lower bit resolution than 16 bit because of the relative low dynamic range of the tunneling current. However, as mentioned above, the system should be usable for both, the video mode as well as for the conventional scan mode, which requires a minimum resolution of 16 bit because of the high dynamic range of the z signal. The specific combination of output and sampling rates, voltage range and resolution of the ADC and DAC units is therefore a compromise to enable imaging at video rate while not restricting the conventional scan mode.

The *PCIe 6361* DAQ device was directly integrated by a common *PCIe x1* (*Peripheral Component Interface Express,* version 1.1) interface onto the mainboard of a custom PC. An internal FIFO (first in – first out) memory allows for buffering of data in case the readout of the data by the PC temporarily falls behind the data acquisition rate.

2.5.1.2 Feedback Loop

The conventional feedback loop of the VT-STM setup, an integral controller, has a maximum bandwidth of around 10 kHz. For the usual slow measurements in the *constant-current* mode, the frequency response was set to about 2.3 kHz in order to prevent oscillation of the feedback circuit. When speeding up the scanning, all structures on the sample surface that correspond to temporal frequencies above 2.3 kHz would hence not be recognized by the feedback loop.

A quite simple solution to this problem is the *quasi constant-height* mode. In this mode, the cut-off frequency of the feedback controller is set to a low value, so that slow changes caused by thermal drift and sample tilt are still compensated. Fast changes caused by the atomic structure are not compensated but cause a variation of the I_t signal that is recorded.

All STM movies acquired within this work were measured in this *quasi constant-height* mode.

2.5.1.3 Voltage Amplifiers

The scan ramps in x and y direction as well as the feedback output signal z become magnified by a factor of three by the voltage amplifiers in the “40V-Unit” before being applied to the scan piezo. The bandwidth of the voltage amplifier for the *z* signal is 260 kHz, sufficient when scanning in the video mode.

For the signal amplification of the scan ramps in *x* and *y* direction the bandwidth of the amplifiers is limited to 3 kHz, which is below the intended frequency in the fast scanning direction of around 4 kHz. Frequencies in the range of the bandwidth and above will be amplified less efficiently. In order to estimate the loss in signal amplitude when scanning close to or even above the bandwidth, the signal gain was experimentally determined in dependency of the frequency of the input signal. Figure 2.5 shows the Bode plot of the voltage amplifiers for *x* and *y* signal.

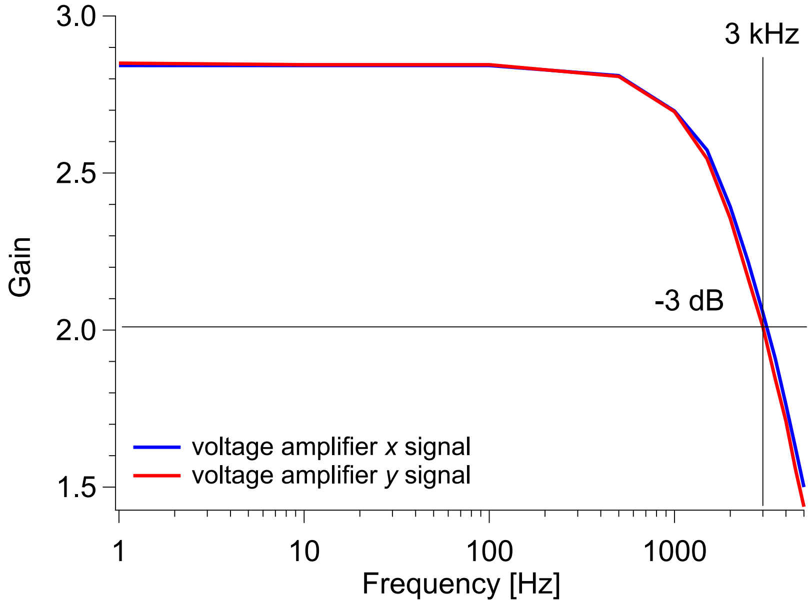

Figure 2.5: Bode plot of the voltage amplifiers in the "40 V-Unit" for *x* and *y* signal for frequencies between 1 and 5000 Hz. The bandwidth of both amplifiers lies at 3 kHz.

The gain of both signals remains constant up to a frequency of approximately 500 Hz. At higher frequencies the gain slightly reduces. The measurement confirms the bandwidth of both signal amplifiers at 3 kHz, defined as the frequency at which the output voltage is lowered to $1/\sqrt{2}$ of the input voltage. This point is indicated in Figure 2.5 by the crossing of the two solid black lines.

For the desired range of scan frequencies (in the low kHz regime) the main effect of the limited bandwidth on the sine-shaped scan waves will be an apparent lowering of the *x conversion* in comparison to the conventional slow scan mode. However, the usage of the existing voltage amplifiers does not impair high speed scanning. As the resulting effect can be easily corrected by a recalibration of the conversion, the voltage amplifier system is left unchanged. Table 2.1 lists the remaining gain factor referenced to the gain for an input signal of 1 Hz for several frequently used scan frequencies. These percentage values can be used to correct the *x conversion* for different scan speeds.

Table 2.1: Loss of signal gain for several scan frequencies in the voltage amplifier of the *x* signal.

Scan Frequency *f*	**Gain(*f*)/Gain(1 Hz)**
500 Hz	100 %
1000 Hz	95 %
1500 Hz	90 %
2000 Hz	84 %
2500 Hz	78 %
3000 Hz	71 %
3500 Hz	67 %
4000 Hz	62 %

2.5.1.4 Current Preamplifier

The images in the video mode would typically be between 100 and 200 Å wide. With a metallic lattice constant of roughly 3 Å a single line would therefore contain between 30 and 70 atoms. If one wants to achieve resolving this atomic pattern at least by its lowest Fourier component, the bandwidth of the current amplifier, given an intended line frequency of 4 kHz, should be between 240 and 560 kHz (including a factor of two for forward and backward scan). For this reason a bandwidth of the preamplifier in the high kHz range is necessary. This is a challenging demand as the noise of electric compounds typically increases proportionally to $\sqrt{\text{Hz}}$, which results in a decreasing signal-to-noise ratio.

The employed preamplifier in the initial VT-STM setup was a commercial *Femto DLCPA-200* I/V converter that had been operated with an amplification factor of 10^8 V/A in the “low noise” mode. The cut-off frequency in this mode is 7 kHz, which is sufficient for slow scanning studies but far below the just estimated bandwidth necessary for video-rate imaging with atomic resolution. The preamplifier could also be operated in a "high speed" mode with a higher bandwidth of 200 kHz (gain 10^8 V/A), but test measurements in this mode revealed a high background noise level of around 100 mV that impaired imaging significantly.

Therefore the *Femto* I/V converter has been replaced by a home-built preamplifier designed and built by Dr. Joachim Wiechers. This preamplifier features an even higher bandwidth than the commercial one with a cut-off frequency of 300 kHz at a fixed gain of 10^8 V/A. Furthermore it shows a significantly better signal-to-noise ratio. The background noise level in the I_t signal was determined to around 40 mV, which corresponds to a current noise of 0.4 nA. Thus, to achieve high-enough contrast in the resulting images, the base level for I_t in the *quasi constant-height* mode has to be set to at least 1 nA.

2.5.2 Mechanical Properties of the STM

When driving the STM tip at high scan speeds vibrations of the STM head and the whole sample-STM setup can be excited by the tip motion. For video-rate imaging scan frequencies lie in the low kHz regime, which is in the range of the eigenfrequencies of *beetle-type* STMs.[83-85] Coupling of the fast scanning motion to resonant modes of the STM setup can strongly impair the spatial resolution, create image distortions, or in the worst case, cause tip crashes. The knowledge of the mechanical properties of the STM setup is thus a precondition to avoid unwanted effects when speeding up the tip motion.

The mechanical properties of the present STM were investigated by using one of the four piezoelectric tubes for excitation. A directional mechanical vibration was excited by applying a sine wave of variable frequency in the range of 100 Hz to 7 kHz with an amplitude of 300 mV between the inner electrode and one of the four outer contacts of a piezo. To study the cross coupling between different piezo tubes, the piezoelectric voltage signal at other piezo tubes was monitored in parallel and perpendicular direction (configuration 1). Strong resonances were found at around 680 Hz, 1 kHz, and 3.6 kHz and are listed in Table 2.2. In a second configuration, it was also tested if the scan piezo itself is subject to resonance effects during scanning at high speed. For this purpose the "x+" contact of the central piezo was excited by the sinusoidal voltage and the response was monitored at the "x-"

and one y contact (configuration 2). Resonances were only found in parallel direction at around 6.6 kHz and 6.8 kHz.

Table 2.2: Overview of the measured major resonance frequencies of the VT-STM setup. The gray circle represents the aluminum body of the STM beetle. Numbers I to IV mark the four different piezoelectric tubes.

Configuration 1		**Configuration 2**	
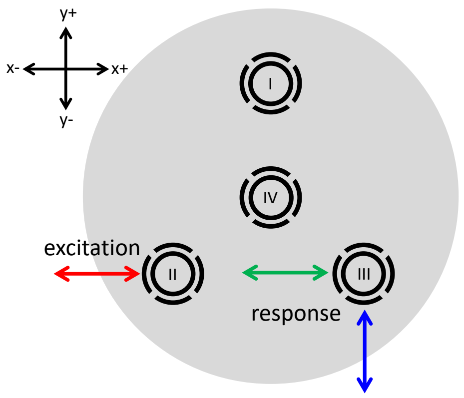		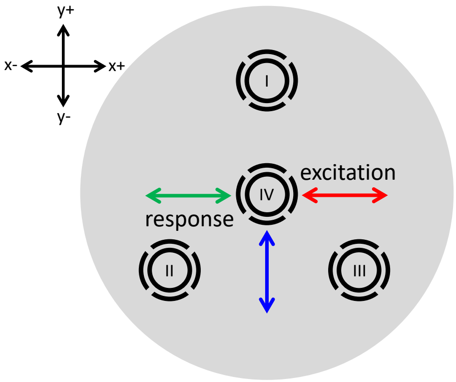	
resonance frequencies [Hz]		resonance frequencies [Hz]	
parallel	perpendicular	parallel	perpendicular
680	-	6620	-
1010	1010	6800	-
3550	3570		
3620	3620		
3660	-		

In literature, the causes of the vibrational response of a *beetle-type* STM were investigated by Behler and coworkers.[83] Strong resonances were found in a wide frequency range between 3 and 10 kHz. Supported by theoretical calculations these could be attributed to intrinsic resonant modes of the STM head, such as translational and rotational motions. This is in good agreement with the higher resonance frequencies found in configuration 1 for the STM setup and also with the resonance frequencies identified in configuration 2. Modes that are only detected in the parallel direction correspond to a pure translational mode, e.g., at

3660 Hz, while resonances that appear in both, parallel and perpendicular direction, e.g., at 3620 Hz, may result from a rotational or more complicated mode.

Furthermore Behler *et al.* detected several less strong but quite sharp resonances in the range between 500 and 1700 Hz.[83] The amplitude and the frequencies at which these occurred turned out to be strongly dependent on the position of the STM head on the helical ramp of the sample holder and thus were ascribed to result from a "rattling", as it was termed in the work of Behler *et al.*, of the whole STM head on the sample holder. Most probably the resonances found in the present STM setup at 680 and 1010 Hz can also be attributed to such a "rattling" of the STM head. This assumption is supported by the following observation: While setting up the video mode of the STM, a scan frequency of exactly 1 kHz was often used for testing purposes. Sometimes it was possible to obtain atomically resolved images, while in one of the next experiments, in which the STM head was repositioned on the sample ramp, imaging at 1 kHz turned out to be impossible. This strongly hints at a vibrational mode that is dependent on the contact of the STM head via the stainless steel balls to the helical ramp. Such "rattling" resonances can be somewhat annoying as they appear at different and non-predictable frequencies in every measurement. However, their appearance can also be easily changed for better or for worse by moving the STM head by a few μm.

Although during an STM experiment the excitation occurs at the tip piezo, like in configuration 2, the comparison with the literature as well as the observed behavior of the STM, described above, show that both configurations are suitable to detect relevant eigenmodes of the STM. The first measured intrinsic resonance frequency of the STM head at around 3.5 kHz is thus below the intended line frequency of 4 kHz. However, the mechanical resonances do not act as an upper limit for the possible scan frequencies. That *beetle-type* STMs can be operated at frequencies above or in between resonant modes was shown by Esch *et al.*.[59]

The usual waveform for the tip movement in the line direction is a triangular wave, see Figure 2.6, upper inset. Each single triangle therein corresponds to a back and forth movement of the tip to image one line of the sample in forward and backward direction. This scan wave is commonly used, since the linear slope, i.e., the linear relation between tip position and time, results in a uniform spatial width of all pixels. No image distortions are introduced. However, these triangular scan waves do also contain higher frequency components besides the fundamental scan frequency. Figure 2.6 shows the *Fourier transform* (FT) of the triangular-shaped wave with a frequency of 1000 Hz in the upper panel. Besides the main frequency at 1000 Hz several higher frequency components are visible in the FT transform. Thus, when using triangular waves for scanning of the tip unwanted mechanical resonances of the setup might be excited by the higher frequency components, even when the base frequency of the scan wave is still far below the resonant modes. Scanning close to or in between resonant modes of the STM is almost impossible with this kind of scan wave.

This problem can be avoided, if a pure sine wave is used for scanning, as first proposed by Wintterlin *et al.*.[41] A sine wave with a frequency of 1000 Hz only contains one distinct frequency in the FT transform (Figure 2.6, lower panel). By using the sinusoidal scan function one can thus drive the tip close to the eigenmodes of the STM without interference with the resonant modes of the STM.

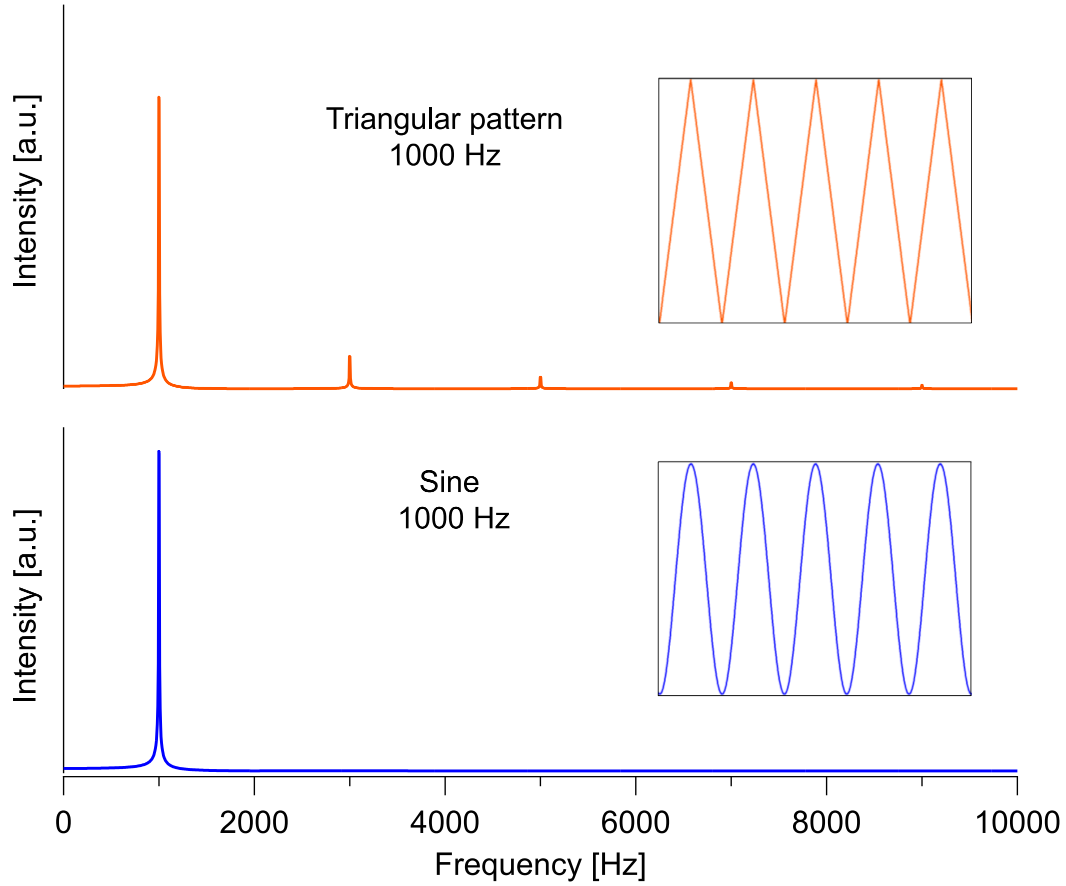

Figure 2.6: Fourier transform of a triangular scan wave and a sinusoidal scan wave with a frequency of 1000 Hz. Time plots of the two different scan waves are shown in the respective inset.

The use of a sinusoidal scan wave has been adopted since then by several groups for fast-scanning applications[58, 59] and it is also employed in this work to enable video-rate scanning. The price to be paid for scanning with a sine wave is image distortions (see section 2.6.2), as the tip-to-sample velocity changes along the image. The deformed images thus have to be corrected in the post-processing of the STM data. This step will be discussed in section 3.3.

2.5.3 Video-STM Software

The functionalities of the DAQ device *PCIe 6361* were set and controlled by a customized *IGOR Pro* graphical user interface (GUI) using the software add-on *NIDAQ Tools MX* (both by *Wavemetrics*). As a starting point for the development of the Video-STM software in the *IGOR Pro* environment, Prof. Dr. Rolf Schuster provided an STM control and image acquisition program as used in his working group at the *KIT* for conventional STM studies. This software was modified and enhanced in the scope of this work to achieve compatibility with the existent hardware setup and to match the defined speed demands for Video-STM. The structure and features of the new Video-STM software are described in the following.

- **Full control of all scan parameters**

  Scan parameters, such as the image size in Ångströms and in pixels, a possible offset of the imaged area, the scan speed, and the conversion factors in x, y, and z direction are set in the GUI. Furthermore, three different imaging modes that determine in which way images are scanned in y direction have been implemented: an upward, a downward, and a combined upward/downward imaging mode. In the upward mode acquisition starts in the lower left corner of an image and the frame is build up line by line from bottom to top. The upper left corner is the starting point for imaging in the downward mode from top to bottom. In the combined mode consecutive images are alternately scanned in upward or downward direction.

- **Selection between two input signals: z and I_t**

  It can be selected whether the z signal, corresponding to the *constant-current* mode, or the tunneling current I_t, corresponding to the *constant-height* mode, is used as input signal. This signal is then read out from the DAQ device, displayed and subsequently saved.

- **Two measurement modes: a conventional and a video mode.**

  Furthermore two different scan modes are available: a conventional scan mode and a video mode, and the software can switch between these two modes. In the conventional mode scan ramps have the common triangular shape, whereas in the video mode sinusoidal ramps are used. As a careful design of the scan ramps turned out to be crucial for the resulting image quality when scanning at video-rate, a detailed description of the scan ramp signals follows in the subsequent section 2.5.3.1.

- **Signal averaging to enhance signal-to-noise ratio (conventional mode only)**

  In the slow scanning mode, when the effective scan speed is well below the maximum sampling rate of the DAQ device (<2 MHz), the signal value for one pixel is obtained by averaging over multiple measurements at the same position in order to improve the signal-to-noise ratio. For each measurement, the number of measurements Z_{av} at a point is calculated by the software depending on the set scan speed and image resolution. In the video mode Z_{av} is always set to one.

- **Three live display modes of the collected data**

  The software provides three modes for displaying the STM data during an ongoing recording process. The unmodified original data and a background corrected version of the current data input can be displayed. For background correction, each image line is scaled between 0 and 1 and displayed in the full range of the gray scale. As a third mode, it is also possible to display a height profile of the currently scanned line, i.e., the measured signal in Volts versus the line pixels, corresponding to $z(x)$ or $I_t(x)$ for *constant-current* or *constant-height* mode, respectively.

  Therefore, the input signal in Volts is plotted against the line pixels. Using the *z conversion*, the input voltage is also translated into a height variation in Ångströms for scans in the *constant-current* mode.

- **"Safe modes" in tip control**

  To avoid jumps in the supply voltage of the tip piezo that could lead to tip-sample crashes, the software features "safe modes" that control the tip movement immediately before and after the imaging process. Before starting the scanning process, the tip is slowly driven to its starting position for the subsequent image acquisition. After termination of the imaging process, the tip is safely brought back from its current position to its zero position (compare section 2.5.3.1 "Scan Ramp Generation").

- **Clear and easy to use GUI**

  A GUI was developed for easy control and monitoring of the scan and data acquisition process during a measurement. A screenshot of the finalized GUI is shown in Figure 2.7. Panels for setting and monitoring scan and acquisition parameters are framed in orange. Windows for representation of the currently acquired data are framed in purple. Additionally, the *IGOR Pro* history (framed in green) is useful to monitor the status of the ongoing data acquisition process.

- **Matching of the defined speed requirements**

  In the current configuration the Video-STM software provides reliable and stable STM control and data acquisition with all three display modes enabled up to a sampling rate of 1.8 MHz. When turning off the live background correction of the collected data, the software also allows for sampling at the maximum rate of the DAQ device (2 MHz). The combined hardware and software system thus fulfills the defined speed requirement of 1.6 MHz in all modes of operation. The resulting STM movies consist of up to $3 \cdot 10^8$ data points, corresponding to 3731 images in one measurement for the typical 200 x 200 pixel image size. Depending on the respective imaging rate, this equals three (20 images/s) to six minutes (10 images/s) of steady imaging of the sample surface. Data are saved as an *igor binary wave* (*.ibw*) file, which ensures compatibility with the established STM analysis tools. The specific realization of the data readout from the DAQ device as well as the saving procedure were speed-critical for the video-rate data acquisition. Therefore, these steps are presented in detail in section 2.5.3.2.

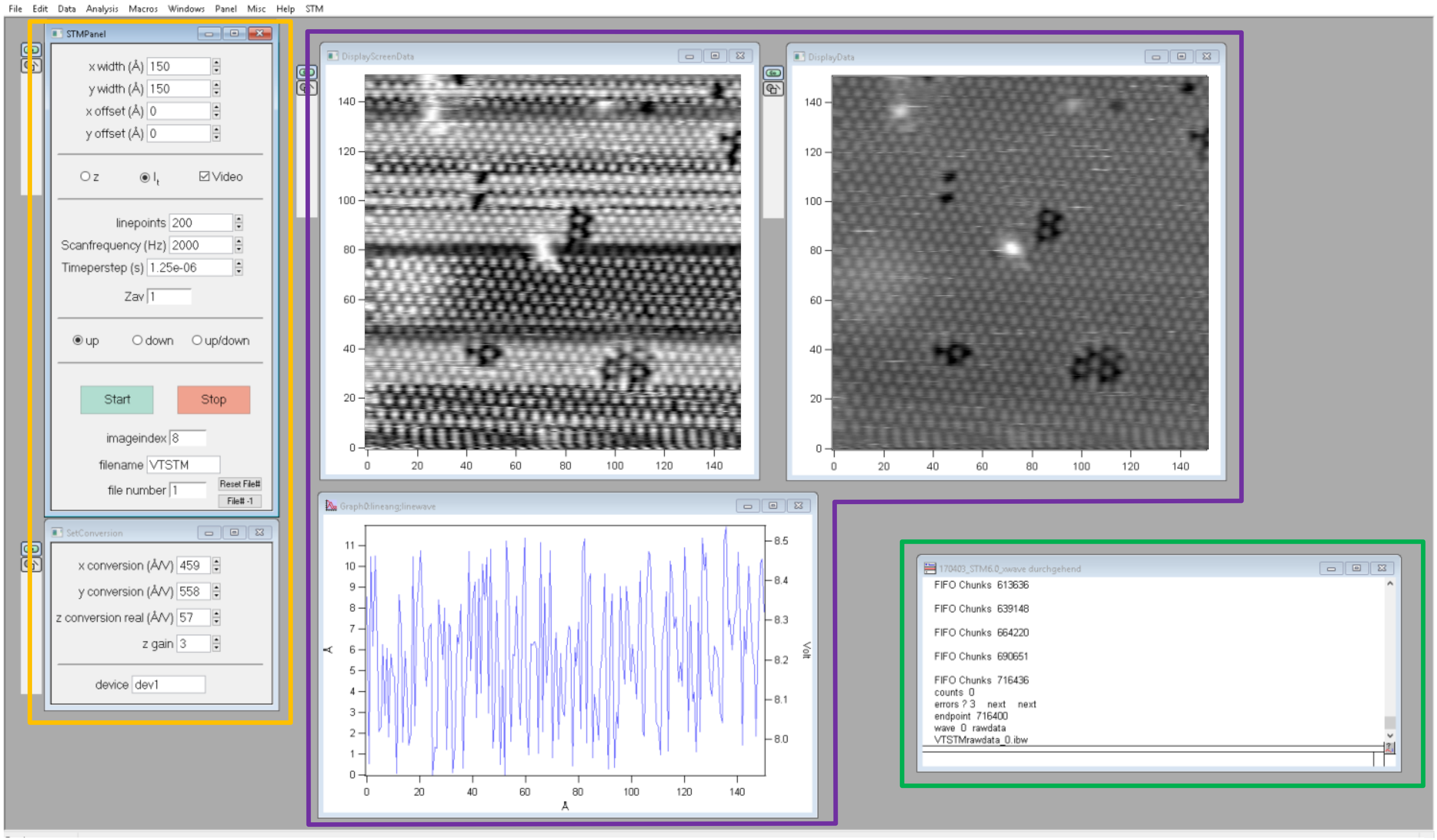

x width (Å) 150
y width (Å) 150
x offset (Å) 0
y offset (Å) 0
☑ Video
linepoints 200
Scanfrequency (Hz) 2000
Timeperstep (s) 1.25e-06
Zav 1
● up ○ down ○ up/down
imageindex 8
filename VTSTM
file number 1

x conversion (Å/V) 459
y conversion (Å/V) 558
z conversion real (Å/V) 57
z gain 3
device dev1

```
FIFO Chunks  613636

FIFO Chunks  639148

FIFO Chunks  664220

FIFO Chunks  690651

FIFO Chunks  716436
counts  0
errors ? 3    next    next
endpoint  716400
wave  0  rawdata
VTSTMrawdata_0.ibw
```

Figure 2.7: Screenshot of the Video-STM *IGOR Pro* GUI. Scan and acquisition control panels are framed in orange, windows for displaying the STM data in purple and the *IGOR Pro* history in green.

2.5.3.1 Scan Ramp Generation

As the shape of the scan ramps strongly influences the imaging process, the design of the scan ramps implemented in the Video-STM software, is presented in detail in the following. Exemplarily, Figure 2.8 shows the scan ramps in *x* (blue) and *y* (red) direction in the conventional scanning mode for the following set of parameters:

- *x width*, *y width*: 1000 Å
- *x offset*, *y offset*: 0 Å
- *x conversion*, *y conversion*: 500 Å/V
- *linepoints*: 50
- *Scanfrequency*: 50 Hz
- Z_{av}: 1
- Imaging mode: *upward*

x width and *y width* denote the scan range in Ångströms. The parameter *linepoints* represents the number of pixels in *x* and *y* direction of the resulting image. The number of pixels is always the same in *x* and *y* direction to enable exact timing of both ramps; however, scan amplitudes can be different. The scan speed is determined by the parameter *Scanfrequency*, which is the line frequency in the fast-scanning direction in Hz, i.e., the inverse time for one forward and one backward scan of the tip.

The scan range in Å divided by the respective conversion factor determines the amplitude of the scan waves. In the present example the peak to peak amplitude for both waves is 2 V ($1000\ \text{Å} / 500 \text{Å}\cdot\text{V}^{-1}$). In order to allow for large scan areas, scan ramps are generated in such a way that the image center is the point of zero voltage supply at the piezo contacts (for the case of no applied offset). Both, the *x* and the *y* ramp are thus centered around 0 V.

According to the preset number of *linepoints*, the *x* ramp consists of 50 triangles, each representing a single line of the resulting image. During these 50 triangles the *y* ramp is gradually increased in 50 steps from -1 to +1 V, giving in total 50 lines. A more detailed view of the scan waves of Figure 2.8 between 0.94 and 1.02 s is shown in Figure 2.9 a). The linear increase of the voltage in the first half of a triangle describes a forward scan of the STM tip in *x* direction, followed by the inverse motion (backward scan) as the voltage decreases again. Each triangle consists of

100 data points, 50 in the forward and 50 in the backward scan. The image will later be built up by using only forward or only backward scans.

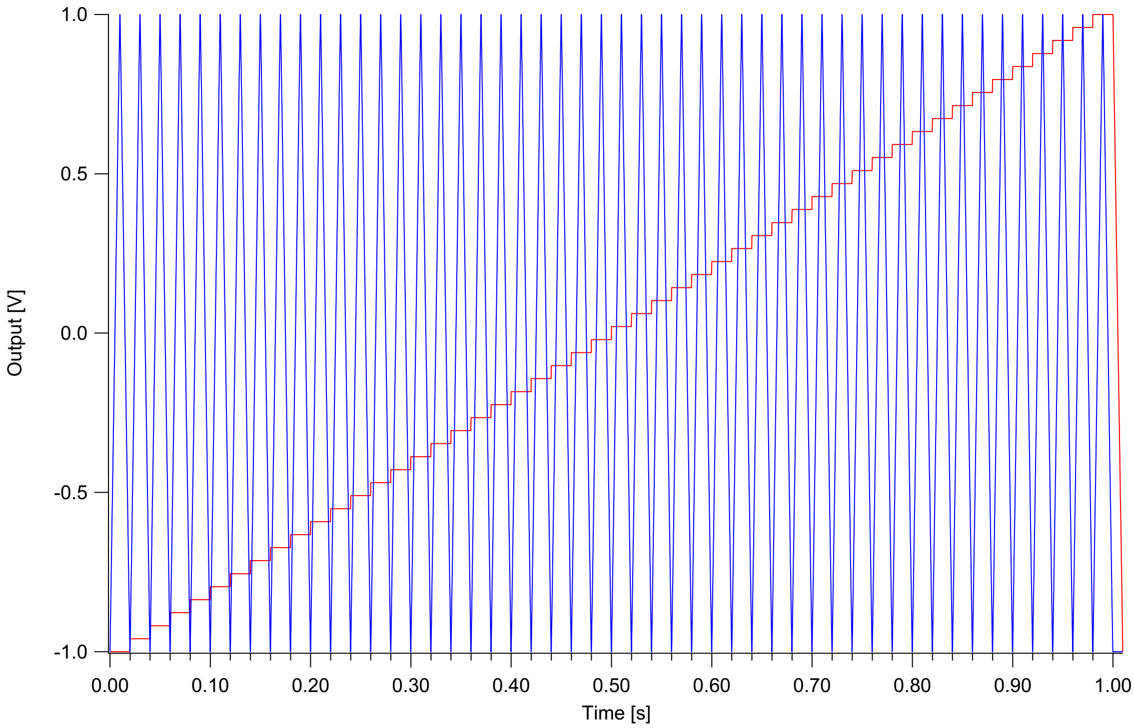

Figure 2.8: Scan ramps in *x* (blue) and *y* (red) direction for a complete 50 x 50 pixels image acquired with a scan frequency of 50 Hz in the upward imaging mode.

According to the scan frequency (=line frequency) of 50 Hz in the example, each triangle takes exactly 0.02 s, giving a total time of 1.00 s for the 50 lines. Yet the overall time for the full image (Figure 2.8) is somewhat higher. This is because the ramps are exemplarily shown for imaging in the *upward* mode and thus also have to include a back scan from top to bottom in *y* direction in between two consecutive images. The vertical black line in Figure 2.9 a) marks the completion of the image. To reach the starting point of the successive image, the *y* ramp is linearly decreased to its initial value, during which the tip does not move in *x* direction. The back scan in *y* takes half the time (0.01 s) of a full line scan in *x*.

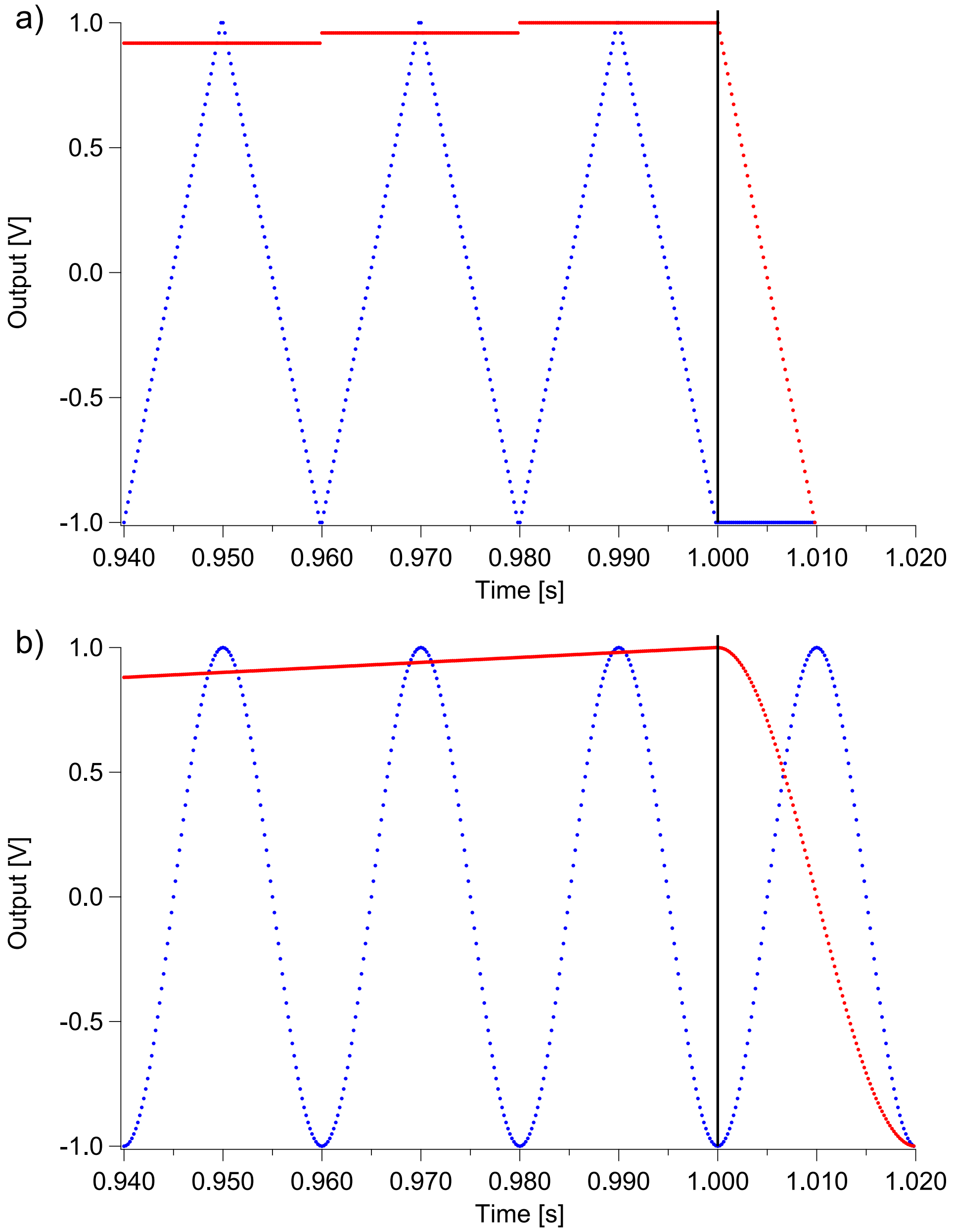

Figure 2.9: Comparison of the scan ramps a) in the conventional and b) in the video mode. *x* ramps are depicted in blue, *y* ramps in red; each dot corresponds to a set voltage and a data point. a) Zoom-in into the scan ramps of Figure 2.8 between 0.940 and 1.020 s. Shown are the last three lines and the back scan in *y* direction of a 50 x 50 pixels image acquired with a scan frequency of 50 Hz in the upward imaging mode. b) Scan ramps in the video mode with the same imaging parameters as for a). Each image line is represented by a full period of a sine function. The back scan in *y* is designed as a half sine wave with doubled wavelength in comparison to the *x* ramp.

In the video mode, the triangular wave form of the *x* ramp is replaced by a sinusoidal wave. Figure 2.9 b) shows the respective scan waves in the video mode for the same parameter set as in Figure 2.9 a). Each image line is now described by a full period of a sine function. In contrast to the ramps in the conventional scan mode, the *y* ramp no longer follows a stepwise increase, but rises continuously throughout the whole image acquisition process. This is done to avoid any discontinuities when scanning in the fast mode, since any abrupt change in the tip movement can induce image distortions. Another difference lies in the shape of the back scan in *y* direction. In order to avoid an abrupt stop, the scanning in *x* direction is continued during the back scan in *y* direction, see Figure 2.9 b). For this reason, the time for the back scan in *y* is expanded to a full *x* sine wavelength. Furthermore the back scan is not performed in a linear way but as a half sine function. In this way the crossover between the linear *y* ramp and the back scan is rounded off, for the same reason as above.

As the point at which a voltage of zero is applied to the scan piezo (0,0) is set to the image center, particular attention must be paid to the start of a measurement as the piezo will otherwise jump in one step to the starting point at (-1,-1). Such uncontrolled movements of the STM tip have to be avoided as they involve a high risk of tip crashes with the sample. Therefore, after initiating a measurement with the software, linear waves (one in *x* and one in *y* direction) are generated that slowly bring the tip to its starting point before the actual imaging process begins. The motion of the tip on the way to the starting point is slowed down by a factor of three compared to the scan speed in the following image acquisition process. A similar problem arises after termination of the measurement, because in this moment the tip might be located at any point in the image and would directly jump to the image center, since no scan ramps are applied anymore. To avoid this, an internal counter of the DAQ device is used to calculate the actual position of the tip in the image at the end of the measurement and the tip is safely brought back from its position to the (0,0) origin.

2.5.3.2 Data Readout and Saving

The DAQ device contains an onboard FIFO memory in which the data are stored after analog-to-digital conversion for intermediate buffering. From the FIFO the data are frequently forwarded to the *IGOR Pro* software and stored in a one-dimensional (1D) buffer data wave. This buffer wave thus always contains the most recently collected data, i.e., the latest readout of the FIFO. Subsequently the data are transferred into a predefined 1D data wave of $1 \cdot 10^8$ (normal mode) or $3 \cdot 10^8$ chunk size (video mode), in which all acquired data points from a measurement are concatenated in series. To meet the speed requirements, the complete memory for this large wave is allocated in the random access memory (RAM) at the beginning of the acquisition process. During the measurement, this predefined empty space is consecutively filled with the recorded data points.

If the pre-allocated memory for the data wave is not completely used at the end of a measurement, all empty entries in the wave are deleted in order to reduce the memory required for saving. The data wave is subsequently automatically saved to the hard disk as an *.ibw* file together with a second file that contains the software-controlled parameters of the measurement. The entries of this parameter file can be used in the later data processing to generate the images from the one-dimensional wave and to reproduce measurement conditions.

Figure 2.10 shows an example of a one-dimensional data wave that contains ~$1.8 \cdot 10^8$ data points, as saved by the Video-STM software. The wave represents a movie of 2208 consecutive STM images from a measurement in *quasi constant-height* mode. The wave content is the amplified and converted tunneling current signal in Volts (amplification factor: 10^8 V/A). The tunneling current is negative, because a negative tunneling voltage was used.

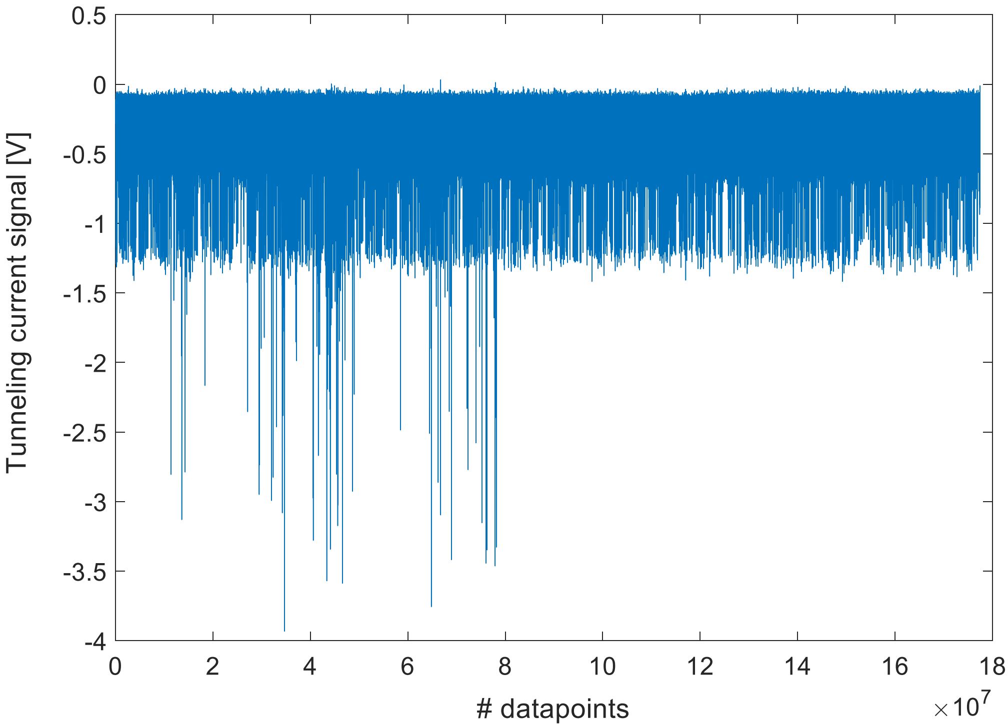

Figure 2.10: Example of the saved output of the Video-STM software. The depicted data wave represents a movie of 2208 consecutive STM images acquired in *quasi constant-height* mode.

With the current software/hardware combination, it is not possible to directly write the data wave to hard disk during an ongoing data acquisition as hard drive accession times are too long (in the millisecond range). New generation SSDs (solid state drives) with write latencies in the µs regime may be capable of overcoming this restriction and enabling direct saving of the data on-line without a need for the intermediate step using the RAM. As the Video-STM software has been developed in *IGOR Pro* Version 6.02A, which is a 32 bit program, the maximum RAM space the program can access is limited to approximately 2 GB. The reason for this is that a 32 bit program can only address 2^{32} Bytes ~ 4 GB of memory. Under *Windows* operating systems half of this memory is reserved for system resources, so that only ~2 GB remain usable for the program. In the present configuration, the size of the data wave is thus limited to the available allocated storage space in the RAM and restricts the maximum number of data points that can be acquired in one measurement to around $3 \cdot 10^8$. This is not a severe drawback, however, as it still allows for the acquisition of more than 3700 consecutive images (200 x 200 pixels). Furthermore after termination of the data acquisition process for saving, a new measurement can be started within less than half a minute. As an outlook on future work, the upgrade of the Video-STM software to the now available 64 bit versions of *IGOR Pro*, *IGOR Pro 7* and *IGOR Pro 8*, would give access to more RAM space and thus annihilate the current data limitation for the data wave.

2.6 Implications of the Video Mode

With the described hardware and software setup, Video-STM measurements with imaging rates that match the design requirements are possible. However, the design of the scan ramps as well as the fact that the STM is driven close to its eigenmodes have several effects on the appearance of the acquired images. This section provides a description of the image deformations as well as their causes. Some of the distortions can already be corrected on-line during a measurement; others have to be removed during post-processing of the STM data.

2.6.1 Phase Shift

When driving an oscillator close to its eigenfrequencies, the phase of the actual oscillation falls behind the phase of the exciting force. In principle, this phase shift can be calculated from the amplitude and frequency of the driving force and the eigenfrequency of the oscillator.[86] This effect of phase-shift is also observed when scanning the STM tip at high speed. The phase of the actual piezo movement is changed with respect to the phase of the electronic drive signal, resulting in a distortion, in particular the appearance of a vertical mirror axis in the images. An example for this effect is shown in Figure 2.11 a). The STM image shows an ordered $(\sqrt{3} \times \sqrt{3})R30°$ structure of CO molecules on a Ru(0001) surface. CO molecules are imaged as dark spots.

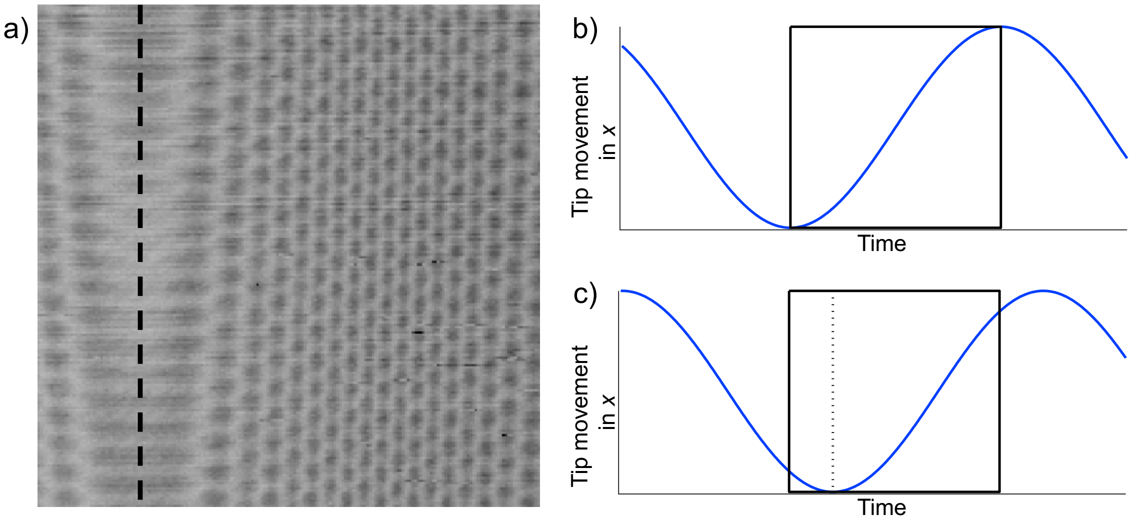

Figure 2.11: A phase shift between actual tip motion and the scan signal leads to the appearance of a vertical mirror plane in the image, indicated by a dashed line in a). The 200 x 200 pixels image was acquired with a scan frequency of 2 kHz. (V_t = -0.22 V, I_t = 10 nA, ~85Å · 85Å). b) Ideal imaging: The extrema of tip movement (blue) and the image edges are synchronized. c) Delay between actual tip motion and imaging: The tip movement is phase-shifted with respect to the image edges.

The mirror axis, marked by the black dashed line, results from the inversion of the scanning direction of the tip. Ideally, the extreme points of the tip movement in *x* direction, see blue curve in Figure 2.11 b), are aligned with the edges of the image (black box). For high scan frequencies a delay in the actual tip motion occurs. The actual mechanical tip movement is then phase-shifted with respect to the driving voltage that defines the image edges, see Figure 2.11 c). However, in contrast to the model of a conventional forced oscillator, the phase shift occurring here is not only dependent on the resonance frequency of the STM but also on the STM electronics.

Nevertheless, the lag between excitation signal and tip motion turned out to be well predictable and just depending on the scan frequency: the higher the scan frequency, the larger the phase shift. Moreover, the phase shift is perfectly stable throughout a measurement for a given set of scan parameters, so that a phase correction needs to be determined only once at the beginning of the data acquisition. Experimentally determined delays between actual tip movement and excitation signal are listed in Table 2.3 for several scan frequencies.

Table 2.3: Measured phase shift between tip motion and the electronic excitation signal in dependency of the scan frequency between 500 and 3000 Hz.

Scan Frequency	Phase Shift	
500 Hz	0.07π	12.7°
1000 Hz	0.10π	18.3°
1500 Hz	0.17π	32.3°
2000 Hz	0.21π	41.3°
2500 Hz	0.25π	51.8°
3000 Hz	0.27π	58.0°

In principle, this effect could be easily removed in the post-processing of the image data, but it is of great benefit to obtain an almost undistorted image already while monitoring and controlling data acquisition. For this purpose, a tunable analog phase shifter, built at the *FHI* Berlin, was introduced into the STM electronic setup to manually match mirror axis and image edge. The phase shifter is implemented in the signal route of the fast-scanning signal (*x* ramp) between DAC unit and power amplifiers as indicated in Figure 2.14. As the phase shifter works properly only for pure sinusoidal signals, an analog switch was installed prior to the phase shifter to bypass it when not scanning in the video mode. The triangular scan wave in the conventional scan mode would otherwise become highly distorted by the phase shifter.

2.6.2 Sine Scanning

With the on-line phase-corrected STM, images acquired in the video mode look like the one shown in Figure 2.12 a). The ordered CO superstructure is deformed in *x* direction as a result of the sinusoidal scan wave. That is because during a measurement pixels are acquired in equidistant time intervals, depicted as uniform black and gray boxes on the *x* axis in Figure 2.12 b). Due to the shape of the scan wave, the spatial information is not uniformly distributed over the pixels (*y* axis). The slope of the scan wave near the image edges is small implicating a smaller displacement of the tip during acquisition of the outer pixels of a line. For this reason the CO molecules at the image edges in Figure 2.12 a) appear strongly elongated in *x* direction. In the center of a line, the slope of the sine wave is greater than one. Features thus appear compressed with respect to conventional imaging with a linear scan ramp.

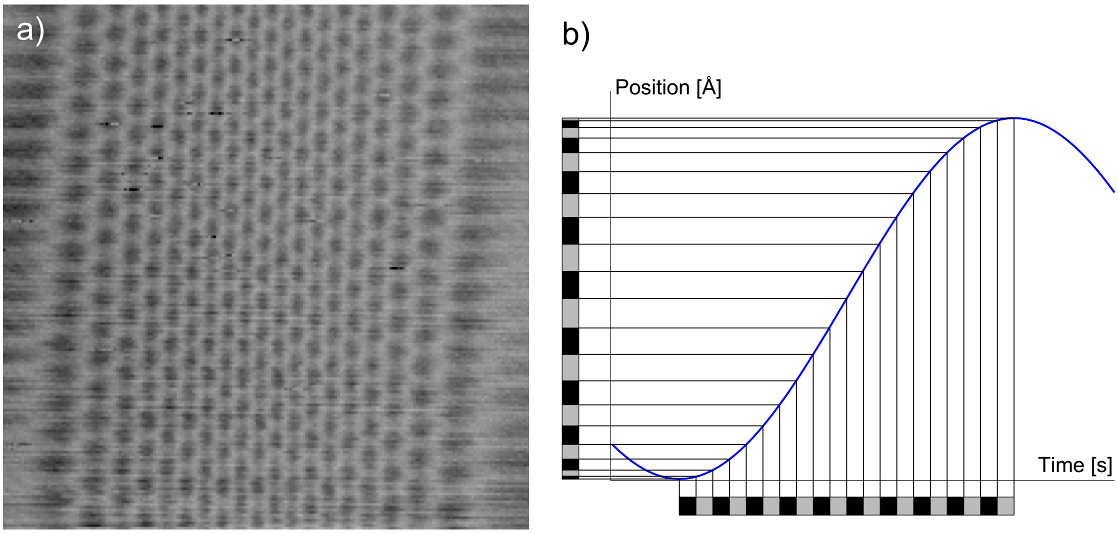

Figure 2.12: Deformation of STM images introduced by the use of a sinusoidal *x* scan ramp. a) The projection of the periodic CO-($\sqrt{3} \times \sqrt{3}$)R30° structure on Ru(0001) illustrates the non-uniform tip-sample velocity in *x* direction (V_t = -0.22 V, I_t = 10 nA, ~85Å · 85Å). b) Pixels acquired at equal time intervals (*x* axis) result in an inhomogeneous distribution of spatial information (*y* axis).

Image deformation due to the use of a sinusoidal scan ramp in *x* direction is not corrected on-line during a measurement, since it would require too much computational resource and thus decelerate data uptake. A post-processing routine developed to rectify the STM images is described in section 3.3.

2.6.3 Vibration Artifacts

Sudden changes in the tip movement can induce transient distortions in the images. An example for such an effect is illustrated in Figure 2.13. It shows the first two images of an STM movie acquired at an imaging rate of 10 Hz at room temperature. Frame 1 of the movie exhibits bright and dark stripes roughly oriented along the *x* direction that are most prominent in the lower part, but are visible throughout the whole image. The major component is an oscillation of the tip-sample distance along the *y* direction. These distortions have almost completely vanished in the second frame of the movie.

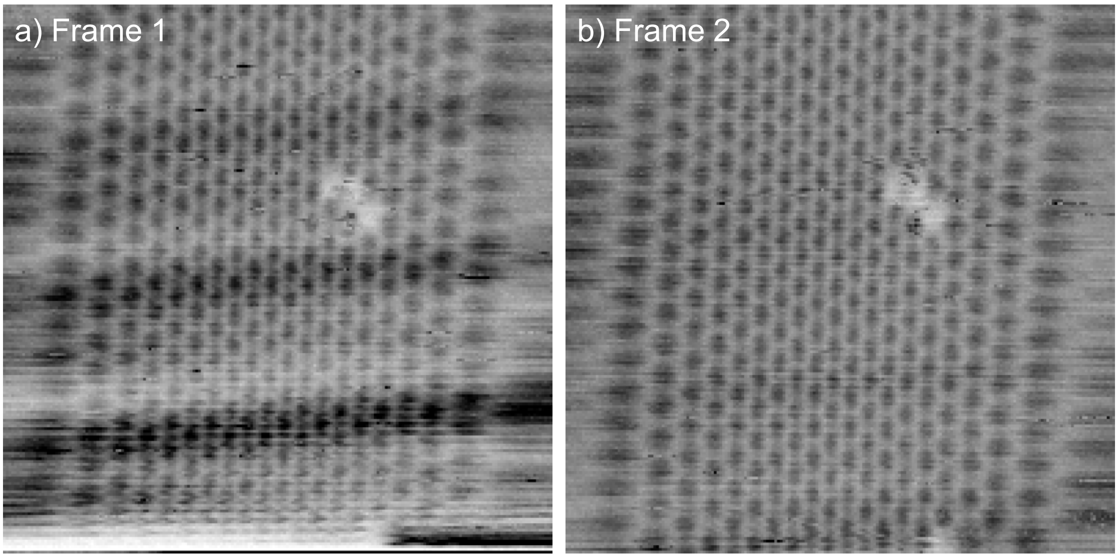

Figure 2.13: Comparison of the first and the second frame of an STM movie, taken with an imaging rate of 10 Hz in the upward imaging mode (V_t = -0.22 V, I_t = 10 nA, ~85Å · 85Å). Starting point for image acquisition is the lower left corner. The first image shows the presence of vertical vibrations of the tip along the slow scanning direction (*y* direction), which disappeared in frame 2. These vibrations result from the initiation of the scanning process. Both images exhibit additional, less pronounced artifacts in the first scanned lines that can be attributed to the back scan in *y* in between images.

Similar strong artifacts as in Figure 2.13 a) appear in the first image of every movie acquired in the video mode. As these features disappear almost completely in the consecutive images, they can be attributed to the initiation of the scanning process at the beginning of each measurement. The abrupt transition from the slower movement during the linear motion to the starting position of image acquisition to the fast sinusoidal scan wave obviously excites transient responses of the STM head that lead to those imaging artifacts.

These findings underline the importance of a continuous scan motion of the tip throughout the whole measurement, also in between the acquisition of images. Stopping of the tip in x direction, e.g., during a back scan in y direction, results in similar strong artifacts in every image, which could be avoided by a careful design of the scan ramps, compare Figure 2.9 b).

In addition much less pronounced distortions in the first few lines are also present in the second, see Figure 2.13 b), and all subsequent frames of the movie. As the scanning motion in x is not interrupted, these distortions have to be attributed to the back scan in y direction between two consecutive images. These might arise partly from ongoing creep of the piezoelectric scanner in y direction after the completion of the back scan. Partly they might arise from transient mechanical vibrations of the STM head that are excited by the comparatively abrupt changes of the tip motion during a back scan. The transition from the slowly increasing linear y ramp to the rapid sinusoidal back scan and vice versa contains high frequency components that are capable of exciting vibrations, when close to an eigenmode of the STM. A post-processing algorithm to remove these artifacts is presented in section 3.4.3.1.

2.7 Summary

2.7.1 The new Setup

A scheme of the complete revised STM setup is depicted in Figure 2.14. The configuration for video-rate scanning in the *quasi constant-height* mode is shown in solid black, while modifications needed for measurements in the conventional *constant-current* mode are indicated in gray.

The digital part of the setup has been completely newly designed. A *National Instruments PCIe 6361* DAQ device is used for signal conversion. The DAQ device can be integrated into any normal PC via a *PCIe* interface. Scan ramp output and data acquisition is controlled via an *IGOR Pro* software, developed in the course of this work. Conversion rates of the DAQ device fully satisfy the demand of 1.6 MHz defined in section 2.4. Input and output ranges as well as the bit resolution of the DAQ device are identical to the DAC and ADC units of the initial VT-STM configuration, guaranteeing the same lateral and vertical resolution in the new setup in comparison to the old one.

For an on-line phase correction when scanning in the video mode, the *x* ramp signal is routed through an analog phase shifter. As a phase correction is not necessary (and detrimental) in the conventional scan mode, an analog switch may be used to bypass the phase shifter. The previously used commercial current preamplifier has been replaced by a home-built version that features a bandwidth of 300 kHz and thus allows for imaging with atomic resolution in the fast scan mode.

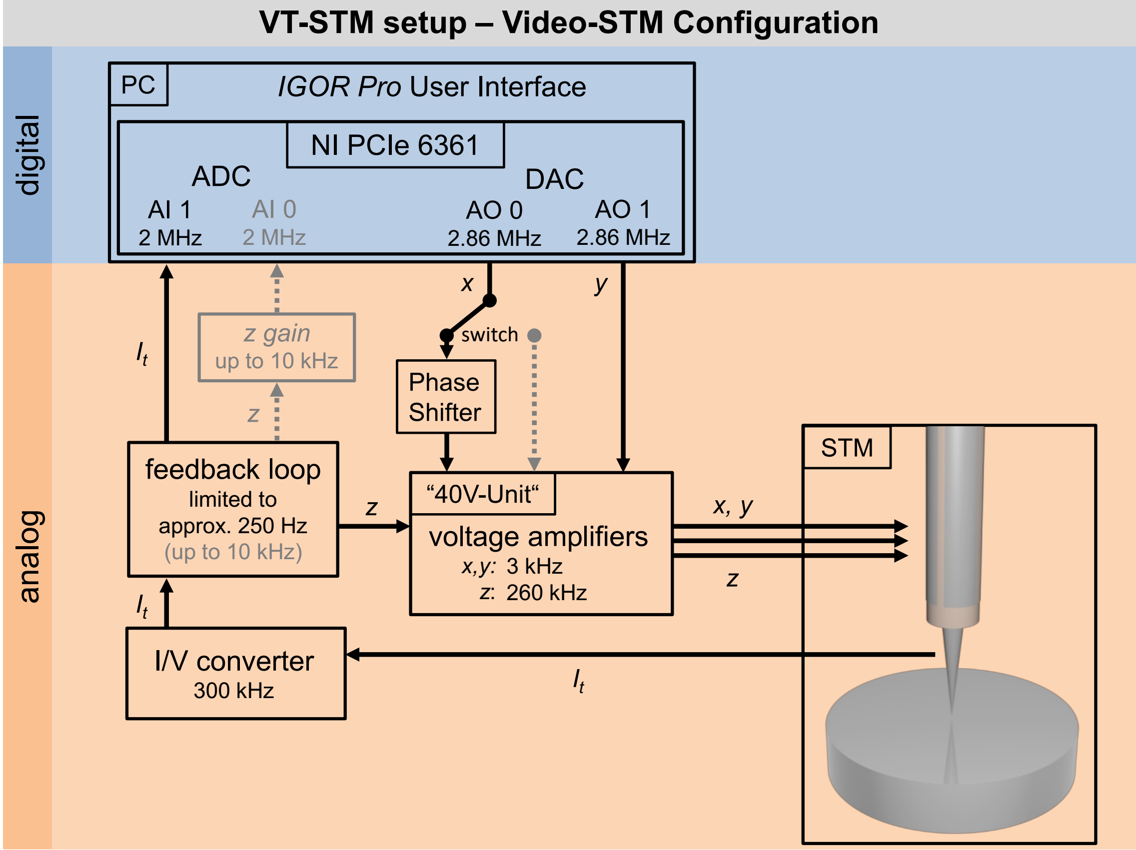

Figure 2.14: Block diagram of the revised VT-STM setup developed to enable Video-STM scanning. The digital scan control and data acquisition system is highlighted in blue, the analog signal part of the setup in orange. The configuration for video-rate scanning in the *quasi constant-height* mode and the corresponding bandwidths are indicated in black. Modifications needed when scanning in the conventional slow mode are shown in gray.

In the *quasi constant-height* mode, the structural information of the sample surface is contained in the tunneling current signal I_t, which is read from the DAQ device by selection in the GUI. The response of the feedback loop is limited to around

250 Hz, sufficient to correct for drift and tilting of the sample in the slow scanning direction. When switching back to the conventional slow scan mode, the bandwidth of the feedback loop can be increased again to typical values of around 2.3 kHz with a potentiometer. The input signal type may be changed to the *z* signal by choice in the Video-STM software.

2.7.2 Performance

All components, hardware and software, allow for scanning with data rates well above the required 1.6 MHz. Therefore, the goal of being able to scan images with 200 x 200 pixel resolution at an imaging rate of 20 frames per second is achieved. However experiments revealed that scanning with the intended line frequency of 4 kHz is impeded by the mechanical properties of the STM itself. Movies showing atomic resolution were obtained for scan frequencies up to 3.3 kHz and then again for 5 kHz. Scanning in between those two line frequencies was tried several times for different scan frequencies, e.g., 3.6, 4.0 and 4.5 kHz, but turned out to be challenging and usually quickly ended with a loss of resolution. In this frequency range the tip motion obviously excited mechanical resonances of the STM head that impaired resolution or even impeded imaging at all. This result is in agreement with the measured eigenmodes of the STM head at 3.5 to 3.7 kHz (see section 2.5.2).

For 200 x 200 pixel images a maximum frame rate of 15 Hz was realized. This rate corresponds to a scan frequency of 3 kHz and a data rate of 1.4 MHz. Scanning 200 x 200 pixel images at higher frequencies was firstly impeded by the resonance modes of the STM, as mentioned above. Secondly for scan frequencies at around 5 kHz, the corresponding data rate of 2.1 MHz exceeded the maximum sampling rates of the setup (2 MHz). However, these high scan frequencies could be realized by reduction of the pixel resolution. Table 2.4 shows the respective maximum realized imaging rates depending on the image size in pixels. With the new setup the acquisition of atomically resolved images was realized up to a rate of 50 Hz (100 x 100 pixel).

Table 2.4: Realized imaging rates for different image resolutions.

Pixel	Imaging Frequency	Scan Frequency	Data rate
200 x 200	15 Hz	3000 Hz	1.4 MHz
150 x 150	22 Hz	3300 Hz	1.1 MHz
100 x 100	50 Hz	5000 Hz	1.1 MHz

Figure 2.15 shows a selection of realized scan frequencies. For each chosen frequency a single STM image is depicted to illustrate the resolution and quality of the data. For all experiments the sample is a Ru(0001) single crystal covered by a full monolayer of CO (dark spheres). The ordered $(\sqrt{3} \times \sqrt{3})R30°$ structure of CO with a periodicity of ~4.7 Å is clearly resolved in all images. Some images additionally show single oxygen atoms (bright features) that are incorporated into the ordered CO structure. An overview of the measurement parameters of all images is given in Table B.4 in the appendix.

All images shown were acquired in the upward imaging mode. The vibrational artifacts in the first lines of each image, resulting from the back scan in *y* direction in between two images (compare section 2.6.3), are negligible for the scan frequencies up to around 2400 Hz. When going to higher frequencies they become more and more visible. These effects are attributed to a transient vibrational response of the STM to changes in the tip motion during the back scan in *y* direction. A faster back scan in *y* leads thus to a more significant distortion of the tip motion as it contains higher and more intense frequency components. The two images shown for the highest scan frequency of 5 kHz were acquired with identical scan parameters but were recorded on two different days. The occurrence of the distortions throughout the images is quite similar and supports the proposed nature of this distortion by excitation of an eigenfrequency of the STM head. Nevertheless, these images prove that the new STM setup allows for video-rate scanning over a wide range of scan frequencies, even above eigenfrequencies of the STM, while atomic resolution is preserved.

Furthermore the new setup with a DAQ system that is controlled by newly developed software offers the possibility for easy future modifications, e.g., of the scan ramp design, as all output and input signals are fully accessible. Virtually any signal form can be generated in the *IGOR Pro* user interface and output by the DAQ device. Moreover by combination with one or several other DAQ units, the DAQ device can be easily expanded to allow for other measurement modes such as *Scanning Tunneling Spectroscopy*.

Switching between the two scanning modes, i.e., the conventional slow and the video mode, is easy and does not require any hardware changes. The selection of the scan mode and the type of input signal is conveniently set in the software. Apart from that one only has to change the switch position at the phase shifter and set the bandwidth of the feedback loop by means of a potentiometer.

The implementation of the video mode was realized without affecting the properties of the original VT-STM setup. Therefore, with the combined Video-VT-STM setup, atomically resolved STM images could be scanned with up to 50 images per second, while the sample temperature is variable between -220 °C and +230 °C.

In principle the Video-STM setup is applicable to any conventional STM setup, as it does neither require a special design of the STM scanner itself nor a particular computer system for scan control and data readout. The Video-STM system can also easily be transferred to all existing STM setups in the Wintterlin group. Furthermore, the *.ibw* data format preserves compatibility with the originally used *IGOR Pro* routine for STM image analysis.

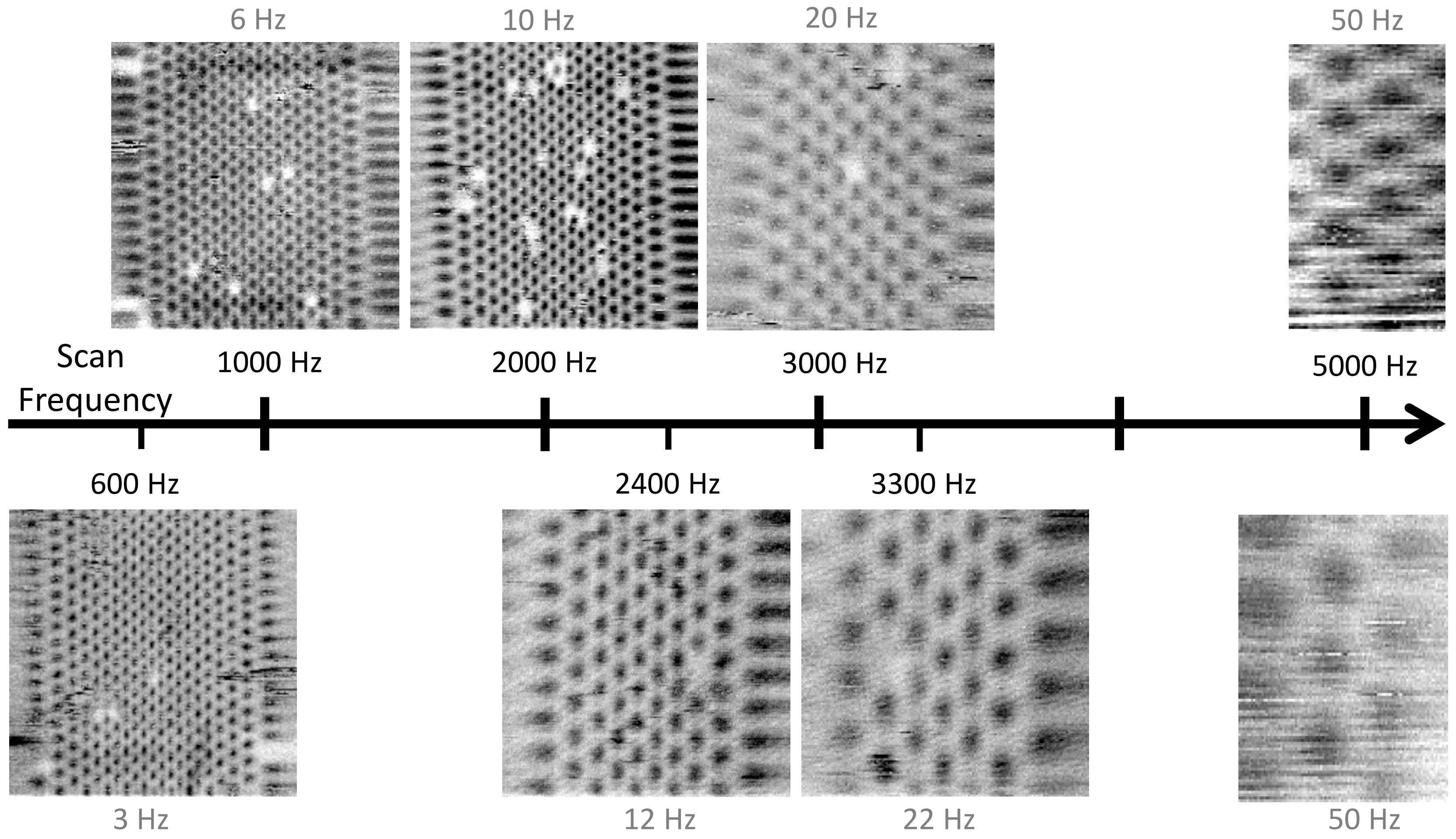

Figure 2.15: STM images of the $(\sqrt{3} \times \sqrt{3})R30°$ structure of CO molecules (dark) on Ru(0001) extracted from STM movies that were acquired at various scan (line) frequencies between 0.6 and 5 kHz (black labels). The corresponding frame rates are indicated in gray. Single oxygen atoms in the CO layer are imaged bright. All movies were acquired in the upward imaging mode. Scan parameters are listed in Table B.4 in the appendix.

3. Image Processing and Analysis

3.1 Introduction

The Video-VT-STM technique provides the opportunity to study dynamic processes on surfaces with atomic resolution. All dynamic effects, such as restructuring, epitaxial growth, and catalytic reactions, involve the diffusion of atoms, molecules, or larger particles. Because diffusion of single particles is a stochastic process, good statistics are required to access the underlying mechanisms. For STM, this means that the process of interest needs to be monitored many times and a high number of STM images has to be evaluated to extract statistically significant information on the dynamics. This can be done “by hand” by comparing the atomic configurations in hundreds of consecutive STM images. Such a time-consuming procedure would, however, severely restrict the statistical significance that can be achieved and thus the processes that can be studied. The development of automatic evaluation routines to analyze the process of interest in a more rapid and also reproducible manner is therefore worth striving for.

A central step to enable automated evaluation of STM movies is the detection of particles and their tracking through thousands of consecutive images. In the course of this work, this step was realized in cooperation with Philipp Messer and Don C. Lamb (*LMU*). Based on their work in the tracking of fluorescent-labelled particles in biological systems,[87, 88] they developed a detection algorithm in *MATLAB* (*Mathworks*) that was modified in the present work for the requirements of STM data analysis.

In addition to particle detection, several other elementary processing steps are required to allow for an automated evaluation of dynamics from STM data. One general problem in STM measurements is thermal drift. As drift results in a shift of the imaged area over the sample, an additional motion vector is added to the processes observed on the surface. Therefore, one step of the analysis is the removal of drift from the data. Furthermore, the individual images need to be rectified prior to particle detection to remove image deformations introduced by the use of the sinusoidal scan wave during acquisition. This step is necessary to create images consisting of pixels all of which contain the same spatial information, so that diffusion pathways over a distinct number of pixels correspond to the same length in Å independent of the atom position in the image.

All of these steps require the handling of large amounts of data, as an STM movie may consist of several thousand images that need to be processed. So far, the displaying and analysis of individual STM images in the working group Wintterlin has been performed in the *IGOR Pro* environment (Version 6.02) using software functions developed by Prof. Dr. Sebastian Günther (*Technical University of Munich*). However, the loading and displaying of longer STM movies (>500 images) is not possible with these tools because the maximum data volume that can be managed by the *IGOR Pro* version used is exceeded. Therefore, new tools for the processing and analysis of the STM movies had to be developed. It was decided to establish the image processing and analysis routines in *MATLAB* (*Mathworks*, Version R2017b), as the particle detection and tracking algorithm of P. Messer and D. Lamb was *MATLAB*-based and the environment allows for processing of large amounts of data.

This chapter describes the processing routines that were developed in the present work and enable the analysis of STM movies, acquired with the Video-STM software. The analysis covers the process from the one-dimensional data wave file to the extraction of concrete trajectories of individual particles. Specifically, the analysis involves the following steps:

1) Loading of the 1D data wave in *MATLAB* and conversion into a three-dimensional image stack → Section 3.2

2) Correction of the sinusoidal deformation of the images → Section 3.3

3) Particle detection and linking of positions in consecutive images to receive particle trajectories → Section 3.4

4) Removal of thermal drift from the particle trajectories → Section 3.5

A tabular overview of the *MATLAB* scripts that have been developed in the course of this work is given in Appendix C.1.

3.2 Loading of Data Wave Files

The output of the Video-STM software is saved as an *igor binary wave* (*.ibw*) file, which ensures compatibility with the new data acquisition program as well as with the previous *IGOR Pro* STM analysis tools in the working group. As mentioned above, for larger datasets, i.e., movies with more than ~500 images, the analysis environment had to be changed to *MATLAB*. The first step in the post-processing of the STM data is thus the loading of the 1D data wave into a *MATLAB*-compatible format.

When choosing an *.ibw* file for loading, the corresponding parameter file is automatically loaded as well and the scan parameters are extracted. With these information, the 1D data vector (Figure 2.10) is transferred into a three-dimensional (3D) stack of matrices, in which each matrix represents a single STM image. This step also provides the opportunity to re-adjust the phase between actual tip movement and driving voltage, if it was not properly corrected for during the measurement (section 2.6.1).

Depending on the imaging mode, a possible back scan in y between consecutive images and the backward scan in each line are deleted in this step, but are retained in the original data file for possible future analysis. The thus created 3D matrix stack forms the basis for all further processing steps.

3.3 Sine-Correction

Due to the sinusoidal scan ramp in the fast scanning direction during Video-STM acquisition, the images in the resulting 3D stack are deformed (section 2.6.2). Figure 3.1 a) (bottom) illustrates the scan process in which image pixels are collected in uniform time intervals throughout a line in x direction (alternating black and gray boxes at the bottom axis). As a consequence of the non-linear relation between time and space elements, the pixels contain different amounts of spatial information. The periodic structure of a $(\sqrt{3}\,\mathrm{x}\,\sqrt{3})$R30°-CO overlayer (CO molecules are imaged as depressions) in the STM image in a) thus appears elongated on both sides of the image and squeezed in the middle of the image. This distortion strongly complicates the desired particle motion analysis. If left uncorrected, the movement of a particle by a certain distance would correspond to different numbers of pixels depending on where in the image the particle is located. Especially if particles are observed over longer time periods and wander through the entire image, it is almost impossible to correct this deformation afterwards in the obtained trajectories of the particles. For this reason, a rectification routine has been developed to remove the scan ramp-induced deformation from the images prior to particle tracking.

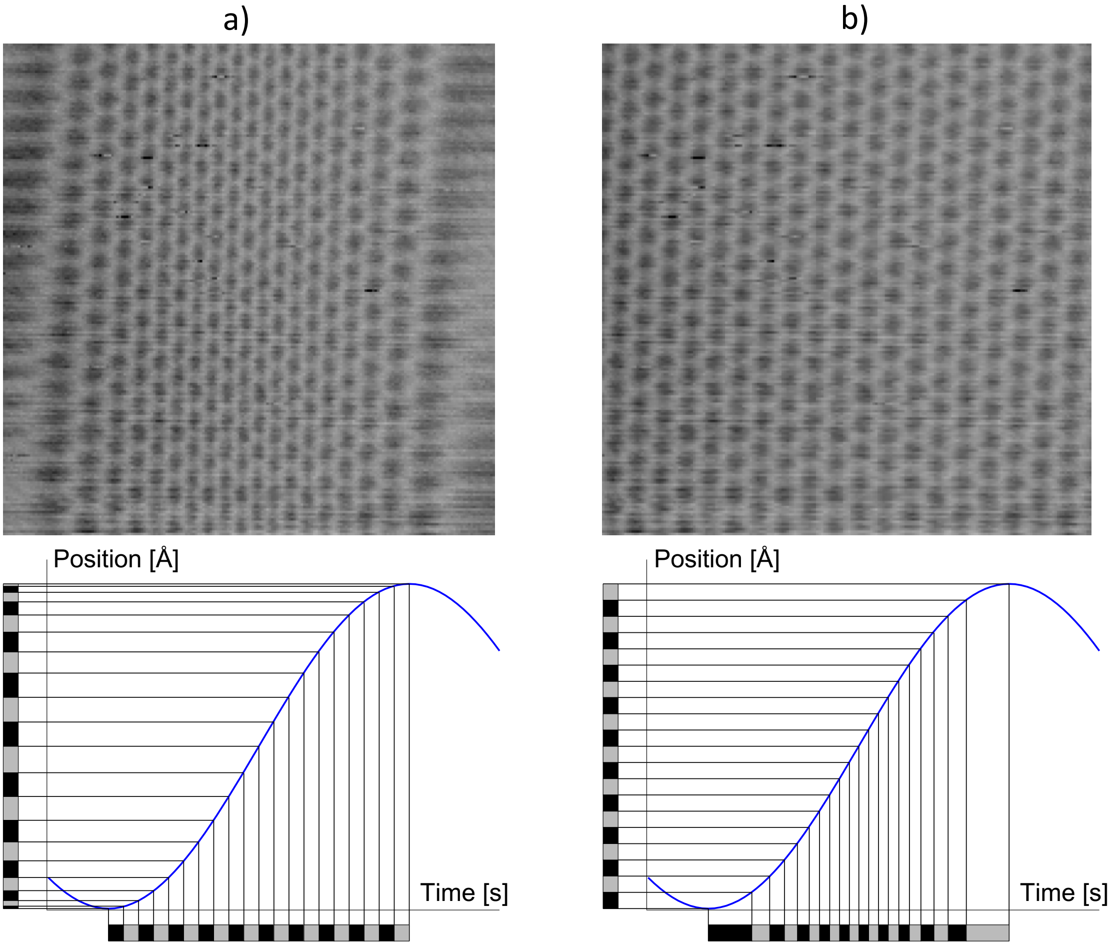

Figure 3.1: Image deformation induced by the sinusoidal scan wave. a) The STM image (200 x 200 pixels, V_t = -0.22 V, I_t = 10 nA, ~85 Å·85 Å) is deformed due to the usage of a sinusoidal scan wave in *x* direction. When data points (alternating black and gray boxes) are measured in equal time intervals (bottom axis), the pixels contain varying spatial information (left axis). A periodic structure, here the ($\sqrt{3}$ x $\sqrt{3}$)R30°-CO structure on Ru(0001), will thus appear deformed. b) The same STM image as shown in a) after applying a rectification routine (199 x 200 pixels). Pixels are now equally spaced in position, but no longer in time.

Figure 3.2 illustrates how this correction is achieved. If τ is the acquisition time for the individual pixels taken at uniform time intervals (from now on called *time pixel*) and *Δx* is the length of the equidistant pixels in the space domain (*space pixel*), then each *space pixel* of number *i* can be created by a combination of a distinct number N_i^t of *time pixels*. *Space pixel* number 1, e.g., is created by combining N_1^t *time pixels* τ in the time interval Δt_1, as highlighted in red in Figure 3.2. *Space pixel* number 2 is generated from N_2^t *time pixels*, which represent the time interval Δt_2. All other *space pixels* are created accordingly.

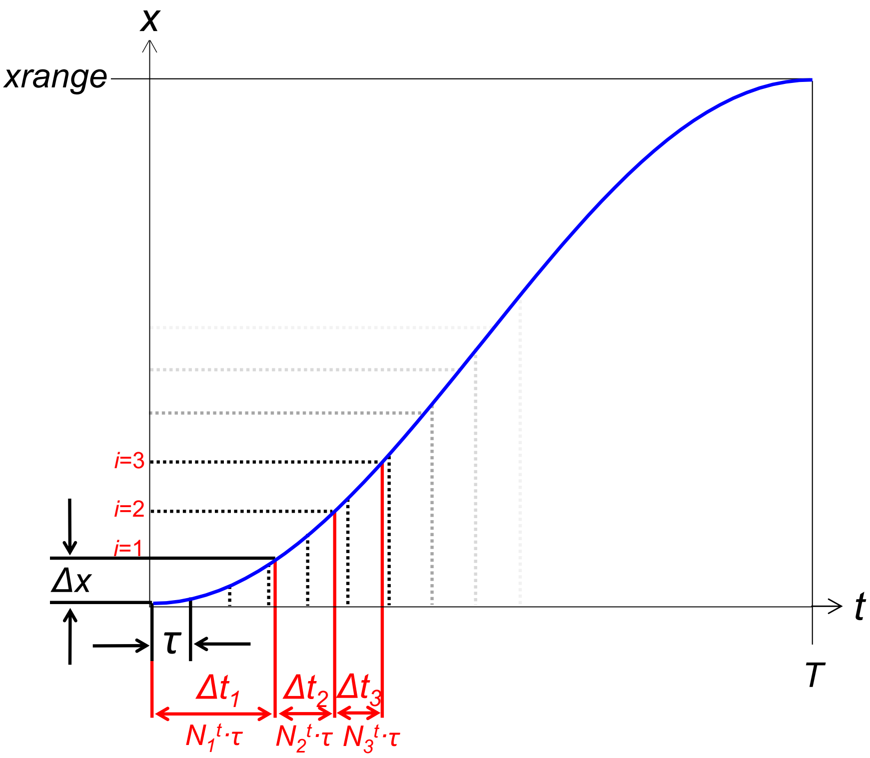

Figure 3.2: Schematic illustration of the image rectification routine. In order to create an image consisting of equidistant pixels Δx, the number N_i^t of time pixels τ has to be calculated for each *space pixel* of number *i*. N_i^t can be estimated from the slope of the function $t = f(x)$.

The numbers for N_i^t can be calculated from the ratio of Δt_i to Δx, which can be approximated by the first derivative ${}^{dt}/_{dx}$ of the function $t = f(x)$. What is known, is the inverse function $x = f(t)$, the scan ramp in x direction:

$$x = -\frac{xrange}{2}\cos\left(\frac{t}{T}\pi\right) + \frac{xrange}{2} \tag{3.1}$$

Here $xrange$ is the amplitude of the sine (or cosine) wave and T is the time for one forward scan, i.e., half a period of the sine (or cosine) function. The required function $t = f(x)$ and its first derivative ${}^{dt}/_{dx}$ are then given by equations 3.2 and 3.3. The ratio $\frac{\Delta t_i}{\Delta x}$ is approximated with 3.3.

$$t = \frac{T}{\pi} \arccos\left(1 - \frac{2x}{xrange}\right) \tag{3.2}$$

$$\frac{\Delta t_i}{\Delta x} \approx \frac{dt}{dx} = \frac{T}{\pi}\left[\frac{1}{\sqrt{1-\left(1-\frac{2x}{xrange}\right)^2}}\right] \cdot \frac{2}{xrange} \tag{3.3}$$

By expansion of 3.3 with equations 3.4 to 3.7, in which $Z^x$and Z^t are the respective numbers of *space pixels* and *time pixels* in a full forward scan, an expression for N_i^t is obtained (equation 3.8).

$$\Delta x = \frac{xrange}{Z^x} \tag{3.4}$$

$$x = i\Delta x = \frac{i}{Z^x} \cdot xrange \tag{3.5}$$

$$\Delta t_i = N_i^t \cdot \tau \tag{3.6}$$

$$T = Z^t \cdot \tau \tag{3.7}$$

$$N_i^t = \frac{2}{\pi}\frac{Z^t}{Z^x}\left[\frac{1}{\sqrt{1-\left(1-2\frac{i}{Z^x}\right)^2}}\right] \tag{3.8}$$

Equation 3.8 provides a function that estimates the number N_i^t of *time pixels* that need to be combined for the respective *space pixel* i at position $x = i \cdot \Delta x$. Figure 3.3 shows a plot of equation 3.8 for typical values of $Z^t = Z^x = 200$. As evident from the plot, for the creation of the first and the last ~20 *space pixels* of a line, multiple *time pixels* have to be averaged. For the *space pixels* in the middle of the image, approximately between *space pixel* 20 and 180, each *space pixel* corresponds to less than one *time pixel*. The intensity of one *time pixel* in this region thus determines the intensity of several *space pixels*.

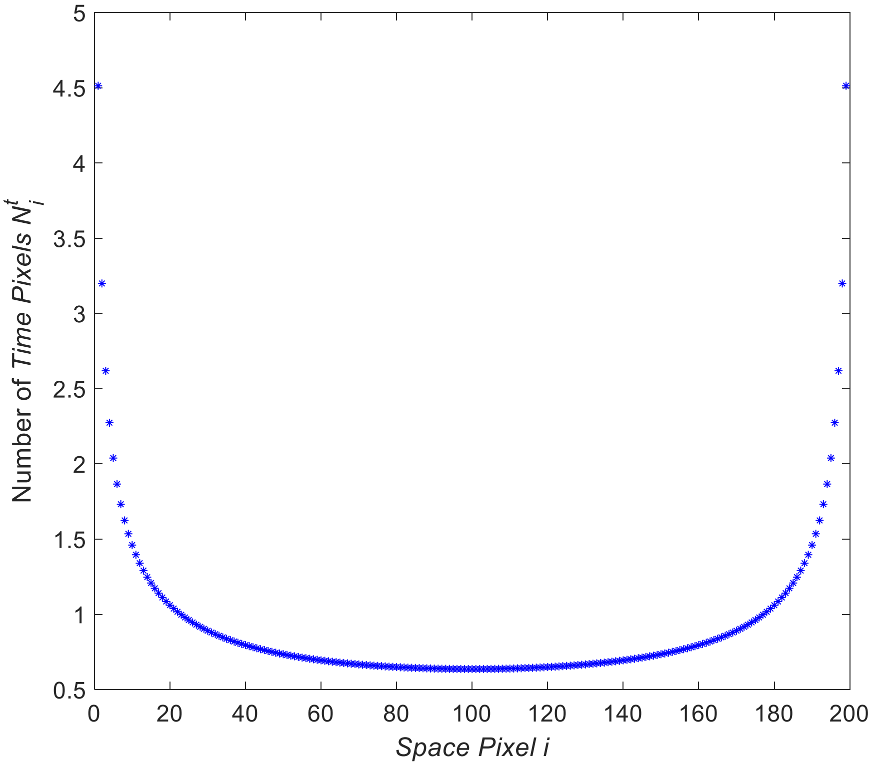

Figure 3.3: Calculated number N_i^t of *time pixels* that need to be combined to generate the respective *space pixel* i. The plot shows the result of equation 3.8 for typical values of $Z^t = Z^x = 200$.

For $i \rightarrow 0$ and $i \rightarrow Z^x$ the function goes to infinity. The sum over all real entries of N_i^t [between $i = 1$ and $i = (Z^x - 1)$] is thus lower than Z^t implying that not all time pixels are taken into account for the generation of the rectified image. The offset value, given in equation 3.9, quantifies the number of *time pixels* that are discarded at the image edges.

$$offset = \frac{1}{2}\left(Z^t - \sum_{i=1}^{Z^x-1} N_i^t\right) \tag{3.9}$$

For the example Z^t=Z^x=200 this offset is ~6.6 time pixels. The first *space pixel* is thus generated by averaging the intensities of ~4.5 consecutive *time pixels* (N_1^t~4.5, see Figure 3.3) starting to count at *time pixel* 6.6. For the second *space pixel*, the intensities of the following ~3.2 *time pixels* (N_2^t~3.2) are averaged. This procedure is continued for all other *space pixels* until $i = (Z^x - 1)$. The last 6.6 *time pixels* of a line are discarded again. For the chosen example in total ~13.2 *time pixels* are neglected that correspond to one single *space pixel*. The resulting new image therefore consists of only $(Z^x - 1)$ *space pixels* in the *x* dimension. The rectification procedure thus implies the loss of $1/_{Z^x}$ of information. For typical scan parameters of 200 points per line and a scan range of 100 to 150 Å, this loss corresponds to a negligible value of 0.5 to 0.75 Å.

The functionality of the rectification procedure is demonstrated with the STM image in Figure 3.1 b). The original 200 x 200 pixel image, shown in a), acquired with uniform *time pixels*, is transformed into a 199 x 200 pixel image in b), which consists of equidistant *space pixels*. The image is rectified in the *x* dimension, whereas the *y* dimension is left unchanged. The almost perfect periodic appearance of the ordered $(\sqrt{3} \text{ x } \sqrt{3})$R30°-CO overlayer illustrates the good performance of the rectification procedure.

3.4 Particle Tracking

The rectified STM images are used in the next analysis step, the particle tracking. This step was realized in cooperation with Philipp Messer and Don C. Lamb (*LMU*). The routines presented in this section were implemented by Philipp Messer in the *MATLAB* programming environment.

The central step of the automated tracking is the detection of the particles of interest in every image. This is challenging, because the signal-to-noise ratio in STM measurements is rather low compared to other microscopy techniques and the appearance of the images can vary greatly during an STM movie because of changes in the tip state. Most algorithms for STM image analysis are based on thresholding of absolute height values of the image.[89] All pixels above (or below) a certain value will be recognized as a particle. This method is quite simple and easy to automatize but requires an absolutely flat and even background throughout the image. An uneven background will introduce a varying recognition probability for particles in different parts of the image. Hence, this detection method is barely usable for STM movies consisting of thousands of individual images.

A more sophisticated particle detection method was presented by Renisch.[90] For each dataset, he selected a small portion of an image containing a single atom that was defined as a model atom. This portion was then convoluted with the STM images to be analyzed. For all positions on which the image was similar to the model atom, the convoluted image showed high intensities. A threshold was used in the subsequent step to define whether a particle is detected or not. As the intensities of the resulting convolution directly depended on the absolute height information of the original images, this procedure exhibits the same disadvantage as the simple height thresholding described above. A further problem was that also the usual temporal distortions occurring in STM images led to comparably high values in the convolution. This fact severely complicated the setting of the threshold value. Moreover, a model atom had to be created for each dataset, since the exact appearance of single atoms and particles can vary strongly from experiment to experiment, because it is influenced by the state of the STM tip and imaging conditions.

In this work a different approach for particle detection is used that is based on an *à-trous wavelet decomposition* of the images. This method was developed by Olivo-Marin[64] for the detection of fluorescent-labelled objects in biological images and has been modified in the course of this work to fulfill the requirements for particle detection in STM images. The decomposition of the STM images into different levels of resolution by a so-called *wavelet transform* (WT) allows for a precise detection of the particles of interest by size and shape selection.

3.4.1 Wavelet Transform

To interpret a time-dependent signal $f(t)$, extract its characteristics, and also to forecast the signal evolution, it can be analyzed in the time and frequency domain with different analysis approaches. Both, the FT as well as the WT decompose a signal into a set of orthogonal basis functions that yield a univocal representation of the signal by a set of coefficients. In the FT, the basis functions are sine or cosine functions of different frequencies. All information of the signal is represented by a combination of these frequencies and their phases, but no information in the time domain is obtained as sine and cosine functions are non-localized in time. A schematic representation of the time and frequency resolution of a *discrete* FT is given in Figure 3.4 on the left. The lines express the information content in the two domains. The denser the lines in the time domain, the better the temporal resolution.

The denser the lines in the frequency domain, the larger the frequency range that can be detected. While the standard FT exhibits perfect resolution in the frequency domain, it does not deliver any temporal information.

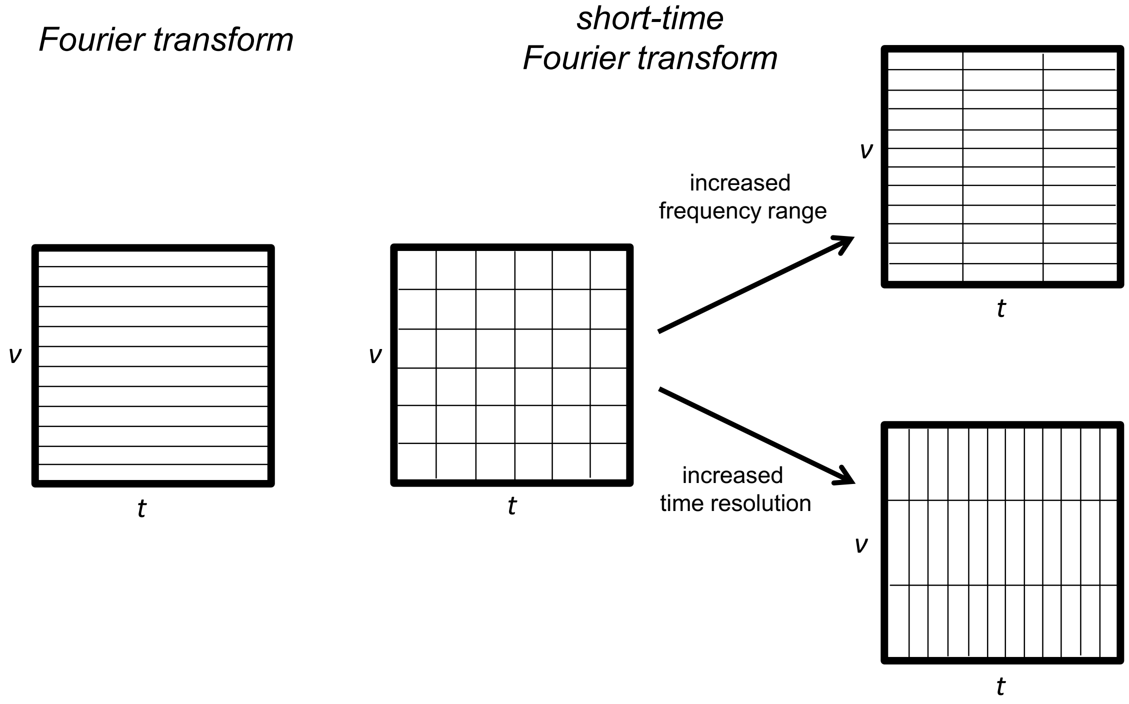

Figure 3.4: Schematic illustration of the information content in the time t and frequency v domain for the *discrete Fourier transform* (left) and the *short-time Fourier transform* (middle and right).

In many fields of application signals are non-stationary. In this case not only the frequency content but also its temporal distribution is of interest, such as in the geological study of seismographic activity.[91-94] When do special frequencies occur, how long are they present in the signal, and how does the signal evolve over time are just some examples for questions in the field of signal processing that require temporal resolution besides frequency information.

Time-localization in the FT can be achieved by the so-called *short-time Fourier transform* (ST-FT), in which a window function is first slid over the signal $f(t)$ to cut out distinct time intervals. These time periods of the signal are then evaluated by the normal FT. The size of the window function determines the temporal resolution of the analysis but also the range of frequencies that can be detected (see Figure 3.4, middle). A small window size yields good temporal resolution while it inevitably restricts the frequencies that can be analyzed, as the largest wavelength that can be detected corresponds to the window size. A larger window enhances the range of detectable frequencies but decreases temporal resolution (Figure 3.4, right). This mutual dependency is known as the *uncertainty principle in signal processing*, in analogy to the uncertainty principle of Heisenberg in quantum mechanics.[95] In the ST-FT, the size of the window function has to be specified prior to the analysis and then remains unchanged. A disadvantage, as the ST-FT requires *a priori* knowledge about the features of interest and it only can analyze features quite similar in size at a time.

In contrast to the FT and ST-FT, in which the signal is decomposed into a basis set of sine or cosine functions, the WT uses a small group of wavelets (=”small waves”) as basis functions.[95-97] These wavelets can be described as rapidly decaying functions containing a few oscillations, well localized in time and thus corresponding to a specific frequency band. One of the simplest wavelets is the *Haar* sequence shown in Figure 3.5, which was first proposed by Alfred Haar in 1910[98, 99] and is also known as the first *Daubechies* wavelet *Db1*.[97]

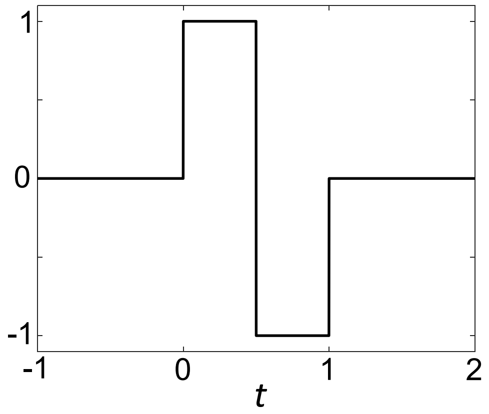

Figure 3.5: The *Haar* sequence, also known as the *Db1* wavelet, is one of the simplest wavelets.

By dilation or compression of the so-called *mother wavelet* ψ along the t axis with a parameter m, the localization properties in time can be altered. At the same time the shape of the wavelet, i.e., the number of oscillations, is preserved. A dilation or compression in the time domain thus leads to a change of the corresponding frequency content. Furthermore ψ can be shifted by a parameter n along the t axis. In this way a number of wavelets $\psi^{m,n}$ can be created from the mother wavelet ψ. These wavelets have different localization properties in time and contain a varying amount of frequency information at different positions of the function, just depending on the parameters m and n. The WT can therefore be regarded as an extension to the described ST-FT, in which the size a of the window function is systematically varied during the analysis to access all information of the signal in the time and frequency domains at different levels of detail. The wavelet acts as a window and an analyzing function at the same time.

To reduce computational effort the WT is usually performed in a discretized version, in analogy to the *discrete* FT, meaning that m and n can take only discrete values. Usually they are varied on a dyadic scale. The decomposition of a signal into its basis of wavelet functions results in the representation of the signal by coefficients in the wavelet domain, analogously to the decomposition of a signal to its basis of sine or cosine functions that leads to its representation in the *Fourier* domain. The signal may also be reconstructed from the wavelet representation analogously to the inverse FT.[75]

The functional principle of a discrete WT is shown in Figure 3.6. In the first step the signal is analyzed on the basis of a wavelet of size a_0. By variation of parameter n the wavelet of size a_0 can be shifted along the t axis and the function can be analyzed at different points. The obtained information exhibits good time resolution, whereas the accessible frequency information is quite limited, because frequencies that exceed the size of the wavelet are not detected. In the next level of analysis, the wavelet is expanded to twice this size by variation of m. The information content in the frequency domain is thus improved, while the localization in time is reduced. This reduction is no disadvantage though, since the information with finer time resolution has already been sampled in the first analysis step. The larger wavelet of size a_1 is again shifted along the t axis to analyze the function at different positions. In principle, these steps can be repeated until a satisfying description of the signal is achieved.

The depicted analysis in Figure 3.6 consists of four resolution levels. This analysis scheme is called a *multiscale* or *multiresolution analysis*[96](MRA) and illustrates the analysis principle of the WT. Usually, to avoid redundancy in the analysis, the information content that has been evaluated by the WT on a specific scale is subsequently subtracted from the signal. Therefore, the WT acts like a bandpass filter, extracting and analyzing a different frequency content in each resolution level.

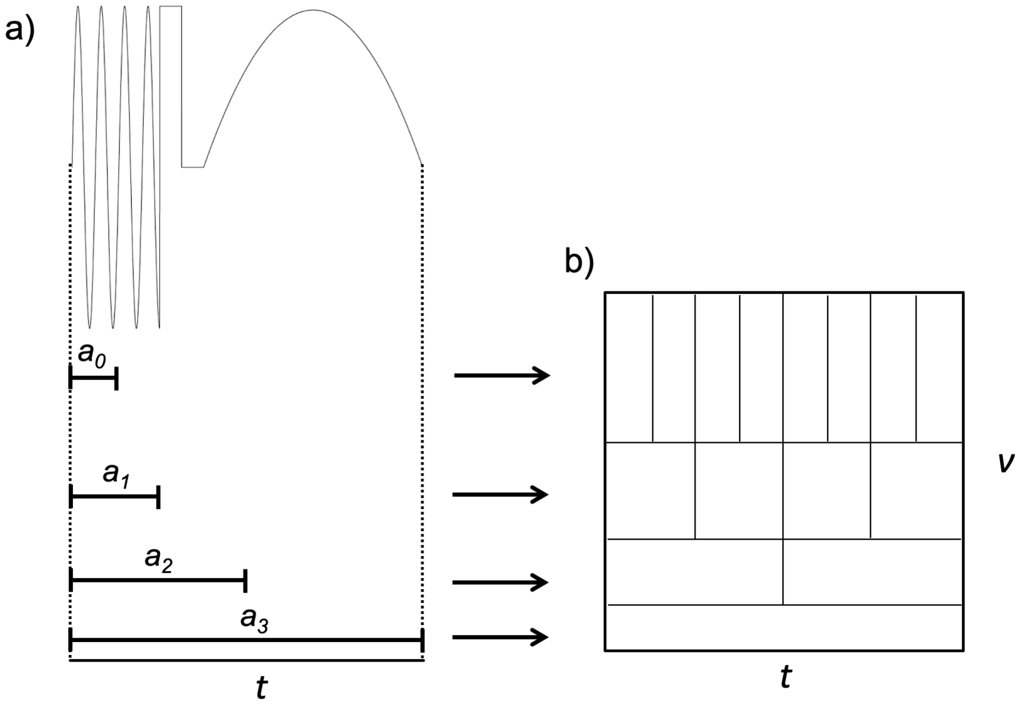

Figure 3.6: The *wavelet transform*. a) Multiresolution analysis of an example function (function taken from reference [95]) at different levels of resolution, depending on the wavelet size *a* b) Schematic representation of time and frequency information content in the different levels for a multiscale WT (in analogy to Figure 3.4 for FT and ST-FT).

When going from 1D time-dependent signals to the analysis of images, the size of the objects in an image correlates to a frequency, whereas their positions in the image corresponds to the time domain in the 1D WT. Because images typically consist of features of quite different sizes, the MRA is especially well suited for image processing and analysis. While the image background provides the coarse context of the image, distinct smaller objects in the image require a much finer resolution. Moreover, images often contain abrupt changes in intensity, e.g., at the edges of a dark object in front of a bright background. Such discontinuities usually require a high number of different frequencies to be accurately described and are therefore more efficiently represented in a WT rather than in an FT. Moreover the WT is, like the FT, separable, a very convenient property for the analysis of two-dimensional (2D) data as each dimension can be transformed separately one after the other. Because of these reasons the multiscale WT is the method of choice for image analysis and is widely used for image denoising,[100-102] compression,[103] and feature detection.[64, 104]

Instead of convoluting the signal with a wavelet, like in the 1D WT, in the MRA of 2D signals the computation of the wavelet representation is usually performed by convolutions with a set of a high-pass and a low-pass filter. As mentioned above, the analysis of a signal by the WT can be interpreted as a band-pass filtering step on each resolution level. This can be achieved by either convoluting the signal with the wavelet itself (which corresponds to a distinct frequency band), like in the 1D WT, or instead by using a combination of a high-pass and a low-pass filter, like in the 2D WT. An example for a widely used wavelet and its corresponding filters is given in Figure 3.7, which shows the *Db42* wavelet [Figure 3.7 a)]. A *Db42* WT was used in this work for the removal of line artifacts from the STM images (section 3.4.3.1). For the calculation of the 2D WT, the images were convoluted with the corresponding high-pass and low-pass filters shown in b) and c). The filters are specific to each wavelet and allow for a lossless decomposition and reconstruction of the signals.[95, 96]

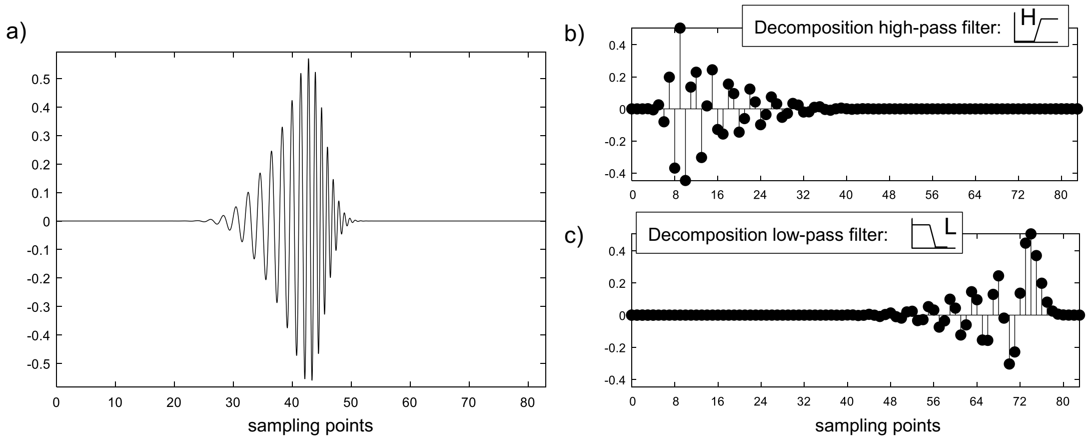

Figure 3.7: a) The *Db42* wavelet and the corresponding decomposition b) high-pass and c) low-pass filters.

As illustrated in Figure 3.6, when the signal has been analyzed at a specific resolution level in a WT process, for the analysis on the next resolution level the size of the wavelet is increased. In analogy to this step, in the 2D WT the sizes of the two filters are increased. This approach to go from one resolution level to the next is also called *stationary* WT or *à-trous* algorithm and was used in the course of this work for particle detection in the STM images.

More commonly, a slightly different WT approach developed by Mallat[96] is used for signal and image analysis. Instead of increasing the wavelet/filter size throughout the decomposition, a coarser representation of the signal/image is obtained by dyadic downsampling in each analysis step. The downsampling can be achieved by averaging over consecutive data points in the signal or just neglecting every second one. The next analysis step is then performed at half the number of data points, while the filter sizes remain unchanged. This algorithm was applied for filtering purposes of the STM images and is explained in more detail in section 3.4.3.1.

3.4.2 The *à-trous* Algorithm

In the *à-trous wavelet transform* or *stationary wavelet transform* an image A_0 is decomposed into planes of different resolution by iterative low-pass filtering steps. Each plane contains structural information of objects on a certain scale, meaning that small objects have a high contribution in high resolution planes while large objects contribute more to low resolution planes.

A smoothed approximation A_i of the image A_{i-1} is created by convolution with a low-pass filter. The corresponding wavelet plane W_i is then created by subtracting the smoothed image A_i from the previous one A_{i-1} according to equation 3.10. The wavelet plane W_i thus contains the structural information between the two scales A_{i-1} and A_i in analogy to a bandpass filter, like in the regular WT.

$$W_i(x,y) = A_{i-1}(x,y) - A_i(x,y) \qquad \forall\, i \in \mathbb{N} \tag{3.10}$$

Here, x and y denote the indices of the image pixels or wavelet coefficients. By iterative decomposition up to the lowest resolution level $i = J$, the image A_0 is thus split into J wavelet planes W_i and the low-pass approximation A_J at level J. The complete image information can be restored reversely according to equation 3.11.

$$A_0(x,y) = A_J(x,y) + \sum_{i=1}^{J} W_i(x,y) \tag{3.11}$$

Due to separability of the transform in x and y direction, the smoothed approximations are created by a row-by-row, followed by a column-by-column, convolution with a discrete filter. In each resolution step, the filter size is increased to allow for the creation of a coarser approximation in the next decomposition step. The specific application of the *à-trous* WT to an STM image is explained in detail in section 3.4.3.2 and illustrated in Figure 3.11.

The *à-trous* algorithm is size-preservative in contrast to the above mentioned approach by Mallat. This property means that all low pass approximations and wavelet planes consist of the same number of pixels or coefficients as the original image. This property is advantageous for particle detection, because the wavelet coefficients at different resolution levels belong to the same pixel in the original image, which is the basis for a precise position determination.

3.4.3 Application to STM images

The specific realization of the particle tracking in this thesis is demonstrated in the following using STM images of single O atoms that move in an ordered CO layer on a Ru(0001) surface. The O atoms are the particles of interest that shall be detected and tracked. A short overview of the required steps for particle tracking is given below, while each individual step is described in more detail in the subsequent subsections.

Prior to the particle detection step, the STM images are filtered by two different approaches in order to enhance the signal-to-noise ratio. A combined WT-FT filtering approach is used to remove line artifacts introduced by the scanning process, while a subsequent *Fourier* filtering step reduces high and low frequency noise components in the images. The filtered images are then decomposed into different resolution scales with an *à-trous* WT. By a smart combination of different wavelet planes, a particle mask can be created to selectively detect the O atoms. Detected particle positions in each STM image are linked to create trajectories of the O atoms throughout consecutive images in an STM movie.

3.4.3.1 Filtering

STM images often contain line artifacts in the fast scanning direction as a result of tip instabilities during the scan process. Furthermore, line artifacts are introduced in the Video-STM data at the beginning of an image when scanning in the upward or downward imaging mode (section 2.6.3). These distortions influence the particle detection accuracy as, on the one hand, they can alter the appearance of particles so that they may be overlooked. On the other hand, they can lead to misdetections, especially when the size of the particles of interest lies in the range of only a few pixels. Hence, removing of these distortions prior to particle tracking can improve the tracking accuracy. This filtering was achieved by the implementation of a combined *wavelet-Fourier filtering* step according to Münch *et al.*,[104] realized by P. Messer (Group of Prof. Don C. Lamb, *LMU* Munich). In this approach, the images are first decomposed by a WT. The wavelet representations that contain the line artifacts are then Fourier transformed, and the artifacts are filtered out in the Fourier space. Finally the image is reversely reconstructed from the filtered wavelet planes. This combined WT-FT filtering process is explained in more detail in the following.

Wavelet transform step

The separability of the WT provides the possibility of applying different filters in the two dimensions. Following the multiresolution algorithm by Mallat[96], illustrated in Figure 3.8, an image (here exemplarily of 512 x 512 pixels) can be decomposed into three different wavelet planes and one low-pass approximation (each 256 x 256 pixels). Low-pass filtering in both dimensions leads to a smoothed approximation A_i of the image A_{i-1} in the manner of the *à-trous* wavelet transform (compare section 3.4.2). By applying the low-pass filter along the rows of the image and then the high-pass filter along the columns, objects that are elongated in the horizontal but short in the vertical dimension of the image are preserved. The corresponding wavelet plane $W_{i,horizontal}$ thus contains structural information on the objects that are mainly oriented along the *x* direction of the image, e.g., such as STM stripe artifacts. Accordingly, by applying a high-pass filter in *x* and a low-pass filter in y direction, the resulting wavelet plane $W_{i,vertical}$ mainly contains objects that are elongated in the y dimension. By applying a high-pass filter to both dimensions the diagonal wavelet components $W_{i,diagonal}$ are obtained.[96]

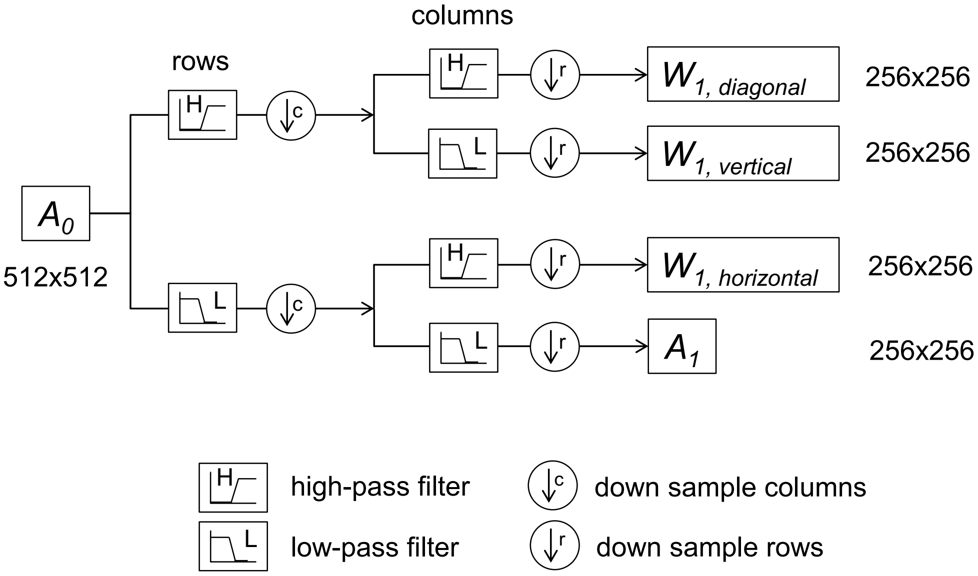

Figure 3.8: First decomposition step of an image A_0 into its diagonal, vertical, and horizontal detail images ($W_{1,diagonal}$, $W_{1,\ vertical}$, $W_{1,horizontal}$) and its low-pass approximation A_1 by a WT.

Figure 3.9 illustrates the decomposition of an image into its vertical, horizontal, and diagonal detail bands by a *sym2*[97] WT. Here, *sym2* indicates the mother wavelet that determines the filters in the WT. Shown are the first low-pass approximation A_1 of a photograph of the VT-STM setup, and the three different *wavelet* planes at the first resolution level. It is clearly visible that high-intensity wavelet coefficients in the horizontal detail band correspond to pixels that belong to a structure that is oriented in horizontal direction, such as, e.g., the plates of the copper stack in the lower part of the image (compare Figure 2.2). Analog examples can be found for the other two detail bands.

To remove horizontal stripe artifacts with the combined WT-FT filtering approach, STM images are first separated by a discrete WT into their vertical, horizontal, and diagonal components at multiple resolution levels by a *db42*[97] WT (compare Figure 3.7), according to Münch *et al.*.[104] For the decomposition the STM images become padded with mirrored values at the edges. By the decomposition step, the stripe information is condensed to the horizontal detail planes as explained above and is thus already well separated from the image information that does not have horizontal components.

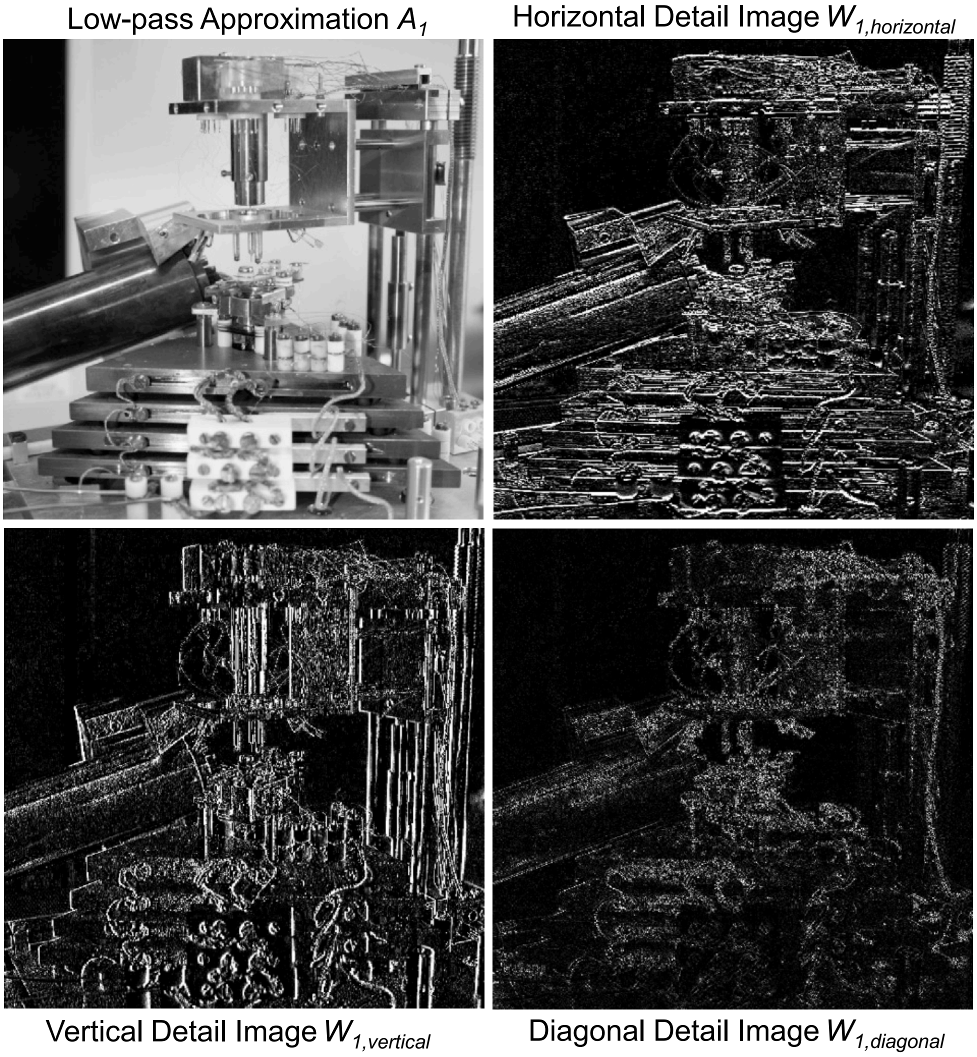

Figure 3.9: Demonstration of a *sym2*-WT decomposition according to the multiresolution approach by Mallat,[96] into horizontal, vertical, and diagonal detail images. The original image A_0 is a photograph of the VT-STM setup (Figure 2.2). Shown are the first level detail images and the corresponding low-pass approximation A_1.

Fourier transform step

Only the horizontal detail bands $W_{i,horizontal}$ that contain the stripe information are then used in the next step of the combined WT-FT filtering approach, the FT. The $W_{i,horizontal}$ on all levels are then *Fourier* transformed. As horizontal stripes do not exhibit large variation in x direction and their irregular occurrence in y direction has to be presented by many frequencies in y direction, the FT further condenses the artifact information in a stripe in $\hat{y}$ direction around $\hat{x} = 0$ in the *Fourier* domain. $\hat{x}$ and $\hat{y}$ denote *Fourier* coefficients. The coefficients around $\hat{x} = 0$ are then damped with a *Gaussian* function (not for $\hat{x} = 0$ and $\hat{y} = 0$) and stripe artifacts are thus removed. The filtered horizontal detail bands are subsequently restored by an inverse FT. Finally, the original but destriped image is reconstructed from all detail bands and the low-pass approximation by an inverse WT.

Performance of the combined WT-FT filtering

The efficiency of the destriping method is demonstrated in Figure 3.10 for two different kinds of stripe artifacts. The original STM image in Figure 3.10 a) (rectified according to section 3.3) shows typical defects that occur in STM measurements. Because of tip instabilities one line or several consecutive lines of the image may appear bright or dark, as the tip-sample distance is suddenly much smaller or larger than before. The original image in a) contains five of these prominent line defects, indicated by black arrows, that may hamper a reliable automated particle detection. In the image, filtered with the combined WT-FT method in Figure 3.10 a) on the right, these line artifacts have been removed. The intensity jumps between consecutive lines are no longer visible, while the rest of the image remains unchanged.

Figure 3.10 b) shows a second STM image taken from a different dataset. The image exhibits very good spatial resolution and contrast, and does not show any of the just mentioned line defects. Nevertheless, the original STM image contains thin horizontally-oriented stripes that almost extend over the entire image in x direction and result most likely from slight mechanical vibrations in the STM-sample setup during image acquisition (section 2.6.3). Furthermore, a second type of horizontally oriented, short stripe-like features is present. Two of these features are indicated by white arrows in Figure 3.10 b), left.

The extended stripe-like features in the original image are again removed in the filtered STM image, while the shorter stripe-like structures are still present. This second type of “stripes” is (most likely) not a scanning artifact but represent real processes on the imaged surface, such as diffusion events that occur on a shorter time scale than the imaging process. These features are not filtered out by the WT-FT routine as they are less elongated in the horizontal direction. Because of that, they are not that tightly condensed around $\hat{x} = 0$ by the FT step and are thus less strongly damped in the FT domain.

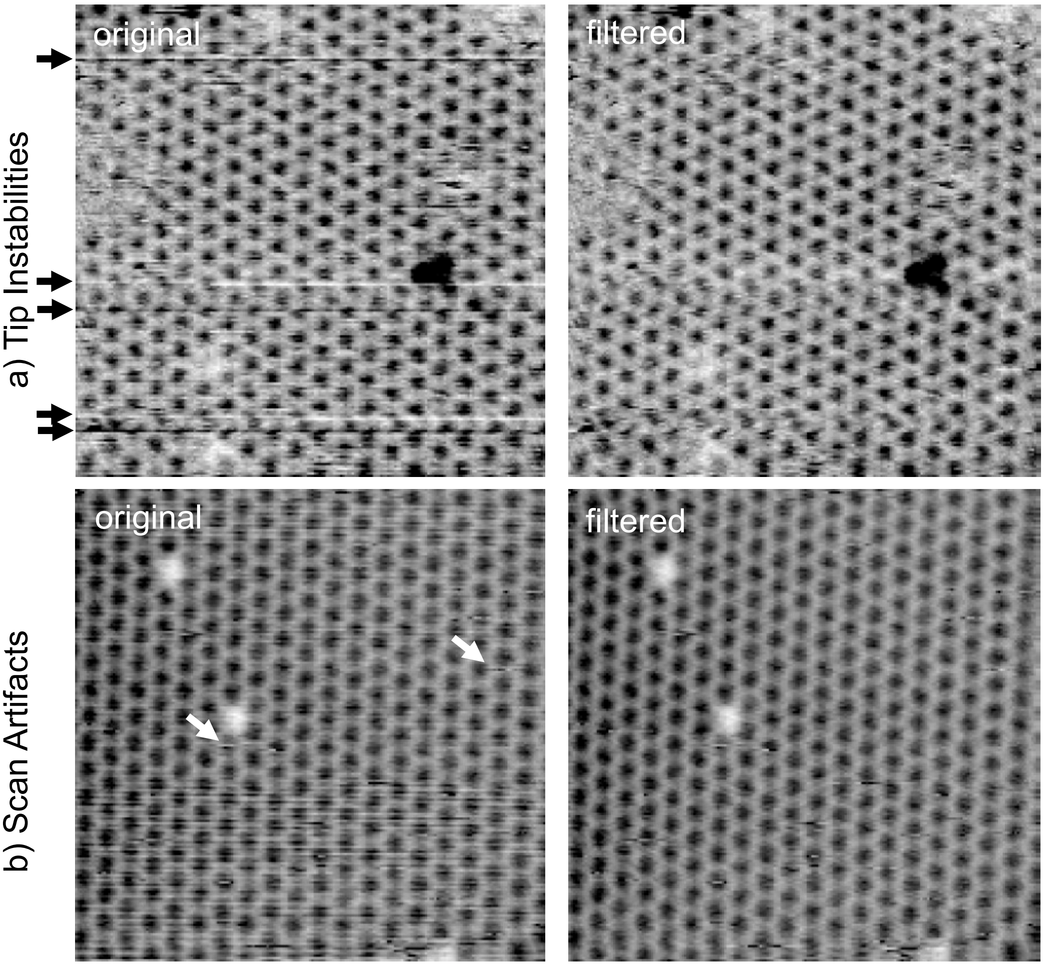

Figure 3.10: Stripe artifact removal in STM images. a) The original image on the left shows line defects typical for STM measurements due to changes in the tip state (V_t = -1.45 V, I_t = 3 nA, ~85 Å·85 Å). These artifacts are removed in the filtered image (right). b) Left: The original STM image contains line artifacts that arise from slight vibrations of the tip during the scanning process (V_t = -0.22 V, I_t = 10 nA, ~85 Å·85 Å). These have vanished in the filtered image (right). By contrast, short stripes (white arrows), possibly marking atomic hopping events, are still present after filtering.

After removal of the stripe artifacts, the images are further filtered in the frequency domain to remove spatial frequencies from the image that are either much too high or much too low to represent the particles of interest. The images are therefore multiplied with a ring-like mask in the *Fourier* domain. Inner and outer diameters of the ring mask have to be adjusted according to the Ångström-to-pixel ratio of the particular dataset.

3.4.3.2 Particle Detection

For particle detection the filtered STM images are first filled up with mirrored values at the image edges to avoid edge effects during the subsequent *à-trous* WT. The number of added values is determined by the filter size in each decomposition step. As a low-pass filter, a kernel h_{filter} (eq. 3.12) is used that was developed for filtering and restoration of astronomical images by Starck *et al.*.[102] The explicit filter h_i at each resolution level i is derived by inserting $(2^{i-1}-1)$ zeros between adjacent entries in h_{filter}, thus leading to an increased filter size at every resolution level.

$$h_{filter} = \begin{bmatrix} \frac{1}{16} & \frac{1}{4} & \frac{3}{8} & \frac{1}{4} & \frac{1}{16} \end{bmatrix} \tag{3.12}$$

Figure 3.11 shows the *à-trous* wavelet decomposition of an STM image with the typical size of 199 x 200 pixels. In the first step, the original image A_0 is convoluted with the discrete low-pass filter $h_1 = h_{filter}$ in each dimension to give the smoothed image A_1. The wavelet plane W_1 is created by subtracting A_1 from A_0. In this way the original image is split into a high-frequency and a low-frequency part. All structural information that is present in A_0 but filtered out in A_1 is thus stored in W_1. In the next step A_1 is decomposed into A_2 and W_2. In principle, the decomposition can be continued in this way indefinitely, but a reasonable termination point is reached when the particles of interest have been extracted from the image. In the depicted example the STM image is decomposed into five different scales after which a good description of the oxygen atoms has been reached, whereas the low-pass approximation at the coarsest resolution scale A_5 does not contain any more structural information of the O atoms. The same decomposition depth was used by default for all datasets in the course of this work.

To locate the particles in the next step, Olivo-Marin proposed the creation of a so-called correlation image $P(x,y)$, which is the product of the wavelet coefficients on all scales.[64] The idea is that particles should, in contrast to additive noise in the image, have coefficients greater zero on all scales. For this reason the product of all $W_i(x,y)$ should only be significant for positions (x,y) that represent a particle. Low resolution planes can thus be used to obtain a coarse approximation of the particle position, while higher resolution levels are then used to confirm and refine it.

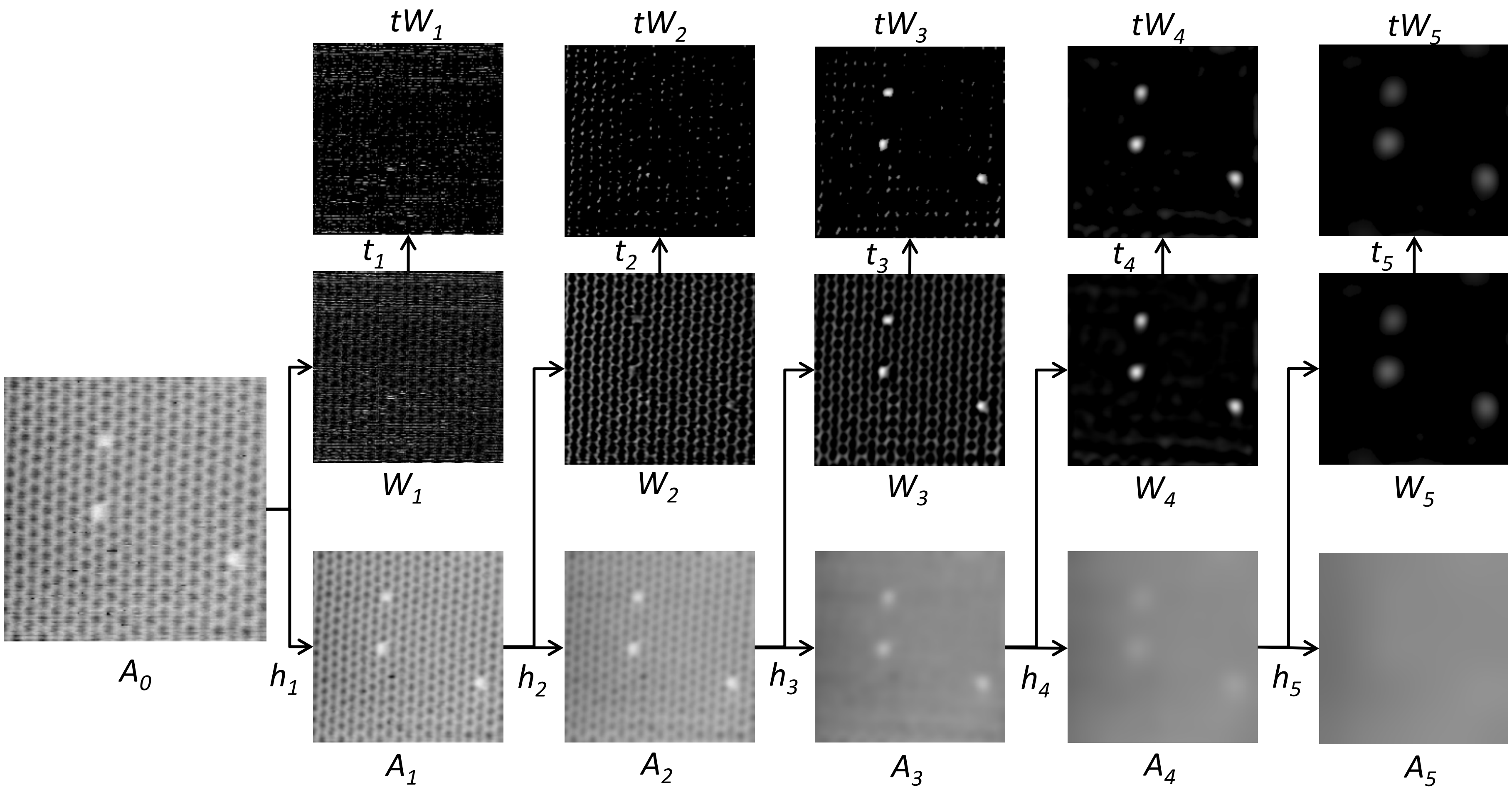

Figure 3.11: Decomposition of an STM image A_0 with the *à-trous* algorithm. In each detail level i, a smoothed approximation A_i is obtained by a convolution of A_{i-1} with a low-pass filter h_i. The wavelet plane W_i is obtained according to $W_i = A_{i-1} - A_i$. Finally, a level-dependent threshold t_i is used to select the significant wavelet coefficients and the filtered wavelet planes tW_i are created.

Olivo-Marin showed this method to be well suited for automated spot detection in biological images. For the present case of STM images, a slightly different approach was used, as the task here is not only to automatically detect all particles on a noisy background, but to selectively detect particles of interest in images that may additionally contain other types of particles or features. Therefore, instead of creating a correlation image $P(x,y)$ from all $W_i(x,y)$, only a subset (*a*,*b*) of all resolution levels i is used to distinguish the particles of interest from other structures, noise, as well as from the background of the image. A particle mask $P_{a,b}(x,y)$ is created according to equation 3.13, in which a and b are determined for each dataset based on an *a priori* knowledge of the particle size.

$$P_{a,b}(x,y) = \prod_{i=a}^{i=b} W_i\,(x,y) \tag{3.13}$$

From the analysis shown in Figure 3.11, it is evident that the O atoms are mainly contained in the wavelet planes of scale 3 and 4 and to a lower degree on scales 2 and 5. By contrast, the periodic structure of the CO layer mainly contributes to resolution levels 2 and 3. To create a particle mask sensitive to the oxygen atoms, it is therefore reasonable to combine the wavelet planes in which the O atoms have high coefficients, i.e., in W_3 and W_4. In addition, it is also important to consider the scales in which the O atoms are the most prominent features, like in W_5, but not like in W_2 in which the CO structure is at least as prominent as the O atoms. The optimum choice of scales is, of course, dependent on the size of the particles in the image and thus also on the parameters used for image acquisition, such as image range and image size in pixels. An overview of typically used scales for the detection of O atoms for different sets of imaging parameters is given in Table 5.1 on page 121.

The resulting particle masks for the data of Figure 3.11 for $a = 3$ and $b = 4$ as well as for $a = 3$ and $b = 5$ are shown in Figure 3.12 in the upper left and in the upper right panel, respectively. Comparison with the original image shows that the oxygen atoms are well represented by both particle masks. While $P_{3,4}$ still contains much of the features arising from the periodic CO layer, the combination of three different wavelet planes in $P_{3,5}$ leads to an enhanced suppression of contributions from the CO structure. Nevertheless, the CO structure is still noticeably present in both particle masks.

A more selective particle mask can be created by removing low intensity coefficients, e.g., from stationary noise, from all wavelet planes W_i by a hard thresholding step prior to the creation of $P_{a,b}$.[64] For this purpose each wavelet plane is filtered with a level-dependent threshold t_i (eq. 3.15) to give a filtered wavelet plane tW_i according to equation 3.14. Only significant wavelet coefficients are preserved, whereas wavelet coefficients below t_i are set to zero.

$$tW_i(x,y) = \begin{cases} W_i(x,y), & W_i(x,y) \geq t_i \\ 0, & W_i(x,y) < t_i \end{cases} \tag{3.14}$$

with

$$t_i = m \cdot \sigma_i^{noise} = m \cdot \frac{\bar{\sigma}_i}{0.67} \tag{3.15}$$

σ_i^{noise} is the standard deviation of the noise coefficients at scale i that can be estimated from the *median absolute deviation* $\bar{\sigma}_i$ of all coefficients at level i.[105] m is an adjustable parameter that is usually set to $m = 3$.[64, 102] For the analysis of the STM images, m was set to 1.35 to filter less harshly. The filtered wavelet planes tW_i are also shown in Figure 3.11. Evidently, the thresholding step suppresses a part of the unwanted contribution from the CO structure in the wavelet planes 3 and 4, while the appearance of the O atoms is not altered.

When these filtered wavelet planes tW_i are used to create the particle mask, all features that do not significantly contribute on all chosen scales are eliminated. The particle masks are shown in Figure 3.12 in the lower panel for $a = 3$ and $b = 4$ on the left and $a = 3$ and $b = 5$ on the right. The contributions from the CO layer are clearly reduced for both cases, $P_{3,4}$ and $P_{3,5}$.

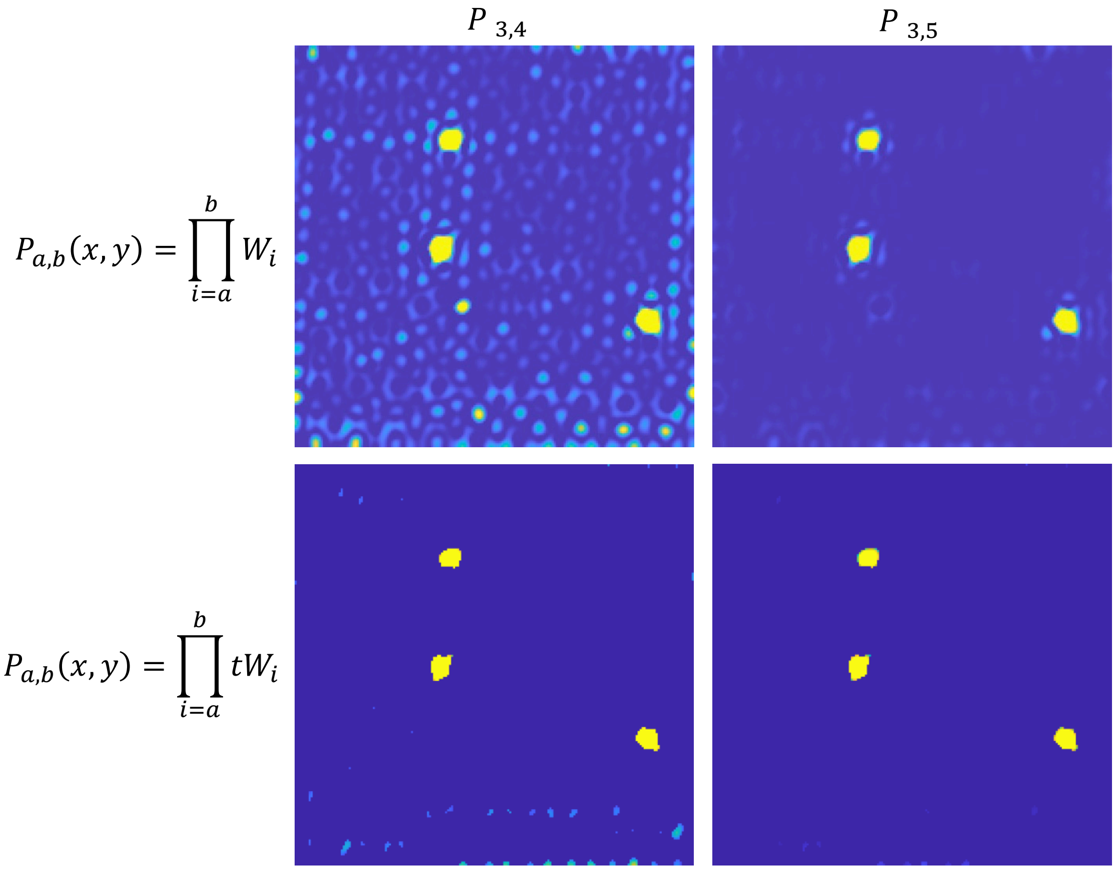

Figure 3.12: Particle masks $P_{a,b}(x,y)$ for detection of the O atoms for the data of Figure 3.11. The upper particle masks are generated by using the unfiltered wavelet planes W_i, while the lower masks are created from the filtered wavelet planes tW_i. The left particle masks were generated for $a = 3$ and $b = 4$, the right ones for $a = 3$ and $b = 5$. (All particle masks are normalized with respect to the highest coefficient and displayed within the same colormap range.)

In the last step of the localization a global detection threshold t_d is introduced to distinguish between detected particles and background of the image in the particle mask $P_{a,b}(x,y)$. Coefficients above or equal to t_d are set to one, while all other coefficients ($<t_d$) are set to zero. t_d has to be determined individually for each dataset. (A detailed explanation of the influence of the detection threshold on the resulting particle tracking is given in section 3.6.) A morphological closing operation is subsequently applied to the created Boolean array to remove single zero valued pixels that lie within a detected particle. Neighboring coefficients with value one are then counted as one particle. The particle position is subsequently determined by the center of mass of all pixels that belong to one particle resulting in a sub-pixel localization. Particles with less than 5 pixel size are disregarded in the further analysis.

3.4.3.3 Linking of Particle Positions

In the next step, in order to create particle trajectories from the detected particle positions in each STM image, the positions have to be linked between consecutive images in a dataset. Therefore the distances between all particles found in consecutive frames are determined. Particles are then linked based on a nearest-neighbor approach, but only if their distance is below a predefined tolerance value. Distances are calculated between images in up to five sequential frames in case particles were not recognized in some of the individual frames.

If the algorithm locates more than one particle within the tolerance radius, no linking is performed and the trajectory ends in order to prevent artifacts. New trajectories start as soon as the two particles are again separated by more than the predefined value. This assignment works fine for low particle coverages, but it leads to problems for higher coverages, where particles often come close to each other or cross each other's path. (In the latter case, for the same kind of particles, a reliable linking is even impossible by manual analysis.) However, for the present case of single O atoms in a CO layer where the O atoms are well separated from each other and interfere only rarely, the particle linking performs well.

Still, the definition of an appropriate tolerance radius is critical for the analysis result. If the tolerance radius is chosen too large, particles will be lost quite often during analysis as the possibility for detection of a second particle within the larger tolerance range increases. On the other hand, if chosen too small, the defined tolerance value will systematically influence the analysis result, as the movement of a particle by more than the tolerance value will always lead to the ending of the trajectory and thus systematically exclude longer movements. Consequently, the determination of the tolerance radius is a compromise between those two effects. In principle, both effects do not constitute a major problem as they can be corrected after the automatized analysis by manual connection of trajectories that belong to the same particle. But, of course, such a step significantly increases the manual work load for analysis. However, a finalizing manual reviewing step of the obtained trajectories is reasonable, as misdetections cannot be completely avoided and have to be sorted out before using the trajectories to extract kinetic parameters.

3.5 Drift Correction

The obtained particle trajectories are subject to drift of the STM setup. In principle, there are two different sources for drift. One reason is creep of the piezoceramic tubes after a change of the applied voltages, as the piezo material displays, in addition to the immediate length response, a small length change on a longer time scale. During the usual periodic scanning movement of the tip, this creep can be neglected, as a steady state is reached after a few periods. However, a change of the scanning area by adding an offset to the applied scan voltages leads to a rather significant creep that can be visible over several minutes in the images.

A second type of drift is thermal drift resulting from a non-uniform temperature of the sample-STM setup. This effect is especially relevant for STM studies in which the temperature is varied to monitor the temperature dependence of a process. For the presented VT-STM setup (section 2.3), temperature inhomogeneities of sample and STM head can be assumed to be rather large as different sample temperatures are realized by a combination of cooling with a liquid helium cryostat and radiative heating. Thermal drift is therefore an inevitable effect in these experiments even though the setup is optimized for temperature stability.

As drift results in a shift of the imaged area over the sample surface, it adds an additional motion vector to the movement of the particles. This effect can be a problem for the analysis of the dynamics as it deforms the trajectories, see Figure 3.14 b). Consequently, a drift correction has to be applied to the particle trajectories before further analysis. A standard procedure to determine drift is to do a 2D cross-correlation between consecutive images. The shift at which the images match best gives the drift vector in integer pixel values for x and y direction.

In the present Video-STM setup operated at typical imaging rates of more than 10 Hz, the drift between two consecutive images is generally much smaller than one pixel, so that the drift determination could not be performed by calculating the drift between pairs of consecutive STM images. A reasonable interval of images had to be found for each dataset, in which the drift was calculated and then distributed between the images in that range. The simplest approach would be to determine the drift by cross-correlation between the first and the last image in each STM movie, but this approach leads to problems for longer movies, as the imaged areas of first and last image of a dataset often do not overlap anymore. Furthermore, in most cases the drift is not constant in a dataset. Prior to the start of a new movie, the imaging range and position as well as the temperature were often changed leading to a comparatively large drift at the beginning of a movie that decreased in the course of the acquisition process. Moreover, the resulting drift vector was a sum of the two individual drift types, creep and thermal drift, which can have different directions. The resulting direction of drift could thus change in the course of a movie depending on how fast the two drift types decreased. Calculating the drift only between the first and last image would not account for such an inhomogeneity.

Therefore, in the present case, each dataset consisting of n_{frames} STM images is first split up into a number n_{int} of smaller intervals of length t_{int}. In each interval the drift is calculated by 2D cross-correlation between the first image n and the last image m in that interval. In this way, for the whole dataset, two vectors of length n_{int}, one for the shift in x and one for the shift in y direction, are created, which contain the determined drift values for each interval. Finally, the drift between two consecutive images is calculated by linearly interpolating in each interval. Smaller intervals are therefore well suited when the drift is quite inhomogeneous in a dataset, whereas a rather small drift can be more accurately corrected if the intervals are chosen larger, as the drift can only be determined to integer pixel values by the 2D cross-correlation. The length of the intervals thus has to be chosen individually for each dataset depending on the properties of the occurring drift.

The reliability of drift correction by this approach depends on the quality of the two selected images for cross-correlation. If at least one of the two images is of low quality, the cross-correlation may fail and give unreasonable pixel shifts for this image interval. “Low-quality” in this case means that an image may have a bad spatial resolution or may contain plenty of scan artifacts due to tip instabilities, such as line artifacts or spikes that do not allow for a reasonable overlay of the two images. Furthermore, when monitoring the dynamics on a surface in an STM movie, sometimes larger features (in comparison to the monitored atoms) intermediately move into the imaged area and then leave again or just appear in one image. It is unclear what causes those features, but they could for example be clusters of atoms that result from a change of the STM tip and end up on the sample surface. If such a feature is present in one of the selected images for cross-correlation the drift determination may also fail.

Moreover, drift correction is particularly problematic for the case of oxygen atoms in an ordered CO layer that was studied here. Because the cross-correlation gives high values for good agreement of the two images, static features are needed as reference points. The periodic structure of CO that is present in both compared images is static, but it also leads to periodic maxima in the correlation image. The O atoms are dynamic and cannot serve as reference. A slight distortion of one of the images may therefore lead to a false drift determination. Therefore, to detect and, if possible, eliminate such false drift determinations, two quality criteria were introduced to validate the calculated drift values for the individual image intervals.

Firstly, for each interval the drift is not only calculated between the first image n and the last image m, but also between $n+2$ and $m+2$, as well as between $n+4$ and $m+4$. In this way, three drift values are obtained for the drift in x and three values for the drift in y direction in each interval. The three values are then compared with each other in order to check if they are reasonable. If the first value is in agreement, or only +/- one pixel different from at least one of the other two values, it is taken as valid. If not, the second and third value are compared. They are again assumed to agree if they differ by not more than one pixel. In this case the second value is taken as the correct drift value. If in an interval of the dataset no pair of the three values is in agreement with each other, the drift determination is considered unreliable.

Table 3.1 and Table 3.2 illustrate the drift correction procedure for a fictive dataset consisting of a total number n_{frames} of 870 images. The dataset is split up into intervals of length $t_{int} = 100$, meaning eight intervals that cover 100 transitions from one image to a consecutive one and one interval of 69 transitions, resulting in $n_{int} = 9$ intervals.

The first interval is from image number 1 to image number 101. The drift in this first interval is then determined three times, by cross-correlation of image 1 and 101, image 3 and 103, and image 5 and 105. The three values for x and y, respectively, are subsequently compared according to the above mentioned selection rules. In Table 3.1, the first value for the shift in x is considered reliable as it is in agreement with the second one. For the shift in y, the first value is not confirmed by one of the two other values, but as the second and third value agree with each other, these values are considered reliable and the second value is used. The resulting pair of drift values is (-5,3) and the drift between two consecutive images in interval 1 is thus estimated as $\left({}^{-5}/_{100}, {}^{3}/_{100}\right)$. In an analog manner the drift is determined for interval two, which covers images 101 to 201 and all other intervals up to interval number $(n_{int} - 1) = 8$ (corresponding to images 701 to 801).

Table 3.1: Drift determination for a dataset of 870 images and an interval length of t_{int} = 100 for interval number 1. The drift determination for interval number 2 up to interval number $(n_{int} - 1)$ (not shown) would be analogous.

Interval 1: Image 1 to 101 (analog for intervals 2 to $(n_{int} - 1) = 8$)					
	n – m 1-101	(n+2) – (m+2) 3-103	(n+4) – (m+4) 5-105	**resulting drift**	**drift per image**
Shift in x	-5	-6	-3	**-5**	**-5/100**
Shift in y	15	3	4	**3**	**3/100**

For the last interval n_{int} = 9 the drift is determined for three different pairs of images. The first value is determined by use of the first and the last image of the interval *n* = 801 and *m* = 870 in analogy to the drift correction in the other intervals. As image 870 is also the last image of the dataset, the second drift value is determined by using images *n-2* and *m-2* instead of *n+2* and *m+2*, the third value by using images *n-4* and *m-4* instead of *n+4* and *m+4*. The resulting drift for *x* and *y* is again determined according to the mentioned rules. The drift per image is then obtained by division by 69 (Table 3.2).

Table 3.2: Drift determination for a dataset of 870 images and an interval length of t_{int} = 100 for interval number n_{int} = 9.

Interval n_{int} = 9: Image 801 to 870					
	n – m 801-870	(n-2) – (m-2) 799-868	(n-4) – (m-4) 797-866	**resulting drift**	**drift per image**
Shift in x	0	2	1	**0**	**0/69**
Shift in y	2	-6	3	**2**	**2/69**

With the quality criterion described, wrong drift values that may arise from the use of individual low-quality images in the cross-correlation step can be detected and eliminated. For a small sequence of low quality images, if, e.g., all images in the range of *m* to *m+4* contain many spikes, the quality criterion detects an unreliable drift correction, as three mismatching drift values are found. In such a case the interval length is changed and a new drift correction is performed. However, this quality check would not work for the case in which a prominent feature, such as an adsorbate cluster, does not only appear in one or two individual images, but is visible over a higher number of consecutive frames. In such a case, the cross-correlation might result in three very similar drift values, so that the quality check would not detect any problem whereas the real drift value might be quite different from the determined one.

To address this problem, a second quality check has been introduced that determines the drift in a similar manner as explained above, but for half as large intervals of length $\frac{t_{int}}{2}$. Again, for each of the newly created shorter intervals, the drift is calculated between the limits *n* and *m*, *n+2* and *m+2* and *n+4* and *m+4*. The same selection rules are applied for identifying the reliable value out of the three calculated ones. In the next step the drift values for each two consecutive shorter intervals are added up to obtain a drift value for the original interval size of t_{int}. This sum is then compared to the previously obtained value for the original intervals t_{int}. An example for this process is given in Table 3.3 for the same dataset as in Table 3.1 and Table 3.2.

For the first two smaller intervals 1a and 1b, covering images 1 to 51 and images 51 to 101, the drift in *x* is determined to -3 pixels each. This results in a total drift of -6 for frames 1 to 101 (highlighted in light gray in Table 3.3). In comparison to the drift determined with the original interval length t_{int} (highlighted in dark gray in Table 3.3), there is a difference of one. In an analog manner the drift is determined to +4 from the smaller intervals 1a and 1b for the shift in *y* direction. Again the absolute value differs by one from the value obtained with the original interval length for interval 1. As a result the difference for both drift values (in *x* and in *y* direction) for the first interval amounts to 2. In the same way the drift is determined and compared for all other intervals in the dataset.

Finally, the sum of the absolute differences in all intervals *Diff_total* is used as a quick indicator for a problem in the drift correction procedure. A high value points to a large discrepancy in at least one interval and could thus indicate a problem of the original drift correction. Because the height of *Diff_total* depends on the number of intervals created in the dataset, a value *Diff_norm*, normalized with respect to n_{int}, is used to evaluate the conformity of the two drift corrections. While *Diff_norm* values of ~1 are typical and reflected the usual uncertainty in the drift determination, values for *Diff_norm* ≥2 could point at a problem of the original drift determination. This second quality check can be interpreted as a warning signal to further check the reasonability of the determined drift. Yet, it does not serve as a sufficient criterion to rule out certain drift correction results as erroneous, as a high total difference could also arise from a failed drift determination while using the shorter intervals $\frac{t_{int}}{2}$.

Table 3.3: Illustration of the second quality check in the drift determination procedure for a dataset of 870 images (compare Table 3.1 and Table 3.2). The drift is calculated for half as large intervals of length $\frac{t_{int}}{2} = 50$. The sum of each two adjacent intervals (highlighted in light gray) is compared to the drift correction obtained for the original interval length t_{int} =100 (highlighted in dark gray).

			Interval length $\frac{t_{int}}{2}$				**Interval length t_{int}**		**Difference $\frac{t_{int}}{2}$ to t_{int}**
Interval #		images	Shift in *x*	Sum *x*	Shift in *y*	Sum *y*	Shift in *x*	Shift in *y*	in *x* and *y*
1	1a	1-51	-3	-6	2	4	-5	3	**2**
	1b	51-101	-3		2				
2	2a	101-151	-2	-4	2	3	-4	3	**0**
	2b	151-201	-3		1				
…	…	…	…	…	…	…	…	…	**…**
9	9a	801-851	0	0	1	1	0	2	**1**
	9b	851-870	0		0				
								Total Difference *Diff_total*	**3+…**
								Normalized Difference *Diff_norm*	$\mathbf{\frac{3+\cdots}{9}}$

The first quality check is therefore applied to exclude drift corrections that are not considered reliable. The second check has more the role of an add-on for verification that points to possible problems not detected by the first criterion.

In practice the drift correction and their evaluation by the two quality criteria are performed automatically for many different interval sizes to find the most suitable interval length for each individual dataset. A schematic overview of this procedure is shown in Figure 3.13. In the first step the drift is determined for a start value of t_{int} (input parameter, blue). t_{int} has to be even-numbered, since $\frac{t_{int}}{2}$ must be an integer as well. A reasonable starting value is $t_{int} = 20$. The drift is calculated for this interval length and the resulting drift correction is evaluated by the first quality criterion as explained above. If the first quality check fails for at least one interval, t_{int} is incremented by 10 and the drift correction and the first quality check are repeated until the resulting drift correction fulfills the first criterion.

The drift correction is then passed on to the second quality check, in which the drift is determined for half intervals $\frac{t_{int}}{2}$ and the difference *Diff_norm* is calculated. If *Diff_norm* is lower than a user-set threshold value *Diff_thr* (input parameter, blue) the drift correction is considered reliable. If *Diff_norm* is above *Diff_thr*, t_{int} is increased by 10, and the whole procedure is repeated with the new interval length. If no drift correction is found that fulfills both criteria for $t_{int} \leq 500$, the procedure is aborted. The analyses performed in this work showed that for larger intervals the overlap between first and last images becomes too small to produce reliable results in the cross-correlation step.

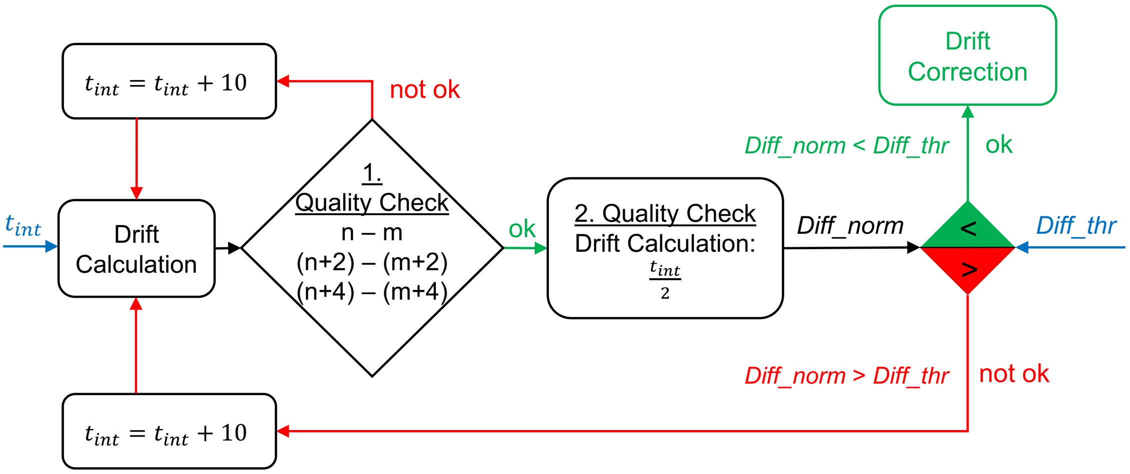

Figure 3.13: Schematic overview of the drift correction and evaluation procedure. The required input parameters t_{int} and *Diff_thr* are marked in blue.

The user-defined value *Diff_thr* can be used to fine tune the drift correction, because it determines how well the two drift corrections for t_{int} and $\frac{t_{int}}{2}$ have to match in order to be accepted. Reasonably, in the beginning of a drift-correction procedure a rather strict threshold value of *Diff_thr* ~1.0 should be used to enforce good agreement. If no valid drift correction is found, the *Diff_thr* threshold can be systematically loosened to allow for less exact matches in the subsequent runs.

If a successful drift correction is found, it is applied to the particle trajectories by shifting the x and y coordinates of each determined particle position by the drift value for the corresponding image. An example for a successful drift-correction of particle traces is presented in the following section 3.6.

The STM images themselves remain uncorrected, as the shift between two consecutive images is always only a fraction of a pixel. In order to create a drift-corrected version of STM images, the intensity values of the individual pixels would have to be partially shifted between adjacent pixels. Depending on the respective drift vector, new intensity values would thus have to be calculated for every pixel in every image, a computational costly procedure, which is therefore avoided.

3.6 Resulting Particle Trajectories

Particle trajectories obtained from a dataset acquired at -6 °C with an imaging rate of 10 Hz are shown in Figure 3.14. The whole movie consists of 2490 images. A single frame of the rectified dataset is depicted in Figure 3.14 a). This dataset is well suited to demonstrate the performance of the particle tracking and drift correction routines for the O/CO/Ru(0001) system as it contains the most frequently occurring features. The periodic structure of dark spots is the $(\sqrt{3} \times \sqrt{3})R30°$ structure of CO on Ru(0001). The edge of a (2 x 2) island of oxygen atoms (bright spots) is visible at the right border of the image. Two individual O atoms move in the scanning area, while there are also three immobile single atomic features of unknown nature. These are most likely nitrogen atoms, because of their higher diffusion barrier on Ru(0001) compared to O.[106] The corresponding uncorrected particle trajectories are depicted in Figure 3.14 b). The drift-corrected particle traces are shown in c). Different trajectories are illustrated in different colors. As a guide to the eye, the positions of the three static features are marked with a red, yellow, and purple arrow in the individual parts of Figure 3.14. The individual O atoms are highlighted by a green and a blue arrow.

The uncorrected particle trajectories in b) are strongly deformed due to instrumental drift during the measurement. This becomes particularly clear in the traces of the three static features. They appear strongly elongated, mostly in y direction. Especially interesting are the immobile particles marked in yellow and purple, as they are present in the imaged sample area over the entire time in the STM movie. Thus, in principle the drift vector for the whole dataset can be directly seen from the two corresponding uncorrected trajectories. While the particle belonging to the purple trajectory was tracked as one throughout the whole dataset, the particle marked by the yellow arrow was lost two times in between. Therefore, the corresponding total trajectory consists of three differently colored parts: green, black, and yellow. Both traces stretch out over a range of ~70 Pixels. The particle marked by the red arrow is not visible in the first part of the dataset, but then enters the imaged area from above. The form of the corresponding trace [red, Figure 3.14 b)] therefore follows the form of the two other trajectories (yellow and purple) at their lower end. After drift-correction [Figure 3.14 c)], the trajectories of the three static particles are projected onto a small spot, which proves a successful drift correction.

Here, an interval size of t_{int} = 110 has been used for the drift-correction. The resulting *Diff_norm* value is 0.61, indicating that the automated drift correction performed very well in the presented case. The reason for this is that the images contain several static features, such as the (2 x 2)-O island and the single immobile atoms, which allow for an unambiguous assignment in the 2D cross-correlation. A detailed listing of the determined drift values for this dataset is provided in Appendix C.2.

The particle traces at the right edge of the trajectory image in b) and c) correspond to the (2 x 2) island of oxygen atoms that is also visible in a). O atoms located inside the oxygen islands appear somewhat different due to the close proximity to the other bright O atoms. In comparison to single O atoms, the atoms inside the islands contribute more towards lower resolution wavelet planes in the WT decomposition, so that if one is only interested in individual O atoms, the O atoms in an island can be sorted out in this step by a smart creation of the particle mask and the setting of the finalizing detection threshold. On the other hand, atoms at the edges of the islands closely resemble the appearance of the individual O atoms and cannot be distinguished by the tracking algorithm, so that these edge atoms must be manually removed prior to the next analysis step.

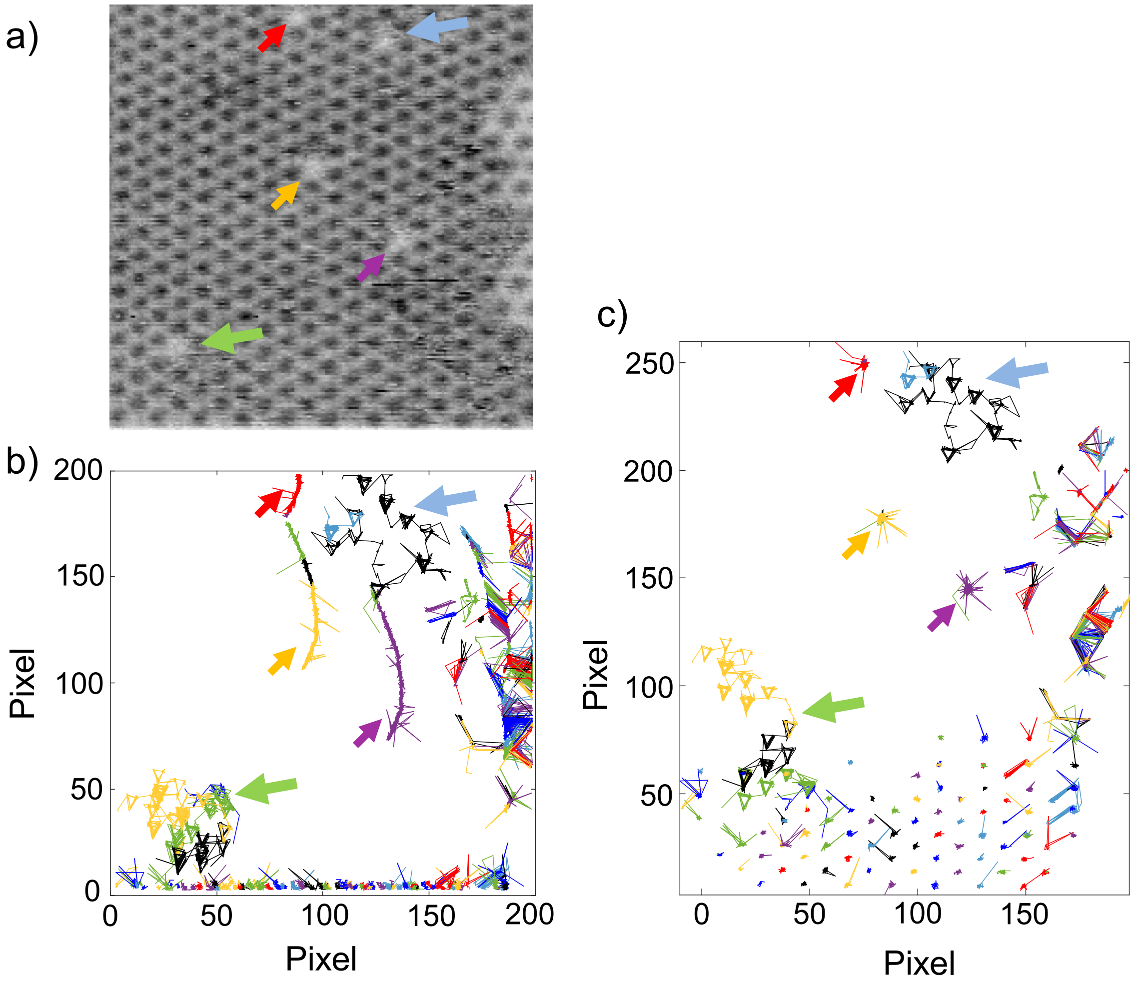

Figure 3.14: Drift correction of particle trajectories. a) Single STM image from a movie of individual O atoms (bright, marked by the blue and green arrows) in the $(\sqrt{3}\,\mathrm{x}\,\sqrt{3})$R30°-CO structure (dark) on Ru(0001) (~85 x 85 Å, 199 x 200 Pixel, 2490 frames, T=- 6°C, V_t = -0.7 V, I_t = 3 nA). b) Uncorrected output of the particle tracking algorithm. c) Drift-corrected version of the particle traces depicted in b). Different trajectories are illustrated in different colors. Three immobile atoms and their corresponding trajectories are marked by a red, yellow, and purple arrow, respectively.

The detected particles along the lower edge of the image [Figure 3.14 b)] are not real but result from an artifact created by the video-rate STM acquisition. The movie has been acquired in the upward imaging mode, i.e., starting at the lower edge of the image. Because the scanning in y changes from down to up at this edge the piezo creep leads to a small initial motion opposite to the nominal scanning direction in y. The result is a slightly deformed CO structure in the first few lines of every image, so that the bright interspace between adjacent (dark) CO molecules is imaged similarly as the particles of interest, the O atoms, and is therefore detected. This effect shows up very clearly in the drift-corrected trajectories, as the detected particles at the lower edge form a $(\sqrt{3} \times \sqrt{3})R30°$ lattice when drift-corrected. The occasionally visible connections between two adjacent $(\sqrt{3} \times \sqrt{3})R30°$ "lattice points" or CO molecules result from the fact that the tolerance value for particle detection for this dataset has been in the range of the lattice constant of the $(\sqrt{3} \times \sqrt{3})$ structure.

The two single oxygen atoms that move on the surface show a rather complex diffusion behavior. Their trajectories in the lower left (green arrow) and in the upper right corner (blue arrow) in Figure 3.14 b) consist of equilateral triangles of the same size and orientation that are connected with each other. Whereas the trace in the upper right part of the image exhibits clear triangular structures, the trajectory in the lower left corner appears blurred and the triangles smeared. After drift-correction, both trajectories show nice and well-arranged sequences of triangles forming a $(\sqrt{3} \times \sqrt{3})R30°$ lattice with respect to the Ru substrate, like the CO structure. A detailed study of the diffusion mechanism of single O atoms in a full layer of CO on Ru(0001) follows in section 5.4.

In order to evaluate the performance of the particle tracking routine, the properties of the resulting trajectories for the two single oxygen atoms can be compared to the original movie data. The O atom in the lower left corner (green arrow) is visible as a whole in the movie from frame 1 to frame 2435. The corresponding trajectory in Figure 3.14 c) ranges from image 1 to 2437, consisting of 2405 single positions. The difference means that the O atom was not recognized by the detection routine in 33 individual images. On the other hand, the routine also detected the atom in two images in which it was only partly visible at the edge of an image. The O atom is lost four times in this range as indicated by the differently colored parts of the trajectory.

The trajectory of the second O atom (blue arrow) in the upper right quadrant of the image covers frames 1412 to 2490, exactly the same range in which the O atom is fully visible in the original data. In this range of 1079 consecutive images, the O atom has been detected 1068 times and the trajectory is interrupted once.

These results demonstrate that the individual oxygen atoms are tracked very efficiently throughout the STM movie. On average, for this dataset, the O atoms are detected in ~99 % of the images in which they are present in the movie. In the remaining one percent of the images, the appearance of the O atoms is altered to such an extent that they become suppressed by the detection threshold and are thus not recognized. Such changes of the shape of the O atoms in individual images can happen because of measurement artifacts, e.g., line defects or spikes, or by real processes on the surface, such as that intermediately some molecule (that itself is not detected) comes close to the atom. By variation of the detection threshold value t_d in the particle detection routine, the percentage of images in which the O atoms are detected can be tuned. A less restrictive, i.e., lower, threshold would further increase this value, while at the same time the number of misdetections (detections of other features than the particles of interest) would also rise. A harsher (higher) threshold, on the other hand, would significantly decrease misdetections, but would also lead to a higher number of images in which the O atoms are not identified.

In the present case, the O atoms are tracked on average over ~500 consecutive images until they are lost by the tracking algorithm. Such a loss is the result of either two particles being detected within the tolerance radius, a jump of the particle over a larger distance than the defined tolerance (section 3.4.3.3), or that the particle is not detected in five or more consecutive frames. Here, the selected detection threshold has opposing influences on the length of the trajectories. If the particles of interest are less efficiently detected, because of a high value for t_d, the corresponding trajectories might by disrupted with increased regularity, because the abort criterion of no detection in five or more consecutive frames is met more often. On the other hand, as the number of misdetections rises because of a comparatively low detection threshold, trajectories will end more frequently because two features are detected within the tolerance radius. The selection of the detection threshold has to be a trade-off between the mentioned effects.

Irrespective of the value for t_d, the resulting particle trajectory image will always contain traces of several other detected features besides the particles of interest. This is not because of a weakness in the particle detection algorithm, but because many features on the surface are of similar size and appearance. In the case of the dataset of Figure 3.14 the immobile single atoms or the deformed CO structure in the first few lines of the images appear similar to the O atoms. In the case of the (2 x 2) oxygen islands, the particles are even identical, and only their surrounding is a little bit different.

On one hand, the presence of these additional static features in the trajectory image eases the validation of the performed drift-correction just by looking at the trajectory image, as their trajectories have to be projected onto one spot afterwards. Yet, these additional trajectories need to be identified and removed prior to any further analysis that is based on the traces. Therefore, despite all the achieved automation in the evaluation procedure, a final manual reviewing step remains necessary. In this reviewing step all trajectories that do not belong to the particles of interest are sorted out. Furthermore trajectories that technically belong to the same particle are connected to eliminate the influence of the tolerance value defined in the particle tracking step and thus to exclude the influence of systematic errors.

3.7 Summary

In the course of this work, a complete image processing and evaluation procedure has been established that enables the automated analysis of STM movies with regard to the dynamics of individual particles on the surface. All image processing and analysis tools have been developed in the *MATLAB* programming environment. By changing the analysis environment from the default *IGOR Pro* software in the working group Wintterlin to *MATLAB* even the largest acquirable STM datasets can be handled.

An overview of the developed image processing routines and analysis steps and their resulting effects on the data is provided in Figure 3.15 using a single frame of a STM movie consisting of 1695 individual images. Firstly, the original STM data (1) are rectified (2) to remove the image deformation introduced by the use of a sinusoidal scan ramp. In the second step the images are filtered (3) to reduce noise and suppress imaging artifacts, especially line defects. For the example in Figure 3.15 the filtering step only marginally increases the quality of the STM image and would thus not be necessary for further analysis, but, of course, the aim has been to develop the routines in such a way that datasets with poorer quality can be evaluated as well.

For particle detection each image is decomposed by an *à-trous* WT and a particle mask (4) is created by combining the wavelet planes on the most characteristic scales for the particles of interest. The particle positions in each frame are determined by their center of mass and then linked in consecutive frames by a nearest-neighbor approach. The example shows the resulting particle trajectories over a sequence of 1695 consecutive STM images (5). The positions in the individual frames are connected by lines. The positions of the three individual O atoms in the rectified STM image (2) are circled in red in the trajectory image (5). The shown trajectories also arise from several other particles that entered or left the imaged area during the STM movie. The trajectories are subsequently corrected for drift (6). After drift correction the particle trajectories form a well arranged lattice. The edges of the triangles of all trajectories coincide, e.g., for the blue and yellow trajectories in the image center. A manual selection step in which the quality of the trajectories is checked, trajectories that belong to the same particle are reconnected and misdetections are sorted out, finalizes the particle tracking.

All in all, the developed evaluation routine allows for automated extraction of surface dynamics from STM measurements. The information from thousands of individual STM images are finally condensed into the particle trajectories that contain both, spatial and temporal information. The trajectories form the starting point for the detailed analysis of the underlying movement principles of the particles of interest. This will be shown in section 5.3 for the case of the diffusion of individual O atoms in the full layer of CO on Ru(0001). The great reduction of manual workload in the analysis thus allows for a significant improvement of the statistics.

An overview of all *MATLAB* scripts developed in this work together with a short description of their functionality is given in Appendix C.1.

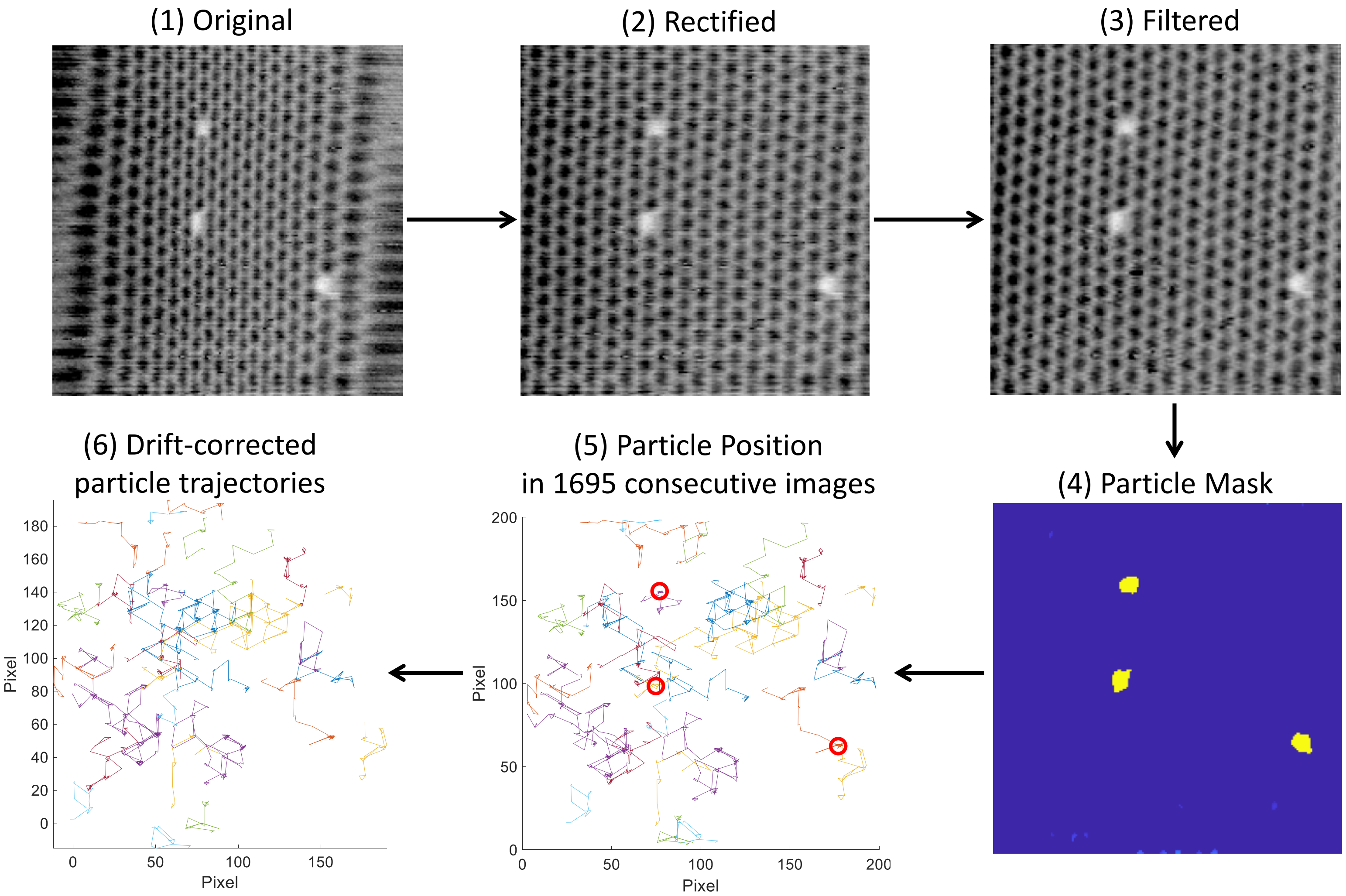

Figure 3.15: Overview of the developed image processing and evaluation routines for the extraction of trajectories of single particles from STM images.

4. Experimental Setup and Methods

4.1 Ultra-High Vacuum System

Within this work experiments were performed in a UHV chamber of the Wintterlin group at *LMU* Munich that houses the VT-STM setup described in chapter 2. The UHV chamber was originally designed by T. Gritsch at the *FHI*.[107] The system is pumped by a combination of a titanium sublimation pump, an ion getter pump, and a turbo molecular pump with a rotary pump for generating the primary pressure. The setup provides a base pressure of $<1 \cdot 10^{-10}$ Torr, which is measured by a *Bayard-Alpert* ion gauge by *Arun Microelectronics Limited* (*AML*). A quadrupole mass analyzer (QMS/QMA 200, *Pfeiffer Vacuum*) is used for analyzing the residual gas phase. For this work Ar (Purity: 99.999 Vol.%, *Linde Minican*), O_2 (Purity: 99.995 Vol.%, *Linde Minican*), CO (Purity: unknown, *Linde* glass container), H_2 (purity: 99.999 Vol.%, *Linde Minican*) were available for dosage into the UHV chamber. Gas dosing was generally performed via background dosing.

The preparation of the sample is performed using the manipulator of the chamber. The manipulator is equipped with a tungsten filament mounted at the backside of the sample, by which temperatures of up to 600 °C are achieved by radiative heating. To reach higher temperatures a high voltage (max. 2 kV) is applied between filament and sample by which the sample can be heated to T >1500 °C by electron bombardment. Furthermore, the manipulator allows for cooling of the sample. Using a rotary pump liquid nitrogen can be pumped through a tube that leads into the UHV chamber and ends in a copper block located close to the sample holder of the manipulator. The copper block acts as cooling reservoir. Copper braids connect the sample holder and the copper block. In this way minimum sample temperatures of approximately -165 °C can be reached.

The sample surface is cleaned by ion bombardment. Using a *sputter gun* by *Leybold-Heraeus* argon atoms are ionized and accelerated with an energy of 1 keV to the sample. The impinging Ar^+ ions remove the topmost atom layers of the sample.

The UHV chamber further houses a four-grid low energy electron diffraction (LEED) optics and an Auger electron spectrometer to analyze the chemical composition of the sample surface. The Auger electron spectroscopy (AES) system (*Perkin-Elmer*) consists of an electron gun usually operated at an acceleration voltage of 3 kV, a single-pass cylindrical mirror analyzer for energy-separation, and a *Channeltron* for detecting the *Auger* electrons. To enhance the signal-to-noise ratio, the signal is amplified and differentiated with respect to the electron energy (dN/dE) by a lock-in amplifier (Model 5209, *EG&G*). By means of an analog-to-digital converter (±10 V, 12 bit, PS-2115, *Pasco*) the signal is recorded using the program *Data-Studio* (*Pasco*). For the Ru crystal the energy scales of the spectra were referenced to the main ruthenium signal ($M_5N_{4,5}N_{4,5}$) at a kinetic energy of 273 eV[108, 109].

The central element of the chamber is the video-rate VT-STM, described in chapter 2, to which the sample can be transferred by means of a wobble stick manipulator. In this work, the piezoelectric conversion factors of the VT-STM setup were calibrated using ordered superstructures of CO [$(\sqrt{3} \times \sqrt{3})$R30° structure] and O [(2 x 2) structure] on the Ru(0001) surface. Values of 0.459 Å/mV were obtained in x direction, 0.527Å/mV in y, and 0.057 Å/mV in z direction. For vibration isolation the whole chamber is mounted on four pneumatic vibration isolators (*Newport XL-A*) and turbopump and rotary pump are shut down during STM measurements. The vacuum is then maintained by the ion getter pump.

4.2 Sample Setup and Temperature Measurement

The employed sample is a Ru(0001) single crystal that has a disk-like shape and features two grooves on opposite sides of the crystal for mounting. Figure 4.1 illustrates the sample holder that was modified for the special properties of the Ru crystal. The sample holder contains a segmented helical ramp that acts as platform for the *beetle-type* STM. Two tantalum clamps in the grooves of the crystal hold the sample [Figure 4.1 a)]. The specific form of the clamps adjusts the height of the crystal relative to the sample holder. The sample together with the Ta clamps is inserted from the rear side into the sample holder and fixed with a tantalum ring and three molybdenum screws, see Figure 4.1 b). Figure 4.1 c) visualizes the complete sample setup.

As the preparation of a clean Ru crystal requires temperatures of up to 1500 °C[110, 111] all materials used for the sample setup need to be temperature stable at least up to this temperature. The components of the sample holder are therefore exclusively made from molybdenum (melting point: 2617 °C, vapor pressure at 1500 °C: $<10^{-11}$ Torr[112]), tantalum (melting point: 2998 °C, vapor pressure at 1500 °C: $<10^{-11}$ Torr[112]), and Al_2O_3. The mounting of the sample with the two Ta clamps is necessary to ensure only little mechanical contact between crystal and sample holder in order to minimize the heat flux from the sample during heating. Otherwise the required preparation temperatures would not be reached with the available heating power.

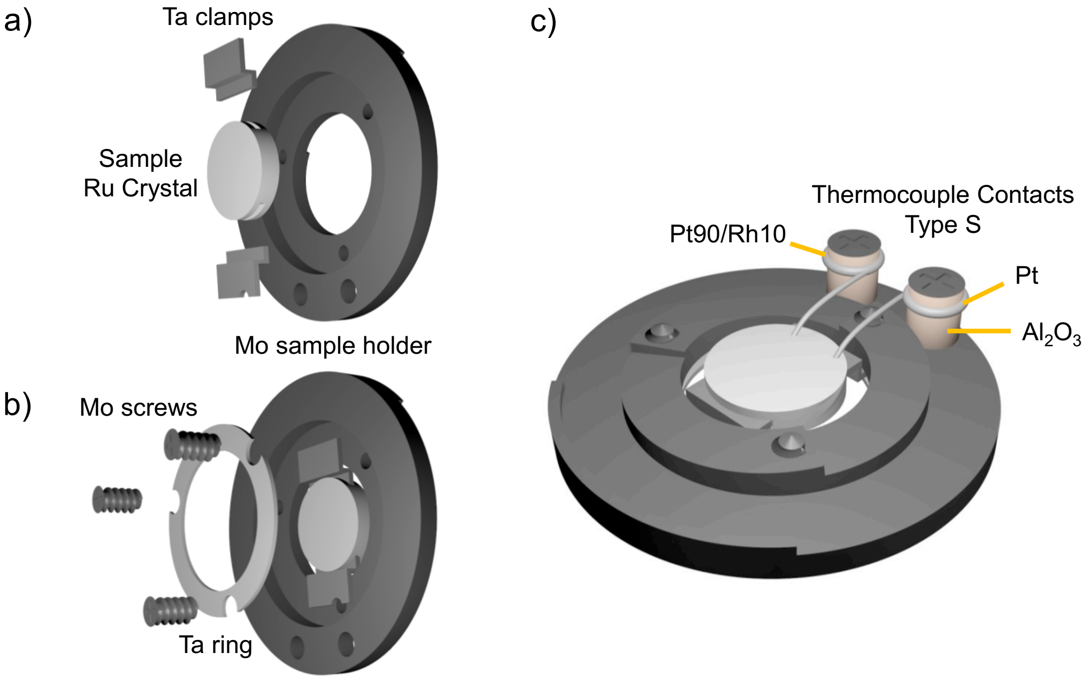

Figure 4.1: Scheme of the sample setup. a) The slit Ru single crystal is inserted from the back into the molybdenum sample holder together with two tantalum clamps b) A tantalum ring fixes the crystal in the sample holder c) Complete sample setup. For temperature measurements a type S thermocouple is spot-welded to the sample surface.

Temperature measurement of the sample is performed with a thermocouple pair spot-welded onto the sample surface, see Figure 4.1 c). The two thermocouple wires are passed on from the sample to two separate corundum (Al_2O_3) ceramics, which are mounted at the rim of the sample holder with two Mo screws. The ceramics ensure the electric insulation of the thermocouple from the rest of the sample holder.

For this work the standard type K thermocouple could not be used, as the melting points of the two components lie below the required preparation temperature for the Ru sample (*alumel* Ni95(Al+Mn+Si)5, melting point: 1315-1390 °C; *chromel* Ni90Cr10; melting point: 1420 °C). Instead, a type S thermocouple was used, which consists of Pt and a Pt90Rh10 alloy. The two components have melting points well above 1500 °C (Pt: 1770 °C; Pt90Rh10: 1830-1855 °C) and allow for temperature measurements between -50 °C and +1768 °C.

Despite their high melting points, the positioning of the thermocouple wires relative to the crystal turned out to be crucial in the sample preparation process. It was first tested to mount the wires at the backside of the crystal, but this configuration reproducibly led to burning of the thermocouples during heating of the crystal even when the crystal temperature was still below 1500 °C, obviously because of the close distance to the heating filament and the low thermal conductivity of the thin wires (Ø = 0.05 mm). This problem could be avoided by attaching the thermocouple wires to the top site of the Ru crystal, as indicated in Figure 4.1 c).

When inserting the sample into the manipulator or the STM, the two ceramics that hold the thermocouple wires are guided into two slots. Here, contact is made between the thermocouple on the sample holder and clamps of the same thermoelectric materials that lead to a feedthrough at the UHV chamber. As the materials of the type S thermocouple are comparatively expensive, the thermocouple feedthrough (*Allectra GmbH*) is realized with OFHC copper (*oxygen free high conductivity*) and *copper alloy 11* (Cu95Ni3Mn2[113]) as compensating leads for the type S thermocouple. The room temperature at the transition point between thermoelectric wires and normal cables serves as reference for the resulting thermoelectric voltage. In this work, the room temperature was therefore constantly measured with a *Pt1000* resistance thermometer; a thin Pt layer with a defined resistance-temperature relation (1000 Ω at 0 °C) housed in a ceramic compound. The determined room temperature was also frequently crosschecked with a mercury thermometer. Additionally, the sample temperature is determined from outside of the UHV chamber using a pyrometer (*Impac*, wavelength 1.45 μm to 1.8 μm, emissivity(Ru) = 0.224), applicable for sample temperatures above ~350 °C and therefore only used during sample preparation.

The use of the type S instead of type K thermocouple implicates problems for measurements at low temperatures, as the thermoelectric voltage is only defined and tabulated down to -50 °C. In order to find out if also lower temperatures can be measured the Ru crystal was contacted with both, a type S and a type K thermocouple for a calibration measurement. The contact points for the two thermocouples were as close as practically possible. The sample was then cooled in the STM from room temperature to approximately -200 °C by use of the liquid helium cryostat. Then the sample was slowly heated up by the combined liquid helium cooling and radiative heating with the tungsten filament at the back of the sample to simulate the temperature adjustment during the STM measurements.

The measured thermoelectric voltage of the type S thermocouple is plotted against the voltage of the type K thermocouple in Figure 4.2. All values are corrected for the room temperature and thus referenced to 0 °C. The measured type K thermoelectric voltages were also converted into °C, depicted on the upper axis. As a reference the tabulated values down to -50 °C are given for both thermocouples in yellow.

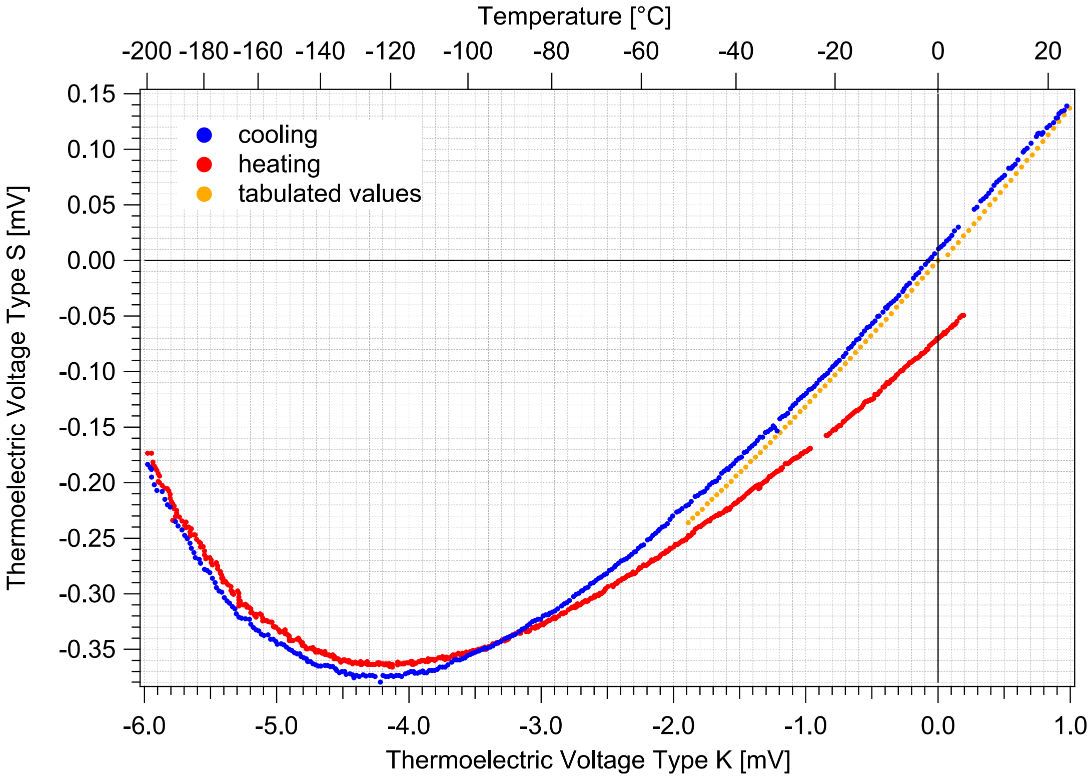

Figure 4.2: Temperature calibration of the type S thermoelectric voltage against a type K thermocouple. Blue: Cooling of the sample with liquid helium. Red: Heating of the sample starting at ~-200 °C by combined liquid helium cooling and radiative heating. Yellow: Tabulated standard values for type S and type K between -50 °C and room temperature.

While cooling down (blue dots) the type S voltage nicely follows the standardized values down to -50 °C. The small positive offset might arise from the correction of the measured values by the room temperature. Below -50 °C, the curve becomes flatter and reaches a minimum at approximately -125 °C. For even lower temperatures the thermoelectric voltage of the type S thermocouple increases again. For the minimum temperature of around -200 °C, a voltage of -0.018 mV is measured.

The shape of the voltage curve has two implications for temperature measurement. Firstly, because of the minimum the type S thermoelectric voltages at low temperatures are not unambiguous. It can be determined, however, whether the measured voltage corresponds to a temperature below or above the minimum by slightly varying the temperature by increasing or decreasing the current through the heating filament. When the thermoelectric voltage decreases after this step, the sample temperature is below -125 °C and vice versa. Secondly, voltage variations between approximately -110 °C and -140 °C are small (below 1 μV per K) corresponding to a relative high uncertainty in the temperature value. Despite these constraints, temperatures below -50 °C can be measured with a type S thermocouple.

The heating curve (red dots in Figure 4.2) agrees reasonably well with the cooling curve below the minimum, but increasingly deviates at higher temperatures. The deviation can be explained by the fact that during the heating curve both, the heating filament and the liquid helium cooling, are on, so that there is a permanent heat flow across the sample. A temperature gradient builds up that, because of the different positions of the type S and type K thermocouples on the sample, leads to a temperature difference.

For the STM measurements the helical ramp of the sample holder must be freely accessible to set down the STM head. The position at which the thermocouple can be attached to the crystal surface and passed on to the ceramics at the rim of the sample holder is therefore quite restricted. The type S thermoelectric wires were therefore mounted as depicted in Figure 4.1 c) and Figure 4.3 b). The position is directly above a Ta clamp. A second calibration measurement was therefore performed to quantify the temperature gradient over the sample. For this purpose the type K thermocouple was spot-welded to the sample at locations midway between the two Ta clamps [Figure 4.3 a) and b)]. At these locations the temperature gradient from the center of the crystal (where the STM tip would usually be positioned) to the rim of the crystal should be minimal. (The coldest points of the sample are close to the Ta clamps.)

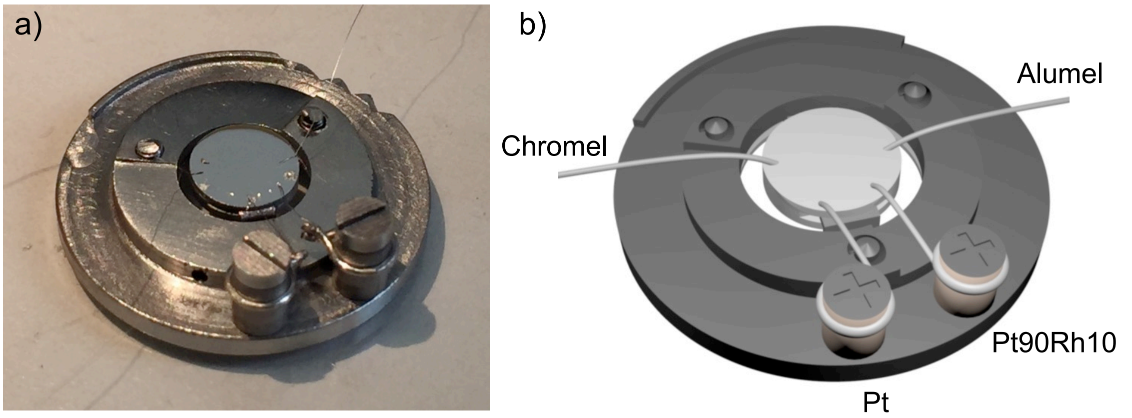

Figure 4.3: Setup for temperature calibration at different points of the Ru sample. The Ru(0001) crystal is contacted with a type S and a type K thermocouple. a) Photograph and b) graphical illustration of the sample setup.

The calibration measurement was performed between -50 °C and +20 °C, the relevant temperature range for the STM data presented in this work. Figure 4.4 a) depicts the relation between the measured temperature at the position of the type S thermocouple and the one at the position of the type K thermocouple. The data in fact show deviations between approximately 10 and 20 K, and the difference [Figure 4.4 b)] almost linearly increases with temperature. All temperatures used in this thesis are the corrected values according to this calibration.

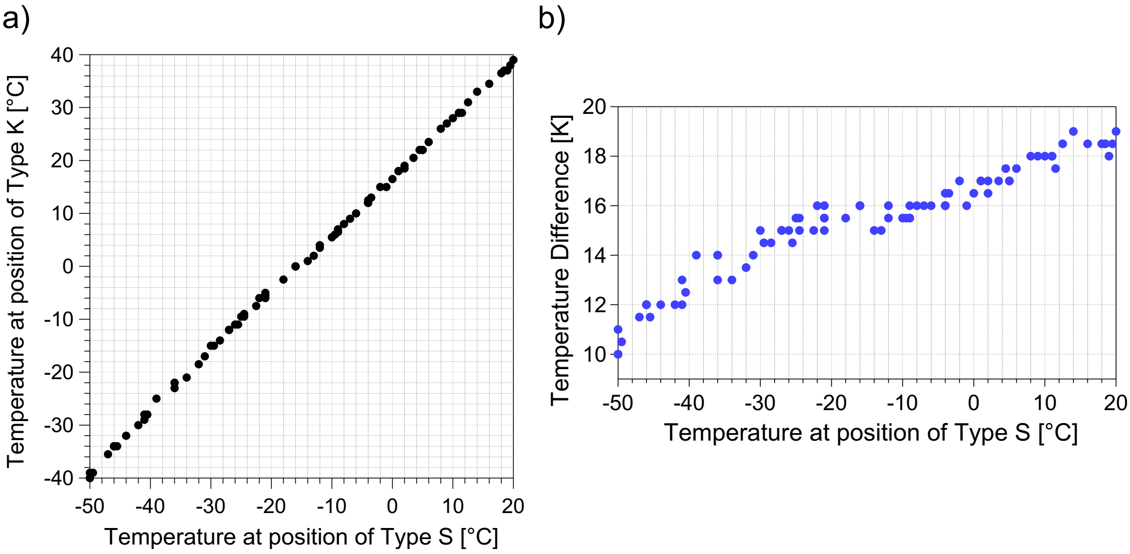

Figure 4.4: Temperature calibration at the positions on the Ru crystal surface shown in Figure 4.3. The type K thermocouple was mounted in the middle between the two Ta clamps, the type S thermocouple close to one of the Ta clamps. a) Temperature relation between the two measurement positions. b) Temperature difference between the two measurement positions.

4.3 Analysis Methods

4.3.1 Auger Electron Spectroscopy

Within this project Auger electron spectroscopy (AES) was used to verify the cleanliness of the sample surface prior to STM experiments and to check for possible contaminations during the sample preparation. It is based on the so-called *Auger* effect,[114] which is illustrated in Figure 4.5.

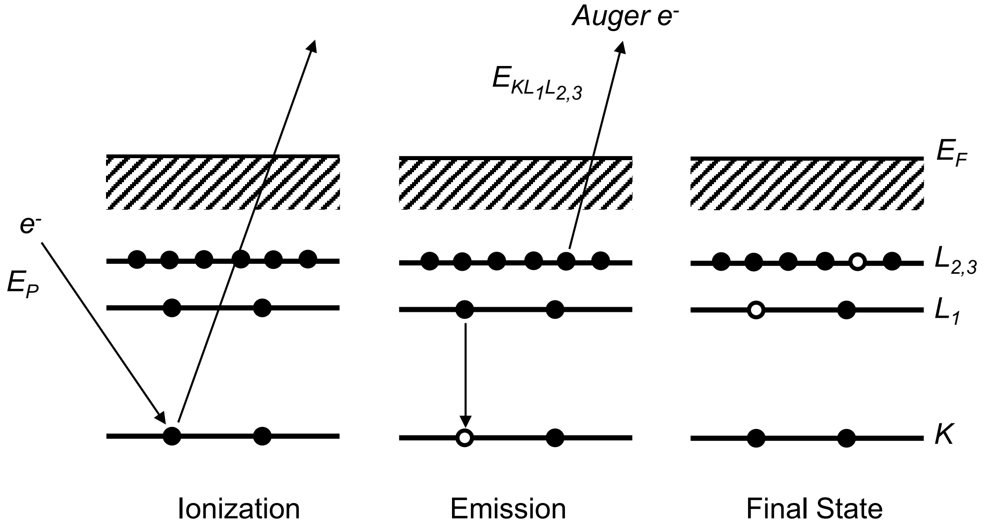

Figure 4.5: Energy scheme of the *Auger* process. Left: An inner shell is ionized by an incident electron. Middle: The electron hole is filled by relaxation of an electron from a higher shell. The released energy is transferred to another electron that leaves the sample as an *Auger* electron. Right: The final configuration.

An incident electron with energy E_P ionizes an inner shell of a sample atom, here the *K* shell (Figure 4.5, left). The resulting electron hole can be filled by an electron from a higher shell. In the depicted example an electron from the L_1 shell relaxes into the *K* shell. The released energy difference $E_K - E_{L_1}$ is either radiatively emitted (*X-ray fluorescence*) or transferred to a third electron that leaves the sample as an *Auger* electron (middle) with a kinetic energy $E_{KL_1L_{2,3}}$, according to equation 4.1.

$$E_{kin}^{Auger} = E_{KL_1L_{2,3}} = E_K - E_{L_1} - E_{L_{2,3}}^* \tag{4.1}$$

where E_i is the binding energy of an electron in shell *i* and E_i^* the binding energy of shell *i* in the presence of an electron hole. The kinetic energy of the resulting *Auger* electrons is therefore only dependent on the involved energy levels and thus characteristic for the elements present. *Auger* spectra are typically recorded in differential form in order to remove a high smooth background of secondary electrons.

Auger electrons have typical energies between 10 and 1000 eV for which the inelastic mean free path in solids is only a few atomic layers. This means that only electrons generated close to the sample surface can leave the bulk and become detected. AES is therefore a surface sensitive method. For electron energies between 10 and 1000 eV the information depth can be roughly estimated to one to ten monolayers.[114]

AES is therefore especially well-suited to check for small residual amounts of foreign atoms or molecules on the sample surface and to identify them, such as oxygen, sulfur and silicon. The most frequently occurring contamination is carbon, which is typically dissolved in metals and may segregate to the surface during sample preparation. For Ru samples the determination of the carbon content on the surface is difficult as the C *KLL* signal at 272 eV and the main Ru signal at 273 eV overlap.[108, 115, 116] However, in the differentiated spectrum the signal forms of the two transitions differ significantly which can be used to quantify the amount of carbon.[108, 115, 116] While the *MNN* transition of ruthenium has a very symmetric peak form, the C *KLL* signal of graphitic carbon is highly asymmetric showing a pronounced negative-going peak. The overlap of the Ru and C signals thus leads to an increasingly asymmetric peak shape at ~273 eV for an increasing amount of carbon, so that the intensity ratio *r* of the upper to the lower half of the signal can be taken to evaluate the carbon amount.

Exemplarily, Figure 4.6 a) shows *Auger* spectra of a clean (blue curve) and a carbon containing Ru sample (black curve). For the clean Ru surface, the MNN multiplet peaks in the range between 180 and 280 eV exhibit an almost symmetric shape and the ratio *r* between the negative and the positive going half of the main signal at 273 eV lies at 1.26 in agreement with the literature.[108, 117] The carbon containing sample on the other hand shows a significantly increased *r* value of ~1.84. In Figure 4.6 b) the two signals are directly placed on top of each other in order to clarify the peak form alteration in the presence of carbon on the Ru sample surface. Although it is possible by using this method to detect carbon on a Ru surface, the signal overlap impedes the detection of very small amounts.

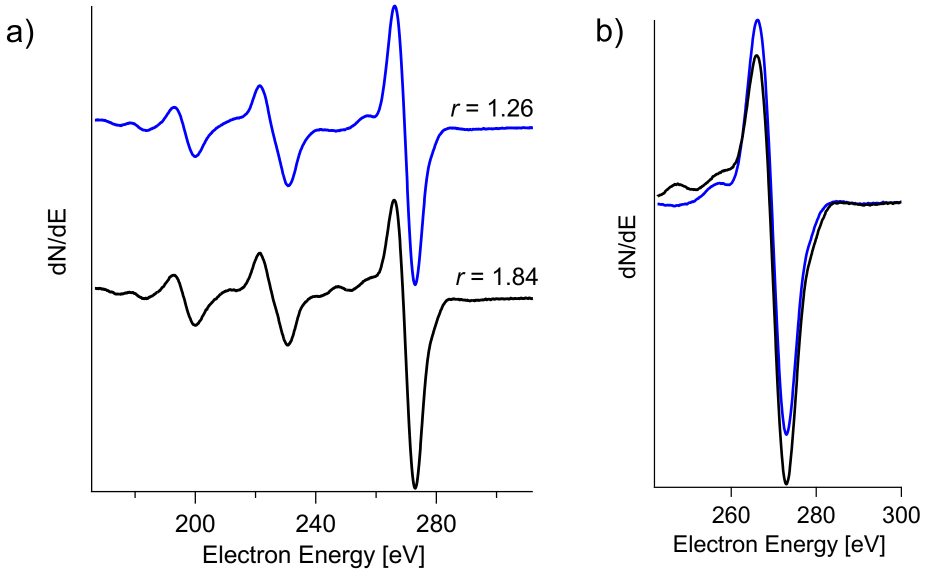

Figure 4.6: *Auger* spectra of a clean (blue) and a carbon contaminated Ru sample (black). a) The *MNN* peaks of Ru; b) overlay of the main Ru $M_5N_{4,5}N_{4,5}$ signal at 273 eV of both samples.

4.3.2 Low-Energy Electron Diffraction

By diffraction of low-energy electrons (LEED), a projection of the 2D reciprocal space of a sample surface can be visualized. In this work, it was used to estimate the required dosages of O and CO for the respective STM experiments as well as to check the cleanliness of the sample surface.

In a LEED experiment, a monochromatic electron beam, whose *de-Broglie* wavelength $\lambda_{de-Broglie}$ is in the order of the lattice constant of the sample, is diffracted at the sample surface. For this purpose kinetic energies E_{kin} of the electrons between 20 and 500 eV are required. Therefore, LEED is, like AES, a surface sensitive method. The *de-Broglie* relation is given in equation 4.2. Here, h is the *Planck* constant, p the momentum, and m_e the electron mass.

$$\lambda_{de-Broglie} = \frac{h}{p} = \frac{h}{\sqrt{2m_e E_{kin}}} \tag{4.2}$$

For vertical incidence the diffraction of the electrons follows equation 4.3, in which n is the diffraction order, d_{hk} the lattice constant within the 2D lattice plane and φ the angle between the diffracted electrons and the surface normal.

$$n\lambda_{de-Broglie} = d_{hk}\sin(\varphi) \tag{4.3}$$

As the angle φ is a measurable quantity in the obtained diffraction patterns, lattice constants of surface structures may be determined from LEED experiments.

Figure 4.7 schematically shows the setup of a typical LEED optics. Electrons are generated by thermal emission from a filament and accelerated by a voltage *U*. A set of electrostatic lenses focuses the electron beam, which then enters a field-free space through the drift tube. The electrons are diffracted at the surface of the sample and detected at a fluorescence screen. Prior to detection the electrons pass three grids. The first grid is grounded to guarantee a flight path of the electrons through a field-free space. The second grid serves as a suppressor for inelastically scattered electrons. The third grid is grounded to prevent interference of the high potential of the fluorescence screen with the second grid. For detection the electrons are post-accelerated between the third grid and the fluorescence screen by a voltage in the kV regime.

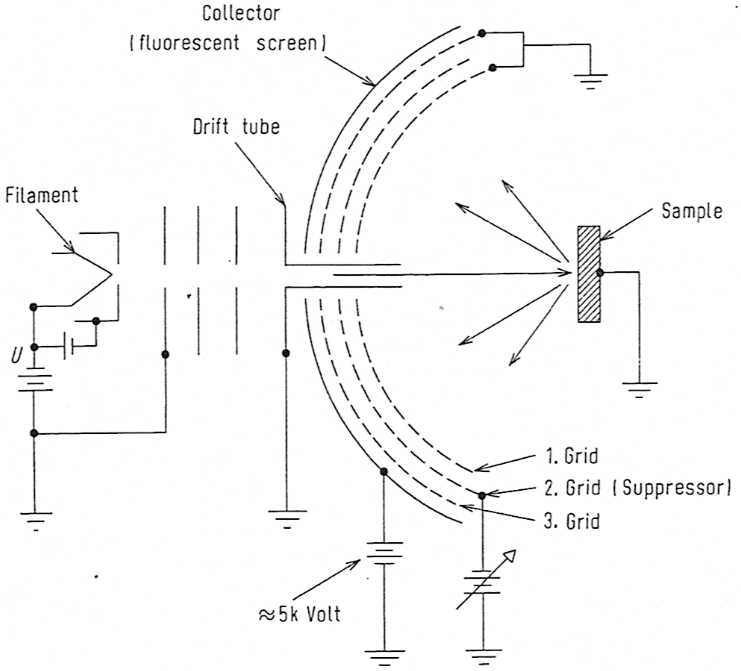

Figure 4.7: Setup scheme of a typical LEED optics (from reference [118]). Electrons are extracted from the heated filament and accelerated by a voltage *U*. After passing through the drift tube, the electrons are diffracted on the sample and detected on a fluorescence screen.

5. Diffusion on a Crowded Surface

5.1 Introduction

As outlined in the introduction (chapter 1) this thesis aims at the question how adsorbed particles can move on an almost fully covered surface, the situation in heterogeneous catalysis.

Mesoscopic studies on mixed adsorbate structures at low and intermediate coverages on transition metal surfaces have shown that the presence of a coadsorbate leads to a significant decrease of the surface mobility of both adsorbates, slowing down the diffusion by several orders of magnitude. In most cases the degree of mobility reduction was found to be dependent on the surface coverage of the coadsorbate. Coverage effects have been attributed to site-blocking in the mixed adlayer,[48] the segregation of the adsorbates into different domains,[47] the formation of trapping states between the adsorbates,[49, 51, 119] and also in some cases to electronic interactions through the substrate.[120] Accelerating effects of adsorbates were only found for self-diffusion of metals by the formation of intermediate metal-adsorbate complexes,[121, 122] but not for the case of a mixed adlayer.

For a fully covered surface, these mesoscopic diffusion studies suggest a decrease in mobility with increasing coverage until complete immobility at saturation. In contrast to these considerations, microkinetic models of catalytic reactions on metal surfaces usually regard diffusion of the reactants to happen on a much shorter time scale than the reaction itself, corresponding to an instant and complete mixing of the adlayer.[123, 124] The influence of diffusion on the reaction rates is thus completely neglected and reaction rates are calculated by using surface coverages as a mean-field quantity. This is only justified, however, if diffusion is rapid compared to the reaction. A detailed understanding of the diffusion process on a crowded surface on an atomic scale is needed to validate whether this assumption is justified. Especially for reactions that follow a *Langmuir-Hinshelwood* mechanism, in which all reactants are adsorbed on the catalysts surface, it seems reasonable to assume that diffusion of the reactants in such a mixed adlayer system has to be taken into account as reaction rates should be significantly influenced by diffusion.

Some atomic-scale STM studies have addressed the question of how particles move when they are embedded in a close-packed 2D layer. For In and Pb atoms in the first layer of a Cu(100) surface, it was found that they move by a *vacancy mechanism* (section 5.2.3).[53, 125, 126] A *direct exchange*, in which two atoms swap sites, has been proposed for the diffusion of H atoms in the Cl terminated Si(100) surface via formation of an intermediate HCl molecule.[127] For the diffusion of S atoms in a full chloride or bromide layer on the surface of a Cu(100) electrode in an electrolyte solution, Rahn *et al.*[128] have suggested two other mechanisms. Whereas the S atoms in the chloride layer move by a concerted ring-like exchange involving three chloride ions, the S diffusion in the bromide layer follows a mechanism in which the S atoms exchange sites with a bromide ion by transiently displacing a Cu atom from the underlying Cu surface. The bromide could then bind to the copper atom leading to the intermediate formation of an S-Cu-Br complex. Both processes were found to be strongly dependent on the applied electrical potential and might thus be specific to the electrochemical environment. Yet, all these systems are chemically and structurally different from adsorbate layers on catalysts.

In this thesis, the diffusion of single oxygen atoms on a Ru(0001) surface coadsorbed with carbon monoxide has been investigated by STM. The system of O and CO on Ru(0001) is especially well suited to investigate coadsorbate effects, since it consists of two well-known individual systems. Moreover, the CO oxidation reaction on Pt group metals is one of the most studied reactions in heterogeneous catalysis and often serves as a model system.[65] The reaction is known to follow the *Langmuir-Hinshelwood* mechanism and thus requires a mixed adlayer of CO and O on the surface of the catalyst.[65, 129] Since metallic ruthenium is the least active platinum-group metal for CO oxidation under UHV conditions at low temperatures,[65, 110, 130] the diffusion processes could be studied without interference from the formation of CO_2, a process that would have complicated the interpretation and understanding of the STM observations.

After a brief introduction to the general concepts of surface diffusion in section 5.2, the known properties of the single-component systems O and CO on the Ru(0001) surface as well as of the coadsorbate system are summarized in section 5.3.

Section 5.4 presents the results on the diffusion of single O atoms in a full layer of the ordered $(\sqrt{3} \text{ x } \sqrt{3})$R30° structure of CO on the Ru(0001) surface. Fast fluctuations in the density of the CO layer allow the O atom to move at a comparable speed as on a clean Ru(0001) surface by the so-called *door-opening* mechanism.[131] This chapter presents the central result of this thesis.

STM observations of the O diffusion on an only partially CO-covered Ru(0001) surface, i.e., for coverages below 0.33 ML (monolayer, O atoms per surface Ru atom), are presented in section 5.5. In this intermediate coverage range, islands of the $(\sqrt{3} \text{ x } \sqrt{3})$R30° structure alternate with disordered areas with lower CO density. O atoms primarily diffuse in the disordered CO areas.

Section 5.6 gives an outlook on first results on the diffusion in domain boundaries on surfaces. Oxygen atoms have been observed to diffuse preferably along boundaries between translational domains of the $(\sqrt{3} \text{ x } \sqrt{3})$R30°-CO structure, pointing to a role of domain boundaries as *high-diffusivity paths*.

5.2 General Concepts

5.2.1 Theory of Diffusion

Diffusion was first phenomenologically described by Adolf Fick in 1855.[132] From his observations of the mixing in a salt-water system, he suggested a linear relation between the flux J_p of diffusing particles and a concentration gradient. With the proclamation of Fick's first law for diffusion, he introduced the diffusion coefficient D as the proportionality factor between J_p and the gradient of the concentration c for diffusion in an isotropic medium. Fick's first law for one-dimensional diffusion in x direction is given in equation 5.1.

$$J_p = -D \frac{\partial c}{\partial x} \tag{5.1}$$

Using the continuity equation (equation 5.2), which describes the evolution of the concentration c in time t by the variation of the diffusion flux, *Fick's first law* transforms into the *diffusion equation* or also called *Fick's second law*. Equation 5.3

shows *Fick's second law* for diffusion in one dimension under the assumption that D is independent of c.

$$\frac{\partial c}{\partial t} = -\frac{\partial J_p}{dx} \tag{5.2}$$

$$\frac{\partial c}{\partial t} = D\frac{\partial^2 c}{\partial^2 x} \tag{5.3}$$

Albert Einstein was the first to attribute the random motion of atoms and molecules, induced by statistical energy fluctuations according to the Boltzmann distribution, to the macroscopic diffusion phenomenon.[133] He connected the diffusion constant D with the mean-square displacement (MSD) of the individual particles. Equation 5.4 shows the Einstein relation for diffusion in one dimension. Here $\langle x^2 \rangle$ denotes the MSD in x direction.

$$D = \frac{\langle x^2 \rangle}{2t} \tag{5.4}$$

For diffusion in solids and on surfaces, which usually exhibit a crystalline order, particles sit on distinct lattice sites and move by jumps on this discrete lattice. Figure 5.1 schematically illustrates the adsorption of a particle (red) in a periodic potential of a surface. The energy minimum represents the most favorable adsorption site. Diffusion occurs by jumps of the particle between neighboring energy minima. These jumps are associated with an activation energy for diffusion E_d^*, which is the difference between the energy minimum and maximum along the diffusion pathway.

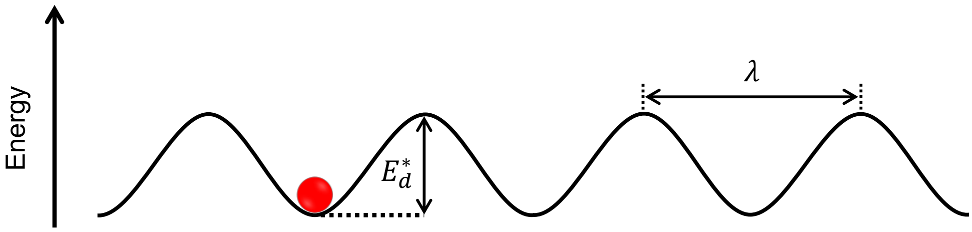

Figure 5.1: Diffusion of a particle (red) in a periodic potential of a surface. The motion from one energy minimum to the next is associated with an energy barrier for diffusion E_d^*. The distance between two energy minima is λ.

The jumps have a length λ, which is typically given by the lattice constant of the surface. A jump frequency Γ, which is the inverse average life time it spends on one adsorption site, characterizes the motion of the particle. For a 2D random walk of a particle on a surface, the MSD $\langle r^2 \rangle$ is the sum of the one-dimensional MSDs in x and in y direction, $\langle x^2 \rangle$ and $\langle y^2 \rangle$. Using the Einstein relation, $\langle r^2 \rangle$ can be expressed as denoted in equation 5.5.

$$\langle r^2 \rangle = \langle x^2 \rangle + \langle y^2 \rangle = 2tD_x + 2tD_y \tag{5.5}$$

For isotropic diffusion the diffusion coefficient in x direction D_x is equal to the diffusion coefficient in y direction D_y. With $\langle r^2 \rangle = \langle n_{jump} \rangle \lambda^2$ equation 5.5 then transforms to:

$$D = \frac{\Gamma \cdot \lambda^2}{4} \tag{5.6}$$

where Γ is the quotient of the average number of jumps $\langle n_{jump} \rangle$ per time interval t. This equation directly connects the diffusion coefficient with the atomic-scale process of individual particles hopping on a 2D lattice of a surface.

Jumping of the adsorbates is a thermally activated process, so that the temperature dependence of the jump rate usually can be described by the Arrhenius law:

$$\Gamma = \Gamma_0 \cdot e^{\frac{-E_d^*}{k_B T}} \tag{5.7}$$

The exponential term represents the probability that the particle has an energy greater than the required activation energy, which is given by the Boltzmann distribution. k_B is the Boltzmann constant and T the absolute temperature. The activation energy is the barrier for diffusion E_d^*, as indicated in Figure 5.1. Based on the classical collision theory the pre-exponential factor Γ_0 can be interpreted as an "attempt frequency," with which the particles try to perform a jump. Typical values for Γ_0 are in the regime of 10^{12} to 10^{13} Hz, which is also the typical timescale for molecular vibrations and phonons.[16, 134] The product of attempt frequency and exponential term is then the rate Γ for successful jumps. As will be shown below, the preexponential factor is also temperature-dependent. However, this dependence is usually disregarded, as its influence on the hopping frequency is negligible in comparison to the exponential dependence on temperature in the second term.

5.2.2 Transition State Theory

The kinetics of diffusion processes can be also described by the *Transition State Theory* (TST) or *Eyring Theory*, developed in 1935 by Henry Eyring to describe the kinetics of chemical reactions.[135] Using TST reaction rates can be determined from the partition functions of the reactants and the transition state (TS).

The TST is based on the idea that the energy states of reactant and product of a chemical reaction are local minima on a potential energy surface (PES), which are separated by a saddle point, the transition state. The path on the PES from reactant to product is called the reaction pathway, characterized by one or several reaction coordinates. For reaction, the reactant has to overcome the energy barrier E^* associated with the transition state. Exemplarily, Figure 5.2 shows an energy profile along one reaction coordinate. In the TST, reactant R and transition state TS are assumed to be equilibrated with the corresponding equilibrium constant $K^\ddagger$. The product P is then formed by the decay of the TS with rate constant $k^\ddagger$. The product of $k^\ddagger$ and $K^\ddagger$ is the rate constant $k_{total} = k^\ddagger K^\ddagger$ in the production rate of the product (equations 5.8 and 5.9).

$$\mathrm{R} \overset{K^\ddagger}{\rightleftarrows} \mathrm{TS} \overset{k^\ddagger}{\rightarrow} \mathrm{P} \tag{5.8}$$

$$[\mathrm{P}] = k^\ddagger[\mathrm{TS}] = k^\ddagger K^\ddagger[\mathrm{R}] = k_{total}[\mathrm{R}] \tag{5.9}$$

In order to determine the overall reaction rate constant k_{total}, the equilibrium constant $K^\ddagger$ and the rate constant $k^\ddagger$ are expressed by means of statistical thermodynamics. $K^\ddagger$, which determines the concentration of the TS, is dependent on the partition functions of reactant and transition state, q_R and q_TS, as well as on the energy difference E^* between R and TS, according to equation 5.10. R is the ideal gas constant and T the absolute temperature.

$$K^\ddagger = \frac{q_\mathrm{TS}}{q_\mathrm{R}} \cdot e^{-\frac{E^*}{RT}} \tag{5.10}$$

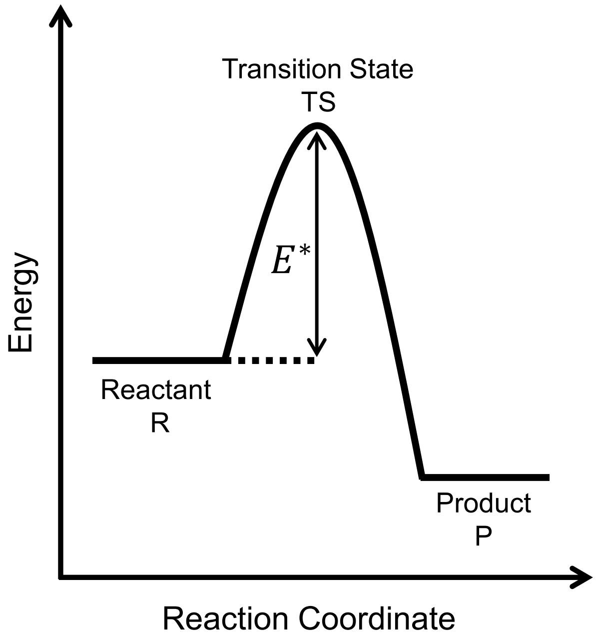

Figure 5.2: Energy scheme of a reaction along the reaction coordinate. The formation of the product P from reactant R involves overcoming the reaction barrier E^*. The transition state TS is the maximum in the energy profile.

The decay rate constant $k^{\ddagger}$ of the TS can be estimated from the frequency ν of the vibration of the TS along the reaction coordinate (equation 5.11). κ_t is a proportionality factor, the so-called transmission coefficient, since not every excitation necessarily has to lead to a decay of the TS, but κ_t is typically assumed to be close to one.[136]

$$k^{\ddagger} = \kappa_t \cdot \nu \tag{5.11}$$

ν is related to the partition function q_{vib} of vibration of the TS. In general, the vibrational partition function is given by equation 5.12

$$q_{vib} = \frac{1}{1 - e^{-\frac{h\nu}{k_B T}}} \tag{5.12}$$

For the vibration along the reaction coordinate the force constant and thus also the vibrational frequency are assumed to be quite low, so that $\frac{h\nu}{k_B T} \ll 1$ (h is the Planck constant). For this coordinate equation 5.12 thus simplifies to $q_{vib} = \frac{k_B T}{h\nu}$.

Under the assumption that the partition function of the vibration along the reaction coordinate can be separated from the overall partition function q_{TS} of the TS, equation 5.10 transforms into 5.13. $\bar{q}_{\mathrm{TS}}$ represents the partition function of the TS reduced by the contribution of the vibration along the reaction coordinate.

$$K^{\ddagger} = \frac{k_B T}{h\nu} \frac{\bar{q}_{\mathrm{TS}}}{q_{\mathrm{R}}} \cdot e^{-\frac{E^*}{RT}} \tag{5.13}$$

The overall rate constant k_{total} is thus determined by the Eyring equation[135]:

$$k_{\mathrm{total}} = \kappa_t \frac{k_B T}{h} \frac{\bar{q}_{\mathrm{TS}}}{q_{\mathrm{R}}} \cdot e^{-\frac{E^*}{RT}} \tag{5.14}$$

The last part of equation 5.14 can be interpreted with the help of equation 5.10 as a reduced equilibrium constant $\bar{K}^{\ddagger}$, that does not contain the contribution of q_{vib} along the reaction coordinate. Neglecting the missing partition function from the vibration along the reaction coordinate, the overall rate constant

$$k_{\mathrm{total}} = \kappa_t \frac{k_B T}{h} \bar{K}^{\ddagger} \tag{5.15}$$

can be transformed by means of equations 5.16 and 5.17. $\Delta G^{\ddagger}$, $\Delta S^{\ddagger}$ and $\Delta H^{\ddagger}$ are the free enthalpy, the entropy and the enthalpy of activation, respectively.

$$\Delta G^{\ddagger} = -RT \cdot \ln{(\bar{K}^{\ddagger})} \tag{5.16}$$

$$\Delta G^{\ddagger} = \Delta H^{\ddagger} - T\Delta S^{\ddagger} \tag{5.17}$$

As a result the Eyring equation transforms into equation 5.18, which offers an additional interpretation of the two parameters of the phenomenologically derived Arrhenius equation (equation 5.19). While the exponential term in the classical Arrhenius relation depends on the activation energy E^*, equation 5.18 contains the respective enthalpy difference. These two quantities are not generally identical, but can be assumed equal for surface diffusion since no gaseous components are involved.

The interpretation of equation 5.19 with 5.18 introduces an entropic contribution to the pre-exponential factor, in contradiction to the classical collision theory. The entropy difference between TS and reactants lowers ($S_{\mathrm{TS}} < S_{\mathrm{R}}$) or increases ($S_{\mathrm{TS}} > S_{\mathrm{R}}$) the pre-exponential factor.

$$k_{total} = \underbrace{\kappa_t \cdot \frac{k_B T}{h} \cdot e^{\frac{\Delta S^{\ddagger}}{R}}}_{} \cdot \underbrace{e^{\frac{-\Delta H^{\ddagger}}{RT}}}_{} \tag{5.18}$$

$$k_{total} = \qquad A \qquad \cdot e^{\frac{-E^{*}}{RT}} \tag{5.19}$$

5.2.3 Diffusion Mechanisms on Surfaces

The fact that particles diffuse on a surface by jumps between adjacent locations, as described in section 5.2.1 for the derivation of diffusion equations on surfaces, is a simplifying statement. Rather, there are different mechanisms how mass transport on a surface can take place, of which *hopping diffusion* of adatoms is only one. Nevertheless, the picture of a particle diffusing by “jumping” with a characteristic frequency Γ holds for all of the mechanisms, if the term “jump” is used to simply denote a change in the particle position between two observations. In the following, the three most common diffusion mechanisms on metal surfaces are explicitly discussed.

The *hopping mechanism* is the most prominent diffusion mechanism for adparticles on metal surfaces. As discussed above, a particle may move on the surface by thermally activated hops from its adsorption site, a local energy minimum, over a saddle point in the PES (Figure 5.1). For diffusion on isotropic surfaces and in the absence of any gradient of the chemical potential, the particle performs a random walk. The jump direction for every new jump is independent of the previous one.

Some foreign atoms were also found to diffuse on surfaces by penetrating into the first layer of the metal and then move within this first layer by a so-called *vacancy mechanism*.[137] This mechanism is also the most prominent one for self-diffusion on metal surfaces as well as in bulk diffusion. The atom, embedded in the first layer of the metal, only moves if one of the mobile vacancies, that exist in a metal at a finite temperature, comes next to the atom so that it can jump in. After the jump of the atom, the vacancy is located at the opposite site of the particle. The vacancies themselves are very mobile and thus difficult to observe, but their motion is visualized by the foreign atoms. The mechanism was first discovered by van Gastel *et al.*, who studied the diffusion of single In atoms moving in a Cu(001) surface.[125, 126, 138] That diffusion in the first layer of a Cu(001) surface is vacancy-mediated has also been shown for other metallic impurities, such as Co,[139, 140] Mn,[141] Pd,[53] and Pb.[142]

While the vacancies themselves perform a random walk, the diffusion of the tracer atom exhibits a characteristic correlation of directions between successive jumps. After the vacancy has changed position with the tracer particle, there is an enhanced probability for the vacancy to return from the same side to the particle than from opposite or perpendicular directions.[143, 144] Moreover, the mechanism is characterized by the observation that the tracer particle is stationary for quite a while in time periods in which no vacancy is close by, and then suddenly diffuses rapidly in the presence of a vacancy, often over several lattice constants.[137, 145] The occurrence of such multiple jumps combined with the correlation of directions of successive jumps leads to a specific distribution of tracer displacements after a given time. This particle distance distribution follows for the *vacancy mechanism* a modified Bessel function instead of the typical *Gaussian* shape for the *hopping mechanism* and can thus be used to discriminate the two mechanisms.[143, 144] It can easily be understood that the vacancy diffusion mechanism is also the most prominent mechanism in bulk diffusion.[137] In a 3D lattice particles are densely arranged without the degree of freedom perpendicular to the surface and the vacancy mechanism allows atoms to move without much distorting the lattice.

Evidence for a third diffusion mechanism, an *atom-exchange mechanism*, on surfaces was first found by field ion microscopy (FIM) investigations of the motion of single metal adatoms on an unreconstructed Pt(110) surface. Whereas Au adatoms diffused solely one-dimensional along the channels of this surface, diffusion of Ir and Pt adatoms was two-dimensional.[146] This *cross-channel* diffusion was confirmed by Wrigley and Ehrlich for W adatoms on Ir(110).[147] After a diffusion event they found the W atom incorporated into the lattice of the first layer Ir, while a single Ir atom occurred in the channel. W and Ir had exchanged places.

An *atom-exchange* diffusion was later also proposed from FIM measurements for self-diffusion on the Pt(100) and Ir(100) surfaces,[148-151] as well as for Re on Ir(100)[152] and Pt on Ni(100).[153] The distinction between the classical *hopping mechanism* and the *atom-exchange* diffusion was made by comparing the sites occupied by an adatom during diffusion. For these systems it turned out that not all of the equivalent surface position were occupied. Rather a c(2 x 2) lattice of atom positions was observed, which is consistent with the picture of the adatom “diving” into the first surface layer, while pushing a surface atom in the same horizontal direction out of its position onto the surface. For simple hop diffusion a (1 x 1) lattice of the favored adsorption sites should have been observed.

Several theoretical studies have addressed the question of when diffusion occurs by an exchange and when by the classical hopping mechanism. Yu and Scheffler proposed tensile stress in the surface layer to encourage exchange diffusion.[154] This finding would go along well with the fact that so far atom-exchange diffusion for these metal-on-metal system has been almost exclusively reported from FIM investigations. In these measurements the sample is a sharp metal tip with the foremost terrace only being a few tens of Å wide. On such narrow terraces additional tensile stress might be induced.

Apart from jumps to nearest-neighbor positions, for all three mechanisms, the contribution of so-called "long jumps" has been discussed. These jumps over two or more lattice constants can occur if dissipation of excess particle energy is not fast enough, so that the particle does not relax into a nearest-neighbor site but rather moves on beyond.[155] Whether long jumps contribute to the diffusion process can be extracted from the particle displacement distribution, the shape of which is changed by the occurrence of long jumps. For self-diffusion in metals long jumps are expected to contribute significantly for temperatures above 20% of the melting temperature.[156] For the diffusion of Pd and Ni on the channeled W(211) surface the existence of long jumps has been proven even for 10% of the melting temperature.[157]

5.3 The Coadsorbate System: O + CO on Ru(0001)

5.3.1 Adsorption of O_2 on Ru(0001)

O_2 molecules dissociate when adsorbing on the Ru(0001) surface at temperatures above 100 K.[110] The O atoms occupy the hexagonal-close-packed (hcp) adsorption site,[158, 159] the threefold site with a Ru atom of the second layer underneath, with an adsorption energy estimated between 4.4 and 5.6 eV.[110, 111, 159-161] Adsorption on the hcp site is favored by 0.3 to 0.5 eV with respect to the alternative threefold coordination site, the face-centered cubic (fcc) site,[131, 159, 161] the threefold site without a second layer Ru atom below.

When increasing the O coverage on a Ru(0001) surface, the O atoms coalesce into islands that show an ordered (2 x 2) structure.[110, 158, 162] For an O coverage of

0.25 ML the formation of a (2 x 2) overlayer is completed. Approximate dosages of 1.5 L (1 L = $1 \cdot 10^{-6}$ Torr · s) of oxygen are necessary for the development of a full (2 x 2) structure, as was deduced from LEED and TDS (thermal desorption spectroscopy) experiments.[110, 163]

Adding more oxygen to the (2 x 2)-O covered Ru(0001) surface, i.e., for coverages between 0.25 and 0.35 ML, leads to the formation of disordered areas in addition to the (2 x 2) structure.[164] Above 0.35 ML a (2 x 1) structure with three different rotational domains evolves. The domains are rotated by 120° with respect to each other.[162-164]

Furthermore, oxygen was found to decorate every second step edge on Ru(0001) with doubled periodicity. This effect can be attributed to the fact that Ru(0001), resulting from its hcp structure, exhibits two alternating types of steps. While the so-called "A" steps show a threefold symmetry, the "B" steps display a fourfold symmetry. The decoration with O occurs preferably at the B steps where the oxygen atoms attach to the step edge on the upper terrace.[165]

Oxygen atoms can move on the Ru(0001) surface by single jumps between nearest-neighbor hcp sites. The contribution of long jumps to the diffusion could be excluded from analysis of the jump width distribution. Assuming a prefactor for diffusion in the range of 10^{10} to 10^{13} Hz, the diffusion barrier on the clean Ru(0001) surface was estimated to 0.55 to 0.70 eV.[166, 167]

Renisch *et al.* further investigated the influence of mutual interactions between O atoms on their diffusion behavior. It has been shown that oxygen atoms separated by more than three Ru lattice constants (lattice constant a_0(Ru) = 2.71 Å) can be regarded as isolated, whereas for distances between $\sqrt{3}a_0$ and $3a_0$ an attractive interaction between the O atoms leads to a decrease of the corresponding jump frequency by up to one order of magnitude. In agreement with the known behavior of oxygen atoms on Ru to form a stable (2 x 2) arrangement, the strongest attraction was found for an O-O distance of $2a_0$.[166]

When imaging O atoms with the STM in the *constant-current* mode they appear as depressions on the Ru surface as the density of states at the Fermi level of the nearby Ru atoms is decreased.[168] At room temperature, oxygen atoms in an O cluster or at a step edge can be nicely imaged in conventional STM measurements, whereas isolated O atoms on the terraces are extremely mobile and are only observed as dark dashes, since their hopping frequency is in the range of the line frequency.[41] At room temperature Γ was determined to 16.6 ± 0.9 Hz by earlier video-rate STM measurements by Renisch *et al.*.[166]

5.3.2 Adsorption of CO on Ru(0001)

Carbon monoxide adsorbs molecularly on the Ru(0001) surface. At coverages of up to 0.33 ML (one CO molecule per three Ru surface atoms) CO is known to preferably arrange in a $(\sqrt{3} \times \sqrt{3})R30°$ structure, in which the CO occupies on-top sites. The CO is bound with its carbon atom to the Ru surface, while the O atom points upwards.[169-174] The adsorption energy for CO on an on-top site was experimentally determined to ~1.65 eV by TDS.[67, 175]

Upon further CO adsorption at room temperature, the $(\sqrt{3} \times \sqrt{3})R30°$ structure vanishes and a disordered structure evolves. At temperatures below 200 K the formation of a $(2\sqrt{3} \times 2\sqrt{3})R30°$ (coverage 0.58 ML) and of a $(5\sqrt{3} \times 5\sqrt{3})R30°$ (coverage 0.65 ML) was observed.[176, 177] In these structures the CO molecules do not occupy distinctive adsorption sites anymore. The formation of such compressed structures was explained by comparatively small energy differences between different binding positions on the Ru surface, so that the CO molecules arrange only in order to minimize the mutual CO-CO repulsion.[169] DFT calculations suggest a difference in adsorption energy between top and hollow sites of around 0.1 eV and between top and bridge sites of around 0.2 eV.[178-180]

5.3.3 Mixed Adsorbate Layers: (O+CO) on Ru (0001)

Adsorption structures of the coadsorbate system of O and CO on the Ru(0001) surface have been extensively studied by various surface sensitive techniques.

CO, when adsorbed on an oxygen pre-covered Ru(0001) surface, was found to intercalate into the ordered oxygen structures. For a (2 x 2) structure of O, the CO molecules sit on on-top sites between three surrounding O atoms, while the oxygen atoms remain on their favored hcp sites. The (2 x 2) periodicity is thus conserved. The resulting structure contains one oxygen and one CO per unit cell, and is termed (2 x 2)-(O+CO) structure.[181, 182] From a LEED-*IV* analysis Narloch *et al.* found a slight tilt of the CO molecules by approximately 12° with respect to the surface normal.[181]

A combined TDS and infrared reflection absorption spectroscopy study revealed that coadsorbed oxygen decreases the CO adsorption energy on the Ru surface. For CO in the (2 x 2)-(O+CO) structure a lowering of the CO adsorption energy in the range of 0.05 to 0.13 eV was found, depending on the respective assumption for the pre-exponential factor.[67] This effect was attributed to the O acting as an electronegative ligand and thus reducing the back donation of the metal into the antibonding $2\pi^*$ orbital of CO. While the C-O bond is thus strengthened, the Ru-CO bond becomes weaker.[67, 174]

Stampfl and Scheffler performed DFT calculations on the mixed (2 x 2)-(O+CO) systems and also found a weakened Ru-CO bond. In comparison to a pure (2 x 2) arrangement of CO molecules on on-top sites on Ru, the adsorption energy of CO is decreased by 0.07eV when in a (2 x 2)-(O+CO) structure. The decrease in Ru-CO bonding strength was attributed to a direct effect of O atoms which bind to the same Ru atom and thereby reduce the bonding order between Ru and CO.[179] Such a weakening effect by coadsorbates is known for several adsorption systems[47, 48] and was also investigated in detail with DFT by Hammer.[183] The decrease in binding strength between adsorbate and substrate can be understood in a bond-order conservation picture.

5.3.4 Preparation of the Coadsorbate Layer

A clean surface is a prerequisite for the reproducible preparation of the coadsorbate layers of oxygen and carbon monoxide on the Ru(0001) crystal. Prior to every STM experiment, the sample was therefore cleaned by repeated cycles of Ar^+-sputtering at room temperature (15 min; 1 keV; ~5 μA) and oxidation in $1.0 \cdot 10^{-7}$ Torr O_2 at 500 to 600 °C to remove carbon and other oxidizable contaminants from the surface. A subsequent flash annealing step to ~1450 °C was used to desorb excess oxygen.[111]

The cleanliness of the sample surface was frequently monitored by AES. Especially, the absence of the following elements was checked at least once during the preparation: oxygen, carbon, nitrogen, and sulfur, which are typical contaminants in UHV experiments, argon, which might result from the sputtering process, nickel and chromium, which could be present on the surface due to the prior use of a type K thermocouple, platinum and rhodium, as the sample temperature was measured with a type S thermocouple, and aluminum and silicon, as these elements were brought into contact with the Ru sample in earlier experiments in the working group Wintterlin.

Furthermore, the quality of the clean Ru(0001) surface was regularly validated by LEED. The clean Ru(0001) crystal shows hexagonal symmetry for an electron energy of 70 eV as shown in Figure 5.3 and Figure 5.4 in the upper left corner, respectively. The absence of a diffuse background and of additional spots indicate a clean Ru(0001) surface.

For experiments on the diffusion of single oxygen atoms in a full layer of carbon monoxide, the coadsorbate layers were prepared by first exposing the clean Ru(0001) sample at room temperature to a small amount of O_2, followed by dosing of CO. The sample was subsequently cooled to the desired measurement temperature and STM measurements were started. In order to estimate the dosages necessary for the preparation of the coadsorbate layers, the sample surface was investigated by LEED after exposure to O_2 (Figure 5.3) and CO (Figure 5.4) at room temperature.

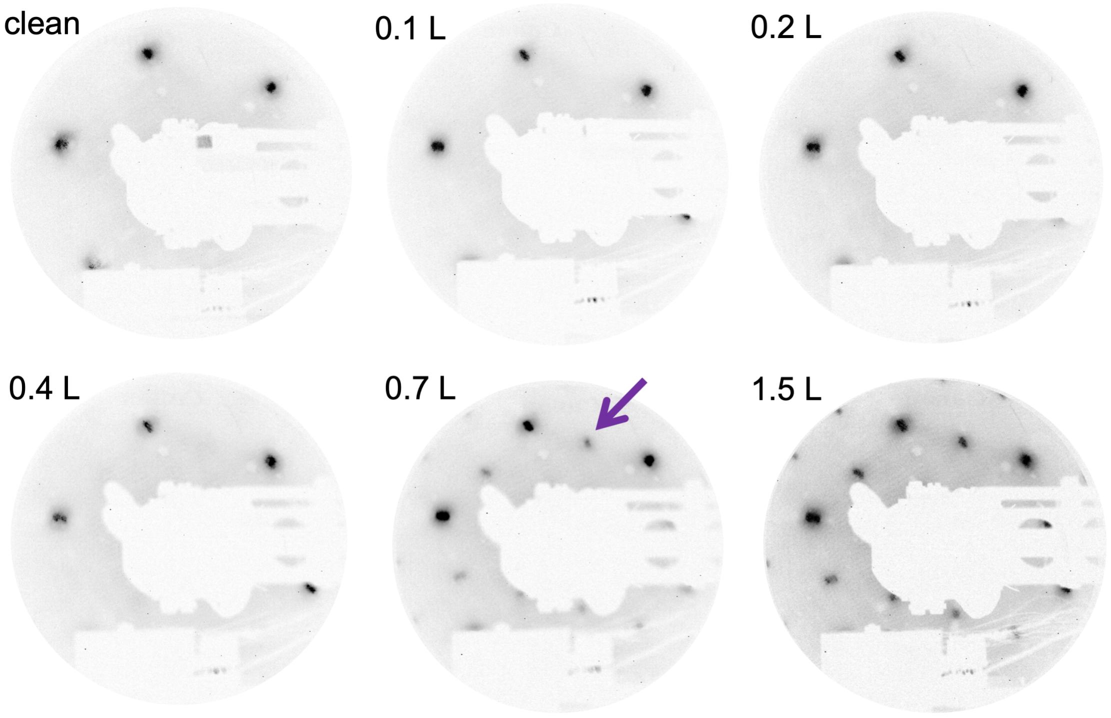

Figure 5.3: LEED patterns of the clean Ru(0001) surface and after various dosages of O_2 at room temperature (electron energy: 70 eV). For higher dosages (≥0.7 L), diffraction spots of the (2 x 2) structure (purple arrow) of atomic O become visible in addition to the hexagonal spots of the clean Ru(0001) surface. The beam splittings are probably an artifact of the electron gun.

For oxygen doses up to 0.4 L, the LEED pattern was the same as for the bare sample surface. Additional diffraction spots that correspond to the onset of (2 x 2)-O island formation were visible after 0.7 L O_2. The purple arrow in Figure 5.3 indicates one of the additional (2 x 2) diffraction spots. LEED experiments were performed up to O_2 doses of 3 L. For higher oxygen dosages than 0.7 L, the observed pattern did not change anymore but the spots of the O structure became more intense. The LEED measurements were in good agreement with the literature for O adsorption on Ru(0001). Madey *et al.* report the highest intensity spots for O dosages of 1.5 L and attributed this to the completion of the (2 x 2) layer formation.[110]

For the diffusion experiments within this work, low coverages of O atoms were required. As 1.5 L of O_2 lead to a fully (2 x 2)O-covered surface,[110] corresponding to an oxygen coverage of 0.25 L, it was estimated that 0.48 L of O_2 should lead to a reasonable coverage of 0.08 ML. Using STM the dosage was later optimized.

When exposing the sample to CO, diffraction spots of the ordered $(\sqrt{3} \times \sqrt{3})R30°$ structure became visible after 0.5 L of CO. A first-order spot of the $(\sqrt{3} \times \sqrt{3})R30°$ structure is indicated by a blue arrow in Figure 5.4. These spots became more intense upon further CO adsorption up to 1.0 L. For dosages >1 L, the intensity of these spots decreased again, as can be seen in the LEED pattern after exposure of 2 L CO. This trend continued for dosages up to 40 L. That the $(\sqrt{3} \times \sqrt{3})R30°$ diffraction spots finally vanished at high dosages is in agreement with the literature.[176] An optimum $(\sqrt{3} \times \sqrt{3})R30°$ CO structure was obtained with dosages of 0.8 to 1.0 L of CO, as concluded from the intensity of the superstructure spots.

However, the LEED patterns at 0.8 L and 2.0 L CO also showed additional diffraction spots that did not arise from the $(\sqrt{3} \times \sqrt{3})R30°$ structure. Such additional spots are marked by the green arrows in the corresponding patterns. Their appearance was also reported in literature. The occurrence and intensity of these spots was found to depend on time and current density of the electron beam, so that the formation of these additional spots was attributed to a beam-induced artifact. Most likely, the beam-induced dissociation of CO led to the evolution of a partial (2 x 2) structure of O.[176, 184]

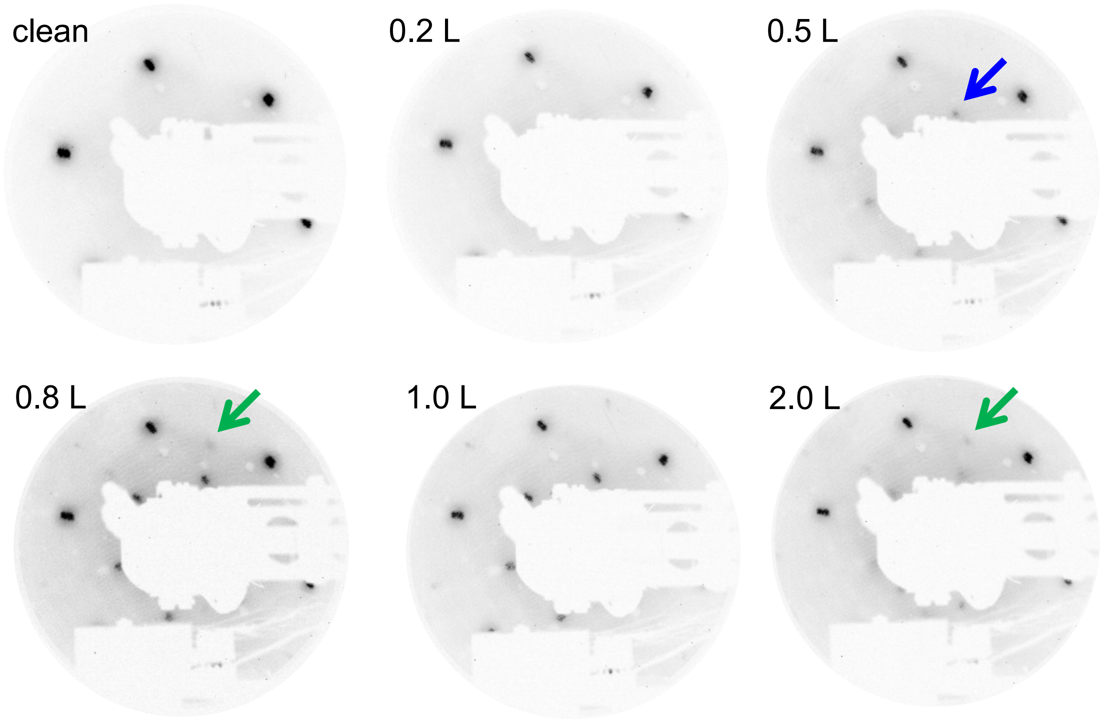

Figure 5.4: LEED patterns of the clean Ru(0001) surface and after various dosages of CO, taken at 70 eV. Diffraction spots of the $(\sqrt{3}$ x $\sqrt{3})$R30° (blue arrow) are visible for CO dosages ≥0.5 L. The LEED patterns at 0.8 L and 2.0 L CO show weak additional diffraction spots that are beam-induced (green arrows).

The estimated O_2 and CO dosages from the LEED experiments were validated by STM experiments. The estimated maximum oxygen dose of 0.48 L turned out to be too high, as isolated O atoms were only rarely observable, but most O atoms were clustered in (2 x 2) islands. The oxygen dose for the diffusion experiments was therefore decreased by a factor of 10 to 0.05 L. For this dosage the corresponding coverage was ~0.01 ML according to LEED and confirmed by STM. At this coverage the distance between two oxygen atoms is, on average, well above three Ru lattice constants, the interaction distance estimated in a previous STM study.[166]

For the diffusion experiments in a full layer of CO, a CO dose of 1.0 L turned out to be sufficient for the preparation of a complete $(\sqrt{3}$ x $\sqrt{3})$R30° structure, in accordance with the LEED experiments. For measurements on an only partially CO-covered surface, CO doses between 0.2 L and 0.8 L were used.

5.4 Diffusion of O atoms in a full layer of CO on Ru(0001)

5.4.1 STM Observations of the mixed Adsorbate Layer

Figure 5.5 a) to c) shows three consecutive STM images of a single O atom in the $(\sqrt{3} \times \sqrt{3})$R30° layer of CO, which were acquired after exposing the clean Ru(0001) sample to 0.05 L O_2, followed by 1 L of CO at room temperature. The images are taken from an STM movie recorded at room temperature at an acquisition rate of 10 frames/s and in the *quasi constant-height* mode at negative bias voltage. Under these tunneling conditions the oxygen atom appears as a bright spot, while the CO molecules are imaged as depressions. This representation of O and CO is in agreement with the inverse contrast seen in the usual *constant-current* measurements.[168]

The CO molecules are arranged in the $(\sqrt{3} \times \sqrt{3})$R30° structure (see section 5.3.2). As can be seen in all three images, the O atom does not sit directly on a lattice site of the $(\sqrt{3} \times \sqrt{3})$R30° structure, marked with a cross in Figure 5.5. Indeed, three different adsorption configurations are found, in which the O atom is slightly displaced to the left in Figure 5.5 a), slightly up in Figure 5.5 b) and to the right in Figure 5.5 c) from the “x” position. This asymmetry can be explained, when O and CO occupy the same adsorption sites as on the clean Ru(0001) surface, namely the on-top sites[177] for the CO molecules and the hcp site for the O atom.[158, 159] The O atom is thus necessarily displaced with respect to the CO lattice.

The corresponding structure models for the three adsorption geometries are shown in Figure 5.5 d), e), and f). One position in the $\left(\sqrt{3} \times \sqrt{3}\right)$R30°-structure of CO molecules (blue) on the Ru(0001) surface (light and dark gray spheres) is vacant (“x”). Adjacent to this empty $\left(\sqrt{3} \times \sqrt{3}\right)$-position, there are six three-fold adsorption sites, three hcp and three fcc sites. Since the O atom favors hcp over fcc adsorption by more than 0.3 eV,[159, 161] it can be assumed that the three experimentally found positions of the O atom as depicted in Figure 5.5 a) to c) correspond to the three hcp sites available around a vacant $(\sqrt{3} \times \sqrt{3})$ lattice site.

From the STM data alone it would not be clear whether the lattice site marked by the “x” is also occupied by a CO molecule, which is imaged differently from the other CO molecules due to its close proximity to the O atom. However, in such a configuration the O and the CO bind to the same Ru atom which from DFT calculations is known to be strongly repulsive.[130] It is therefore excluded that the lattice site marked with an “x” is occupied by a CO.

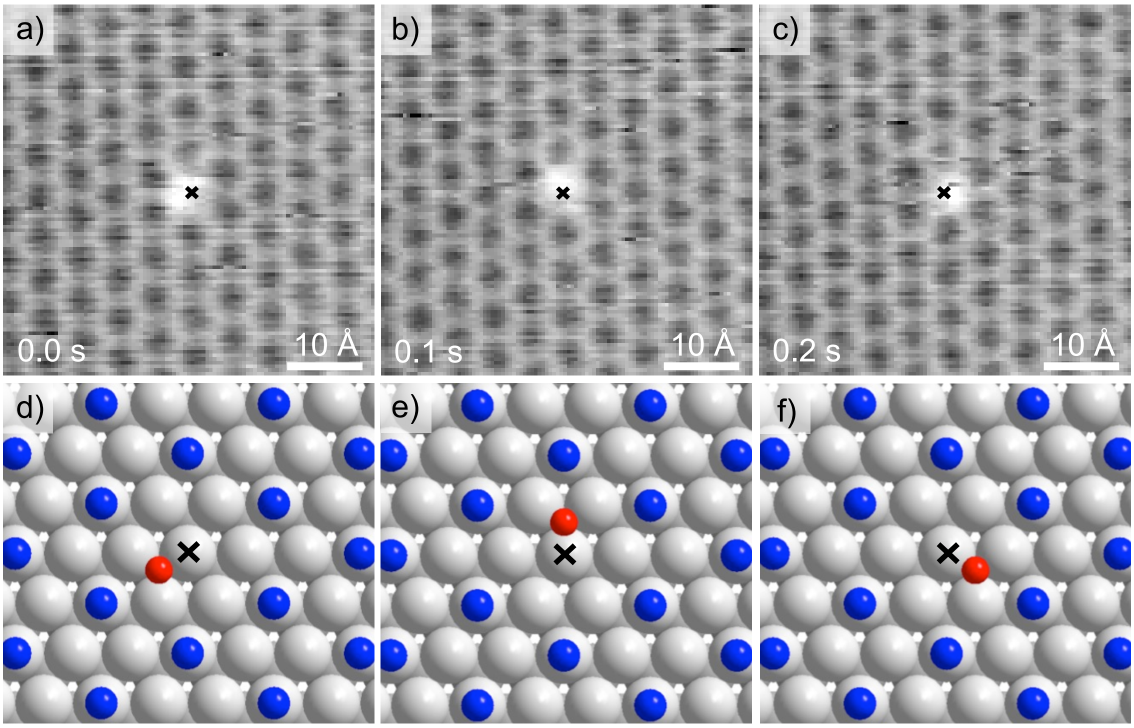

Figure 5.5: O adsorption in CO/Ru(0001). a) to c) Three consecutive STM images of a single oxygen atom (bright) in the ($\sqrt{3}$ x $\sqrt{3}$)R30° layer of CO molecules (dark) on Ru(0001) (not visible) (V_t = -0.22 V, I_t = 10 nA, +27 °C, 10 frames/s). Three different adsorption sites of the oxygen around a vacant ($\sqrt{3}$ x $\sqrt{3}$) position (marked with an "x") are found. Schematic representations of the adsorption geometries are shown in d), e) and f). The oxygen atom (red) occupies three hcp positions around the vacant ($\sqrt{3}$ x $\sqrt{3}$)R30° position (cross) in the ordered layer of CO molecules (blue) on the Ru(0001) surface (gray). (From Henß *et al.*[131]. Reprinted with permission from *AAAS.*)

This conclusion agrees with the observation that the O atom is caught for some time in a confined area around a vacant CO position defined by six surrounding CO molecules. Apparently all other hcp positions, except for the three in the CO "cage" are blocked for occupation by the O atom. Again, this can be explained by the fact that a jump of the O atom to any of the other hcp sites would lead to an energetically unfavorable geometry in which O and CO are bound to the same Ru atom.[130]

Nonetheless, such jumps of the O atom to hcp sites initially blocked by a CO molecule are also observed in the STM measurements, but more rarely. Such an event in which the O atom escapes from its CO cage is shown in the two consecutive images of Figure 5.6 a) and b). The position of the original CO vacancy in a) is marked with a cross at the same position in b). c) and d) schematically illustrate the adsorption configuration of the oxygen in a) and b), respectively. The hopping direction of the O atom is indicated by a black arrow in c). In Figure 5.6 a) the O atom sits on the upper position in a CO cage, whereas in the consecutive STM image [Figure 5.6 b)] it is found on the lower right hcp position in a neighboring CO cage. The occurrence of such a hop necessarily goes along with a displacement of at least one CO molecule, since after the jump [Figure 5.6 b)] the oxygen atom is again surrounded by six CO molecules. In the simplest case the CO molecule on the nearby on-top site has jumped to the vacant ($\sqrt{3}$ x $\sqrt{3}$) lattice position at the original position of the O atom. The net effect is an exchange of the O atom with a CO molecule. However, as will be shown below, the detailed mechanism is more complex than indicated by the arrows in Figure 5.6 c).

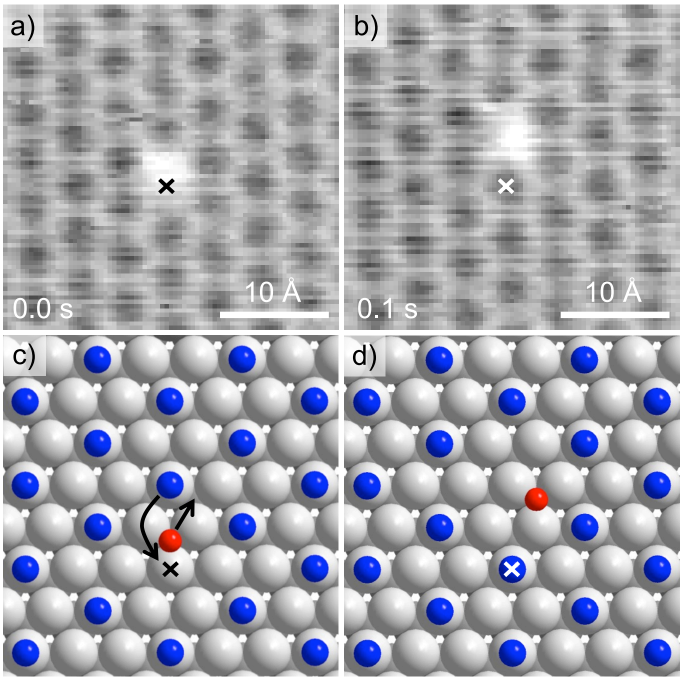

Figure 5.6: O/CO exchange. a) and b) Consecutive STM images of an exchange event between an O atom and a CO molecule (V_t = -0.22 V, I_t = 10 nA, +27 °C, 10 frames/s). c) and d) Schematic representations of the adlayer structure. The O atom (red) changes its position to an initially blocked hcp site close to a CO molecule (blue). This results in a dislocation of the adjacent CO. The site marked by the “x” is the same in both frames. (From Henß *et al.*, reference [131]. Reprinted with permission from *AAAS*.)

5.4.2 Diffusion Trajectories of the Oxygen Atoms

To gain further insight into the diffusion behavior, STM movies of the oxygen movement were recorded at many temperatures in the range between -39 and +29 °C with the combined video-rate variable-temperature STM.

The tracking of the O atoms was performed as described in section 3.4. The STM images covered typical ranges of 30 Å x 30 Å to 150 Å x 150 Å, corresponding to nominal Å-to-pixel ratios between 0.2 and 0.75 for the usual number of pixels (200 x 200 and 150 x 150 pixels). To achieve an optimal tracking result, some tracking parameters had to be individually adjusted for every movie according to the Å-to-pixel ratio of the respective dataset. Table 5.1 summarizes the typical tracking parameters as defined in sections 3.4.3.2 and 3.4.3.3 that were used in this work for tracking of O atoms in CO.

Table 5.1: List of commonly used tracking parameters for typical Å-to-pixel ratios.

Scan Range [Å]	**Linepoints [Pixel]**	**Å-to-pixel ratio**	**Particle Mask scales a:b**	**Tolerance [Pixel]**	**Tolerance [Å]**
150	200	0.75	2:4; 3:4	9-12	6.8-9.0
100	200	0.50	3:4; 3:5	10-16	5.0-8.0
50	200	0.25	4:5	18-25	4.5-6.3
30	150	0.20	4:5	~20	~4.0

In the final manual reviewing step, misdetections as well as detections of O atoms that were less than 10 Å separated from another O atom, a surface impurity or a defect site were sorted out. Moreover, as explained in section 3.4.3.3, the trajectories were checked for a systematic influence of the tolerance value. The analysis of the variation of O atom localizations around a mean position revealed typical precisions for the localization of approximately 0.2 - 0.5 Å in x direction and 0.3 - 0.6 Å in y direction (again depending on the respective Å-to-pixel ratio of the dataset).

A trajectory of an individual O atom diffusing in the $(\sqrt{3}\text{ x }\sqrt{3})$R30° structure of CO obtained in this way is shown in Figure 5.7 a) and b). Each data point of the trajectory represents the position of the oxygen atom in a single STM image. The individual positions are connected by lines to highlight the movement of the O atom. The trace was obtained from measurements at 0 °C and consists of 1512 individual O localizations. Equilateral triangles with a side length of about 2.5 Å appear as prominent features in these atom traces. From the overlay of trace and one STM image of the dataset in Figure 5.7 a) it becomes clear that each triangle is centered around a CO position. Hence, the triangles can be attributed to the alternating occupation of the three equivalent hcp sites around a vacant CO position in a CO cage by the O atom (compare Figure 5.5). These hcp sites are spaced by one Ru lattice constant of 2.7 Å, in reasonable agreement with the experimentally determined side length of the triangles of ~2.5 Å.

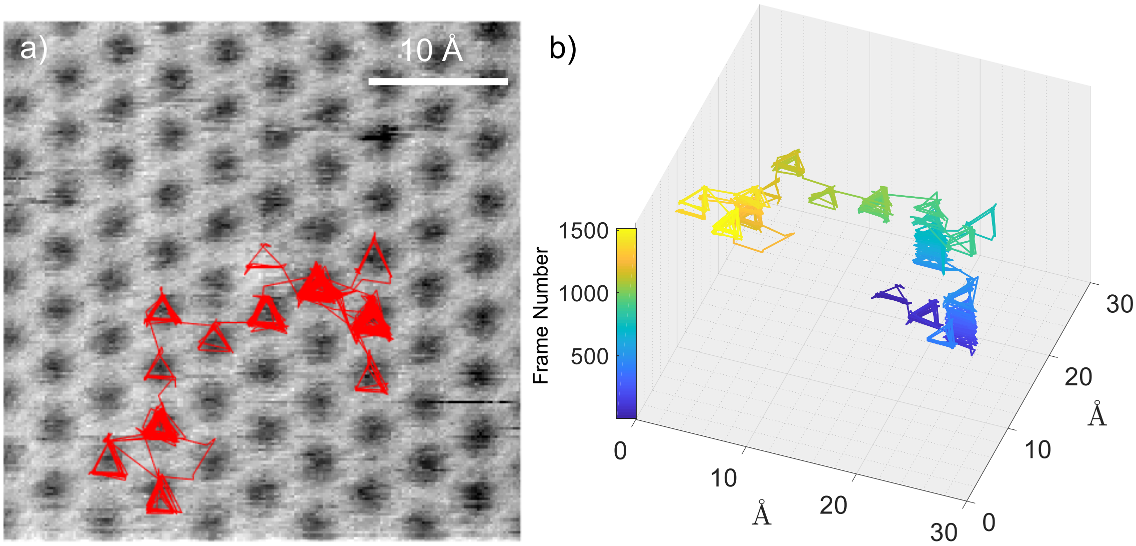

Figure 5.7: Trajectory of an oxygen atom in a $(\sqrt{3} \times \sqrt{3})$R30° layer of CO on Ru(0001) obtained by particle tracking in 1512 consecutive frames. a) STM image (V_t = -0.70 V, I_t = 3 nA, 0 °C, 12 frames/s) overlaid by the O trajectory in red. b) 3D view of the same trajectory. Frame numbers are color-coded.

In addition, the pattern also reveals connections of the same length between the triangles. These connections represent the escape events of an O atom from a CO cage, as already recognized from STM observations (compare Figure 5.6). The O positions are plotted versus the frame number of the STM movie in Figure 5.7 b) to illustrate the temporal evolution of the trajectory. Frame numbers are color-coded. From the 3D view it becomes clear that the O atom always remains in a CO cage for some time, hopping between the three sites in this CO cage. Occasionally the atom leaves the CO cage and becomes trapped in the next cage.

The shape of the O trajectories provides further evidence for the consideration that the O atom moves through the CO matrix by site exchanges with CO molecules. If the oxygen moved just by squeezing into the unmodified CO layer, a simple 2D random walk of the O atom on a hexagonal lattice of sites should be observed instead of the pronounced hopping between three distinct sites plus the exchanges on a slower time scale.

5.4.3 Diffusion Model and Kinetics

The evaluation of the STM movies shows that the diffusion of the O atoms in the CO matrix is different from the diffusion on the bare Ru(0001) surface.[90] Instead of a simple random walk between nearest-neighbor hcp sites, O diffusion appears to consist of two different types of jumps. Jumps between the three hcp sites within a CO cage, in the following termed *triangle jumps*, and *exchange jumps* with CO molecules, describe the experimentally observed trajectories. Figure 5.8 illustrates how the experimental trajectory could be reproduced by the use of these two jump types.

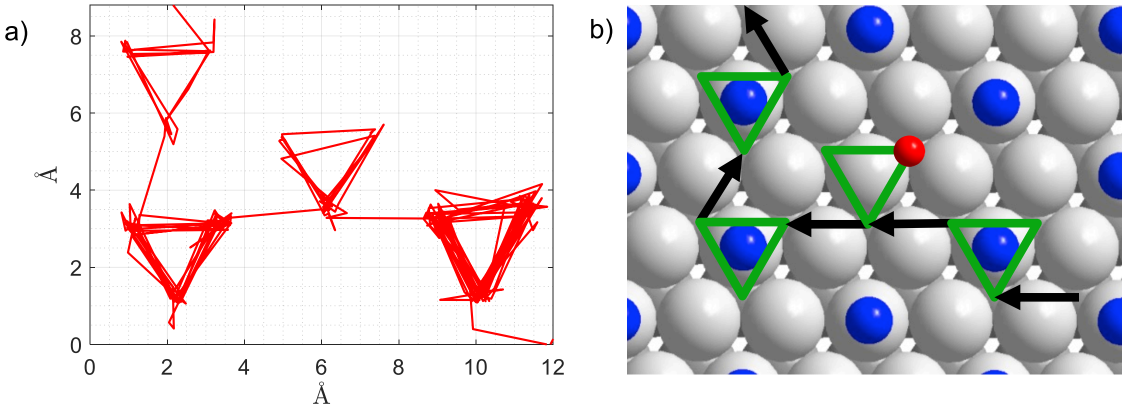

Figure 5.8: Model of two different jump types. a) Detail from the experimental O trajectory of Figure 5.7 b) Model of the trajectory in a) constructed from two different types of jumps: *triangle jumps* (green) and *exchange jumps* (black) with CO (blue).

To access the underlying kinetics of the two jump processes, a mathematical model for the O diffusion has been developed. As a starting point, a configuration was chosen in which the triangle of hcp positions within a CO cage points downwards with one of its tips as shown in Figure 5.8 a). In the configuration of Figure 5.9 a) the O atom occupies the lower tip of the triangle. From there it can perform jumps to the six nearest-neighbor hcp sites, two of which are jumps to the freely available hcp sites in the CO cage, marked by green arrows. A jump frequency Γ_1 characterizes the rate of the *triangle jumps*.

The other four jumps, indicated by black arrows, are *exchange jumps*. If the jumps are assumed to occur over an intermediate fcc position, which is expected based on earlier work on O diffusion on Ru(0001)[161, 166] and has additionally been shown by DFT calculations within this project,[131] the four *exchange jumps* are not equivalent, compare Figure 5.9 b). Whereas for *exchange jumps* with one of the lateral CO molecules the crucial step that leads towards the CO molecule (orange arrow) is from the intermediate fcc to the final hcp position, for the *exchange jumps* with the lower CO molecule, already the first step from hcp to fcc is towards the CO molecule. The energy profiles of these two *exchange jumps* are thus not the same. However, when the O atom has exchanged sites with the lower CO, the reverse of this process is an exchange with a lateral CO, compare Figure 5.9 c). If the O atom has exchanged sites with a lateral CO, the reverse process is equivalent to an exchange with the lower CO, compare Figure 5.9 d). Because the system is in equilibrium the *microscopic reversibility* principle applies, so that both jump processes thus must have the same rates. For the mathematical description of the O diffusion thus only one type of *exchange jumps* needs to be considered. A jump frequency Γ_2 was assigned to the *exchange jumps*.

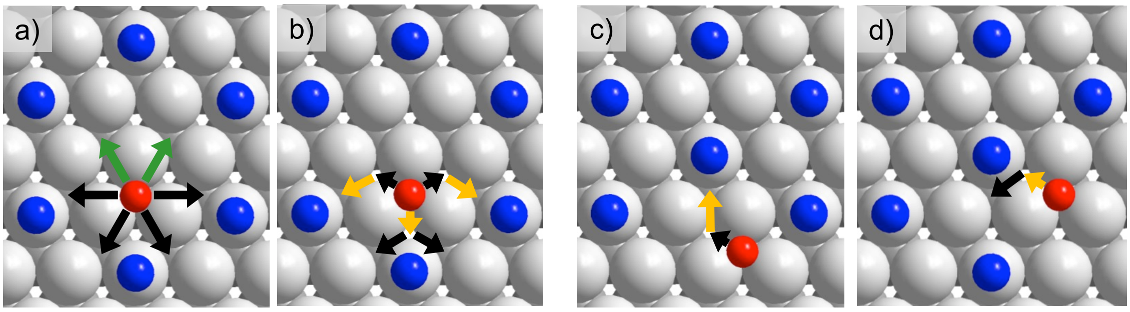

Figure 5.9: Schematic illustration of the diffusion model. a) The O atom (red) may move by *triangle jumps* in two directions (green arrows), whereas jumps in the other four directions are *exchange jumps* (black arrows) with a CO molecule (blue). Ru atoms are indicated in gray. b) The four *exchange jumps* are only pairwise equivalent, if an intermediate fcc position is assumed. Nevertheless, because of microscopic reversibility all four *exchange jumps* must occur at the same rate. c) Reverse process of the exchange in b) with the lower CO. d) Reverse process of the exchange in b) with a lateral CO.

5.4.3.1 Theoretical Modelling of the Displacement Distribution

The probability $\tilde{p}_{t_0}(n)$ that in a statistical process an event, specified by its average frequency Γ, will occur exactly n times within a time interval t_0 is given by the *Poisson* distribution (equation 5.20).

$$\tilde{p}_{t_0}(n) = \frac{(\Gamma \cdot t_0)^n}{n!} \cdot e^{-\Gamma \cdot t_0} \tag{5.20}$$

For STM measurements of surface diffusion t_0 is the time for one image, Γ is the hopping frequency, n the number of jumps between two images, and $\tilde{p}_{t_0}(n)$ the probability that an atom has jumped n times. However, in the present case of O diffusion in CO, two jump processes contribute with their respective frequencies Γ_1 and Γ_2. The two jump processes can be considered to be independent of each other as the time between two jumps is much longer than the duration of the jumps themselves, which should be on a 10^{-12} to 10^{-13} s timescale. The probability $\tilde{p}_{t_0}(n_{1,}n_2)$ for a certain combination of n_1 *triangle* and n_2 *exchange jumps* is thus the product of two *Poisson* distributions (equation 5.21).

$$\tilde{p}_{t_0}(n_{1,}n_2) = \frac{(\Gamma_1 \cdot t_0)^{n_1}}{n_1!} \cdot e^{-\Gamma_1 \cdot t_0} \cdot \frac{(\Gamma_2 \cdot t_0)^{n_2}}{n_2!} \cdot e^{-\Gamma_2 \cdot t_0} \tag{5.21}$$

However, from the STM experiment the probability $\tilde{p}_{t_0}(n_{1,}n_2)$ cannot be measured directly. What can be measured is the probability that a particle located at a certain position in one image appears at a different position in the next image which corresponds to a displacement distribution. To obtain such a displacement distribution, the probability $\tilde{p}_{t_0}(n_{1,}n_2)$ for a distinct combination of n_1 *triangle* and n_2 *exchange jumps* has to be multiplied with the average probability $\bar{w}_{n_1,n_2}(a,b)$ that the particle travels to a specific position (a,b) by the combination of (n_1,n_2) jumps. The probability $p_{t_0}(a,b)$ that an O atom at position $(a,b) = (0,0)$ in one image is at the position with coordinates (a,b) after t_0 in the next image is then given by equation 5.22. The sums run over all possible combinations of n_1 and n_2. A similar approach has been derived earlier by Gert Ehrlich for the analysis of FIM data for the simpler case of one jump type in one dimension.[185]

$$p_{t_0}(a,b) = \sum_{n_1=0}^{\infty} \sum_{n_2=0}^{\infty} \tilde{p}_{t_0}(n_1,n_2) \cdot \bar{w}_{n_1,n_2}(a,b) \tag{5.22}$$

For the derivation of the geometric probability factor $\bar{w}_{n_1,n_2}$ for the O motion in CO, the Ru lattice coordinates (a,b) were first converted into the larger coordinate system of the $(\sqrt{3}$ x $\sqrt{3})R30°$-CO structure. Each position (a,b) (blue lattice, Figure 5.10) is transformed into the coordinates (Y_1,Y_2) of the CO lattice (green lattice, Figure 5.10) plus a character A, B, or C to specify the three possible O positions in a CO cage. As examples the positions (0,0), (0,1) and (-1,1) turn into $(A,0,0)$, $(B,0,0)$ and $(C,0,0)$, respectively.

A possible starting configuration is with the O atom at the lower tip of the triangle at $Y_1 = 0$ and $Y_2 = 0$, i.e., at position $(A,0,0)$, as depicted in Figure 5.10. The probability for this starting configuration is $w_{0,0}(A,0,0) = 1$, whereas $w_{0,0} = 0$ for all other positions. w_{n_1,n_2} for any series of n_1 *triangle* and n_2 *exchange jumps* can then be obtained by recursion from $w_{0,0}$.

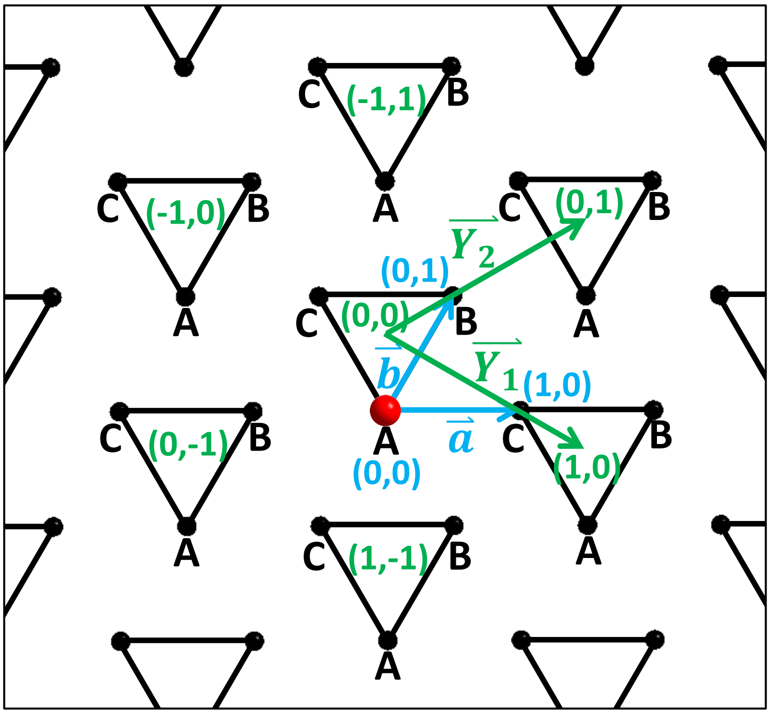

Figure 5.10: Coordinate system for the construction of $\overline{w}_{n_1,n_2}$. Black dots, with coordinates a and b (blue), represent the hexagonal (1 x 1) lattice of the hcp positions visited by the O atom (red); the triangles, with coordinates Y_1 and Y_2 (green), represent the triangular cages within the CO layer. (Adapted from Henß *et al.*, reference [131]. Reprinted with permission from *AAAS*.)

When performing a *triangle jump*, the probability that the atom sits on position (A, Y_1, Y_2) after the jump only depends on the occupation of the two other positions in the same cage (B, Y_1, Y_2) and (C, Y_1, Y_2) before that *triangle jump*. In general, w_{n_1,n_2} can thus be obtained from w_{n_1-1,n_2} by the use of the following three recursion rules:

$$w_{n_1,n_2}(A, Y_1, Y_2) = \frac{1}{2} w_{n_1-1,n_2}(B, Y_1, Y_2) + \frac{1}{2} w_{n_1-1,n_2}(C, Y_1, Y_2) \tag{5.23}$$

$$w_{n_1,n_2}(B,Y_1,Y_2) = \frac{1}{2}w_{n_1-1,n_2}(A,Y_1,Y_2) + \frac{1}{2}w_{n_1-1,n_2}(C,Y_1,Y_2) \tag{5.24}$$

$$w_{n_1,n_2}(C,Y_1,Y_2) = \frac{1}{2}w_{n_1-1,n_2}(A,Y_1,Y_2) + \frac{1}{2}w_{n_1-1,n_2}(B,Y_1,Y_2) \tag{5.25}$$

The factors 1/2 account for the fact that the particle that starts at a specific position jumps equally likely to the two alternative positions in the triangle. For example, for equation 5.23 this means that only half of the jumps starting at (B,Y_1,Y_2) and only half of the jumps starting at (C,Y_1,Y_2) land on (A,Y_1,Y_2).

For an *exchange jump*, w_{n_1,n_2} can be obtained in a similar way from w_{n_1,n_2-1}. Four different starting positions are possible from which position (A,Y_1,Y_2) can be reached by exactly one *exchange jump* (compare Figure 5.10).

$$\begin{aligned} w_{n_1,n_2}(A,Y_1,Y_2) \\ &= \frac{1}{4}w_{n_1,n_2-1}(C,Y_1+1,Y_2) + \frac{1}{4}w_{n_1,n_2-1}(B,Y_1+1,Y_2-1) \\ &+ \frac{1}{4}w_{n_1,n_2-1}(C,Y_1+1,Y_2-1) + \frac{1}{4}w_{n_1,n_2-1}(B,Y_1,Y_2-1) \end{aligned} \tag{5.26}$$

The factors 1/4 reflect the four possibilities for an *exchange jump* the particle has at each of the four starting positions, only one of which lands on (A,Y_1,Y_2). Analog recursion rules apply for $w_{n_1,n_2}(B,Y_1,Y_2)$ and $w_{n_1,n_2}(C,Y_1,Y_2)$.

$$\begin{aligned} w_{n_1,n_2}(B,Y_1,Y_2) \\ &= \frac{1}{4}w_{n_1,n_2-1}(C,Y_1+1,Y_2) + \frac{1}{4}w_{n_1,n_2-1}(A,Y_1,Y_2+1) \\ &+ \frac{1}{4}w_{n_1,n_2-1}(C,Y_1,Y_2+1) + \frac{1}{4}w_{n_1,n_2-1}(A,Y_1-1,Y_2+1) \end{aligned} \tag{5.27}$$

$$\begin{aligned} w_{n_1,n_2}(C,Y_1,Y_2) \\ &= \frac{1}{4}w_{n_1,n_2-1}(A,Y_1+1,Y_2-1) + \frac{1}{4}w_{n_1,n_2-1}(B,Y_1-1,Y_2) \\ &+ \frac{1}{4}w_{n_1,n_2-1}(A,Y_1-1,Y_2) + \frac{1}{4}w_{n_1,n_2-1}(B,Y_1,Y_2-1) \end{aligned} \tag{5.28}$$

By consecutively using the above equations, w_{n_1,n_2} is generated for any series of n_1 and n_2 jumps. However, the resulting position distribution depends on the order of the jumps, e.g., a hopping sequence of one *triangle jump* followed by one *exchange* *jump* will lead to a different position distribution than the reverse order. Both jump sequences are equally likely as jumps are considered uncorrelated. Therefore, in order to obtain the average probabilities $\bar{w}_{n_1,n_2}$ in equation 5.22, the probabilities $w^i_{n_1,n_2}$ for all possible permutations i of n_1 *triangle* and n_2 *exchange jumps* have to be calculated and subsequently averaged.

$$\bar{w}_{n_1,n_2} = \frac{1}{n_{Perm}} \sum_{i=1} w^i_{n_1,n_2} \tag{5.29}$$

According to enumerative combinatorics, the number of possible permutations n_{Perm} for a certain (n_1, n_2) combination can be calculated by

$$n_{Perm} = \binom{n_1 + n_2}{n_2} \tag{5.30}$$

The number of permutations quickly becomes very high with increasing values of n_1 and n_2. For example, for n_1 = 30 and n_2 = 5 equation 5.30 gives n_{Perm} = 324632, and the calculation of $\bar{w}_{30,5}$ by equation 5.29 already takes ~2.5 hours on a desktop computer. The calculation of $\bar{w}_{n_1,n_2}$ by equation 5.29 by recursion from $w_{0,0}$ was thus prohibited by the high computational cost for large values of n_1 and n_2.

However, the calculations could be simplified as demonstrated for the example $\bar{w}_{n_1,n_2}$ with n_1 = 2 and n_2 =2 in Table 5.2. For this case there are six permutations, i.e., six different but equally likely sequences of *triangle* and *exchange jumps* (column two in Table 5.2). For example, sequence 1 consists of two *triangle jumps* followed by two *exchange jumps*. By using the straightforward (but computationally costly) method one sequentially applies for each of the six sequences the respective equations 5.23 to 5.28 giving six probabilities $w^i_{2,2}$ (column three in Table 5.2). The average probability is obtained according to equation 5.29:

$$\bar{w}_{2,2}^{1\ to\ 6} = \frac{1}{6}\left(w^1_{2,2} + w^2_{2,2} + w^3_{2,2} + w^4_{2,2} + w^5_{2,2} + w^6_{2,2}\right) \tag{5.31}$$

In an alternative method the sequences are first split into two partial sequences (columns four and six in Table 5.2) at the point before the last exchange step. The six first partial sequences are then grouped according to the same steps in the second partial sequences. In the present case, three groups result. The averaging is then performed with the first partial sequences in the three groups (column five in Table 5.2):

$$\overline{w}_{2,1}^{1\ to\ 3} = \frac{1}{3}\left(w_{2,1}^{1} + w_{2,1}^{2} + w_{2,1}^{3}\right) \tag{5.32}$$

$$\overline{w}_{1,1}^{1\ to\ 2} = \frac{1}{2}\left(w_{1,1}^{1} + w_{1,1}^{2}\right) \tag{5.33}$$

$$\overline{w}_{0,1}^{1} = w_{0,1}^{1} \tag{5.34}$$

These averages are then used as starting configurations for the calculations of the steps of the second partial sequences by applying equations 5.23 to 5.28. The results $\overline{w}_{2,2}^{1\ to\ 3}$, $\overline{w}_{2,2}^{4\ to\ 5}$, and $\overline{w}_{2,2}^{6}$ (column seven in Table 5.2) are finally weighted according to the number of sequences contributing and summed up to give $\overline{w}_{2,2}^{1\ to\ 6}$.

$$\overline{w}_{2,2}^{1\ to\ 6} = \frac{3}{6}\overline{w}_{2,2}^{1\ to\ 3} + \frac{2}{6}\overline{w}_{2,2}^{4\ to\ 5} + \frac{1}{6}\overline{w}_{2,2}^{6} \tag{5.35}$$

Appendix D shows for the case of $n_1 = 2$ and $n_2 = 2$ that the results of the two methods, the explicit calculation by recursion starting from $w_{0,0}$ and the alternative approach, are identical. The alternative method is generalized for arbitrary n_1, n_2 combinations by splitting the total sequences into partial sequences according to the number of exchange jumps. In general, $\overline{w}_{n_1,n_2}$ can be obtained in this way by using the averaged displacement distributions for one *exchange jump* less $\overline{w}_{m_1,n_2-1}$ for m_1 from 0 up to n_1. In the depicted example $\overline{w}_{2,2}$ is determined from $\overline{w}_{2,1}$, $\overline{w}_{1,1}$, and $\overline{w}_{0,1}$.

This alternative method leads to a dramatic decrease of the number of calculations that have to be performed and thus to reasonable computational costs. Only by using this method $\overline{w}_{n_1,n_2}$ values could be calculated up to $n_1 = 100$ and $n_2 = 10$. These limits are certainly extreme – they mean that the model includes cases in which the O atom has jumped 100 times in a CO cage and has exchanged ten times with a CO molecule between two STM images – but they make sure that the analysis is “on the safe side.”

Table 5.2: Example for the determination of $\overline{w}_{n_1,n_2}$ for n_1 = 2 and n_2 = 2. *Triangle jumps* are abbreviated as “tri” and *exchange jumps* as “ex”.

Sequence number	**Possible Sequences**							**1st partial sequence**					**2nd partial sequence**			
i	**tri**	**ex**	**tri**	**ex**	**tri**			**tri**	**ex**	**tri**			**ex**	**tri**		
1	2	1	0	1	0	$w_{2,2}^{1}$	$\overline{w}_{2,2}^{1\ to\ 6}$	2	1	0	$w_{2,1}^{1}$	$\overline{w}_{2,1}^{1\ to\ 3}$	1	0	$\overline{w}_{2,2}^{1\ to\ 3}$	$\overline{w}_{2,2}^{1\ to\ 6}$
2	0	1	2	1	0	$w_{2,2}^{2}$		0	1	2	$w_{2,1}^{2}$					
3	1	1	1	1	0	$w_{2,2}^{3}$		1	1	1	$w_{2,1}^{3}$					
4	1	1	0	1	1	$w_{2,2}^{4}$		1	1	0	$w_{1,1}^{1}$	$\overline{w}_{1,1}^{1\ to\ 2}$	1	1	$\overline{w}_{2,2}^{4\ to\ 5}$	
5	0	1	1	1	1	$w_{2,2}^{5}$		0	1	1	$w_{1,1}^{2}$					
6	0	1	0	1	2	$w_{2,2}^{6}$		0	1	0	$w_{0,1}^{1}$	$\overline{w}_{0,1}^{1}$	1	2	$\overline{w}_{2,2}^{6}$	

The calculation leads to a set of matrices (three for each combination of n_1 and n_2 up to n_1 = 100 and n_2 = 10). The elements of the matrices are the probabilities $\overline{w}_{n_1,n_2}$ that the O atom reaches a triangular cage at a certain site (Y_1, Y_2) on the $(\sqrt{3} \text{ x } \sqrt{3})$R30° lattice by a given combination of n_1 and n_2. There are three sets of matrices because of the three possible positions A, B, or C in a triangle. This set of matrices can be seen as a geometric factor that only depends on the symmetry of the O/CO adsorption system on Ru(0001) (displayed in Figure 5.10) and is thus the same for all experiments analyzed. The probability $p_{t_0}(a, b)$ that a site is actually occupied is finally obtained by multiplying this geometric factor with the time-dependent factor $\tilde{p}_{t_0}(n_{1,}n_2)$ according to equation 5.22.

5.4.3.2 Experimental Displacement Distribution

The hopping frequencies were determined by comparing the analytically derived expression to the experimental displacement distributions of the O atom. Therefore, the jump vectors between consecutive STM images had to be extracted from the atom trajectories.

For this purpose, a routine was developed to assign each point in the experimentally determined trajectories to a lattice point of the (1 x 1)-hcp lattice of the Ru substrate. In order to ensure comparability of measurements regardless of the orientation of the crystal, the trajectories in this step were rotated such that the tips of the triangles pointed downwards. The experimental scatter of the atom positions were removed by defining an area around each hcp lattice site and merging all positions within such an area to the respective lattice site. O atom localizations that could not clearly be allocated to one lattice point were sorted out. The indexing of the lattice points was performed manually and the (0,0) point was always assigned to the lower tip of one of the triangles, in accordance with the starting configuration for the theoretical displacement distribution.

Figure 5.11 shows the result of this assignment step for the experimental trace in Figure 5.7. The experimental trace, rotated by 180° with respect to Figure 5.7, is shown on the left, the resulting trajectory on the (1 x 1) lattice of hcp positions on the right. Both traces are color-coded according to the respective frame numbers. To validate the correctness of this assignment step, the resulting trajectories were checked manually by a comparison with the original trace in the 2D and 3D perspective to exclude additional jumps added by accident.

As a result, a list is obtained that contains the coordinates of the particle position on the hcp lattice (a, b) and the corresponding image number. The jump vector could then be determined by taking the difference between the positions in two consecutive images. However, a jump vector in a certain direction can represent different types of jumps depending on the starting position. For example, when the atom is at the lower tip of a triangle (position A), a jump in the direction of $\vec{a}$ is an *exchange jump* (see Figure 5.10). The same is valid for starting at the B position, but from position C, a jump along $\vec{a}$ is a *triangle jump*. Therefore, also the starting positions for the jumps have to be taken into account.

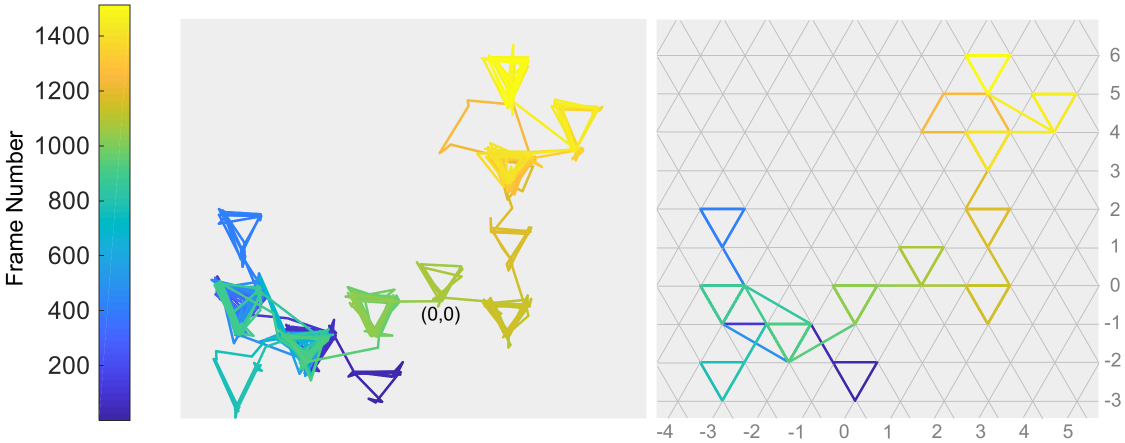

Figure 5.11: Left: Experimental particle trajectory of a single O atom in CO from Figure 5.7. The (0,0) lattice point is assigned to the lower tip of a triangle. Right: Trajectory after mapping the experimental trajectory to the (1 x 1)-hcp lattice of the Ru substrate (gray).

Whether a specific position with coordinates (a, b) corresponds to an A, B, or C position in a triangle is determined by converting the (1 x 1) lattice coordinates into the coordinates of the $(\sqrt{3} \text{ x } \sqrt{3})R30°$ structure. The two lattice vectors of the $(\sqrt{3} \text{ x } \sqrt{3})R30°$ lattice (green, Figure 5.10) can be expressed by the two lattice vectors $\vec{a}$ and $\vec{b}$ of the (1 x 1) lattice (blue, Figure 5.10) by equations 5.36 and 5.37.

$$\overrightarrow{Y_1} = 2\vec{a} - \vec{b} \tag{5.36}$$

$$\overrightarrow{Y_2} = \vec{a} + \vec{b} \tag{5.37}$$

If the O atom is on an A position, the position coordinates (a, b) can be constructed by a linear combination of integer multiples of the vectors $\overrightarrow{Y_1}$ and $\overrightarrow{Y_2}$, because also

(0,0) is an *A* position since each trajectory was first rotated such that the starting position was the O atom on an *A* position.

$$\text{Position } A: \qquad (a,b) = Y_1 \cdot \overrightarrow{Y_1} + Y_2 \cdot \overrightarrow{Y_2} \qquad \text{with } Y_1, Y_2 \in \mathbb{Z} \tag{5.38}$$

Equation 5.38 gives non-integer values for Y_1 and Y_2 if the atom is located at position *B* or *C*. Instead equations 5.39 and 5.40 are valid in these cases, respectively. Which equations gives integer solutions for Y_1 and Y_2 thus provides the position in the triangle and the integer solutions for Y_1 and Y_2 directly represent the coordinates of the triangle in which the O is located.

$$\text{Position } B: \qquad (a,b) - (0,1) = Y_1 \cdot \overrightarrow{Y_1} + Y_2 \cdot \overrightarrow{Y_2} \qquad \text{with } Y_1, Y_2 \in \mathbb{Z} \tag{5.39}$$

$$\text{Position } C: \qquad (a,b) - (-1,1) = Y_1 \cdot \overrightarrow{Y_1} + Y_2 \cdot \overrightarrow{Y_2} \qquad \text{with } Y_1, Y_2 \in \mathbb{Z} \tag{5.40}$$

The analysis routine thus determines for each pair of consecutive STM images *i* and *i+1* whether the starting point for the jump in image *i* is a position *A*, *B*, or *C* in a triangle. If the atom starts at an *A* position, the jump vector is the difference between the two positions in the images. If the starting position is a *B* position, the (1 x 1) lattice is first rotated by -120° for both images. Rotation is performed around the centroid of the triangle at position $Y_1 = 0$ and $Y_2 = 0$ ($a = -{}^{1}/_{3}$ and $b = {}^{2}/_{3}$) to merge the *B* position with an *A* position. Rotation angles are positive for counterclockwise rotation.

The positions in images *i* and *i+1* are then given by their new coordinates (a', b'), which are obtained by applying a rotation matrix *M* around $\left(-{}^{1}/_{3} \quad {}^{2}/_{3}\right)$ to the former coordinates (a, b).

$$\begin{pmatrix} a' \\ b' \end{pmatrix} = M \cdot \left[\begin{pmatrix} a \\ b \end{pmatrix} - \begin{pmatrix} -{}^{1}/_{3} \\ {}^{2}/_{3} \end{pmatrix} \right] + \begin{pmatrix} -{}^{1}/_{3} \\ {}^{2}/_{3} \end{pmatrix} \tag{5.41}$$

The jump vector is then obtained by taking the difference between the new positions (a', b') in both images. For a starting position *C* in image *i*, the positions in both images are rotated by +120°. The rotational matrices are:

$$M_{-120^\circ} = \begin{pmatrix} 0 & 1 \\ -1 & -1 \end{pmatrix} \tag{5.42}$$

$$M_{+120^\circ} = \begin{pmatrix} -1 & -1 \\ 1 & 0 \end{pmatrix} \tag{5.43}$$

The determined jump vectors are subsequently converted into coordinates on the $(\sqrt{3}\,\mathrm{x}\,\sqrt{3})R30^\circ$ lattice according to equations 5.38 to 5.40 for compatibility with the theoretically determined distributions.

All transition events by equivalent jump vectors are then summed up and normalized with respect to the total number of images evaluated. The displacement distribution is then saved in a cell containing three (23 x 23) matrices. The matrix indices represent the lattice coordinates (Y_1, Y_2) of the respective triangle, where the triangle at Y_1 = 0 and Y_2 = 0 corresponds to the entries at position (12,12) in the matrices. The matrix size of (23 x 23) thus covers up to ten *exchange jumps* in each direction The three matrices reflect the three possible positions of the O atom A, B, or C in a triangle.

5.4.3.3 Extraction of Jump Frequencies

Figure 5.12 shows an experimental displacement distribution (magenta bars) obtained from 10889 frames of STM measurements at +18 °C. The imaging frequency was 10 Hz. The marked green triangle represents the three positions in the triangle at Y_1 = 0 and Y_2 = 0 and the starting position for the O atom is the (0,0) or $(A, 0{,}0)$ position. The absolute error for each experimental bar is estimated using $\pm\sqrt{N}$ where N is the number of jumps to this position.

For a clearer representation only positions for $Y_1 \leq |2|$ and $Y_2 \leq |2|$ are shown, because displacements to positions further away contributed only negligibly. The three high central bars for which $p_{t_0}(x, y)$ is approximately 0.3 reflect the comparatively long time the O atom spends within a CO cage. The probabilities of displacements to the first nearest-neighbor triangles are already two orders of magnitude lower, i.e., in the range of 0.005.

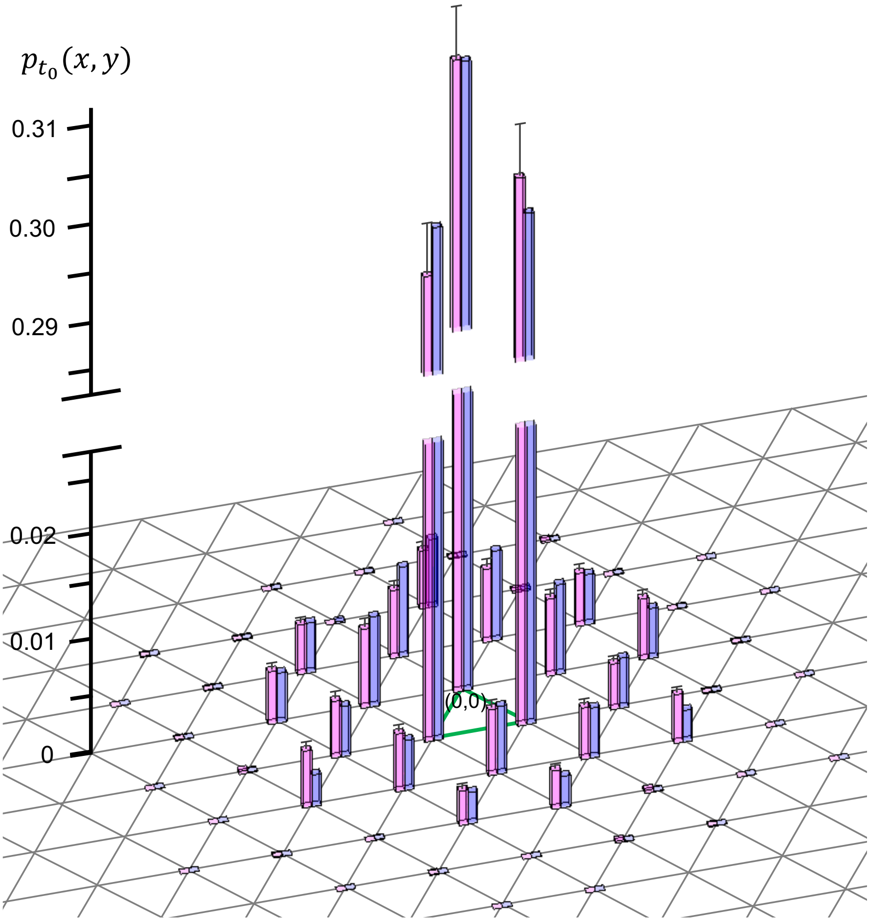

Figure 5.12: Fit (blue bars) of the experimental displacement distribution (magenta bars) with equation 5.44. (Adapted from Henß *et al.*, reference [131]. Reprinted with permission from *AAAS*.)

The jump frequencies were determined by fitting the experimental displacement distributions with the theoretical distribution from the model, using a Levenberg-Marquardt method.[186-188] Fitting was performed with equation 5.44 adapted from equation 5.22 for the change of the coordinate system. pos is the position in the triangle, i.e., A, B, or C. The infinite sums were terminated at n_1 = 100 and n_2 = 10, as these numbers of jump events were sufficient to describe all experimental distributions. The time interval t_0 is given by the imaging rate of the respective STM movie. The only fitting parameters are the hopping frequencies Γ_1 and Γ_2.

$$p_{t_0}(pos, Y_1, Y_2) = \sum_{n_1=0}^{100} \sum_{n_2=0}^{10} \tilde{p}_{t_0}(n_1, n_2) \cdot \overline{w}_{n_1,n_2}(pos, Y_1, Y_2) \qquad (5.44)$$

The result is shown in Figure 5.12 as blue bars. The jump frequencies determined in this way are Γ_1 = 28.5 Hz and Γ_2 = 0.997 Hz. Theoretical and experimental distribution are in excellent agreement with a least-squares error of only $5.71 \cdot 10^{-5}$. Similarly good agreement was achieved for measurements at other temperatures, see section 5.4.3.4. The good matching between fit and experiment can be taken as a strong indication that the model of two independent jump types between nearest-neighbor sites is a valid description of the diffusion mechanism. There are no indications of a contribution of long jumps.

At temperatures above +18 °C, the O atom hopped too fast between the three positions in the triangles, for a reliable position assignment. An example for a trace at +27 °C is depicted in Figure 5.13. The triangles are difficult to identify, as in most cases only one of the three positions in a triangle is occupied. At some positions in the trajectory the structure of the triangles can still be guessed. However, these triangles appear smaller than in the trajectory in Figure 5.7. This is because of the rapid movement of the atom in a CO cage, it is often observed at more than one of the hcp sites in a triangle in an image. So that the detection algorithm localizes the particle in between the three positions. Instead the hexagonal pattern of the $(\sqrt{3} \text{ x } \sqrt{3})$R30° structure appears as prominent feature in the traces.

In these cases, only the sum S of all three positions in a triangle $p_{t_0}(S, Y_1, Y_2)$ could be extracted from the experimental trajectories:

$$p_{t_0}(S, Y_1, Y_2) = p_{t_0}(A, Y_1, Y_2) + p_{t_0}(B, Y_1, Y_2) + p_{t_0}(C, Y_1, Y_2) \tag{5.45}$$

In most cases even the orientations of the triangles in the trace (tip pointing upwards or downwards) could no longer be determined, and only the distances of the triangles with respect to the starting position were available. In order to still make use of these data, the sums of the three positions in the innermost triangle $p_{t_0}(S, 0{,}0)$, the sums of all positions in the six nearest-neighbor (NN) triangles $\sum p_{t_0}(S, NN)$, the sums of all positions in the twelve second nearest-neighbor (*2NN*) triangles $\sum p_{t_0}(S, 2NN)$, and so on were formed from the experimental distributions and fitted.

The resulting averaged position distributions still depend on both hopping frequencies, since the number of *triangle jumps* determines the directions in which *exchange jumps* can occur, so that in principle both frequencies should be determinable. It turned out, however, that the distributions were no longer unambiguous for the range of the *triangle jump* frequencies at temperatures above +18 °C, so that depending on the initial guess for the fit, different values for Γ_1 were obtained.

In contrast, the *exchange jump* frequencies were independent of the start values, and were therefore considered valid.

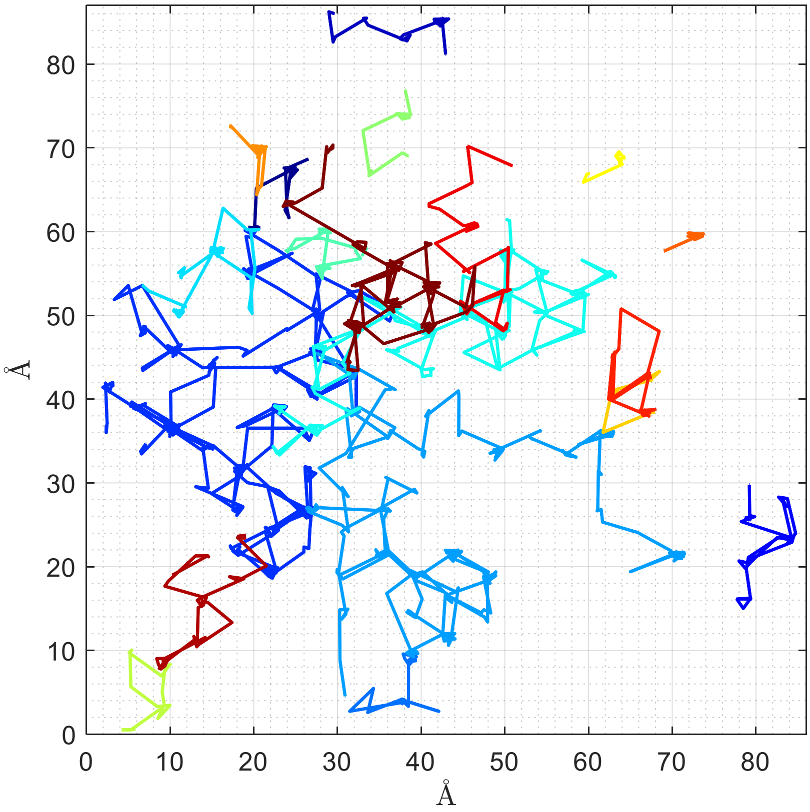

Figure 5.13: O atom trajectories from a dataset acquired at +27 °C. Different colors represent different trajectories.

5.4.3.4 Temperature Dependence

The hopping frequencies Γ_1 and Γ_2 for 14 different temperatures in the range between -39 °C and +29 °C are listed in Table 5.3. Hopping frequencies over five orders of magnitude could be measured. This is in the same range or even better than what has been achieved by atom-tracking STM[52] and by tunneling current fluctuation measurements,[54] both of which methods do not involve direct observation of the atomic processes.

The temperature dependence of the two hopping frequencies is very well described by the Arrhenius law as demonstrated in Figure 5.14. The hopping frequencies for the *triangle jumps* (green squares) and for the *exchange jumps* (black squares) follow a straight line, as one would suggest for thermally activated processes. This fact can be taken as a further strong indication that the diffusion model consisting of two independent thermally activated hopping processes is accurate.

Table 5.3: Hopping frequencies Γ_1 (*triangle jumps*) and Γ_2 (*exchange jumps*) determined in the temperature range between -39 °C and +29 °C together with the total number of STM images evaluated at the given temperature. (Adapted from Henß *et al.*, reference [131]. Reprinted with permission from *AAAS.*)

Temperature [°C]	Temperature [K]	# STM images	Γ_1 [s^{-1}]	Γ_2 [s^{-1}]
-39	234.15	15703	0.134	0.00160
-34	239.15	29955	0.258	0.00316
-28	245.15	18832	0.367	0.0308
-22	251.15	16290	0.858	0.0417
-15	258.15	2395	1.31	0.0632
-12	261.15	2972	2.07	0.0621
-11	262.15	10026	2.22	0.0549
-9.5	263.65	2625	2.24	0.0936
0	273.15	7092	7.56	0.162
12	285.15	17738	25.2	0.544
18	291.15	10889	28.5	0.997
22	295.15	12036		2.10
27	300.15	7652		3.15
29	302.15	4285		3.46

From the slopes of the Arrhenius fits, the activation energies for the two jump types are determined to $E_1^* = 0.57 \pm 0.02$ eV for the *triangle jumps* and $E_2^* = 0.63 \pm 0.03$ eV for the *exchange jumps* with CO. Pre-exponential factors Γ_0 were $\Gamma_{0,1} = 10^{11.4\pm0.4}$ Hz and $\Gamma_{0,2} = 10^{11.1\pm0.7}$ Hz, respectively, in reasonable agreement with the expected 10^{12} to 10^{13} Hz range.[6, 189]

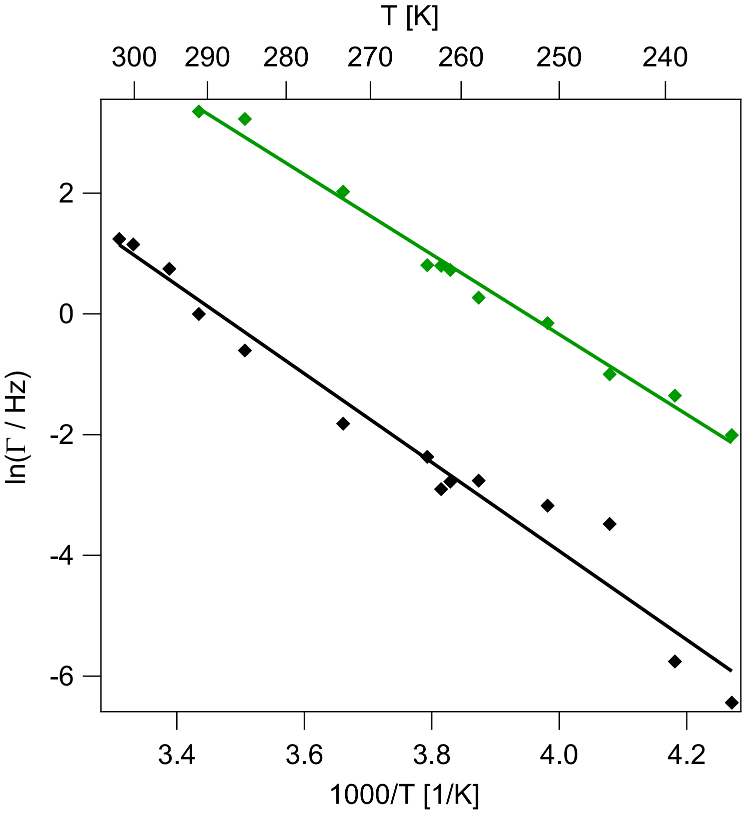

Figure 5.14: Arrhenius plot of the temperature dependence of the two hopping rates. Green squares represent the frequencies obtained for the *triangle jumps* (Γ_1), black squares the ones for the *exchange jumps* (Γ_2). The green and black lines are the corresponding linear fits. (From Henß *et al.*, reference [131]. Reprinted with permission from *AAAS*.)

5.4.3.5 Investigation of Tip Influences

To investigate possible effects of the scanning tip on the diffusion process, two tests were performed.

Firstly, a correlation between jumping directions of the O atoms and the scan direction of the tip might be expected if the movement of the tip had influenced the motion of the O atoms. For the measurements of O in CO/Ru(0001) in this work, the orientation of the specific positions within a triangle with respect to the scanning directions are known. The STM data could thus be checked for a systematic tip influence by analysis of the displacement distributions in dependence of the respective starting position for the jump.

Figure 5.15 shows the results of the experimental displacement distribution from STM movies acquired at 0 °C. In all evaluated movies the orientation of the triangles with respect to the scanning directions of the tip in x and y direction was as shown in Figure 5.15 a). Furthermore, all datasets were recorded with the same scan speed and frame rate. A total number of 7092 frames was evaluated.

Figure 5.15 b) gives the displacement probabilities for the three positions in the triangular CO cage. The color code indicates the starting position for the displacements. Jumps started at position A are marked in blue, jumps from position B in purple and jumps from position C in green. For example, an O atom that was on position B in one image, is with a probability of 0.2057 on position C and with a probability of 0.2158 on position A in the next image. The displacement probabilities in the triangle show no clear indication for a tip influence. All transitions are equally likely within the experimental errors. The same conclusion is valid for the analogous analysis for the *exchange jumps* [Figure 5.15 c)]. The values vary around an average of ~0.0025. However, the variations cannot be correlated with a specific direction of the tip motion. In conclusion, the analysis presented here shows no clear indication of a directional dependence of the O jumps on the tip movement.

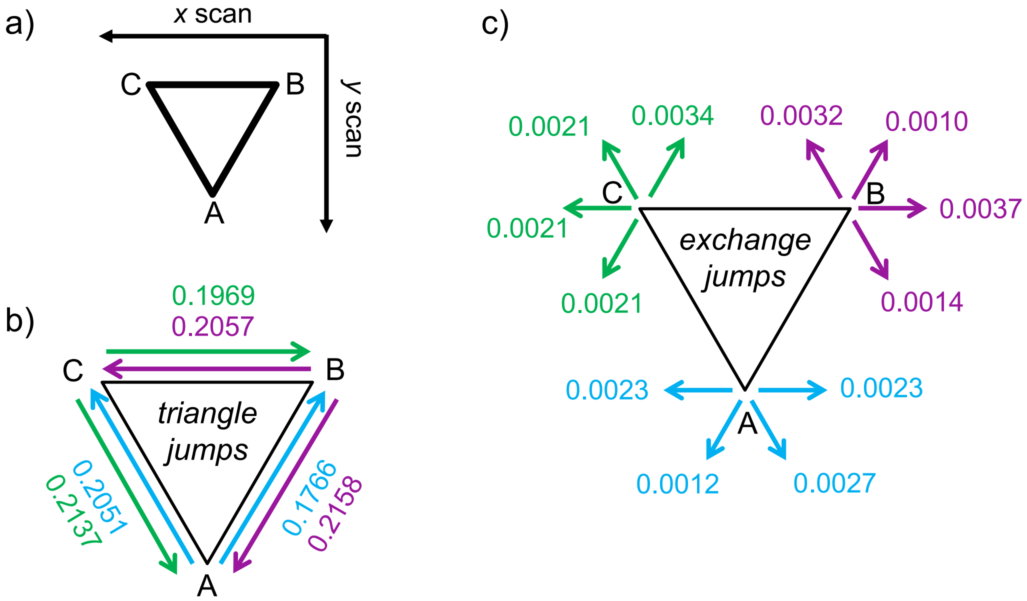

Figure 5.15: a) Orientation of the triangular cage with positions A, B, and C with respect to the scanning directions of the STM tip. b) Displacement probabilities in dependence of the starting position for *triangle jumps* and c) for *exchange jumps*.

As a second check of tip influences, it has been determined whether the hopping frequencies depend on the scan frequencies and thus on the interaction time of the tip with the atom. STM measurements at -34 °C were performed at four different scan speeds and were individually evaluated. Table 5.4 summarizes the results. All measurements were recorded on the same day immediately after each other so that the influence of temperature variations could be minimized. The images were all of the same pixel and Ångström size.

Table 5.4: Hopping frequencies at -34 °C depending on the scan frequency in *x* direction and on the time intervals t_0 between two images that characterize the scan speed in *y* direction.

Scan Frequency *x* scan [Hz]	**t_0 [s]**	**# Events**	**Γ_1 [Hz]**	**Γ_2 [Hz]**
2000	0.1005	1692	0.264	0
1000	0.201	4316	0.251	0
600	0.335	10437	0.296	$3 \cdot 10^{-3}$
400	0.5025	4570	0.289	$5 \cdot 10^{-3}$

The data show that the hop frequencies are independent of the scan frequency within the experimental errors. Therefore, both performed tests show no tip influence on the O motion. This result is in accordance with the findings of Renisch *et al.*. They investigated O atoms on the bare Ru(0001) surface and found effects of the STM tip only for tunneling resistances below 10^6 Ω.[166] In all datasets analyzed and presented within this thesis, the most extreme tunneling conditions applied were V_t = -0.1 V and I_t = 10 nA, corresponding to a tunneling resistance of 10^7 Ω, one order of magnitude above the value determined by Renisch *et al.*. It can thus be concluded that no evidence for an interaction between STM tip and O diffusion has been found.

5.4.4 The Diffusion Mechanism

In order to gain a complete picture of the diffusion process, the two jump processes were analyzed in more detail to access the underlying diffusion mechanism. DFT was used to investigate the energy landscape in which the jump processes take place. The DFT calculations described in this section were performed by Dr. Sung Sakong and Prof. Dr. Axel Groß of Ulm University. For the calculations a technical setup was used that had previously been shown to be well-suited for the description of the CO/Ru(0001) system.[190, 191] An overview of the technical details of the calculations is given in Appendix E.

The Ru surface was modelled with a three layer slab with a (6 x 6) unit cell that is illustrated in Figure 5.16 a). The Ru atoms of the first and the second layer are shown in light and dark gray, respectively, and CO molecules in blue. The O atom (red) sits on an hcp position, denoted as *hcp1*, in the CO cage. In the following all DFT energies are given with respect to this minimum energy configuration.

5.4.4.1 *Triangle Jumps*

For the *triangle jumps* the DFT calculations revealed that a jump from one hcp site to a second hcp site in the cage occurs via an intermediate fcc position [black arrows in Figure 5.16 a)]. The energy profile for this jump is shown in Figure 5.16 b) in black. For this process an energy barrier of 0.56 eV was found, in good agreement with the experimentally determined value of 0.57 eV ± 0.02 eV for the *triangle jumps* from the analysis of the Arrhenius plot.

Compared to single O atoms on the clean Ru(0001) surface (pink line), the O adsorption is weakened by 0.08 eV when coadsorbed with CO. This decrease in binding strength between O and Ru can be attributed to repulsive interactions with the coadsorbate CO, in accordance with DFT studies on the (2 x 2)-(CO+O) system on Ru(0001) that also showed a lowered adsorption energy for both CO and O compared to the single adsorption systems.[130] A weaker bonding is also expected from the d-band model,[192] according to which an increase of surface coverage in general decreases the binding of the individual adsorbates to the substrate. Such effects of coadsorbates on the bond strength are known for several adsorption systems as described, e.g., by Hammer.[183]

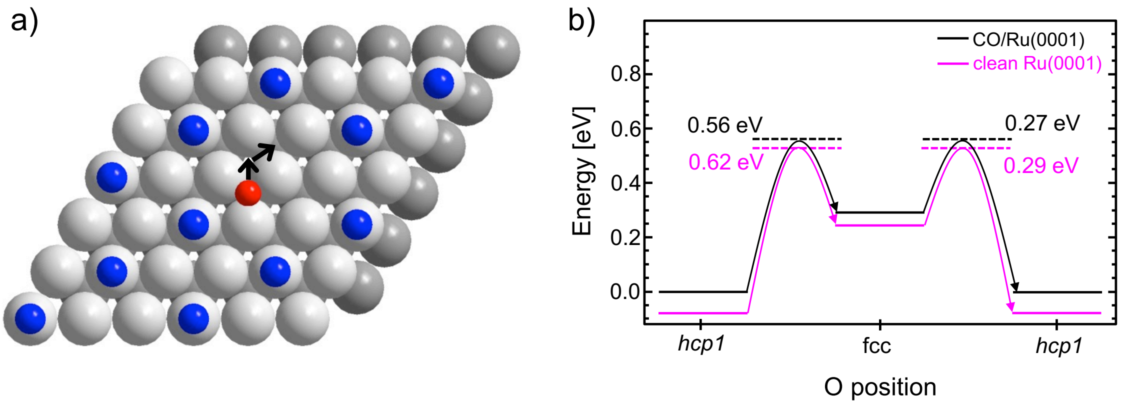

Figure 5.16: Paths and energy diagram of the *triangle jumps*. a) DFT unit cell. Ru atoms are illustrated in gray, CO molecules in blue and the O atom in red. Black arrows indicate the path along which an O moves in a CO cage. b) Energy profile for O hopping in the CO cage (black) and for the O diffusion on the clean Ru(0001) surface (pink). [b) from Henß *et al.*, reference [131]. Reprinted with permission from *AAAS*.]

The effect of a lowered binding strength is less pronounced for the transition state (~0.02 eV) than for the initial hcp state (~0.08 eV). As a result the calculated diffusion barrier for O on the clean Ru(0001) surface (0.62 eV) is slightly higher than for the O hopping in the CO cage (0.56 eV). Extrapolating the Arrhenius plot in Figure 5.14, the jump frequency for the *triangle jumps* at 298 K can be estimated to approximately 50 Hz, whereas for O on clean Ru(0001), Renisch *et al.* measured a jump frequency at room temperature of 16.6 Hz, confirming this result.[166]

5.4.4.2 *Exchange Jumps*

For the *exchange jumps* two fundamentally different mechanisms are thinkable, a vacancy-mediated process or an exchange process of the oxygen with the CO without any vacancy involvement.

For the system of O and CO on Ru, a vacancy-mediated mechanism would include a second vacancy in the CO layer in addition to the one occupied by the oxygen. The oxygen could only perform an *exchange jump* when a vacancy passes by so that the oxygen can jump into that vacancy. As mentioned before in section 5.2.3, the vacancy-mediated hop mechanism displays a characteristic correlation of directions between successive jumps. The reason is that after the vacancy has changed position with the tracer particle, there is an enhanced probability for the vacancy to return from the same side to the particle than from opposite or perpendicular directions.

In order to check for such a correlation of directions over thousand pairs of consecutive *exchange jumps* were evaluated. *Triangle jumps* between two *exchange jumps* were neglected. The result of this analysis is illustrated in Figure 5.17. The direction of the first jump is indicated by the red arrow. The subsequent jump can then occur along one of the six black arrows. If the direction of these second jumps is independent of the direction of the first, then all positions should be equally likely with a probability of 1/6. In the case of a vacancy mechanism, the probability for direction 1 should be higher compared to the other positions. Also directions 2 and 6, which are on the same side as the original position, should be more likely than jumps along directions 3, 4, and 5.

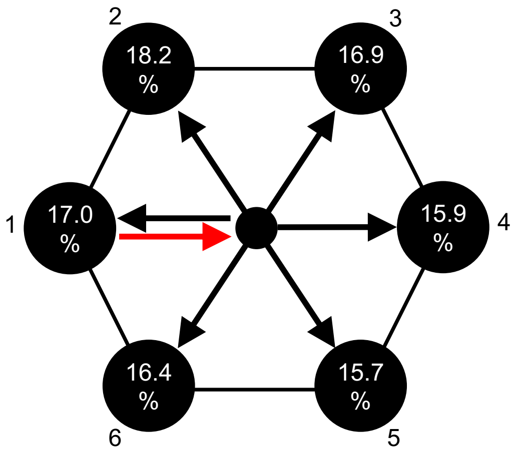

Figure 5.17: Analysis of directions of pairs of consecutive *exchange jumps* derived from 1210 events. The first jump occurs along the red arrow, the consecutive jump along one of the six black arrows.

However, the determined percentages for the different directions, given in Figure 5.17, only show a marginally increased probability for jumps along direction 1 relative to the expected value of 16.66 % for a random distribution. The difference is statistically insignificant since it is even smaller than the difference between the probabilities for direction 2 and 6, as well as between directions 3 and 5, which should be pairwise equivalent and thus exhibit the same probability. A vacancy-mediated diffusion process can thus be ruled out.

Without the participation of a vacancy the O atom has to exchange with a CO molecule. This exchange can follow one of three possible mechanisms:

- a concerted exchange mechanism of O and CO
- a sequential mechanism initiated by the O atom
- a sequential mechanism initiated by a CO molecule

Snapshots obtained from DFT calculations of the initial, intermediate, and final configuration when O and CO are forced into a concerted exchange are shown in Figure 5.18. An important aspect for such a process is the limited space, as O and CO have to come very close during the exchange. There is an intermediate local minimum structure in which a strongly deformed CO_2 molecule is formed, see Figure 5.18 b). The formation of this intermediate structure and thus also the whole process is associated with an activation barrier of ~1.5 eV. This high barrier is in accordance with previous DFT studies that found a comparable intermediate state prior to CO_2 formation and determined the reaction barrier for CO oxidation on metallic Ru to more than 1.4 eV.[130, 193] From the high activation energy for the formation of such an intermediate structure and from the fact that metallic Ru is inactive for CO oxidation, it can be ruled out that O diffusion occurs via such a concerted exchange mechanism.

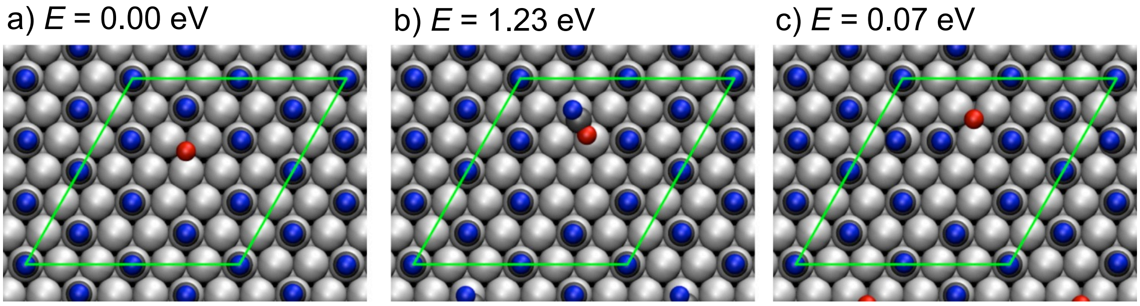

Figure 5.18: Snapshots of the concerted O/CO exchange. The O atom is shown in red, the CO molecules in blue and the Ru atoms in gray. a) Initial state, b) intermediate local energy minimum, and c) final state after the exchange. The DFT unit cell is indicated in green. (from Henß *et al.*, reference [131]. Reprinted with permission from *AAAS*.)

When a sequential movement of O and CO is considered, this process could be initiated by the move of the O atom out of the cage to an hcp site adjacent to a CO molecule (*hcp2* position). Again such a jump was found by DFT to occur via an intermediate fcc position. This diffusion pathway is indicated in Figure 5.19 a) by black arrows. The corresponding energy profile is shown in Figure 5.19 b) as the dotted black line. The first step from the *hcp1* position in the CO cage to an fcc position at the rim of the CO cage requires a relatively high activation energy of 0.98 eV, while the second part of the process, the jump from the fcc to the *hcp2* position adjacent to the CO molecule, has a low barrier of 0.35 eV.

The high barrier of the first step can be explained by the fact that this jump is towards a CO molecule. The repulsion between CO and O as well as the resultant binding situation to the same Ru atom make this step energetically costly. To complete the exchange process after the move of the O, the CO would then have to rearrange and fill up the vacancy left by the O atom. As the barrier for the first step of the O motion is already more than 50 % higher than the experimentally determined activation barrier of 0.63 eV, this sequential mechanism in which the O atom moves first is ruled out.

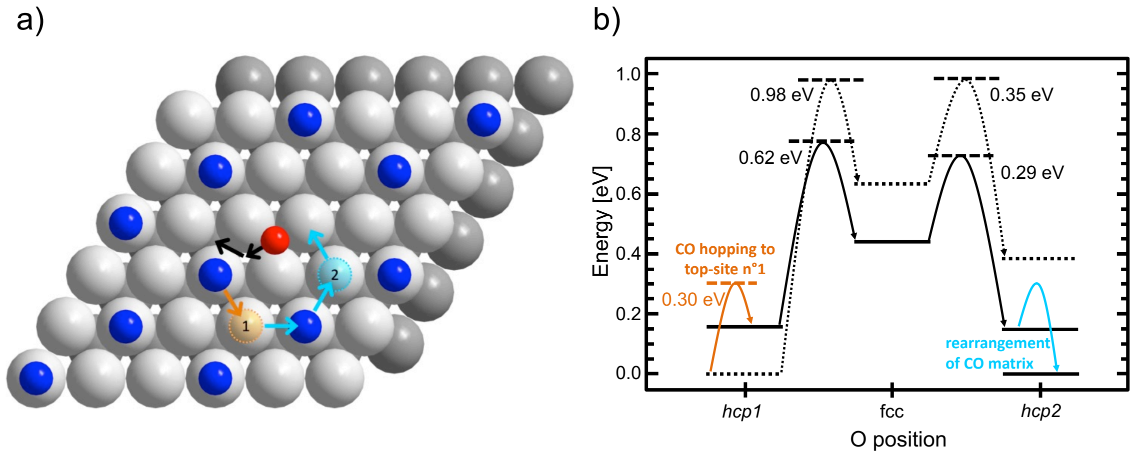

Figure 5.19: Paths and energy diagram of the *exchange jumps*. a) Unit cell used for DFT calculations. Ru atoms are shown gray, CO molecules blue and the O atom red. Black arrows indicate the path along which an O moves from the *hcp1* position via an fcc site to the *hcp2* position. b) Energy profile for O diffusion along the indicated path in a) in the intact ($(\sqrt{3} \times \sqrt{3})$R30° CO structure (dotted black line) and in a disordered CO configuration (solid black line). (from Henß *et al.*, reference [131]. Reprinted with permission from *AAAS*.)

To avoid O-CO repulsion during the *exchange jump*, a mechanism has been investigated which is initiated by a CO molecule in the surroundings of the oxygen. The energy barrier for the displacement of a single CO from its original position in the ordered layer to an adjacent on top site, e.g., to *top-site 1* [orange in Figure 5.19 a)] was found to be only 0.30 eV. This low barrier implies that the ordered

$(\sqrt{3} \times \sqrt{3})$R30° structure in the investigated temperature range is permanently subject to equilibrium fluctuations, in which CO molecules are temporarily displaced from their lattice positions. Because of the low activation barrier compared to the O diffusion barrier, the dislocations happen on a much shorter timescale than the O diffusion itself, so that these fluctuations are too fast to be visible in the STM measurements in the temperature range investigated.

However, the impact of these fluctuations on the energetics of the oxygen diffusion is quite significant, as can be seen from the solid black energy profile in Figure 5.19 b). The dislocation of the CO to *top-site 1* increases the energy of the whole O/CO configuration by 0.16 eV. Similar values are found when the CO is displaced to one of the other neighboring top-sites, which are not directly adjacent to the O atom. The rise in energy can be attributed to the CO-CO repulsion on neighboring top-sites. When, after such a CO displacement, the O atom moves along the *hcp1*-fcc-*hcp2* path indicated in Figure 5.19 a), the barrier is lowered significantly to 0.62 eV. Hence, the disordered CO configuration allows the oxygen to escape from the confined area around a vacant $(\sqrt{3} \times \sqrt{3})$ position, because of the reduced O-CO repulsion. If the oxygen moves along this pathway after a CO has been dislocated, the way back is blocked for the displaced CO molecule. Finally, the CO matrix rearranges restoring the ordered $(\sqrt{3} \times \sqrt{3})$R30° structure and completing the exchange process. This rearrangement is assumed to happen very fast as a sequential hopping of one or several CO molecules. An example how such a rearrangement could occur is indicated in Figure 5.19 a) by the cyan arrows. Here, two CO molecules participate by rearranging in a ring-like hop sequence.

The barrier for the O diffusion step from the initial *hcp1* position to the intermediate fcc position in the disordered CO layer is slightly higher (0.62 eV) than for the *triangle jumps* in the CO cage (0.56 eV). This fact can be explained with the initialization step of the *exchange jump*, the displacement of a CO molecule away from the O atom. This step reduces the coordination of the O atom by CO molecules and thus enhances the binding of the O atom to the substrate. The subsequent jump of the O atom to the fcc site is then a jump partially toward the initially displaced CO molecule, i.e., in a direction in which the repulsion by CO increases. Both effects counteract the above described lowering of the diffusion barrier by the coadsorbate CO. As a result, the calculated barrier in the exchange process for the O jump from *hcp1* to fcc is enhanced to 0.62 eV.

For the comparison with the experimental value the energy contribution of the preceding CO order-disorder transition has to be taken into account. In the picture of a chemical reaction, the equilibrium fluctuations in the CO layer can be interpreted as a pre-equilibrium (highlighted in yellow in Figure 5.20) as they appear on a much shorter time scale than the hopping of the O atom. The jump of the oxygen is the rate-limiting step (highlighted in blue in Figure 5.20). To obtain the activation energy for the whole *exchange jump*, the energy difference between the ordered and the disordered CO configuration of 0.16 eV has to be added to the barrier for the O diffusion step. The reason is given in the following.

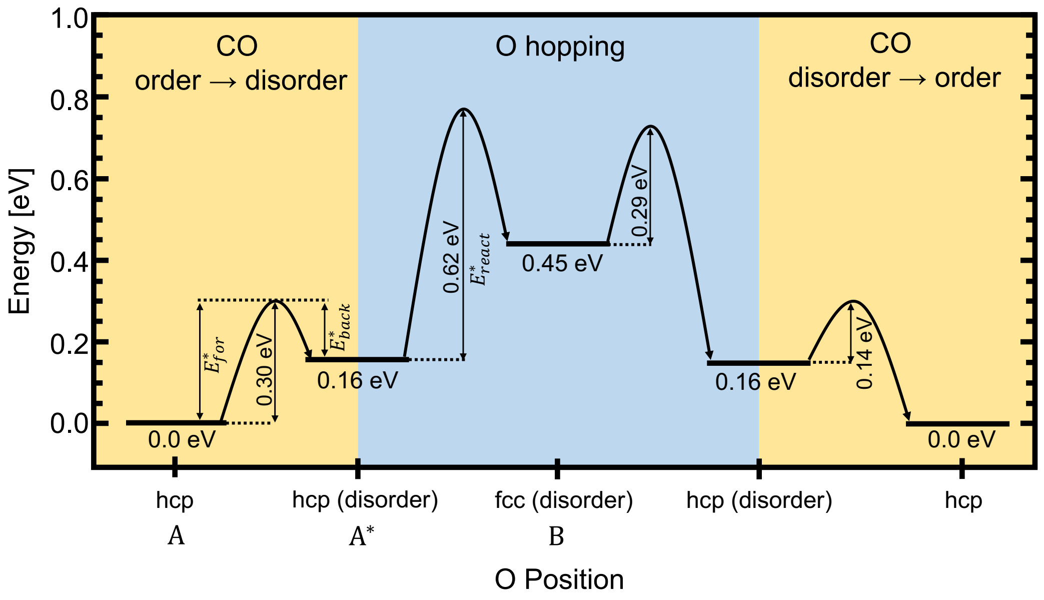

Figure 5.20: Energy profile for the O/CO exchange jump initiated by fluctuations in the CO layer.

Equation 5.46 shows a reaction equation for a chemical reaction containing a pre-equilibrium. The educt A is equilibrated with an intermediate product A*. The rate constants for forward and backward reaction are k_{for} and k_{back}. A* subsequently reacts with the rate constant k_{react} to the product B.

$$\mathrm{A} \underset{k_{back}}{\overset{k_{for}}{\rightleftharpoons}} \mathrm{A}^* \xrightarrow{k_{react}} \mathrm{B} \tag{5.46}$$

The product formation rate $\frac{d[\mathrm{B}]}{dt}$ can be expressed by an overall reaction rate constant k_{total} in dependence of the concentration of the educt [A], according to equation 5.47.

$$\frac{d[\mathrm{B}]}{dt} = k_{react} \cdot [\mathrm{A}^*] = k_{react} \cdot \frac{k_{for}}{k_{back}} \cdot [\mathrm{A}] = k_{total} \cdot [\mathrm{A}] \tag{5.47}$$

$$\text{with} \qquad k_{total} = k_{react} \cdot \frac{k_{for}}{k_{back}} \tag{5.48}$$

Using the Arrhenius law (equation 5.19) for all rate constants in equation 5.48 and sorting terms leads to equation 5.49.

$$A_{total} \cdot e^{\frac{-E^*_{total}}{RT}} = \frac{A_{react} \cdot A_{for}}{A_{back}} \cdot e^{\frac{-\left(E^*_{react}+E^*_{for}-E^*_{back}\right)}{RT}} \tag{5.49}$$

The total activation barrier E^*_{total} for such a reaction is thus the sum of the energy barrier for the rate-limiting step E^*_{react} and the energy difference $E^*_{for} - E^*_{back}$ between the two species A and A*.

Applying this result to the *exchange jumps* shows that the fluctuations in the CO matrix represent the pre-equilibrium and the jump of the O atom the following slow step (Figure 5.20). The O atom on an *hcp1* position in the ordered CO structure can be interpreted as educt A and the O atom on the *hcp1* in the disordered CO environment as the intermediate product A* that is 0.16 eV higher in energy than A. The barrier E^*_{for} is then given by the barrier for the jump of a CO molecule to a neighboring on-top position which is 0.3 eV. Accordingly E^*_{back} is 0.14 eV.

The rate-limiting step in the exchange process is the subsequent jump of the O atom in the disordered configuration from *hcp1* to the intermediate fcc position (product B). All following steps, such as the hopping of the O from fcc to *hcp2* and the rearrangement of the CO matrix, have comparatively low activation barriers and are assumed to occur in a sequential manner, so that the barriers of the individual steps do not add up. These downstream steps thus do not contribute to the barrier of the overall process.

The activation barrier for the whole exchange process that is initiated by the move of a CO molecule is thus given by the barrier for the oxygen diffusion itself (0.62 eV, E^*_2) plus the energy difference of the two O/CO configurations (0.16 eV, $E^*_{for} - E^*_{back}$), resulting in a total barrier of 0.78 eV for the *exchange jump*.

The experimentally determined pre-exponential factors for the *triangle jumps* and the *exchange jumps* are very similar, $\Gamma_{0,1} = 10^{11.4\pm0.4}$ Hz and $\Gamma_{0,2} = 10^{11.1\pm0.7}$ Hz. Both values are in the range expected for hop diffusion on surfaces.[17, 189] For a concerted exchange mechanism, a significantly lower pre-exponential factor would be expected, since two particles have to move at the same time. However, for the sequential exchange mechanism proposed here, equation 5.49 demonstrates why the two pre-exponential factors should be similar. The two factors for the forward and backward reaction in the pre-equilibrium can be assumed to be equal, since both characterize a simple jump of a CO molecule. The overall pre-exponential factor A_{total} is therefore equal to the one of the rate-limiting step A_{react}, i.e., the O diffusion step.

This mechanism is associated with the lowest energy value of all mechanisms tested for the *exchange jump*. The resulting activation barrier of 0.78 eV can be considered in reasonable agreement with the experimentally determined value of 0.63 eV. It is thus concluded that the O/CO exchange occurs in a sequential manner, in which density fluctuations in the CO matrix in the close surrounding of the O atom create pathways along which the O atom can move with comparatively low activation energy.

5.4.5 Results and Discussion: The *door-opening* Mechanism

The diffusion of oxygen atoms through a full $(\sqrt{3} \times \sqrt{3})$R30° layer of CO molecules on the Ru(0001) surface consists of two different types of jumps. One is the local hopping between three hcp sites within the confined area defined by the surrounding CO molecules. The second jump type is an exchange between O and a CO molecule. Local density fluctuations in the CO layer virtually open a door for the oxygen to escape from the confined area around a vacant $(\sqrt{3} \times \sqrt{3})$ position by the creation of low-energy diffusion pathways for the O atom, because of an intermittently reduced O-CO repulsion.

Such a *door-opening* mechanism for diffusion of particles in close-packed surfaces has not been reported so far. Furthermore it has no analog in 3D diffusion. Typically, 3D diffusion in solids is defect-mediated by the participation of vacancies and interstitials.[137] That the diffusion in the system investigated here occurs without participation of vacancies or other defects can be explained by the fact that the surface is not very densely packed. Although the CO layer forms an ordered structure the CO molecules can leave their equilibrium position relatively easily, as was found by the low activation barrier of 0.3 eV for a CO move.

Because of the low barrier in comparison to O diffusion, these fluctuations happen on a much shorter time scale than the O diffusion itself. In the investigated temperature range, these CO movements are thus too fast to be imaged with the STM.

As an example, for the lowest temperature of -39 °C, a hopping barrier of 0.3 eV results in a jump frequency of ~$3.5 \cdot 10^6$ Hz; 100000 times faster than O hopping.

At much lower temperature it should be possible to observe local disorder in the CO layer. In fact STM measurements of submonolayers of CO on Ru(0001) at around -220°C, show arrangements in the ordered $(\sqrt{3} \times \sqrt{3})R30°$ CO structure that can be interpreted in this way. Figure 5.21 a) shows a dark triangle (marked by the white arrow) in the $(\sqrt{3} \times \sqrt{3})R30°$ structure that moved through the island. When the triangle reached the edge of the island in Figure 5.21 b), it vanished and at the same time an additional CO molecule appeared at the rim of the island, see Figure 5.21 c) indicated by the black arrow. These observations point to an interstitial CO molecule in the CO island that corresponds to a denser CO configuration than in the $(\sqrt{3} \times \sqrt{3})R30°$ structure.

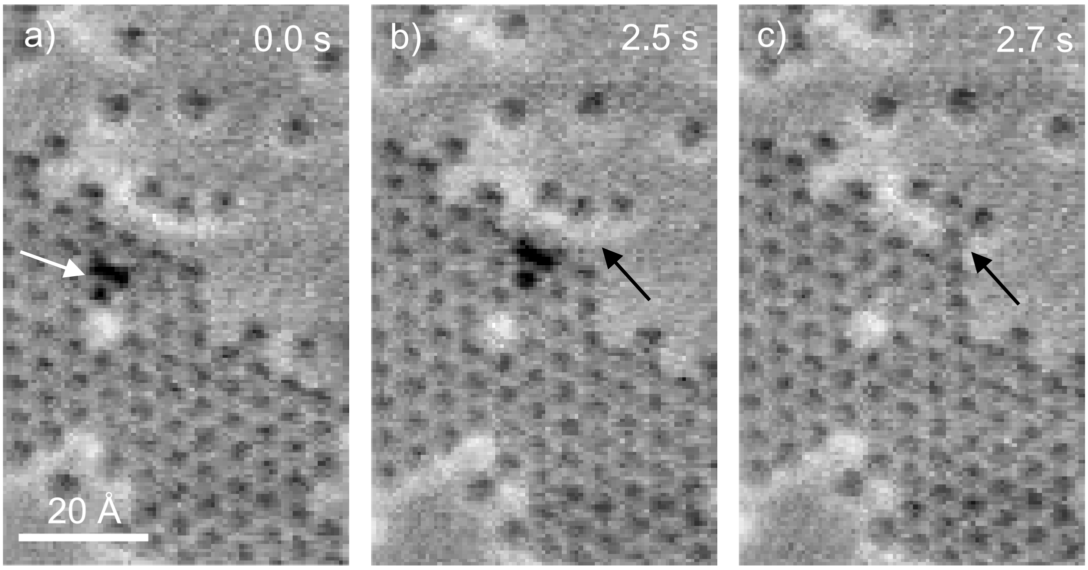

Figure 5.21: STM observations of CO molecules (dark spheres) on Ru(0001) at -220 °C (V_t = -1.68 V, I_t = 3 nA, 10 frames/s). The black arrows mark the same position in b) and c).

To further evaluate the effect of the coadsorbate on the O diffusion, the results for diffusion in CO can be compared to an STM investigation by Renisch *et al.* on the diffusion of O atoms on the bare Ru(0001) surface.[166] At room temperature a hopping frequency of 16.6 Hz was measured. Because at that time no temperature-dependent measurements were possible no data for the activation energy and the pre-exponential factor could be obtained.

Since the hoppings of the O in the confined area around a CO vacancy do not lead to a movement over the surface, the occurrence of *exchange jumps* determines the velocity at which the O travels across the surface. In this work the rate for the *exchange jumps* has been determined to 3.2 Hz at room temperature. To be comparable with the value for O diffusion on the bare Ru(0001) surface, the exchange rate has to be normalized by the number of directions along which the jumps can occur. To perform an exchange with CO the O atom can jump in four directions, whereas on the bare surface it can jump in six directions. If the exchanges were also possible in six directions the rate at which the O atoms leaves its site would therefore be $^6/_4 \cdot 3.2$ Hz = 4.7 Hz. Compared to the value of 16.6 Hz for the hopping frequency on the clean surface this frequency is only by a factor of 3.5 lower, a most surprising result, considering the fact that the O atom has to move through a fully CO-covered surface.

This relatively small decrease of surface mobility can be attributed to two factors. Firstly, the presence of the CO lowers the binding strength of O to the substrate, making the O more mobile in general. Secondly, the fluctuations in the CO layer that act as a door opener are low-energy processes. The effect of site-blocking that was held responsible in literature for the large decrease in mobility in coadsorbate systems is to some extent circumvented by the appearance of the equilibrium fluctuations in the CO layer.

The *door-opening* mechanism might act as general principle for diffusion in mixed adsorbate systems on catalyst surfaces in which one adsorbate is considerably more mobile than the other. Strongly bound particles such as O, N, or C atoms are intermediates in many catalytic reactions and the *door-opening* mechanism may facilitate surface mobility even in a crowded layer of weakly bound coadsorbates.

Rapid diffusion on surfaces ensures the mixing of the reactants on the catalyst's surface, which is relevant for a correct description of the kinetics of heterogeneously catalyzed reactions. Only if the surface mobility is high enough to constantly randomize the particle distribution, the usual neglect of the diffusion process in kinetic analyses may still be justified also in the situation of a crowded adsorbate layer.

5.5 Diffusion of O Atoms on partially CO-covered Ru(0001)

STM experiments on the diffusion of individual O atoms were also performed on an only partially CO-covered Ru(0001) surface. For these experiments, the clean Ru(0001) was first exposed to 0.05 L O_2. In the following step, a lower CO dose than in the experiments discussed in the previous section was used. Instead of 1.0 L, that was sufficient to create a full $(\sqrt{3} \times \sqrt{3})$R30° layer of CO ($\theta$ = 0.33 ML), here dosages between 0.2 and 0.8 L were applied.

5.5.1 STM Observations

Figure 5.22 a) and b) shows two STM images taken from an STM movie acquired at -5 °C. O atoms are again imaged as bright features under the applied tunneling conditions, whereas CO molecules appear dark.

Both images, taken at a time difference of 3.9 s, show the same area of the sample. An O island with the characteristic (2 x 2) periodicity is visible in the lower part of the images. Furthermore both images show several individual O atoms, highlighted by arrows. A part of the Ru surface is covered by the $(\sqrt{3} \times \sqrt{3})$R30° structure of CO, whereas in between no ordered structure is resolved. The STM movies reveal strong fluctuations of the ordered CO areas in accordance with the low hopping barrier for CO on Ru(0001).[194, 195] This high mobility manifests itself in the different forms of the CO islands in the two images shown. It also becomes manifest in the contrast of the $(\sqrt{3} \times \sqrt{3})$R30° islands. The contrast is high in the interior of the islands – dark CO molecules and bright interspaces – and becomes continuously weaker towards the borders of the islands. These contrast variations are a dynamic effect caused by increasing fluctuations of the CO layer at the island edges.

Despite appearing uniform, the areas between the $(\sqrt{3} \times \sqrt{3})$ islands are also covered with CO, as revealed by STM experiments of CO/Ru(0001) at lower temperatures and known from literature.[170] The coverage in these disordered areas is, however, not high enough to form the ordered structure. The disordered CO is very mobile and thus too fast to be imaged with the STM at the prevailing temperature.

The O atoms are predominantly found in these disordered CO areas. Interestingly in a), three dark spots are observed around most of the single O atoms. A closer view of the same situation is provided in Figure 5.22 c). The STM image originates from a dataset acquired at the same temperature as a) and b), but after an additional dosage of 0.2 L CO. Three individual O atoms are visible in the image, all of which show such pronounced three dark spots around them.

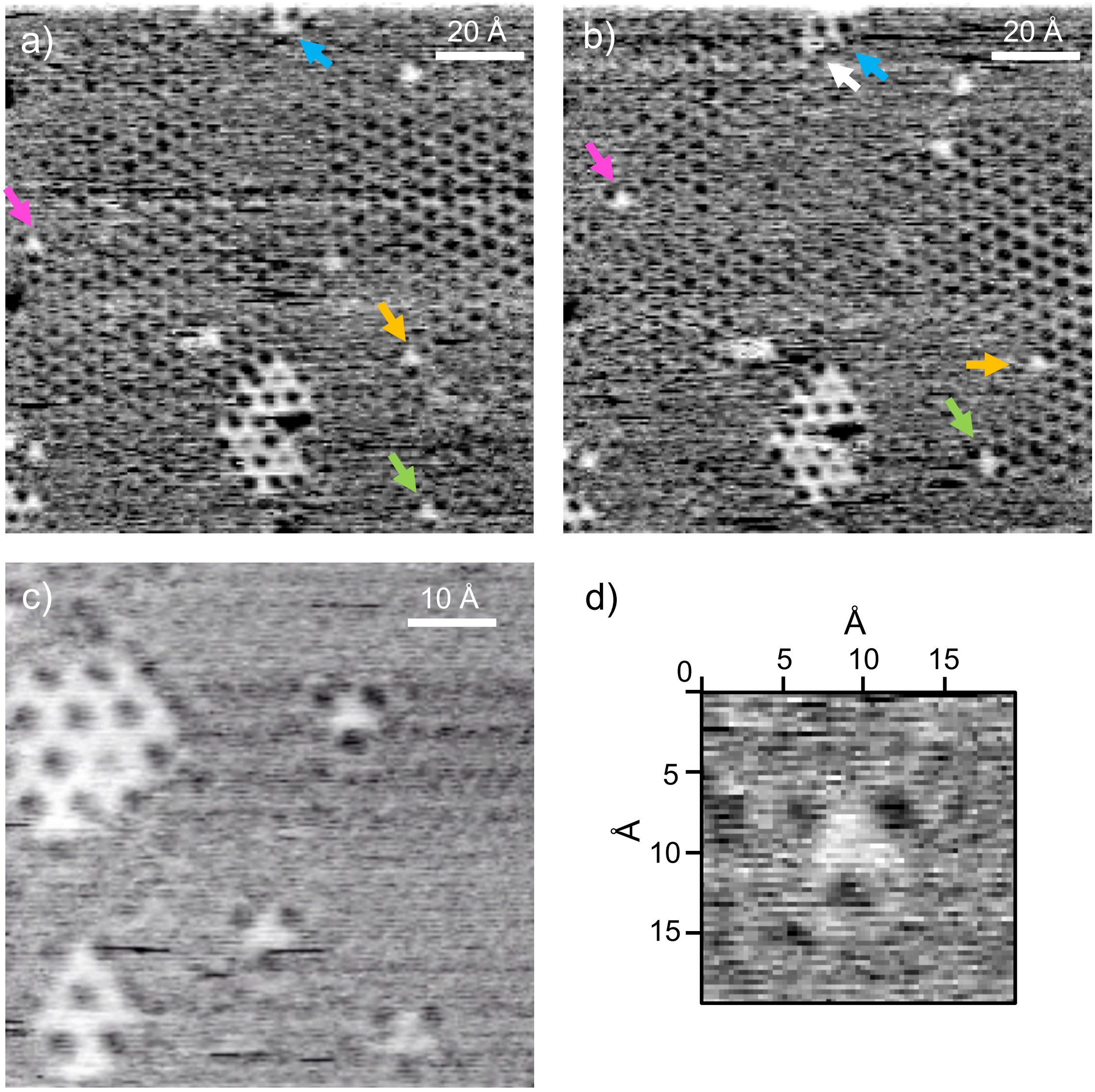

Figure 5.22: Coadsorption of O (bright) and CO (dark) on Ru(0001). a) and b) Two STM images after dosage of 0.05 L O_2 and 0.2 L CO (V_t = -0.6 V, I_t = 3 nA, -5 °C, 10 frames/s). The time difference between the two frames is 3.9 s. Colored arrows highlight the same individual O atoms in both images. c) STM image after dosage of 0.05 L O_2 and 0.4 L CO (V_t = -1.7 V, I_t = 10 nA, -5 °C, 10 frames/s). d) Detail showing a single O atom from the same dataset as c).

Figure 5.22 d) shows a close-up of the triangular structure. The detail is taken from the same STM movie as the image in c). The dark spots form an equilateral triangle around the O with sides oriented along the close-packed directions of the

Ru(0001) surface. The side length is ~6 Å, i.e., approximately two Ru-Ru distances. Such a triangular arrangement of three spherical spots of inverse contrast around an O atom has neither been observed for O on clean Ru(0001),[41, 168, 196] nor for O in the full $(\sqrt{3} \times \sqrt{3})$R30° CO structure.[131]

The cause for these three spots could be an electronic effect. The O atom could alter the *LDOS* of the surrounding surface sites in such a way that they are imaged as depressions. For O on the bare Ru(0001) surface the superposition of the *LDOS* of the oxygen and the surrounding metal atoms leads to a triangular representation of the O atoms.[41, 168, 196] However, a configuration in which the O is surrounded by three relatively sharp spherical spots of inverse contrast has not been reported before. Within this work these structures were observed using different tunneling conditions and in several different measurements when O was coadsorbed with less than 1 L of CO. Moreover, it could be excluded that these features are an imaging artifact of the tip, since the orientation of the triangles changed by 60° from one terrace to the next. [On the (0001) surface the orientation of the hcp sites changes by 60° from one lattice plane to the next.] A sole electronic effect is therefore unlikely.

A second possibility is that the O atom is surrounded by three other adsorbates that seem to move together with the O over the surface. These adsorbates would most likely be CO molecules, as they are imaged similarly to the CO molecules in the $(\sqrt{3} \times \sqrt{3})$ islands. Moreover, when an O atom with its three surrounding adsorbates comes close to a CO island, shifts of the adsorbates around the O can be observed. The colored arrows in Figure 5.22 a) and b) mark the same O atoms in both images. Whereas all O atoms highlighted in a) are surrounded by three black spots, the same O atoms are found in various other configurations in b). The O atoms marked orange and green have approached a CO island in b). The adsorbates around the atom marked green have rearranged to fit to the $(\sqrt{3} \times \sqrt{3})$ structure to the right of the atom. A similar behavior is found for the O atom marked yellow. The O atom marked blue has been approached by a second O atom (white arrow) that came into the imaged area from the top. The close proximity of the two atoms also led to displacements of the surrounding adsorbates resulting in an almost quadratic coordination of the left O atom. The O atom marked by the pink arrow has kept its triangular coordination in both images. In a) it is attached with its lower tip to an ordered CO area, whereas in b) the upper right tip is connected to a $(\sqrt{3} \times \sqrt{3})$R30° island. All of these observations indicate that it is attractive for the adsorbates that accompany the O to incorporate into the $(\sqrt{3} \times \sqrt{3})R30°$ structure, as one would expect for CO molecules.

Further evidence that the O atoms are indeed coordinated by CO molecules comes from the appearance of the O(2 x 2) islands. In Figure 5.22 a) as well as in b) and c), the O islands are similarly surrounded by dark adsorbates like the single O atoms. Each O atom is surrounded by one CO molecule below and two above to the left and to the right. Furthermore, most of the positions in the (2 x 2) islands between the O atoms seem to be occupied by CO as well, as they are imaged comparably dark. This finding is in accordance with the observation of a mixed (2 x 2)-(O+CO) structure in LEED experiments.[181, 182] CO intercalates into the (2 x 2)-O structure when adsorbed on an O pre-covered surface. The CO molecules were found to sit on on-top sites between the O atoms that remained on their favored hcp sites. That some of the positions between the O atoms in the (2 x 2) islands are imaged differently, brighter than the other positions can be explained by the fact that they are unoccupied.

With the assumption that the adsorbates around the O atoms are CO molecules, two models for the observed triangular features around the single O atoms can be proposed, see Figure 5.23. The O atom (red) sits on an hcp position and is surrounded by three CO molecules (blue). The three surrounding CO molecules can either occupy three on-top sites, shown in Figure 5.23 a), or three fcc sites, see Figure 5.23 b). Both configurations lead to an equilateral triangle oriented along the Ru(0001) close-packed directions and display a side length of two Ru lattice constants, as observed in the STM images.

The STM images further reveal that the three CO molecules around the single O atoms are always oriented in the same manner as the O/CO configurations in the O islands. As in the solved structure of the mixed (2 x 2)-(O+CO) phase the CO molecules occupy on-top sites,[181, 182] it is most likely that the CO molecules also occupy on-top sites around the single O atoms. Hence, the adsorption geometry shown in Figure 5.23 a) is the most likely configuration.

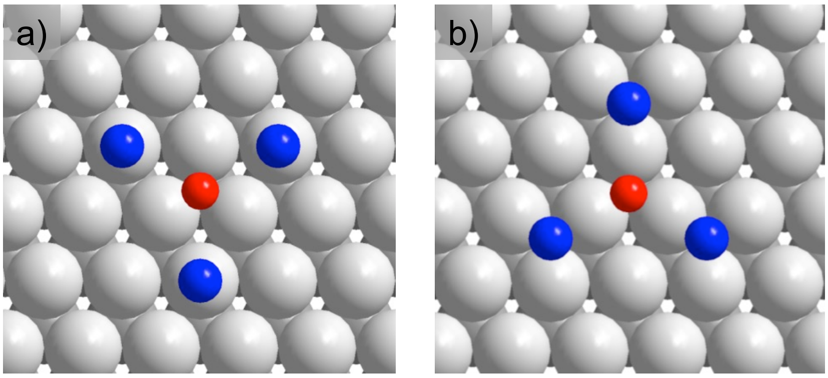

Figure 5.23: Proposed adsorption geometries. The O atom (red) binds to an hcp position on Ru(0001) (gray) and is surrounded by three CO molecules (blue) on on-top positions in a) or on fcc sites in b).

Preliminary DFT calculations by Dr. Sung Sakong (*Ulm University*) confirmed that the observed O/CO configuration is energetically favorable in comparison to similar other configurations. Configurations with CO molecules on on-top positions were always more favorable than with CO on fcc positions. For CO on on-top positions, several configurations were tested as illustrated in Figure 5.24 a). The O atom (red) sits on an hcp position. A neighboring CO molecule can occupy four different on-top sites close to the O atom. The green position corresponds to the experimentally observed configuration. Qualitatively, the energy trend for the different CO positions around the O atom is shown in Figure 5.24 b). The dashed line is only meant to guide the eye. Not surprisingly, the lowest energy is found for an infinite O-CO distance. However, at the finite CO coverages of the experiments this configuration is no longer possible. Hence, the green configuration, which represents a local energy minimum, is adopted.

That the orange position is energetically unfavorable can be explained by the short O-CO distance and the corresponding high repulsion. However, the reason why a CO molecule on the green on-top position is stable, where it is closer to the O atom than on the blue and purple positions is unclear. A direct adsorbate-adsorbate interaction, as well as a substrate mediated effect are possible. Further theoretical investigations are needed to elucidate the nature of this interaction.

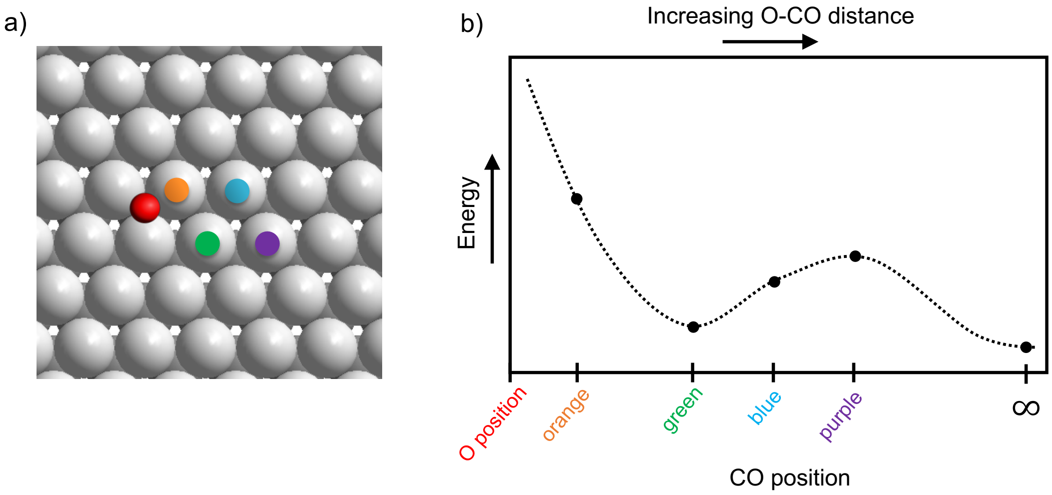

Figure 5.24: O/CO configurations used for DFT calculations. a) CO on-top positions around an O atom on an hcp site are indicated by different colors. b) Qualitative energy trend for the CO positions. Color-code according to CO positions in a).

5.5.2 Diffusion Trajectories

Trajectories of the individual O atoms on a partially CO-covered surface are shown in Figure 5.25. The positions of the O atoms in the individual frames are connected by lines. The trajectories were recorded in an STM measurement at -20 °C. Particle tracking was performed in an analog way as for O diffusion on the $(\sqrt{3} \times \sqrt{3})R30°$ CO-covered surface, compare section 5.4.2.

Instead of the triangular diffusion pattern that was observed for O diffusion in the full $(\sqrt{3} \times \sqrt{3})R30°$ layer (see Figure 5.7), the trajectories show a hexagonal movement of the O atoms over the surface. From the enlarged representation of the two framed trajectories, the distance between two positions of the resulting hexagonal pattern can be estimated to approximately 3 Å, corresponding to one Ru lattice constant. All transitions in the trajectories are oriented along the close-packed directions of the Ru substrate. The movement of the O atoms on the partially CO-covered surface therefore resembles the random walk between nearest-neighbor hcp sites known for O atoms on the clean Ru(0001) surface.[90, 166] Events in which an O atom moves from the disordered area into a $(\sqrt{3} \times \sqrt{3})R30°$ island which would have to go along with a change of the diffusion mechanism were not observed.

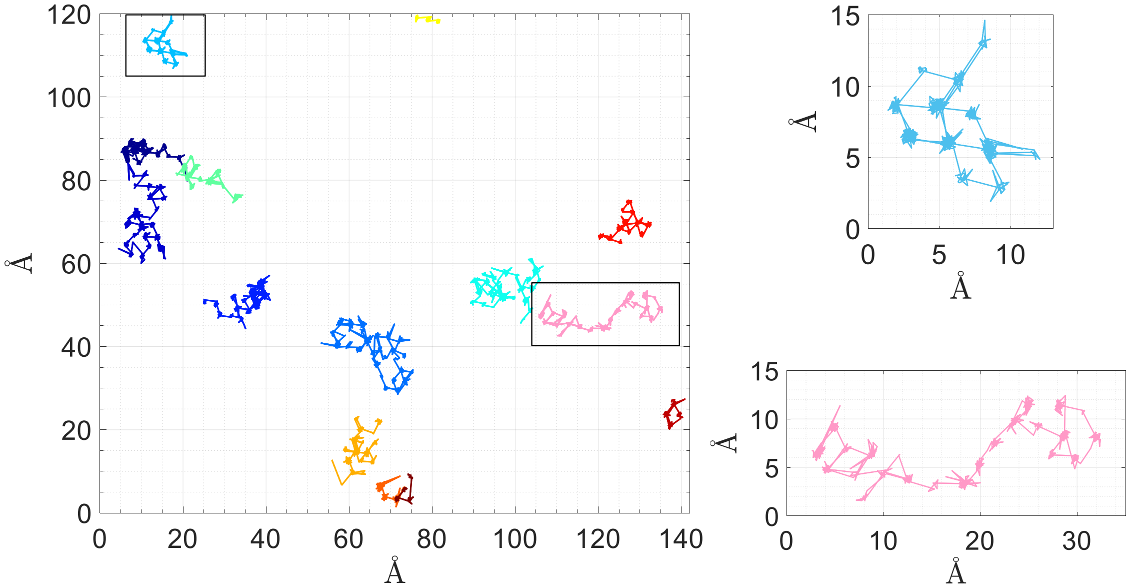

Figure 5.25: Trajectories of O atoms coadsorbed with CO on Ru(0001) for $\theta_{CO} < 0.33$ ML. Different colors represent different trajectories. The framed trajectories are shown enlarged on the right. O positions in the individual STM images are connected by lines.

5.5.3 Results and Discussion

For O coadsorbed with CO on Ru(0001) at $\theta_{CO} < 0.33$ ML, the STM measurements revealed that the O atoms preferably stay in the disordered areas between the ordered CO structure and move by jumps between nearest-neighbor hcp sites. During this movement the O atoms are coordinated by three CO molecules in a triangular configuration, as shown in Figure 5.23 a).

Qualitatively the trajectories display the same random walk pattern as the O atoms on the bare Ru(0001) surface. This surprising independence of the CO matrix can be explained by the fact that the CO molecules are much more mobile in the disordered areas than in the ordered $(\sqrt{3} \times \sqrt{3})$R30° structure. Fluctuations in the disordered layer are expected to be even more facile than in the ordered structure in which a fluctuation is necessarily connected with a small but finite energy increase. The lack of order in the CO layer thus allows the O atoms to move without certain positions being blocked.

From the STM movies it cannot be decided whether the O atom jumps alone or together with the tree surrounding CO molecules. However, a concerted motion of four adsorbates seems unlikely and is associated with a high activation barrier. Exact jump frequencies or activation barriers have not been extracted from these data so far, but it is clear that the hopping frequencies are in the same range as for O diffusion on the clean surface and in the ordered CO structure.[131, 166] A concerted mechanism should lead to significantly reduced jump frequencies and can thus be ruled out. It is much more likely that the coordination by three CO molecules is restored after every jump.

Such configurations in which CO molecules sit on on-top sites with a spacing of two Ru lattice constants to each other and a distance of $2/3 \cdot \sqrt{3} \cdot a_0(\mathrm{Ru})$ to the O atom must be energetically slightly more attractive than other similar O/CO configurations. This was also confirmed by preliminary DFT calculations. The average life time for CO molecules on these positions is thus enhanced and the STM is able to image them. The appearance of the O/CO clusters in this system can therefore be interpreted in the way that the O atom induces a local order in the disordered CO areas.

Figure 5.26 illustrates that the model of the O/CO complex can also explain the processes at the borders of the oxygen islands. Two STM images from the same dataset as the images in Figure 5.22 c) and d) are depicted in Figure 5.26 a) and b). Corresponding structure models that indicate the positions of the individual O atoms and CO molecules are shown in c) and d). CO molecules are only indicated on positions where they are resolved in the STM images.

Figure 5.26 a) shows two single O atoms, both coordinated by three CO molecules. In b) the O atom marked by the green arrow has approached the O island and the adjacent CO island. During this process the coordination by CO molecules changed from the triangular into an almost quadratic configuration, a similar shift of the CO molecules as observed for the individual O atoms in Figure 5.22 a) to b). From the structure models it becomes clear that the CO molecules around the O atom have rearranged in order to fit into the local $(\sqrt{3} \times \sqrt{3})$R30° CO order below the O atom. Obviously, the CO molecules only leave the triangular O/CO configuration in the presence of a stronger driving force, the attractive second nearest-neighbor interactions in the $(\sqrt{3} \times \sqrt{3})$R30°-CO structure.

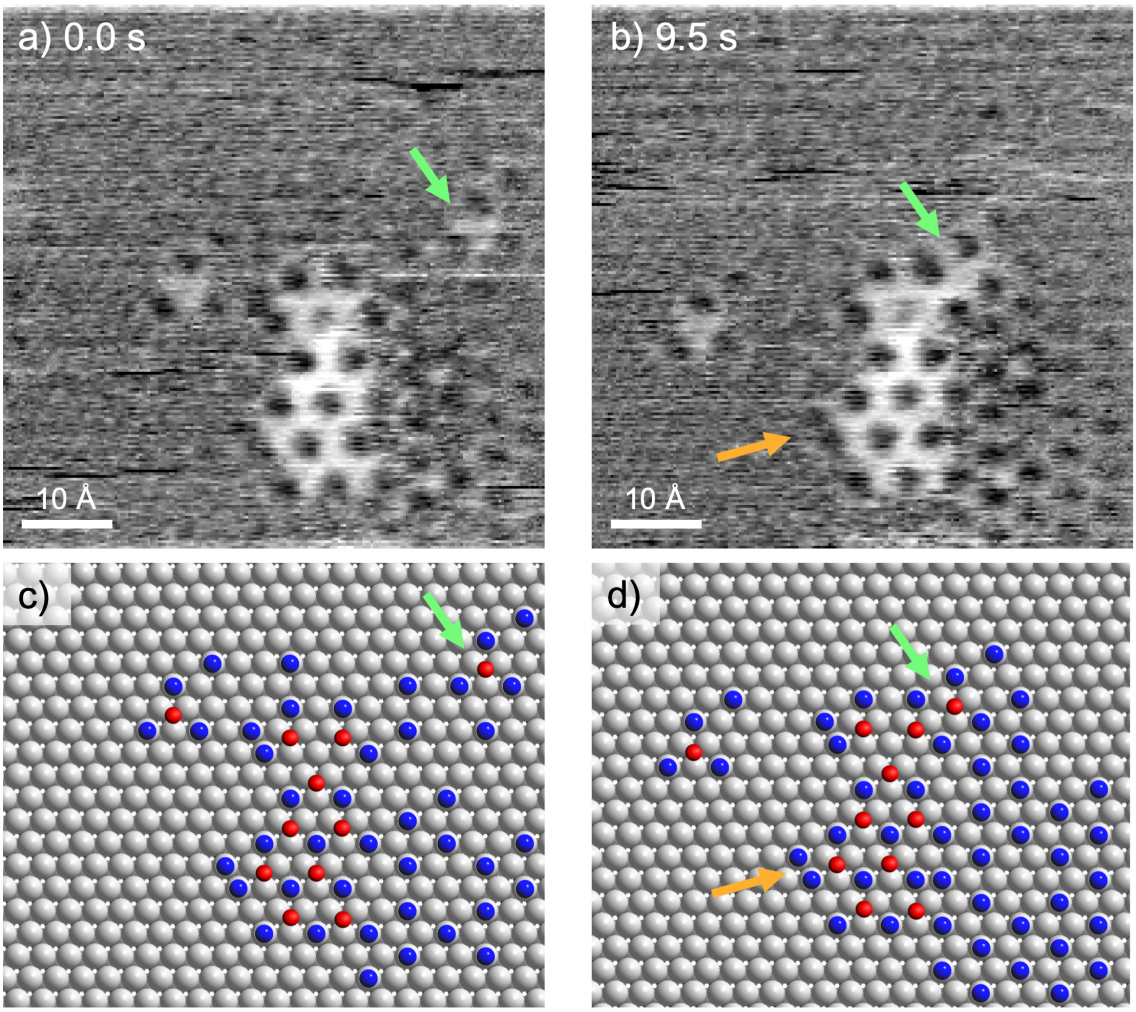

Figure 5.26: Mixed O/CO adsorbate structures. a) and b) STM images taken at -5 °C after dosing of 0.05 L O_2 and 0.4 L CO (V_t = -0.7 V, I_t = 3 nA, 12 frames/s). c) and d) Corresponding adsorption geometries. O atoms are indicated red, CO molecules blue and Ru atoms gray. The green arrow marks the same O atom in a) to d).

However, the structure models in Figure 5.26 c) and d) also suggest the presence of several configurations in which CO molecules sit on neighboring on-top sites. One of these configurations is highlighted by the orange arrow in b) and d). These features could arise either from two CO molecules that sit on adjacent on-top sites or from alternating occupation of both sites by one CO at a speed too fast to be captured by the STM. If the positions were both occupied, the CO molecules would take the energy cost to sit on neighboring on-top sites, just to have both, a ($\sqrt{3}$ x $\sqrt{3}$) CO-CO interaction for one CO molecule and an O/CO triangle in which the other CO participates. In this case it could be deduced that the energy cost for a short CO-CO bond must be less than the energy gain to keep the O/CO triangular structure. If the two positions are alternatingly occupied, the energy gain in the

O/CO configuration must be less than the additional energy needed to form a short CO-CO bond. However, from the STM measurements alone, these two cases cannot be distinguished.

5.6 Diffusion of O Atoms at CO Domain Boundaries

The $(\sqrt{3} \times \sqrt{3})$R30° CO structure has a lower translational symmetry than the Ru(0001) surface and thus forms translational domains even on perfect terraces of the ruthenium surface. As a consequence domain boundaries arise at the interfaces between CO islands.

Diffusion at domain boundaries is of special interest at it can be seen as a 2D analog to grain boundary diffusion in 3D solids. For bulk metals Barnes[197] already noted in 1950 that diffusion rates along grain boundaries are much higher than in the lattice itself. Grain boundaries are thus often termed *high-diffusivity paths*. Diffusion along the boundaries dominates mass transport in many different kinds of solids and therefore also their properties for technological applications, such as thin film applications.[137] It is assumed that enhanced jump rates at grain boundaries are due to an increased concentration of defects, such as interstitials and vacancies, but also concerted moves of several atoms are discussed.[137] However, a detailed understanding of the atomic processes underlying grain boundary diffusion is missing.

In the experiments performed on the O diffusion in the ordered $(\sqrt{3} \times \sqrt{3})$R30° CO structure on Ru(0001), O diffusion at boundaries between two CO domains has been observed. This section presents first results on the adsorption geometry and the diffusion behavior of single O atoms in such domain boundaries.

5.6.1 STM Observations

Figure 5.27 a) shows an STM image from a measurement at -1 °C after dosage of 0.05 L O_2 and 1.0 L CO. Two translational $(\sqrt{3} \times \sqrt{3})$R30° domains of CO (dark spheres) are visible. The domain boundary runs from the middle of the right image edge via the center of the image to the middle of the top edge. The two CO domains are highlighted in red and blue in Figure 5.27 b), the area of the domain boundary is left uncolored. Four single O atoms, imaged as bright features between the CO molecules, are present in the domain boundary.

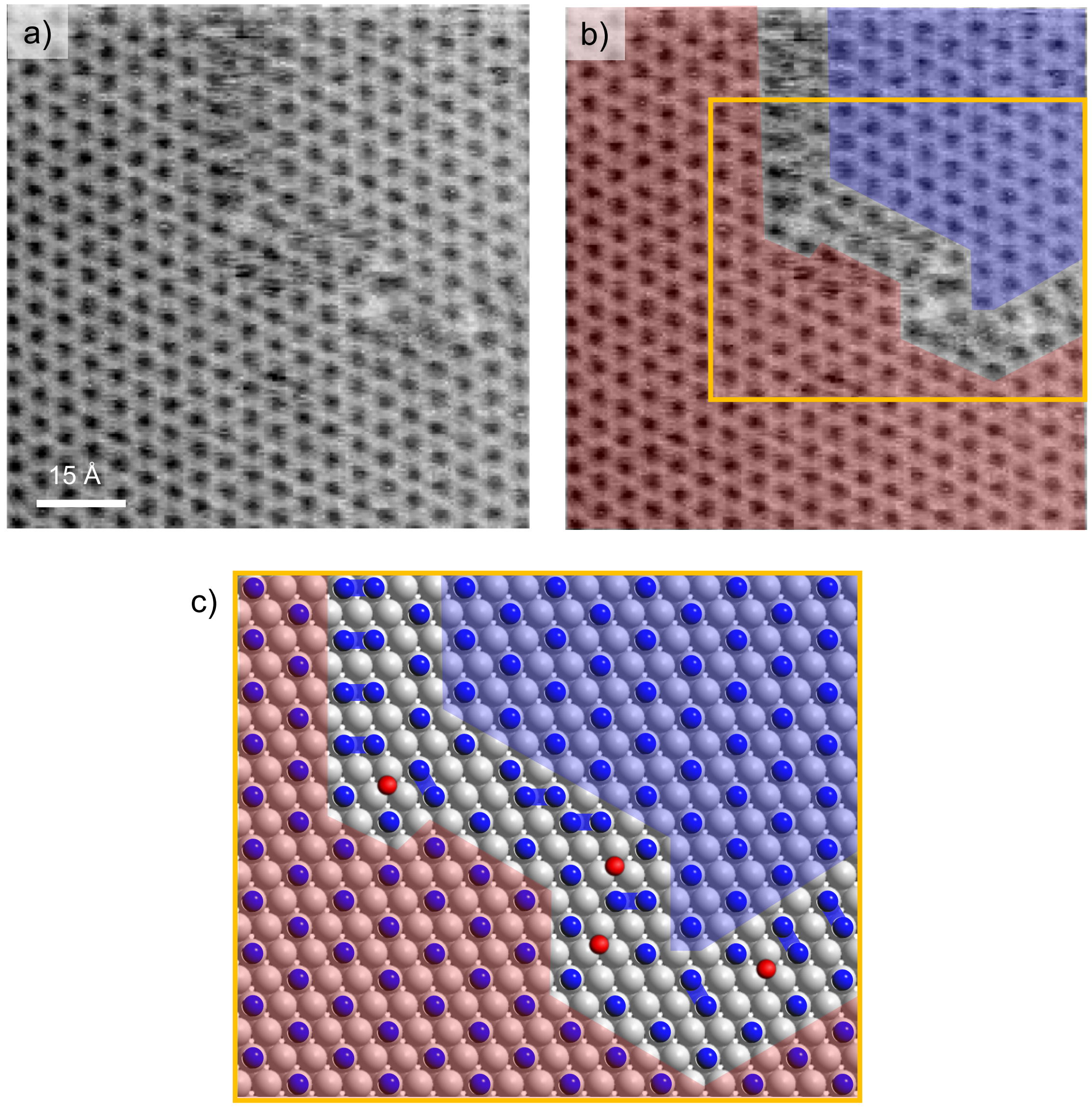

Figure 5.27: O atoms at a domain boundary of the ($\sqrt{3} \times \sqrt{3}$)R30° CO overlayer on Ru(0001). a) STM image showing four single O atoms at the domain boundary (V_t = -0.7 V, I_t = 3 nA, -1 °C, 12 frames/s). b) Same STM image as in a). Different CO domains are highlighted by different colors. c) Model of the adsorption geometry of the part in b) framed orange. CO molecules are depicted in blue, O atoms in red and Ru atoms in gray.

Figure 5.27 c) depicts a model of the domain boundary with the explicit positions of the CO molecules (blue) and O atoms (red) of the framed area in b). CO molecules are assumed to sit on on-top positions and O atoms on hcp sites. Positions for which the STM image shows elongated dark features are represented in the model by two connected CO molecules on neighboring on-top sites. As mentioned in the previous section, these features could either arise from two CO molecules on adjacent on-top sites or from one CO molecule which alternatingly occupies both sites.

As evident from the structure model in c), if both positions are actually occupied by two CO molecules, the resulting grain boundary has a higher CO density than the $(\sqrt{3}\,\mathrm{x}\,\sqrt{3})\mathrm{R}30°$ structure and is termed a *heavy* domain boundary. If the two positions are alternatingly occupied by only one CO molecule, the density of CO molecules is less than in the ordered structure and the boundary would be a *light* domain boundary. For the structure at the upper end and at the right end of the domain boundary, an alternating occupation of the two neighboring sites leads to configurations in which the CO molecules belong either to one or the other $(\sqrt{3}\,\mathrm{x}\,\sqrt{3})\mathrm{R}30°$ domain. Both configurations are thus energetically equal and a hopping of the CO molecule between these positions is expected to be fast, which is in accordance with the idea that one CO molecule could be imaged at both positions. However, the two cases of *light* or *heavy* domain boundary cannot be distinguished from the obtained STM data.

The four single O atoms visible in the area of the STM image sit exclusively at the domain boundary. The closest observed O-CO distance is $2/3 \cdot \sqrt{3} \cdot a_0(\mathrm{Ru})$, the same distance as in the triangular O/CO structures described above. However, no complete O/CO triangles are present. Moreover, no configurations are observed in which O and CO bind to the same Ru atom in accordance with the repulsive nature of such configurations.[130, 131]

5.6.2 Diffusion Trajectories

The two STM images depicted in Figure 5.28 a) and b) show a larger area from the same position as in Figure 5.27. To study the diffusion in the domain boundaries, the four single O atoms, highlighted in Figure 5.28 a) by white arrows, were tracked over 2167 consecutive STM images. Sequences in which the O atoms intermediately interacted with each other were excluded. The resulting drift-corrected trajectories of all O atoms are depicted in Figure 5.28 b) overlaid on the first image of the dataset.

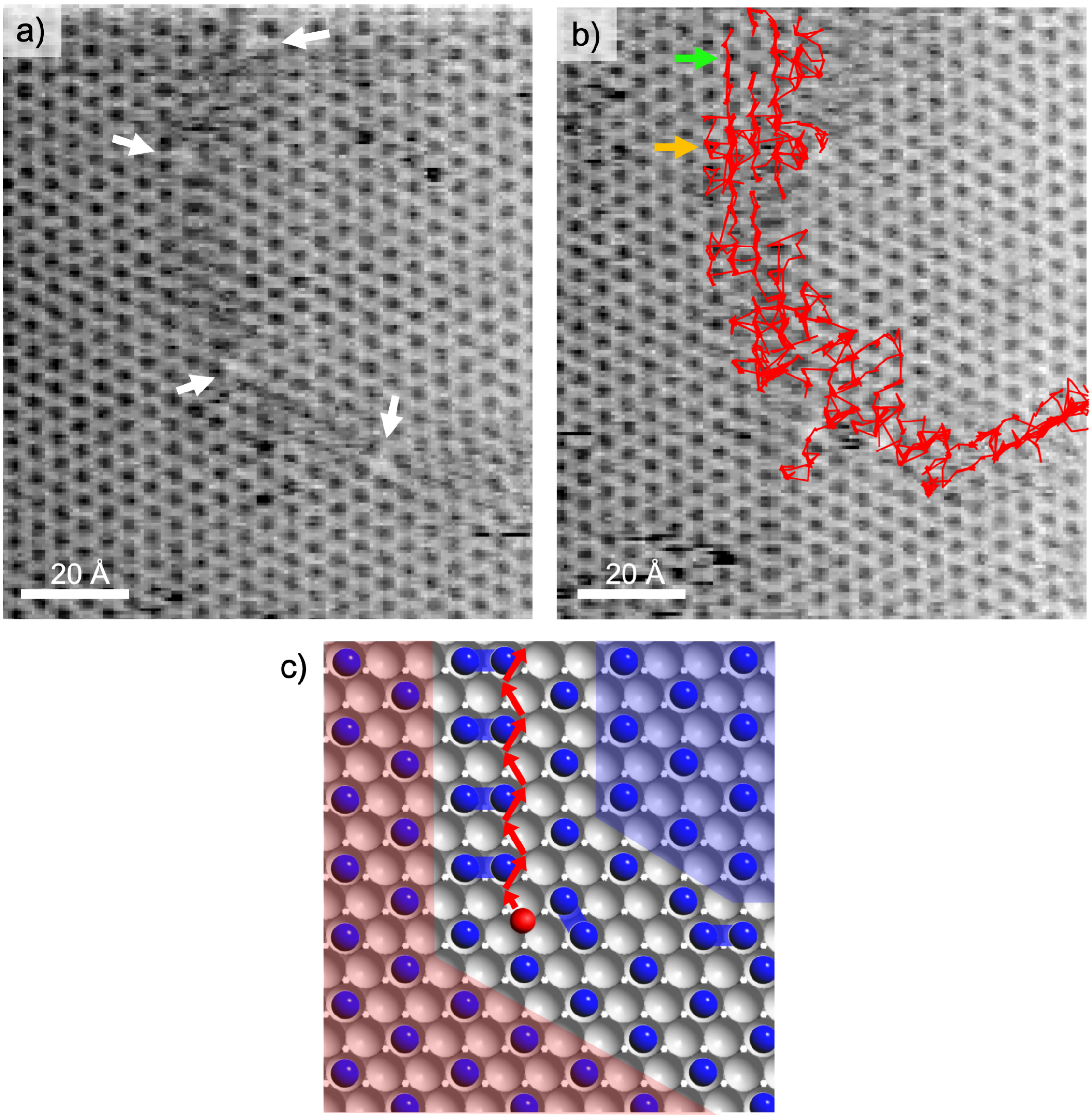

Figure 5.28: O atom diffusion at a domain boundary of the $(\sqrt{3}\ x\ \sqrt{3})R30°$-CO structure on Ru(0001) (V_t = -0.7 V, I_t = 3nA, -1 °C, 12 frames/s). a) Representative STM image showing four single O atoms at the domain boundary, marked by arrows. b) Trajectories of the individual O atoms obtained from 2167 STM images. Trajectories are overlaid the first STM image of the dataset. The positions of the atoms are connected by lines. c) Model of the zig-zag movement between hcp sites in a domain boundary.

The trajectories almost perfectly reproduce the position of the domain boundary, implicating that during the whole observation period the O atoms diffused preferably along the boundary. The most prominent features in the trajectories are longer zig-zag sequences oriented along the direction of the domain boundary. Such sequences are especially well visible in the upper part and at the right edge of Figure 5.28 b). The green arrow indicates one of these sequences in the trajectories. The zig-zag movement can be explained by the hopping of an O atom between nearest-neighbor hcp sites at the boundary. Figure 5.28 c) shows such a zig-zag sequence in the domain boundary model of Figure 5.27 c). If the neighboring (connected) CO positions are alternatingly occupied by one CO molecule, the zig-zag trajectory is a movement between freely available hcp sites in the boundary.

The trajectories are somewhat broader than the disordered CO area at the domain boundary. This fact can be explained by the observation that the domain boundary is highly mobile. Over an observation time of around five minutes, the domain boundary fluctuated by approximately 35 Å around an average position. The width of the trajectories perpendicular to the course of the domain boundary thus does not hint at a movement of the O atoms out of the boundary area, but reflects the dynamic nature of the domain boundary itself.

However, the trajectories also show few examples of transient positions of the O atoms in the ordered CO structure. In these cases, the predominantly linear motion transforms into the triangular movement pattern known from the O diffusion in the $(\sqrt{3} \times \sqrt{3})$R30° structure, compare Figure 5.7. Such an event is marked by the orange arrow to the left of the trajectory in Figure 5.28 b).

5.6.3 Results and Discussion

The STM measurements show that the O atoms preferably stay at the domain boundaries. This fact can be explained as follows: when in the ordered CO structure the O atoms induce a defect in the CO layer by creating a vacancy. However, the order of the CO molecules at the domain boundary is already reduced compared to the $(\sqrt{3} \times \sqrt{3})$R30° structure. Therefore, it appears energetically favorable for the whole system to combine the two “defects,” i.e., the O atoms and the lattice mismatch at the domain boundary, thus preventing a defect in the ordered CO domains. The same effect was discussed in the previous section for the single O atoms on the only partially CO-covered Ru(0001) surface. The O atoms remained in the disordered CO areas rather than penetrating into the $(\sqrt{3} \times \sqrt{3})$R30° islands.

The O trajectories almost perfectly reproduce the shape of the domain boundary, indicating that diffusion along the domain boundary dominates the diffusion process. This fact suggests that the domain boundaries have a lower CO density than the ordered CO structure. In section 5.4 it was shown that for the diffusion of O atoms in a $(\sqrt{3} \times \sqrt{3})$R30° structure of CO, the O/CO repulsion leads to the formation of a CO cage for the O atom. In a perfect CO structure, all diffusion pathways for the O are blocked. It can only escape if one of the CO molecules intermittently leaves its position and makes way for the O atom (*door-opening* mechanism). If the domain boundary was even more dense than the $(\sqrt{3} \times \sqrt{3})R30°$ structure, it can be assumed that the O diffusion along the boundary would be negligible in comparison to diffusion in perpendicular directions. The results discussed here show that the exact opposite is the case: Diffusion along the domain boundary clearly determines the movement of the O atoms.

This finding confirms the notion of domain boundaries as *high-diffusivity paths*. For the system of O atoms in CO on Ru(0001), the enhanced diffusion rates can be ascribed to a reduced CO density and order in the domain boundary in comparison to the $(\sqrt{3} \times \sqrt{3})R30°$ domains. The effect of site-blocking on the O motion is thus decreased in the direction of the domain boundary. In principle the diffusion in the domain boundaries can be understood as a combination of O diffusion of the two above presented systems, diffusion in a full $(\sqrt{3} \times \sqrt{3})R30°$ layer and diffusion on an only partially CO-covered surface. Diffusion along the domain boundary is similar to O diffusion on the only partially CO-covered surface. The O moves in a less dense and more disordered CO environment. In all other directions the surrounding CO molecules are arranged in the $(\sqrt{3} \times \sqrt{3})R30°$ lattice through which the O can only move by the *door-opening* mechanism, leading to a more or less directed motion of the O along the boundaries.

However, a quantitative analysis of the data is still necessary to obtain a complete picture of O mass transport at domain boundaries and to quantitatively confirm higher diffusion rates along the domain boundary.

5.7 Summary

To gain insight into diffusion processes on highly covered transition metal surfaces, the situation in most heterogeneously catalyzed reactions, a mixed adlayer of O and CO on a Ru(0001) surface has been investigated using the video-rate VT-STM setup. The mechanism and kinetics of O diffusion for different coverages of the coadsorbate CO have been studied.

For O diffusion in a full $(\sqrt{3} \times \sqrt{3})R30°$ layer of CO on Ru(0001), STM movies have been acquired between -39 and +29 °C and displacement distributions of the O atoms were extracted with the automated image analysis and particle tracking system. The diffusion process could be modelled with two independent hopping processes: *triangle jumps* in a confined area between three hcp sites in a CO cage and *exchange jumps* with CO molecules. The jump frequencies for both of the two processes showed Arrhenius behavior over the whole temperature range investigated. Activation barriers were determined to 0.57 ± 0.02 eV and 0.63 ± 0.03 eV, respectively. In comparison to the clean Ru(0001) surface, O diffusion in the full CO layer is only moderately slowed down by a factor of 3.5.

Equilibrium fluctuations on the atomic scale in the CO layer were found to occur with an activation energy of only ~0.3 eV. These fluctuations allow the O atom to move through the CO layer, as they intermittently open low-energy pathways for the O. This *door-opening* mechanism for diffusion in a mixed adlayer system has not been reported before and may even be a general phenomenon for diffusion of a relatively strongly bound particle in a coadsorbate layer of more weakly bound particles.

For CO coverages below 0.33 ML, ordered $(\sqrt{3} \times \sqrt{3})$R30° islands alternate with disordered CO areas. O atoms preferably stay in the disordered areas and move by jumps between nearest-neighbor hcp sites like on the bare Ru(0001) surface. The lack of order and thus also the lack of attractive $\sqrt{3}$-CO-CO interactions make the CO molecules more mobile in these disordered areas, so that it can be assumed that the effect of site-blocking on the O diffusion vanishes.

Nevertheless, the presence of the O atoms in the disordered CO areas induces a local order of the CO molecules in their close proximity. O atoms are coordinated by three CO molecules on on-top sites at a O-CO distance of $2/3 \cdot \sqrt{3} \cdot a_0$(Ru). Preliminary DFT results confirm this O/CO configuration as local energy minimum. The reason for this effect remains unclear so far.

First results on the adsorption geometry and diffusion of O atoms at domain boundaries of different translational domains of the $(\sqrt{3} \times \sqrt{3})$R30° CO structure have been presented. Trajectories of individual O atoms mainly follow the domain boundary. Longer zig-zag sequences along the boundary appear as prominent features in the trajectories, a result of the directed motion of the O by jumps between neighboring hcp sites in the boundary region. Diffusion thus primarily occurs along the domain boundaries. Diffusion perpendicular to the domain boundary leads to a transition to the triangular motion pattern known from O diffusion on the fully $(\sqrt{3} \times \sqrt{3})$R30° covered Ru surface.

From the observed diffusion behavior, the density of CO molecules at the domain boundary is assumed to be lower than in the $(\sqrt{3} \times \sqrt{3})$R30° domains. The results furthermore suggest that on a macroscopic scale, surface diffusion of O atoms in a $(\sqrt{3} \times \sqrt{3})$R30° layer of CO on Ru is dominated by diffusion along the domain boundaries. The domain boundaries thus represent a *high-diffusivity path* for the O atoms, as also known for grain boundaries in 3D diffusion processes in solids. The data presented here provide atomic-scale insight into mass transport on such a *high-diffusivity path*.

6. Summary and Outlook

The dynamic behavior of atoms, molecules, and clusters on surfaces plays a vital role in various surface and interface processes, since many surface phenomena, such as growth or dissolution, go along with a structural change of the surface. These processes are governed by mass transport, i.e., the diffusion of single particles on the surface. An atomic-scale comprehension of the underlying diffusion mechanisms is thus relevant to understand macroscopic surface effects. Furthermore, diffusion also plays a crucial role in heterogeneously catalyzed reactions. The movement of the reactants on the catalyst surface has to be rapid compared to the reaction to ensure a permanent and equilibrated mixing of the reactants on the surface. Diffusion thus determines the reactants' ability for reaction.

Most of the techniques for measuring diffusion only give access to diffusion on a macroscopic length scale. Diffusion is thus only treated as a mean-field process and no information on the atomic-scale is gained. On the other hand, techniques that provide atomic resolution do either not include imaging of the surface (atom-tracking STM or tunneling current fluctuation measurements), so that the environment of the diffusing particles remains unknown, or they lack in temporal resolution. Diffusion can only be studied if it is slow enough to be captured. Moreover, observations over a wide temperature range are necessary to determine the kinetics of the process.

In this thesis a variable temperature STM has been upgraded to enable image acquisition at video rate. For this purpose the digital scan control and data acquisition part of the STM setup has been newly designed. A *National Instrument* device has been implemented that serves as interface between the digital and analog part and ensures sufficient conversion rates for fast scanning. The interface is controlled by an *IGOR Pro* software package that has been developed in this work on the basis of an initial version for conventional STM studies by Prof. Dr. Rolf Schuster, *KIT*.

Using the upgraded setup images are scanned in *quasi constant-height* mode in which the tunneling current serves as imaging signal. The vertical feedback is only used to correct for the tilt of the sample and thermal drift. The restriction by the slow feedback controller is thus abandoned. A home-built I/V-converter with a bandwidth of 300 kHz developed by Dr. Joachim Wiechers is used for measurement of the I_t signal, as commercially available amplifiers do not provide sufficiently high bandwidths.

Even though the mechanical eigenfrequencies of the STM setup are in the range of the desired scan frequencies, acquisition with atomic resolution has been realized at scan frequencies up to 5 kHz. The use of a sine wave for scanning in the fast scanning direction as well as a smart design of the scan ramps between two images (scanning in x direction must not be interrupted) allow for measurements close to and even above resonant modes of the STM setup.

The combined setup is capable of acquiring atomically resolved STM images at rates of up to 50 images per second, while the sample temperature at the same time can be varied between -220 °C and +230 °C. The accessible temperature range of the original VT-STM setup is preserved. Conventional “slow” STM measurements have not been restricted by the implementation of the video mode and are still possible with the same resolution and scan ranges as before. The setup is easy to operate as switching between the conventional and the video mode is controlled by the software and does not require any hardware changes. With this combined setup surface processes can be studied with atomic resolution over a wider temperature range than possible before.

STM movies acquired with this setup contain up to several thousand of STM images corresponding to run times of several minutes. In this way, sufficiently large samples of the process of interest can be acquired in a short time. However, the evaluation of these large numbers of images is no longer possible manually. Therefore *MATLAB* routines have been developed to perform an automated image processing and analysis. STM movies are saved as 1D data vectors and are converted into 3D image stacks in the post-processing, followed by a rectification procedure to remove deformations of the images induced by the sinusoidal scan. Particle detection and tracking has been realized in cooperation with M.Sc. Philipp Messer and Prof. Dr. Don Lamb (*LMU* Munich). STM images are decomposed into different levels of resolution by an *à-trous Wavelet transform* and a particle mask for detection is created from the most characteristic decomposition levels. By linking of particle positions in consecutive images and a subsequent drift correction particle trajectories are created from several thousand consecutive images. The analysis routines thus allow to extract information on the surface dynamics from STM measurements, that is, spatially resolved in the sub-Ångström range and temporally resolved on the millisecond timescale.

The video-rate VT-STM setup and the image processing and analysis methods have been used to study the diffusion of individual oxygen atoms on a Ru(0001) surface that is highly covered by CO. This system serves as model system to elucidate the role of diffusion in heterogeneously catalyzed reactions. Whereas diffusion on metal surfaces at close-to-zero coverages is well understood, it has remained an open question how diffusion can occur at high surface coverages, at which particles are closely surrounded by other adsorbates.

For O diffusion in the complete $(\sqrt{3} \times \sqrt{3})$R30° layer of CO molecules, the O atoms are trapped in a confined area defined by the surrounding CO molecules. However, the O atoms can escape from these CO “cages” and move across the CO-covered surface almost as fast as on a completely bare Ru(0001) surface. A detailed study of the diffusion behavior between -39 and +29 °C has revealed a diffusion mechanism that consists of two independent types of jumps of the O atoms, local hoppings in the CO cage and *exchange jumps* with a CO molecule. With the help of complimentary DFT calculations performed by Dr. Sung Sakong and Prof. Dr. Axel Groß (Ulm University) the experimental activation barriers could be interpreted with respect to the underlying diffusion mechanism. Density fluctuations in the CO matrix are found to intermittently open up low-energy diffusion pathways for the O atoms on the highly covered surface. This "*door opening*" takes place so quickly that the movement of the oxygen atoms is only moderately slowed down compared to on the bare surface.

These data provide atomic insight into diffusion in a crowded adsorbate system. The observed *door-opening* mechanism could be of general relevance because the system investigated here is not special: a relatively strongly bound particle, the O atom diffuses in a matrix of a weaker bound coadsorbate. More strongly bound adsorbates, such as C, O, and N atoms, are intermediates in many industrial relevant catalytic reactions, and high coverages of weaker bound coadsorbates, such as CO or H are also quite general.

In the present thesis O diffusion has also been investigated on the only partially CO-covered Ru(0001) surface (θ_{CO} < 0.33 ML) and at domain boundaries of the ordered $(\sqrt{3} \times \sqrt{3})$R30° CO structure. On the partially CO-covered surface, the O atoms move preferably in disordered CO areas by jumps between nearest-neighbor hcp sites, like on the clean Ru(0001) surface. At domain boundaries, the diffusion pathways are along the boundary. The results indicate that also in surface diffusion domain boundaries act as *high-diffusivity pathways* like it is known for grain boundaries in 3D diffusion.

The enhanced temporal resolution of the combined setup has enabled the study of O diffusion over a temperature range of 70 K. In this range, jump frequencies have been determined over five orders of magnitude, unique for STM measurements. In comparison to other atomic-scale techniques for measuring diffusion, such as atom-tracking STM,[54] the present investigations provide complete pictures of the surroundings of the diffusing atoms. Influences of defect sites or interactions with other adsorbates on the surface are directly visible in the images. The presented studies on O diffusion in the disordered areas and in domain boundaries of the CO-covered surface further demonstrate the necessity of knowing the surroundings of the diffusing particle, as the local CO arrangement significantly influences the diffusion behavior of the O atoms.

An interesting experiment for future work would be to increase the surface coverage to above 0.33 ML, the CO coverage in the $(\sqrt{3} \times \sqrt{3})R30°$ structure, and to study how the O diffusion is changed. The $(\sqrt{3} \times \sqrt{3})R30°$ structure of CO investigated here is the densest ordered structure on Ru(0001) that is stable in the temperature range studied. At temperatures below 200 K, two other ordered CO structures are known, a $(2\sqrt{3} \times 2\sqrt{3})R30°$ and a $(5\sqrt{3} \times 5\sqrt{3})R30°$ that correspond to coverages of 0.58 and 0.65 ML. Above 200 K these structures disorder. It might be expected that despite the enhanced surface coverage by CO, the effect of site-blocking may be less pronounced because of the disorder. It would be interesting to investigate whether the O atoms are still as mobile as on the clean Ru(0001) surface or if they get trapped by the surrounding CO.

The developed video-rate VT-STM setup is not limited to diffusion studies. It could also be used to monitor chemical reactions on surfaces or structural changes. Moreover, the video-rate setup is generic and can be attached to other conventional STM systems to speed up measurements. In the working group Wintterlin, the video-rate acquisition system is currently transferred to a high-pressure STM setup. In this combined setup working catalysts can be studied with atomic-resolution and enhanced temporal resolution which may provide insight into the dynamics of catalytic reactions.

References

[1] N. Cabrera, and W.K. Burton, *Crystal growth and surface structure. Part II.* Discussions of the Faraday Society, 1949. **5**(0): p. 40-48.

[2] M. Einax, W. Dieterich, and P. Maass, *Diffusion and Cluster Growth of Binary Alloys on Surfaces*, in *Zeitschrift für Physikalische Chemie*. 2012. p. 355-376.

[3] G.S. Parkinson, Z. Novotny, G. Argentero, M. Schmid, J. Pavelec, R. Kosak, P. Blaha, and U. Diebold, *Carbon monoxide-induced adatom sintering in a Pd–*Fe_3O_4 *model catalyst.* Nature Materials, 2013. **12**: p. 724-728.

[4] F. Besenbacher, F. Jensen, E. Laegsgaard, K. Mortenson, and I. Stensgaard, *Visualization of the dynamics in surface reconstructions.* Journal of Vacuum Science & Technology B: Microelectronics and Nanometer Structures Processing, Measurement, and Phenomena, 1991. **9**(2): p. 874-878.

[5] G.M. Vanacore, M. Zani, M. Bollani, E. Bonera, G. Nicotra, J. Osmond, G. Capellini, G. Isella, and A. Tagliaferri, *Monitoring the kinetic evolution of self-assembled SiGe islands grown by Ge surface thermal diffusion from a local source.* Nanotechnology, 2014. **25**(13): p. 135606.

[6] H. Brune, *Thermal dynamics at surfaces.* Annalen der Physik, 2009. **18**(10-11): p. 675-698.

[7] J.J. Boland, and J.S. Villarrubia, *Formation of Si(111)-(1x1)Cl.* Physical Review B, 1990. **41**(14): p. 9865-9870.

[8] Z. Toroczkai, and E.D. Williams, *Nanoscale Fluctuations at solid surfaces.* Physics Today, 1999. **52**(12): p. 24-28.

[9] F. Rosei, and R. Rosei, *Atomic description of elementary surface processes: diffusion and dynamics.* Surface Science, 2002. **500**(1): p. 395-413.

[10] G. Ertl, H. Knözinger, F. Schüth, and J. Weitkamp, *Handbook of Heterogeneous Catalysis*, ed. G. Ertl, et al. Vol. 2. 2008, Weinheim: WILEY-VHC Verlag GmbH & Co. KGaA.

[11] F. Schüth, *Heterogene Katalyse. Schlüsseltechnologie der chemischen Industrie.* Chemie in unserer Zeit, 2006. **40**(2): p. 92-103.

[12] J.M. Thomas, and W.J. Thomas, *Principles and Practice of Heterogeneous Catalysis*. Vol. 1. 1997, Weinheim: VCH Verlagsgesellschaft mbH.

[13] K. Morgenstern, *Fast scanning tunnelling microscopy as a tool to understand changes on metal surfaces: from nanostructures to single atoms.* physica status solidi (b), 2005. **242**(4): p. 773-796.

[14] T.T. Tsong, *Atomic, molecular and cluster dynamics on flat and stepped surfaces.* Progress in Surface Science, 2000. **64**(3-8): p. 199-209.

[15] T.T. Tsong, *Mechanisms and energetic of atomic processes in surface diffusion.* Physica A: Statistical Mechanics and its Applications, 2005. **357**(2): p. 250-281.

[16] R. Gomer, *Diffusion of adsorbates on metal surfaces.* Reports on Progress in Physics, 1990. **53**(7): p. 917-1002.

[17] J.V. Barth, *Transport of adsorbates at metal surfaces: from thermal migration to hot precursors.* Surface Science Reports, 2000. **40**(3): p. 75-149.

[18] T. Ala-Nissila, R. Ferrando, and S.C. Ying, *Collective and single particle diffusion on surfaces.* Advances in Physics, 2002. **51**(3): p. 949-1078.

[19] M. C. Tringides, *Surface Diffusion: Atomistic and Collective Processes*. Vol. 360. 1997.

[20] T.T. Tsong, *Mechanisms of surface diffusion.* Progress in Surface Science, 2001. **67**(1): p. 235-248.

[21] H.J.W. Zandvliet, B. Poelsema, and B.S. Swartzentruber, *Diffusion on Semiconductor Surfaces.* Physics Today, 2001. **54**(7): p. 40-45.

[22] R. Schaub, E. Wahlström, A. Rønnau, E. Lægsgaard, I. Stensgaard, and F. Besenbacher, *Oxygen-Mediated Diffusion of Oxygen Vacancies on the* TiO_2*(110) Surface.* Science, 2003. **299**(5605): p. 377-379.

[23] M.A. Henderson, *A surface perspective on self-diffusion in rutile* TiO_2*.* Surface Science, 1999. **419**(2): p. 174-187.

[24] U. Diebold, S.-C. Li, and M. Schmid, *Oxide Surface Science.* Annual Review of Physical Chemistry, 2010. **61**(1): p. 129-148.

[25] J. Schoiswohl, G. Kresse, S. Surnev, M. Sock, M.G. Ramsey, and F.P. Netzer, *Planar Vanadium Oxide Clusters: Two-Dimensional Evaporation and Diffusion on Rh(111).* Physical Review Letters, 2004. **92**(20): p. 206103.

[26] E.W. Müller, *Das Feldionenmikroskop.* Zeitschrift für Physik, 1951. **131**(1): p. 136-142.

[27] G. Ehrlich, and F.G. Hudda, *Atomic View of Surface Self-Diffusion: Tungsten on Tungsten.* The Journal of Chemical Physics, 1966. **44**(3): p. 1039-1049.

[28] G. Binnig, H. Rohrer, C. Gerber, and E. Weibel, *Tunneling through a controllable vacuum gap.* Applied Physics Letters, 1982. **40**(2): p. 178-180.

[29] D.D. Dunlap, and C. Bustamante, *Images of single-stranded nucleic acids by scanning tunnelling microscopy.* Nature, 1989. **342**: p. 204-206.

[30] R.J. Driscoll, M.G. Youngquist, and J.D. Baldeschwieler, *Atomic-scale imaging of DNA using scanning tunnelling microscopy.* Nature, 1990. **346**: p. 294-296.

[31] Z. Kun, L. Yan-Feng, J. Shuai-Hua, M. Xucun, C. Xi, and X. Qi-Kun, *Scanning tunneling microscopy studies of topological insulators.* Journal of Physics: Condensed Matter, 2014. **26**(39): p. 394003.

[32] Y. He, J. Kröger, and Y. Wang, *Organic Multilayer Films Studied by Scanning Tunneling Microscopy.* ChemPhysChem, 2017. **18**(5): p. 429-450.

[33] R. Sonnenfeld, and P.K. Hansma, *Atomic-Resolution Microscopy in Water.* Science, 1986. **232**(4747): p. 211-213.

[34] O.M. Magnussen, L. Zitzler, B. Gleich, M.R. Vogt, and R.J. Behm, *In-situ atomic-scale studies of the mechanisms and dynamics of metal dissolution by high-speed STM.* Electrochimica Acta, 2001. **46**(24): p. 3725-3733.

[35] L. Zitzler, B. Gleich, O.M. Magnussen, and R.J. Behm, *Electrochemical Video-STM*, in *Localized In Situ Methods for Investigating Electrochemical Interface*, A.C. Hillier, M. Seo, and S.R. Taylor, Editors. 2000: Proc. Electrochem. Soc. 99-28 p. 29-38.

[36] M. Rößler, P. Geng, and J. Wintterlin, *A high-pressure scanning tunneling microscope for studying heterogeneous catalysis.* Review of Scientific Instruments, 2005. **76**(2): p. 023705.

[37] E. Laegsgaard, L. Österlund, P. Thostrup, P.B. Rasmussen, I. Stensgaard, and F. Besenbacher, *A high-pressure scanning tunneling microscope.* Review of Scientific Instruments, 2001. **72**(9): p. 3537-3542.

[38] F. Besenbacher, J.V. Lauritsen, T.R. Linderoth, E. Lægsgaard, R.T. Vang, and S. Wendt, *Atomic-scale surface science phenomena studied by scanning tunneling microscopy.* Surface Science, 2009. **603**(10): p. 1315-1327.

[39] M. Salmeron, and J. Dunphy, *Chemisorption, diffusion and reactions on surfaces by scanning tunnelling microscopy.* Faraday Discussions, 1996. **105**: p. 151-162.

[40] P. Jiang, X. Bao, and M. Salmeron, *Catalytic Reaction Processes Revealed by Scanning Probe Microscopy.* Accounts of Chemical Research, 2015. **48**(5): p. 1524-1531.

[41] J. Wintterlin, J. Trost, S. Renisch, R. Schuster, T. Zambelli, and G. Ertl, *Real-time STM observations of atomic equilibrium fluctuations in an adsorbate system: O/Ru(0001).* Surface Science, 1997. **394**(1): p. 159-169.

[42] J. Wintterlin, S. Völkening, T.V.W. Janssens, T. Zambelli, and G. Ertl, *Atomic and Macroscopic Reaction Rates of a Surface-Catalyzed Reaction.* Science, 1997. **278**(5345): p. 1931-1934.

[43] C.M. Yim, K.L. Man, X. Xiao, and M.S. Altman, *Low-energy electron microscopy of CO/Pt(111) surface diffusion by nonequilibrium coverage profile evolution.* Physical Review B, 2008. **78**(15): p. 155439.

[44] A. von Oertzen, H.H. Rotermund, and S. Nettesheim, *Diffusion of carbon monoxide and oxygen on Pt(110): experiments performed with the PEEM.* Surface Science, 1994. **311**(3): p. 322-330.

[45] D.A. Mullins, B. Roop, and J.M. White, *Diffusion of coadsorbed CO and D on Ni(100).* Chemical Physics Letters, 1986. **129**(5): p. 511-515.

[46] E.G. Seebauer, and L.D. Schmidt, *Surface diffusion of hydrogen on Pt(111): laser-induced thermal desorption studies.* Chemical Physics Letters, 1986. **123**(1): p. 129-133.

[47] C.H. Mak, A.A. Deckert, and S.M. George, *Effects of coadsorbed carbon monoxide on the surface diffusion of hydrogen on Ru(001).* The Journal of Chemical Physics, 1988. **89**(8): p. 5242-5250.

[48] J.L. Brand, A.A. Deckert, and S.M. George, *Surface diffusion of hydrogen on sulfur-covered Ru(001) surfaces studied using laser-induced thermal desorption.* Surface Science, 1988. **194**(3): p. 457-474.

[49] E.D. Westre, D.E. Brown, J. Kutzner, and S.M. George, *Surface diffusion of carbon monoxide and potassium coadsorbed on Ru(001): Confirmation of a 1:1 CO:K trapping interaction.* The Journal of Chemical Physics, 1996. **104**(18): p. 7313-7324.

[50] X.-D. Xiao, Y. Xie, C. Jakobsen, H. Galloway, M. Salmeron, and Y.R. Shen, *Impurity Effect on Surface Diffusion: CO/S/Ni(110).* Physical Review Letters, 1995. **74**(19): p. 3860-3863.

[51] W. Zhao, and M. Asscher, *Coverage grating template for the study of surface diffusion: K coadsorbed with CO on Re(001).* Surface Science, 1999. **429**(1): p. 1-13.

[52] B.S. Swartzentruber, *Direct Measurement of Surface Diffusion Using Atom-Tracking Scanning Tunneling Microscopy.* Physical Review Letters, 1996. **76**(3): p. 459-462.

[53] M.L. Grant, B.S. Swartzentruber, N.C. Bartelt, and J.B. Hannon, *Diffusion Kinetics in the Pd/Cu(001) Surface Alloy.* Physical Review Letters, 2001. **86**(20): p. 4588-4591.

[54] K. Wang, C. Zhang, M.M.T. Loy, and X. Xiao, *Time-Dependent Tunneling Spectroscopy for Studying Surface Diffusion Confined in Nanostructures.* Physical Review Letters, 2005. **94**(3): p. 036103.

[55] K. Wang, F. Ming, Q. Huang, X. Zhang, and X. Xiao, *Study of CO diffusion on stepped Pt(111) surface by scanning tunneling microscopy.* Surface Science, 2010. **604**(3): p. 322-326.

[56] S. Amirmehdi, P. Bene, and J.W.Z. Harold, *Study of dynamic processes on semiconductor surfaces using time-resolved scanning tunneling microscopy.* Journal of Physics: Condensed Matter, 2010. **22**(26): p. 264007.

[57] A. Bryant, D.P.E. Smith, and C.F. Quate, *Imaging in real time with the tunneling microscope.* Applied Physics Letters, 1986. **48**(13): p. 832-834.

[58] M.J. Rost, L. Crama, P. Schakel, E.v. Tol, G.B.E.M.v. Velzen-Williams, C.F. Overgauw, H.t. Horst, H. Dekker, B. Okhuijsen, M. Seynen, A. Vijftigschild, P. Han, A.J. Katan, K. Schoots, R. Schumm, W.v. Loo, T.H. Oosterkamp, and J.W.M. Frenken, *Scanning probe microscopes go video rate and beyond.* Review of Scientific Instruments, 2005. **76**(5): p. 053710.

[59] F. Esch, C. Dri, A. Spessot, C. Africh, G. Cautero, D. Giuressi, R. Sergo, R. Tommasini, and G. Comelli, *The FAST module: An add-on unit for driving commercial scanning probe microscopes at video rate and beyond.* Review of Scientific Instruments, 2011. **82**(5): p. 053702.

[60] P. Read, and M.-P. Meyer, *Restoration of Motion Picture Film*. Vol. 1. 2000, Oxford: Butterworth-Heinemann.

[61] O. Custance, S. Brochard, I. Brihuega, E. Artacho, J.M. Soler, A. M. Baró, and J.M. Gómez-Rodríguez, *Single adatom adsorption and diffusion on Si(111)-7x7 surfaces: Scanning tunneling microscopy and first-principles calculations.* Physical Review B, 2003. **67**(23): p. 235410.

[62] S. Kuck, J. Wienhausen, G. Hoffmann, and R. Wiesendanger, *A versatile variable-temperature scanning tunneling microscope for molecular growth.* Review of Scientific Instruments, 2008. **79**(8): p. 083903.

[63] F. Besenbacher, E. Lægsgaard, and I. Stensgaard, *Fast-scanning STM studies.* Materials Today, 2005. **8**(5): p. 26-30.

[64] J.-C. Olivo-Marin, *Extraction of spots in biological images using multiscale products.* Pattern Recognition, 2002. **35**(9): p. 1989-1996.

[65] T. Engel, and G. Ertl, *Elementary Steps in the Catalytic Oxidation of Carbon Monoxide on Platinum Metals*, in *Advances in Catalysis*, D.D. Eley, H. Pines, and P.B. Weez, Editors. 1979, Academic Press. p. 1-78.

[66] C. Zhang, P. Hu, and A. Alavi, *A General Mechanism for CO Oxidation on Close-Packed Transition Metal Surfaces.* Journal of the American Chemical Society, 1999. **121**(34): p. 7931-7932.

[67] F.M. Hoffmann, M.D. Weisel, and C.H.F. Peden, *In-situ FT-IRAS study of the CO oxidation reaction over Ru(001): II. Coadsorption of carbon monoxide and oxygen.* Surface Science, 1991. **253**(1): p. 59-71.

[68] Ž. Šljivančanin, and B. Hammer, *CO oxidation on fully oxygen covered Ru(0001): Role of step edges.* Physical Review B, 2010. **81**(12): p. 121413.

[69] C.H. Bartholomew, and R.J. Farrauto, *Fundamentals of Industrial Catalytic Processes*, in *Fundamentals of Industrial Catalytic Processes*, C.H. Bartholomew and R.J. Farrauto, Editors. 2010, John Wiley & Sons.

[70] C. Gerber, G. Binnig, H. Fuchs, O. Marti, and H. Rohrer, *Scanning tunneling microscope combined with a scanning electron microscope.* Review of Scientific Instruments, 1986. **57**(2): p. 221-224.

[71] B. Diaconescu, G. Nenchev, J.d.l. Figuera, and K. Pohl, *An ultrahigh vacuum fast-scanning and variable temperature scanning tunneling microscope for large scale imaging.* Review of Scientific Instruments, 2007. **78**(10): p. 103701.

[72] C.Y. Nakakura, V.M. Phanse, G. Zheng, G. Bannon, E.I. Altman, and K.P. Lee, *A high-speed variable-temperature ultrahigh vacuum scanning tunneling microscope.* Review of Scientific Instruments, 1998. **69**(9): p. 3251-3258.

[73] L. Petersen, M. Schunack, B. Schaefer, T.R. Linderoth, P.B. Rasmussen, P.T. Sprunger, E. Laegsgaard, I. Stensgaard, and F. Besenbacher, *A fast-scanning, low- and variable-temperature scanning tunneling microscope.* Review of Scientific Instruments, 2001. **72**(2): p. 1438-1444.

[74] L. Kuipers, R.W.M. Loos, H. Neerings, J.t. Horst, G.J. Ruwiel, A.P.d. Jongh, and J.W.M. Frenken, *Design and performance of a high-temperature, high-speed scanning tunneling microscope.* Review of Scientific Instruments, 1995. **66**(9): p. 4557-4565.

[75] *LPM Video Rate SPM Control Electronics*. 2019 [cited 2019 10.06.2019]; Available from: http://www.leidenprobemicroscopy.com.

[76] J. Tersoff, and D.R. Hamann, *Theory and Application for the Scanning Tunneling Microscope.* Physical Review Letters, 1983. **50**(25): p. 1998-2001.

[77] J. Tersoff, and D.R. Hamann, *Theory of the scanning tunneling microscope.* Physical Review B, 1985. **31**(2): p. 805-813.

[78] K. Besocke, *An easily operable scanning tunneling microscope.* Surface Science, 1987. **181**(1): p. 145-153.

[79] J. Frohn, J.F. Wolf, K. Besocke, and M. Teske, *Coarse tip distance adjustment and positioner for a scanning tunneling microscope.* Review of Scientific Instruments, 1989. **60**(6): p. 1200-1201.

[80] Z.Q. Yu, C.M. Wang, Y. Du, S. Thevuthasan, and I. Lyubinetsky, *Reproducible tip fabrication and cleaning for UHV STM.* Ultramicroscopy, 2008. **108**(9): p. 873-877.

[81] J. Wiechers, *Entwicklung eines Rastertunnelmikroskops für elektrochemische Anwendungen und "in-situ" Untersuchungen zur Struktur einer Goldelektroden-Oberfläche*, Diplomarbeit, Berlin, 1988.

[82] J. Wiechers, *Aufbau eines Ultrahochvakuum-Rasterkraftmikroskops und erste Messungen an oxidischen Proben*, Dissertation, Berlin, 1993.

[83] S. Behler, M.K. Rose, D.F. Ogletree, and M. Salmeron, *Method to characterize the vibrational response of a beetle type scanning tunneling microscope.* Review of Scientific Instruments, 1997. **68**(1): p. 124-128.

[84] M.H. Jericho, D.C. Dahn, and B.L. Blackford, *Scanning tunneling microscope with micrometer approach and thermal compensation.* Review of Scientific Instruments, 1987. **58**(8): p. 1349-1352.

[85] S. Günther, *Mikroskopische Aspekte beim Wachstum dünner Metallfilme*, Dissertation, Ulm, 1995.

[86] W. Demtröder, *Mechanics and Thermodynamics*. Undergraduate Lecture Notes in Physics, ed. N. Ashby, et al. Vol. 1. 2017: Springer International Publishing AG.

[87] H. Merk, P. Messer, M.A. Ardelt, D.C. Lamb, S. Zahler, R. Müller, A.M. Vollmar, and J. Pachmayr, *Inhibition of the V-ATPase by Archazolid A: A New Strategy to Inhibit EMT.* Molecular Cancer Therapeutics, 2017. **16**(11): p. 2329-2339.

[88] V. Baumgärtel, S. Ivanchenko, A. Dupont, M. Sergeev, P.W. Wiseman, H.-G. Kräusslich, C. Bräuchle, B. Müller, and D.C. Lamb, *Live-cell visualization of dynamics of HIV budding site interactions with an ESCRT component.* Nature Cell Biology, 2011. **13**: p. 469-474.

[89] M.J.J. Jak, C. Konstapel, A. van Kreuningen, J. Verhoeven, R. van Gastel, and J.W.M. Frenken, *Automated detection of particles, clusters and islands in scanning probe microscopy images.* Surface Science, 2001. **494**(2): p. 43-52.

[90] S. Renisch, *Zur Diffusion adsorbierter Teilchen auf Einkristalloberflächen: Dynamische Untersuchungen mit dem Rastertunnelmikroskop*, Dissertation, Berlin, 1999.

[91] P. Goupillaud, A. Grossmann, and J. Morlet, *Cycle-octave and related transforms in seismic signal analysis.* Geoexploration, 1984. **23**(1): p. 85-102.

[92] K.S. Anant, and F.U. Dowla, *Wavelet transform methods for phase identification in three-component seismograms.* Bulletin of the Seismological Society of America, 1997. **87**(6): p. 1598-1612.

[93] O.G. Lockwood, and H. Kanamori, *Wavelet analysis of the seismograms of the 2004 Sumatra-Andaman earthquake and its application to tsunami early warning.* Geochemistry, Geophysics, Geosystems, 2006. **7**(9): p. 2006GC001272.

[94] M. Beenamol, S. Prabavathy, and J. Mohanalin, *Wavelet based seismic signal de-noising using Shannon and Tsallis entropy.* Computers & Mathematics with Applications, 2012. **64**(11): p. 3580-3593.

[95] J. Bergh, F. Ekstedt, and M. Lindberg, *Wavelets mit Anwendungen in Signal- und Bildverarbeitung*. Vol. 1. 2007, Berlin Heidelberg: Springer.

[96] S.G. Mallat, *A theory for multiresolution signal decomposition: the wavelet representation.* IEEE Transactions on Pattern Analysis and Machine Intelligence, 1989. **11**(7): p. 674-693.

[97] I. Daubechies, *Ten Lectures on Wavelets*. 1992, Philadelphia, USA: SIAM.

[98] A. Haar, *Zur Theorie der orthogonalen Funktionensysteme.* Mathematische Annalen, 1910. **69**(3): p. 331-371.

[99] A. Haar, *Zur Theorie der orthogonalen Funktionensysteme.* Mathematische Annalen, 1911. **71**(1): p. 38-53.

[100] Y. Xu, J.B. Weaver, D.M. Healy, and J. Lu, *Wavelet transform domain filters: a spatially selective noise filtration technique.* IEEE Transactions on Image Processing, 1994. **3**(6): p. 747-758.

[101] F. Murtagh, and J.-L. Starck, *Image processing through multiscale analysis and measurement noise modeling.* Statistics and Computing, 2000. **10**(2): p. 95-103.

[102] J.-L. Starck, F. Murtagii, and A. Bijaoui, *Multiresolution Support Applied to Image Filtering and Restoration.* Graphical Models and Image Processing, 1995. **57**(5): p. 420-431.

[103] C. Christopoulos, A. Skodras, and T. Ebrahimi, *The JPEG2000 still image coding system: an overview.* IEEE Transactions on Consumer Electronics, 2000. **46**(4): p. 1103-1127.

[104] B. Münch, P. Trtik, F. Marone, and M. Stampanoni, *Stripe and ring artifact removal with combined wavelet-Fourier filtering.* Optics Express, 2009. **17**(10): p. 8567-8591.

[105] B.M. Sadler, and A. Swami, *Analysis of multiscale products for step detection and estimation.* IEEE Transactions on Information Theory, 1999. **45**(3): p. 1043-1051.

[106] T. Zambelli, J. Trost, J. Wintterlin, and G. Ertl, *Diffusion and Atomic Hopping of N Atoms on Ru(0001) Studied by Scanning Tunneling Microscopy.* Physical Review Letters, 1996. **76**(5): p. 795-798.

[107] T. Gritsch, *Oberflächenstrukturen, Strukturumwandlungsprozesse und Adsorbate auf Pt(110) und Au(110) — Eine STM Untersuchung*, Dissertation, Berlin, 1990.

[108] S. Marchini, S. Günther, and J. Wintterlin, *Scanning tunneling microscopy of graphene on Ru(0001).* Physical Review B, 2007. **76**(7): p. 075429.

[109] L. Davis, N. MacDonald, P. Palmberg, G. Riach, and R. Weber, *Handbook of Auger electron spectroscopy*. Vol. 2. 1978: Physical Electronics Industries, Inc.

[110] T.E. Madey, H. Albert Engelhardt, and D. Menzel, *Adsorption of oxygen and oxidation of CO on the ruthenium (001) surface.* Surface Science, 1975. **48**(2): p. 304-328.

[111] L. Surnev, G. Rangelov, and G. Bliznakov, *Interaction of oxygen with a Ru(001) surface.* Surface Science, 1985. **159**(2): p. 299-310.

[112] M. Henzler, and W. Göpel, *Oberflächenphysik des Festkörpers*. 1991, Stuttgart, Germany: B.G. Teubner.

[113] Isabellenhütte Heusler GmbH & Co. KG. *Datasheet A-Copper 11*. 2014 [cited 2019 21.02.2019]; Available from: https://www.isabellenhuette.de/fileadmin/Daten/Praezisionslegierungen/Datenblaetter_Thermo/Englisch/A-COPPER_11.pdf.

[114] G. Ertl, and J. Küppers, *Low Energy Electrons and Surface Chemistry.* Zeitschrift für Chemie, 1975. **15**(12): p. 499-500.

[115] D.W. Goodman, and J.M. White, *Measurement of active carbon on ruthenium (110): Relevance to catalytic methanation.* Surface Science, 1979. **90**(1): p. 201-203.

[116] M.J. van Staden, and J.P. Roux, *The superposition of carbon and ruthenium auger spectra.* Applied Surface Science, 1990. **44**(4): p. 259-262.

[117] L. Davis, N. MacDonald, P. Palmberg, G. Riach, and R. Weber, *Handbook of Auger electron spectroscopy*. Vol. 1. 1976: Physical Electronics Industries, Inc.

[118] G. Ertl, and J. Küppers, *Low Energy Electrons and Surface Chemistry*. Vol. 2. 1985, Weinheim: VCH.

[119] C.H. Mak, B.G. Koehler, J.L. Brand, and S.M. George, *Surface diffusion of hydrogen on carbon-covered Ru(001) surfaces studied using laser-induced thermal desorption.* The Journal of Chemical Physics, 1987. **87**(4): p. 2340-2345.

[120] Y. Song, and R. Gomer, *Diffusion of CO on the Mo(110) plane.* Surface Science, 1993. **295**(1): p. 174-182.

[121] S. Horch, H.T. Lorensen, S. Helveg, E. Lægsgaard, I. Stensgaard, K.W. Jacobsen, J.K. Nørskov, and F. Besenbacher, *Enhancement of surface self-diffusion of platinum atoms by adsorbed hydrogen.* Nature, 1999. **398**: p. 134-136.

[122] W.L. Ling, N.C. Bartelt, K. Pohl, J. de la Figuera, R.Q. Hwang, and K.F. McCarty, *Enhanced Self-Diffusion on Cu(111) by Trace Amounts of S: Chemical-Reaction-Limited Kinetics.* Physical Review Letters, 2004. **93**(16): p. 166101.

[123] D.-J. Liu, and J.W. Evans, *Chemical diffusion of CO in mixed CO+O adlayers and reaction-front propagation in CO oxidation on Pd(100).* The Journal of Chemical Physics, 2006. **125**(5): p. 054709.

[124] D.-J. Liu, and J.W. Evans, *Realistic multisite lattice-gas modeling and KMC simulation of catalytic surface reactions: Kinetics and multiscale spatial behavior for CO-oxidation on metal (100) surfaces.* Progress in Surface Science, 2013. **88**(4): p. 393-521.

[125] R. van Gastel, E. Somfai, W. van Saarloos, and J.W.M. Frenken, *A giant atomic slide puzzle.* Nature, 2000. **408**(6813): p. 665.

[126] R. van Gastel, E. Somfai, S.B. van Albada, W. van Saarloos, and J.W.M. Frenken, *Nothing Moves a Surface: Vacancy Mediated Surface Diffusion.* Physical Review Letters, 2001. **86**(8): p. 1562-1565.

[127] M.-F. Hsieh, D.-S. Lin, and S.-F. Tsay, *Possibility of direct exchange diffusion of hydrogen on the Cl/Si(100)-2x1 surface.* Physical Review B, 2009. **80**(4): p. 045304.

[128] B. Rahn, R. Wen, L. Deuchler, J. Stremme, A. Franke, E. Pehlke, and O.M. Magnussen, *Coadsorbate-Induced Reversal of Solid-Liquid Interface Dynamics.* Angewandte Chemie International Edition, 2018. **57**(21): p. 6065-6068.

[129] C.T. Campbell, G. Ertl, H. Kuipers, and J. Segner, *A molecular beam investigation of the interactions of CO with a Pt(111) surface.* Surface Science, 1981. **107**(1): p. 207-219.

[130] C.J. Zhang, P. Hu, and A. Alavi, *A density functional theory study of CO oxidation on Ru(0001) at low coverage.* The Journal of Chemical Physics, 2000. **112**(23): p. 10564-10570.

[131] A.-K. Henß, S. Sakong, P.K. Messer, J. Wiechers, R. Schuster, D.C. Lamb, A. Groß, and J. Wintterlin, *Density fluctuations as door-opener for diffusion on crowded surfaces.* Science, 2019. **363**(6428): p. 715-718.

[132] A. Fick, *Ueber Diffusion.* Annalen der Physik, 1855. **170**(1): p. 59-86.

[133] A. Einstein, *Über die von der molekularkinetischen Theorie der Wärme geforderte Bewegung von in ruhenden Flüssigkeiten suspendierten Teilchen.* Annalen der Physik, 1905. **322**(8): p. 549-560.

[134] H. Ibach, *Physics of Surfaces and Interfaces*. Vol. 1. 2006, Berlin Heidelberg: Springer-Verlag.

[135] H. Eyring, *The Activated Complex in Chemical Reactions.* The Journal of Chemical Physics, 1935. **3**(2): p. 107-115.

[136] P.W. Atkins, and J. de Paula, *Physikalische Chemie*. Vol. 4. 2006: Wiley-VCH.

[137] H. Mehrer, *Diffusion in Solids*. 1 ed. 2007, Berlin Heidelberg: Springer-Verlag.

[138] J.W.M. Frenken, R. van Gastel, S.B. van Albada, E. Somfai, and W. van Saarloos, *Diffusion in a surface: the atomic slide puzzle.* Applied Physics A: Materials Science & Processing, 2002. **75**(1): p. 11-15.

[139] T. Siahaan, O. Kurnosikov, H.J.M. Swagten, B. Koopmans, S.V. Kolesnikov, A.M. Saletsky, and A.L. Klavsyuk, *Co diffusion in the near-surface region of Cu.* Physical Review B, 2016. **94**(19): p. 195435.

[140] R. van Gastel, R. Van Moere, H.J.W. Zandvliet, and B. Poelsema, *Vacancy-mediated diffusion of Co atoms embedded in Cu(001).* Surface Science, 2011. **605**(23): p. 1956-1961.

[141] T. Flores, S. Junghans, and M. Wuttig, *Atomic mechanisms for the diffusion of Mn atoms incorporated in the Cu(100) surface: an STM study.* Surface Science, 1997. **371**(1): p. 1-13.

[142] M.L. Anderson, M.J. D'Amato, P.J. Feibelman, and B.S. Swartzentruber, *Vacancy-Mediated and Exchange Diffusion in a Pb/Cu(111) Surface Alloy: Concurrent Diffusion on Two Length Scales.* Physical Review Letters, 2003. **90**(12): p. 126102.

[143] M.J.A.M. Brummelhuis, and H.J. Hilhorst, *Single-vacancy induced motion of a tracer particle in a two-dimensional lattice gas.* Journal of Statistical Physics, 1988. **53**(1): p. 249-278.

[144] E. Somfai, R. van Gastel, S.B. van Albada, W. van Saarloos, and J.W.M. Frenken, *Vacancy diffusion in the Cu(001) surface II: Random walk theory.* Surface Science, 2002. **521**(1): p. 26-33.

[145] R. van Gastel, E. Somfai, S.B. van Albada, W. van Saarloos, and J.W.M. Frenken, *Vacancy diffusion in the Cu(001) surface I: an STM study.* Surface Science, 2002. **521**(1): p. 10-25.

[146] D.W. Bassett, and P.R. Webber, *Diffusion of single adatoms of platinum, iridium and gold on platinum surfaces.* Surface Science, 1978. **70**(1): p. 520-531.

[147] J.D. Wrigley, and G. Ehrlich, *Surface Diffusion by an Atomic Exchange Mechanism.* Physical Review Letters, 1980. **44**(10): p. 661-663.

[148] G.L. Kellogg, and P.J. Feibelman, *Surface self-diffusion on Pt(001) by an atomic exchange mechanism.* Physical Review Letters, 1990. **64**(26): p. 3143-3146.

[149] C. Chen, and T.T. Tsong, *Displacement distribution and atomic jump direction in diffusion of Ir atoms on the Ir(001) surface.* Physical Review Letters, 1990. **64**(26): p. 3147-3150.

[150] A. Friedl, O. Schütz, and K. Müller, *Self-diffusion on iridium (100). A structure investigation by field-ion microscopy.* Surface Science, 1992. **266**(1): p. 24-29.

[151] T.-Y. Fu, and T.T. Tsong, *Structure and diffusion of small Ir and Rh clusters on Ir(001) surfaces.* Surface Science, 1999. **421**(1): p. 157-166.

[152] T.T. Tsong, and C.-L. Chen, *Atomic replacement and vacancy formation and annihilation on iridium surfaces.* Nature, 1992. **355**: p. 328-331.

[153] G.L. Kellogg, *Surface diffusion of Pt adatoms on Ni surfaces.* Surface Science, 1992. **266**(1): p. 18-23.

[154] B.D. Yu, and M. Scheffler, *Physical origin of exchange diffusion on fcc(100) metal surfaces.* Physical Review B, 1997. **56**(24): p. R15569-R15572.

[155] K.D. Dobbs, and D.J. Doren, *Dynamics of molecular surface diffusion: Origins and consequences of long jumps.* The Journal of Chemical Physics, 1992. **97**(5): p. 3722-3735.

[156] G. Antczak, and G. Ehrlich, *Jump processes in surface diffusion.* Surface Science Reports, 2007. **62**(2): p. 39-61.

[157] D.C. Senft, *Atomic jump lengths in surface diffusion: experiment and theory.* Applied Surface Science, 1996. **94-95**: p. 231-237.

[158] M. Lindroos, H. Pfnür, G. Held, and D. Menzel, *Adsorbate induced reconstruction by strong chemisorption: Ru(001)p(2×2)-O.* Surface Science, 1989. **222**(2): p. 451-463.

[159] C. Stampfl, and M. Scheffler, *Theoretical study of O adlayers on Ru(0001).* Physical Review B, 1996. **54**(4): p. 2868-2872.

[160] A.B. Anderson, and M.K. Awad, *Binding of Ru, O, and* RuO_n *(n=1–4) to the Ru(001) surface: Structures, stabilities, and diffusion barriers.* Surface Science, 1987. **183**(1): p. 289-301.

[161] J.A. Herron, S. Tonelli, and M. Mavrikakis, *Atomic and molecular adsorption on Ru(0001).* Surface Science, 2013. **614**: p. 64-74.

[162] H. Pfnür, G. Held, M. Lindroos, and D. Menzel, *Oxygen induced reconstruction of a close-packed surface: A LEED IV study on Ru(001)-p(2x1)O.* Surface Science, 1989. **220**(1): p. 43-58.

[163] S.L. Parrott, G. Praline, B.E. Koel, J.M. White, and T.N. Taylor, *Oxygen chemisorption on a stepped Ru (~001) crystal.* 1979. **71**(8): p. 3352-3354.

[164] K. Meinel, H. Wolter, A. Ch, A. Beckmann, and H. Neddermeyer, *Adsorption stages of O on Ru(0001) studied by means of scanning tunnelling microscopy.* Journal of Physics: Condensed Matter, 1997. **9**(22): p. 4611-4619.

[165] Y. Tison, K. Nielsen, D.J. Mowbray, L. Bech, C. Holse, F. Calle-Vallejo, K. Andersen, J.J. Mortensen, K.W. Jacobsen, and J.H. Nielsen, *Scanning Tunneling Microscopy Evidence for the Dissociation of Carbon Monoxide on Ruthenium Steps.* The Journal of Physical Chemistry C, 2012. **116**(27): p. 14350-14359.

[166] S. Renisch, R. Schuster, J. Wintterlin, and G. Ertl, *Dynamics of Adatom Motion under the Influence of Mutual Interactions: O/Ru(0001).* Physical Review Letters, 1999. **82**(19): p. 3839-3842.

[167] J. Wintterlin, *Struktur und Reaktivität einer Metalloberfläche - eine Untersuchung mit dem Rastertunnelmikroskop am System Al(111)/Sauerstoff*, Dissertation, 1988.

[168] C. Corriol, F. Calleja, A. Arnau, J.J. Hinarejos, A.L. Vázquez de Parga, W.A. Hofer, and R. Miranda, *Role of surface geometry and electronic structure in STM images of O/Ru(0001).* Chemical Physics Letters, 2005. **405**(1–3): p. 131-135.

[169] E.D. Williams, and W.H. Weinberg, *The geometric structure of carbon monoxide chemisorbed on the ruthenium (001) surface at low temperatures.* Surface Science, 1979. **82**(1): p. 93-101.

[170] H. Pfnür, and D. Menzel, *Lateral interactions for CO/Ru(001): Order-disorder transitions of the* $\sqrt{3}$ *structure.* Surface Science, 1984. **148**(2): p. 411-438.

[171] H. Pfnür, D. Menzel, F.M. Hoffmann, A. Ortega, and A.M. Bradshaw, *High resolution vibrational spectroscopy of CO on Ru(001): The importance of lateral interactions.* Surface Science, 1980. **93**(2): p. 431-452.

[172] G. Michalk, W. Moritz, H. Pfnür, and D. Menzel, *A LEED determination of the structures of Ru(001) and of CO/Ru(001)*$-\sqrt{3}x\sqrt{3}$ *R30°.* Surface Science, 1983. **129**(1): p. 92-106.

[173] P. Piercy, P.A. Heimann, G. Michalk, and D. Menzel, *Structure determination by diffuse LEED of disordered CO adsorbed on Ru(001) at low coverages.* Surface Science, 1989. **219**(1): p. 189-205.

[174] G.E. Thomas, and W.H. Weinberg, *High resolution electron energy loss spectroscopy of chemisorbed carbon monoxide and oxygen on the ruthenium(001) surface.* The Journal of Chemical Physics, 1979. **70**(2): p. 954-961.

[175] H. Pfnür, P. Feulner, and D. Menzel, *The influence of adsorbate interactions on kinetics and equilibrium for CO on Ru(001). II. Desorption kinetics and equilibrium.* The Journal of Chemical Physics, 1983. **79**(9): p. 4613-4623.

[176] T.E. Madey, and D. Menzel, *Adsorption of CO on (001) Ruthenium at Temperatures* $\geq$ *300 K.* Japanese Journal of Applied Physics, 1974. **13**(S2): p. 229-235.

[177] G.E. Thomas, and W.H. Weinberg, *The vibrational spectrum and adsorption site of CO on the Ru(001) surface.* The Journal of Chemical Physics, 1979. **70**(3): p. 1437-1439.

[178] J.J. Mortensen, Y. Morikawa, B. Hammer, and J.K. Nørskov, *A Comparison of* N_2 *and CO Adsorption on Ru(001)*, in *Zeitschrift für Physikalische Chemie*. 1997. p. 113-122.

[179] C. Stampfl, and M. Scheffler, *Energy barriers and chemical properties in the coadsorption of carbon monoxide and oxygen on Ru(0001).* Physical Review B, 2002. **65**(15): p. 155417.

[180] J.-S. McEwen, and A. Eichler, *Phase diagram and adsorption-desorption kinetics of CO on Ru(0001) from first principles.* The Journal of Chemical Physics, 2007. **126**(9): p. 094701.

[181] B. Narloch, G. Held, and D. Menzel, *A LEED-IV determination of the Ru(001)-p(2×2)(O+CO) structure: A coadsorbate-induced molecular tilt.* Surface Science, 1995. **340**(1): p. 159-171.

[182] K.L. Kostov, H. Rauscher, and D. Menzel, *Adsorption of CO on oxygen-covered Ru(001).* Surface Science, 1992. **278**(1): p. 62-86.

[183] B. Hammer, *Coverage dependence of* N_2 *dissociation at an N, O, or H precovered Ru(0001) surface investigated with density functional theory.* Physical Review B, 2001. **63**(20): p. 205423.

[184] J.C. Fuggle, E. Umbach, P. Feulner, and D. Menzel, *Electron induced dissociation of CO on Ru(001): A study by thermal desorption and electron spectroscopies.* Surface Science, 1977. **64**(1): p. 69-84.

[185] G. Ehrlich, *Atomic Displacements in One- and Two-Dimensional Diffusion.* The Journal of Chemical Physics, 1966. **44**(3): p. 1050-1055.

[186] K. Levenberg, *A Method for the Solution of Certain Problems in Least-Squares.* Quarterly Applied Mathematics 2, 1944: p. 164-168.

[187] D.W. Marquardt, *An Algorithm for Least-Squares Estimation of Nonlinear Parameters.* 1963. **11**(2): p. 431-441.

[188] J.J. Moré. *The Levenberg-Marquardt algorithm: Implementation and theory.* 1978. Berlin, Heidelberg: Springer Berlin Heidelberg.

[189] V.P. Zhdanov, *Arrhenius parameters for rate processes on solid surfaces.* Surface Science Reports, 1991. **12**(5): p. 185-242.

[190] P. Zhao, Y. He, D.-B. Cao, X. Wen, H. Xiang, Y.-W. Li, J. Wang, and H. Jiao, *High coverage adsorption and co-adsorption of CO and H_2 on Ru(0001) from DFT and thermodynamics.* Physical Chemistry Chemical Physics, 2015. **17**(29): p. 19446-19456.

[191] P.J. Feibelman, B. Hammer, J.K. Nørskov, F. Wagner, M. Scheffler, R. Stumpf, R. Watwe, and J. Dumesic, *The CO/Pt(111) Puzzle.* The Journal of Physical Chemistry B, 2001. **105**(18): p. 4018-4025.

[192] B. Hammer, and J.K. Norskov, *Why gold is the noblest of all the metals.* Nature, 1995. **376**(6537): p. 238-240.

[193] M. Bonn, S. Funk, C. Hess, D.N. Denzler, C. Stampfl, M. Scheffler, M. Wolf, and G. Ertl, *Phonon- Versus Electron-Mediated Desorption and Oxidation of CO on Ru(0001).* Science, 1999. **285**(5430): p. 1042-1045.

[194] Z.-N. Chen, L. Shen, M. Yang, G. Fu, and H. Hu, *Enhanced Ab Initio Molecular Dynamics Simulation of the Temperature-Dependent Thermodynamics for the Diffusion of Carbon Monoxide on Ru(0001) Surface.* The Journal of Physical Chemistry C, 2015. **119**(47): p. 26422-26428.

[195] A.A. Deckert, J.L. Brand, M.V. Arena, and S.M. George, *Surface diffusion of carbon monoxide on Ru(001) studied using laser-induced thermal desorption.* Surface Science, 1989. **208**(3): p. 441-462.

[196] F. Calleja, A. Arnau, J.J. Hinarejos, A.L. Vázquez de Parga, W.A. Hofer, P.M. Echenique, and R. Miranda, *Contrast Reversal and Shape Changes of Atomic Adsorbates Measured with Scanning Tunneling Microscopy.* Physical Review Letters, 2004. **92**(20): p. 206101.

[197] R.S. Barnes, *Diffusion of Copper along the Grain Boundaries of Nickel.* Nature, 1950. **166**(4233): p. 1032-1033.

[198] J. Bialek. *IBWread.m: Igor Pro file format (ibw) to matlab variable*. Copyright (c) 2009, Jakub Bialek. All rights reserved., **2009**.

[199] G. Kresse, and J. Furthmüller, *Efficient iterative schemes for ab initio total-energy calculations using a plane-wave basis set.* Physical Review B, 1996. **54**(16): p. 11169-11186.

[200] B. Hammer, L.B. Hansen, and J.K. Nørskov, *Improved adsorption energetics within density-functional theory using revised Perdew-Burke-Ernzerhof functionals.* Physical Review B, 1999. **59**(11): p. 7413-7421.

[201] S. Grimme, J. Antony, S. Ehrlich, and H. Krieg, *A consistent and accurate ab initio parametrization of density functional dispersion correction (DFT-D) for the 94 elements H-Pu.* The Journal of Chemical Physics, 2010. **132**(15): p. 154104.

[202] S. Grimme, *Density functional theory with London dispersion corrections.* Wiley Interdisciplinary Reviews: Computational Molecular Science, 2011. **1**(2): p. 211-228.

[203] G. Henkelman, and H. Jónsson, *Improved tangent estimate in the nudged elastic band method for finding minimum energy paths and saddle points.* The Journal of Chemical Physics, 2000. **113**(22): p. 9978-9985.

[204] G. Henkelman, B.P. Uberuaga, and H. Jónsson, *A climbing image nudged elastic band method for finding saddle points and minimum energy paths.* The Journal of Chemical Physics, 2000. **113**(22): p. 9901-9904.

Appendix A Abbreviations and Symbols

A.1 Abbreviations

Abbreviation	**Meaning**
1D	One-Dimensional
2D	Two-Dimensional
2NN	Second Nearest-Neighbor
3D	Three-Dimensional
AAAS	American Association for the Advancement of Science
AES	Auger Electron Spectroscopy
ADC	Analog-to-Digital Converter
AI	Analog Input
AO	Analog Output
DAC	Digital-to-Analog Converter
DAQ device	Data Acquisition Device
DFT	Density Functional Theory
fcc	Face-Centered-Cubic
FHI	Fritz-Haber-Institute
FIFO	First-In First-Out
FIM	Field Ion Microscopy
FT	Fourier Transform
FPGA	Field Programmable Gate Array

Abbreviation	**Meaning**
GUI	Graphical User Interface
hcp	Hexagonal-Close-Packed
ibw	Igor Binary Wave
KIT	Karlsruhe Institute of Technology
LEED	Low Energy Electron Diffraction
LMU	Ludwig-Maximilians-Universität
ML	Monolayer
MSD	Mean-Square Displacement
NN	Nearest-Neighbor
PC	Personal Computer
PES	Potential Energy Surface
RAM	Random Access Memory
ST-FT	Short-Time Fourier Transform
STM	Scanning Tunneling Microscopy
TDS	Thermal Desorption Spectroscopy
TS	Transition State
TST	Transition State Theory
TTL	Transistor-Transistor-Logic
Video-STM	Video-Rate Scanning Tunneling Microscopy
UHV	Ultra-High Vacuum
VT-STM	Variable Temperature Scanning Tunneling Microscopy
WT	Wavelet Transform

A.2 Symbols

Symbol	Meaning
A_i	Low-Pass Approximation at Scale *i*
a	Coordinate on the (1 x 1) Ru lattice
a_0	Lattice Constant
b	Coordinate on the (1 x 1) Ru lattice
a'	Rotated Coordinate
b'	Rotated Coordinate
Γ	Jump Frequency
Γ_0	"Attempt Frequency"; Pre-exponential Factor
c	Concentration
D	Diffusion Constant
e	Elementary Charge
E^*	Activation Energy
E_d^*	Activation Energy for Diffusion
E_F	Fermi Energy
E_{kin}	Kinetic Energy
E_{Vac}	Energy of the Vacuum Level
f	Scan Frequency
h_{filter}	Filter kernel
h_i	Filter at scale *i*
h	Planck Constant
$\hbar$	Reduced Planck Constant
I_t	Tunneling Current
J	Lowest Resolution Level in the *à-trous* WT decomposition
J_p	Flux of Diffusing Particles
κ	Decay Length

Symbol	Meaning
κ_t	Transmission Coefficient
k	Rate Constant
K	Equilibrium Constant
k_B	*Boltzmann* Constant
λ	Lattice Constant
$LDOS$	Local Density of States
M	Rotation Matrix
m_e	Electron Mass
ν	Frequency
n_1	Number of *triangle jumps*
n_2	Number of *exchange jumps*
n_{frames}	Number of Frames
n_{int}	Number of Intervals
n_{jump}	Number of Jumps
n_{Perm}	Number of Permutations
N_i^t	Number of *Time Pixels* for *Space Pixel i*
φ_{eff}	Effective Tunneling Barrier
φ_{sample}	Work Function of the Sample
φ_{tip}	Work Function of the Tip
$P(x,y)$	Particle Mask
$\tilde{p}_{t_0}(n_1,n_2)$	Probability for the combination of n_1 *triangle* and n_2 *exchange jumps* in time interval t_0
$p_{t_0}(a,b)$	Probability to find a particle at position (a,b) after t_0
pos	Position A,B, or C in the Triangles
q	Partition Function
R	Ideal Gas Constant
$\langle r^2 \rangle$	Mean-square displacement

Symbol	**Meaning**
$\bar{\sigma}_i$	Mean Absolute Deviation on Scale *i*
σ_i^{noise}	Standard Deviation of the Noisy Coefficients at Scale *i*
s	Tip-Sample distance
θ	Coverage
T	Temperature
t	Time
t_0	Time Interval
t_i	Threshold at Scale *i*
t_{int}	Interval Length
tW_i	Filtered Wavelet Plane at Scale *i*
τ	Life Time
V_t	Tunneling Voltage
W_i	Wavelet Plane at Scale *i*
w_{n_1,n_2}	Geometric Factor for n_1 *triangle* and n_2 *exchange jumps*
x	Direction/Position along the *x*-axis
$\langle x^2 \rangle$	Mean-square displacement in *x* direction
y	Direction/Position along the *y*-axis
Y_1, Y_2	Coordinates on the $(\sqrt{3}$ x $\sqrt{3})$R30° CO lattice
$\langle y^2 \rangle$	Mean-square displacement in *y* direction
z	Direction/Position along the *z*-axis
Z_{av}	Number of Measurements for one Pixel
Δz	Height variation of the tip

Appendix B STM Data

B.1 Overview of STM Data in Chapter 2

Table B.1: List of STM data used in Figure 2.11

File	Frame	Pixel	Nominal Range [Å]	Scan frequency [Hz]	V_t [V]	I_t [nA]	T [°C]	T [K]
170705_4	1047	200	100	2000	-0.22	10	27	300

Table B.2: List of STM data used in Figure 2.12

File	Frame	Pixel	Nominal Range [Å]	Scan frequency [Hz]	V_t [V]	I_t [nA]	T [°C]	T [K]
170705_4	1047	200	100	2000	-0.22	10	27	300

Table B.3: List of STM data used in Figure 2.13

File	Frame	Pixel	Nominal Range [Å]	Scan frequency [Hz]	V_t [V]	I_t [nA]	T [°C]	T [K]
170705_4	1	200	100	2000	-0.22	10	27	300
170705_4	2	200	100	2000	-0.22	10	27	300

Table B.4: List of STM data used in Figure 2.15

Scan frequency [Hz]	File	Frame	Pixel	Nominal Range [Å]	V_t [V]	I_t [nA]	T [°C]	T [K]
600	171130_12	2813	200	100	-0.55	3	-34	239
1000	171128_19	311	200	100	-0.22	3	-32	241
2000	171128_20	596	200	100	-0.22	3	-32	241
2400	170710_58	213	200	50	-0.70	3	0	273
3000	171206_29	4348	150	50	-0.60	3	7	280
3300	170710_59	332	150	30	-0.70	3	0	273
5000	170710_37	3625	100	30	-0.70	10	1	274
5000	170630_21	400	100	20	-0.22	3	25	298

B.2 Overview of STM Data in Chapter 3

Table B.5: List of STM data used in Figure 3.1

File	Frame	Pixel	Nominal Range [Å]	Scan frequency [Hz]	V_t [V]	I_t [nA]	T [°C]	T [K]
170705_4	1047	200	100	2000	-0.22	10	27	300

Table B.6: List of STM data used in Figure 3.10

	File	Frame	Pixel	Nominal Range [Å]	Scan frequency [Hz]	V_t [V]	I_t [nA]	T [°C]	T [K]
a)	170705_10	958	200	100	2000	-1.45	3	-15	258
b)	170705_4	395	200	100	2000	-0.22	10	27	300

Table B.7: List of STM data used in Figure 3.11

File	Frame	Pixel	Nominal Range [Å]	Scan frequency [Hz]	V_t [V]	I_t [nA]	T [°C]	T [K]
170705_4	1311	200	100	2000	-0.22	10	27	300

Table B.8: List of STM data used in Figure 3.14

File	Frame	Pixel	Nominal Range [Å]	Scan frequency [Hz]	V_t [V]	I_t [nA]	T [°C]	T [K]
170705_25	1598	200	100	2000	-0.7	3	-6	267

Table B.9: List of STM data used in Figure 3.15

File	Frame	Pixel	Nominal Range [Å]	Scan frequency [Hz]	V_t [V]	I_t [nA]	T [°C]	T [K]
170705_4	1311	200	100	2000	-0.22	10	27	300

B.3 Overview of STM Data in Chapter 5

Table B.10: List of STM data used in Figure 5.5.

	File	Frame	Pixel	Nominal Range [Å]	Scan frequency [Hz]	V_t [V]	I_t [nA]	T [°C]	T [K]
a)	170705_4	147	200	100	2000	-0.22	10	27	300
b)	170705_4	148	200	100	2000	-0.22	10	27	300
c)	170705_4	149	200	100	2000	-0.22	10	27	300

Table B.11: List of STM data used in Figure 5.6.

	File	Frame	Pixel	Nominal Range [Å]	Scan frequency [Hz]	V_t [V]	I_t [nA]	T [°C]	T [K]
a)	170705_4	3513	200	100	2000	-0.22	10	27	300
b)	170705_4	3514	200	100	2000	-0.22	10	27	300

Table B.12: List of STM data used in Figure 5.7

File	Frame	Pixel	Nominal Range [Å]	Scan frequency [Hz]	V_t [V]	I_t [nA]	T [°C]	T [K]
170710_58	74	200	50	2400	-0.7	3	0	273

Table B.13: List of STM data used in Figure 5.21.

	File	Frame	Pixel	Nominal Range [Å]	Scan frequency [Hz]	V_t [V]	I_t [nA]	T [°C]	T [K]
a)	170505_5	1152	200	150	2000	-1.68	3	-220	53
b)	170505_5	1177	200	150	2000	-1.68	3	-220	53
c)	170505_5	1179	200	150	2000	-1.68	3	-220	53

Table B.14: List of STM data used in Figure 5.22.

	File	Frame	Pixel	Nominal Range [Å]	Scan frequency [Hz]	V_t [V]	I_t [nA]	T [°C]	T [K]
a)	170503_32	1795	200	150	2000	-0.6	3	-5	268
b)	170503_32	1834	200	150	2000	-0.6	3	-5	268
c)	170503_36	1598	200	75	2000	-1.7	10	-5	268
d)	170503_36	90	200	75	2000	-1.7	10	-5	268

Table B.15: List of STM data used in Figure 5.26.

	File	Frame	Pixel	Nominal Range [Å]	Scan frequency [Hz]	V_t [V]	I_t [nA]	T [°C]	T [K]
a)	170503_36	90	200	75	2000	-1.7	10	-5	268
b)	170503_36	185	200	75	2000	-1.7	10	-5	268

Table B.16: List of STM data used in Figure 5.27.

File	Frame	Pixel	Nominal Range [Å]	Scan frequency [Hz]	V_t [V]	I_t [nA]	T [°C]	T [K]
170710_56	2	200	100	2400	-0.7	3	-1	272

Table B.17: List of STM data used in Figure 5.28.

File	Frame	Pixel	Nominal Range [Å]	Scan frequency [Hz]	V_t [V]	I_t [nA]	T [°C]	T [K]
170710_55	897	200	150	2400	-0.7	3	-1	272
170710_55	159	200	150	2400	-0.7	3	-1	272

Appendix C Data and Image Processing

C.1 *MATLAB* scripts

Table C.1: Overview of the *MATLAB* scripts developed for the stepwise analysis of STM images. The column “Contributions” indicates the input to the different scripts by Jakub Bialek (JB), Philipp Messer (PM) and Ann-Kathrin Henß (AH).

	Task Script	required user-defined functions or data	Contributions
1	**Loading and Filtering of STM data for Particle Tracking**		JB, PM, AH
	STM_load_IBW.m	IBWread.m[198] readIBWheaders.m[198] readIBWbinheader.m[198] WT_FFT_Filter.m ring.m save_tiff.m	
2	**Particle Detection and Linking**		PM
	New_GUI.m	Treshold.m a_trous_wavelet.m Wvlt_Thr_Adjustment.m Wvlt_Tracking.m • pdist2_o.m Wave_Partfind.m • pdist_o.m	

3	**Drift Correction of Particle Traces** STM_Driftcorr.m or STM_Driftcorr_SlidingDiff.m or STM_Driftcorr_manually.m		AH
4	**Particle Selection** STM_find_common.m		AH
5	**Displaying and Saving of Traces of selected Particles** STM_selectedParticleTraces.m		PM, AH
6	**Extraction of displacement distributions from Traces** condense_Data.m	rotategrid.m	AH
7	**Combine all particle displacement distributions for one temperature** STM_combine_particles_for_fit.m or STM_combine_ohneDreiecke_fuer_fit.m	wege180119.mat	AH
8a	**Fitting** Fitting.m or	p_t0_neu.m	AH
8b	**Fitting under neglection of the *triangle jumps*** Fitting_ohneDreiecke.m	p_t0_neu_ohne_Dreiecke.m	AH

C.2 Drift Correction: Figure 3.14

Dataset: 170705_25	t_{int} = 110	*Diff_total* = 14
n_{frames} = 2490	n_{int} = 23	*Diff_norm* = 0.61

Table C.2: Drift determination for a dataset of 2490 images and an interval length of t_{int} = 110. The corresponding drift-corrected particle trajectories as well as the uncorrected trajectories are shown in Figure 3.14 in the main text.

Interval #	Image range	x 1.	x 2.	x 3.	**Result *x***	**½ t_{int}**	y 1.	y 2.	y 3.	**Result *y***	**½ t_{int}**
1	1-111	-3	-3	-2	**-3**	**-3**	7	6	5	**7**	**7**
2	111-221	-2	-2	-2	**-2**	**-2**	5	5	5	**5**	**4**
3	221-331	-2	-2	-2	**-2**	**-2**	5	5	5	**5**	**4**
4	331-441	-1	-1	-1	**-1**	**-1**	4	4	4	**4**	**4**
5	441-551	-1	-1	-1	**-1**	**-1**	4	4	4	**4**	**4**
6	551-661	-2	-1	-2	**-2**	**-2**	4	4	4	**4**	**4**
7	661-771	-1	-1	-1	**-1**	**0**	4	4	4	**4**	**4**
8	771-881	0	0	0	**0**	**0**	3	4	3	**3**	**4**
9	881-991	0	0	0	**0**	**0**	3	3	3	**3**	**4**
10	991-1101	-1	-1	-1	**-1**	**0**	3	3	3	**3**	**4**
11	1101-1211	0	0	0	**0**	**0**	3	3	3	**3**	**4**
12	1211-1321	0	0	0	**0**	**-1**	3	3	3	**3**	**3**
13	1321-1431	0	0	0	**0**	**0**	3	3	3	**3**	**3**
14	1431-1541	0	0	0	**0**	**0**	2	2	2	**2**	**2**
15	1541-1651	0	0	0	**0**	**0**	3	3	3	**3**	**2**
16	1651-1761	0	0	0	**0**	**0**	2	2	2	**2**	**2**
17	1761-1871	1	1	1	**1**	**1**	2	2	2	**2**	**2**
18	1871-1981	0	0	0	**0**	**0**	2	2	2	**2**	**2**
19	1981-2091	1	1	1	**1**	**0**	2	2	2	**2**	**2**
20	2091-2201	1	1	1	**1**	**1**	2	2	2	**2**	**2**
21	2201-2311	0	0	0	**0**	**0**	2	2	2	**2**	**2**
22	2311-2421	2	1	1	**2**	**1**	3	3	3	**3**	**2**
23	2421-2490	1	0	0	**1**	**0**	1	1	1	**1**	**1**
Difference *x*					**6**		**Difference *y***			**8**	
Diff_total					**6+8=14**						

Appendix D Calculation of the Geometric Probability Factor

The calculation of the geometric probability factor $\overline{w}_{n_1,n_2}$ is described in section 5.4.3.1. In the direct procedure the $w^i_{n_1,n_2}$ are first explicitly calculated for each specific sequence of n_1 (number of *triangle jumps*) and n_2 (number of *exchange jumps*) by applying the recursive rules (equations 5.23 to 5.28). As all sequences are equally likely the $w^i_{n_1,n_2}$ are subsequently averaged to give the geometric probability distribution $\overline{w}_{n_1,n_2}$. As this explicit procedure is computationally rather costly an alternative method has been developed in order to be able to calculate $\overline{w}_{n_1,n_2}$ also up to high values of n_1 and n_2.

The idea behind is that every sequence can be split up into two partial sequences at the point before the last *exchange jump* (as demonstrated in Table 5.2 in the main text). The averaging step is then performed already with the corresponding $w^i_{m_1,n_2-1}$ (m_1 = 0….n_1) of the first partial sequences (compare column five in Table 5.2). The recursive rules are then applied to these averaged probability distributions $\overline{w}_{m_1,n_2-1}$ according to the jumps in the respective second partial sequence.

In the following, it is briefly demonstrated that moving on with the averaged distributions before the last exchange jump $\overline{w}_{m_1,n_2-1}$ is reasonable as it is equivalent to the calculation of each individual sequence and averaging in the end. The calculation of $\overline{w}^{1\ to\ 3}_{2,1}$ serves as a concrete example in the following. In the straightforward calculation the first three geometric probability distributions $w^1_{2,2}$, $w^2_{2,2}$, and $w^3_{2,2}$ for n_1 = 2 and n_2 = 2 are obtained from the three individual shorter sequences $w^i_{2,1}$, by adding only one *exchange jump* to each sequence. $w^1_{2,2}$ can thus be calculated from $w^1_{2,1}$ by applying the recursion rules for an *exchange jump* (equations 5.26 to 5.28). The same is valid for $w^2_{2,2}$ and $w^3_{2,2}$. Exemplarily shown for the position (A, Y_1, Y_2), $\overline{w}^{1\ to\ 3}_{2,2}$ is then obtained by averaging the three $w^i_{2,2}$.

$$\bar{w}_{2,2}^{1\ to\ 3}(A, Y_1, Y_2) = \frac{1}{3}\left[w_{2,2}^{1}(A, Y_1, Y_2) + w_{2,2}^{2}(A, Y_1, Y_2) + w_{2,2}^{3}(A, Y_1, Y_2)\right] \tag{D.1}$$

When inserting equation 5.26 for $w_{2,2}^{1}(A, Y_1, Y_2)$, $w_{2,2}^{2}(A, Y_1, Y_2)$ and $w_{2,2}^{3}(A, Y_1, Y_2)$ and subsequently sorting the addents accordingly, it becomes clear that each term in square brackets can also be expressed by means of the averaged distribution $\bar{w}_{2,1}$ (equation D.2).

$$\begin{aligned}\bar{w}_{2,2}^{1\ to\ 3}(A, Y_1, Y_2) &= \frac{1}{3}\cdot\frac{1}{4}\left[w_{2,1}^{1}(C, Y_1+1, Y_2) + w_{2,1}^{2}(C, Y_1+1, Y_2) + w_{2,1}^{3}(C, Y_1+1, Y_2)\right]\\ &+\frac{1}{3}\cdot\frac{1}{4}\left[w_{2,1}^{1}(B, Y_1+1, Y_2-1) + w_{2,1}^{2}(B, Y_1+1, Y_2-1) + w_{2,1}^{3}(B, Y_1+1, Y_2-1)\right]\\ &+\frac{1}{3}\cdot\frac{1}{4}\left[w_{2,1}^{1}(C, Y_1+1, Y_2-1) + w_{2,1}^{2}(C, Y_1+1, Y_2-1) + w_{2,1}^{3}(C, Y_1+1, Y_2-1)\right]\\ &+\frac{1}{3}\cdot\frac{1}{4}\left[w_{2,1}^{1}(B, Y_1, Y_2-1) + w_{2,1}^{2}(B, Y_1, Y_2-1) + w_{2,1}^{3}(B, Y_1, Y_2-1)\right]\end{aligned} \tag{D.2}$$

By exploiting this workaround, $\bar{w}_{n_1,n_2}$ can be calculated in principle up to high numbers for n_1 and n_2. For the description of the O diffusion in CO, the calculations were performed up to n_1 = 100 and n_2 = 10. The developed workaround allowed to calculate all combinations in less than three minutes on a standard desktop PC. In comparison, when explicitly calculating each permutation for n_1 up to 100 and n_2 up to ten, the required computation time could be estimated from the average time per permutation to ~600000 years.

Appendix E DFT Calculations

The DFT calculations presented within this thesis were performed by Dr. Sung Sakong of the group of Prof. Dr. Axel Groß, Institute of Theoretical Chemistry at Ulm University. The calculation details necessary to reproduce the findings of the main text (section 5.4.4) are briefly denoted in the following.

The unit cell for DFT calculations is shown in Figure 5.16 a). The Ru(0001) surface was modeled by a three-layer slab with a (6 x 6) surface unit cell. All DFT energies are given with respect to the local minimum energy configuration, as shown in Figure 5.16 a). Calculations were performed by using the software package VASP (*Vienna Ab Initio Simulation Package*).[199] The revised *Perdew-Burke-Ernzerhof* (RPBE) functional was used to evaluate the exchange-correlation energies within the generalized gradient approximation.[200] A *D3* dispersion correction, as proposed by Grimme, was used to account for dispersion interactions between the adsorbates and between the adsorbates and the first Ru layer.[201, 202] The wave functions were expanded up to 350 eV using a plane wave basis set. Obtained energies are converged within 10 meV. This technical setup has been shown by earlier DFT studies to be well suited for the theoretical description of CO/Ru(0001).[190, 191]

Diffusion barriers of O were determined by the *nudged elastic band* (NEB) method.[203] The relatively simple form of the reaction pathway for the diffusion process allowed for the determination of the transition states with four images only. For verification transition states were also explicitly determined with the NEB climbing image method.[204]

Furthermore, harmonic transition state theory was employed to estimate zero point energy effects and entropic effects on the energetics of O diffusion. Both effects were found to only play an insignificant role for this process.

Acknowledgment

“Everything is going to be fine in the end.	„Am Ende wird alles gut,
If it’s not fine,	und wenn es noch nicht gut ist,
it’s not the end.”	dann ist es noch nicht das Ende.“

Dieser Spruch trifft wohl so genau wie nur wenige andere auf experimentelle Doktorarbeiten zu und er hat mich auch während meiner Zeit begleitet. Am Ende ist nun alles gut geworden. Es ist ein tolles Projekt entstanden, das aus so vielen unterschiedlichen Facetten besteht, dass ich es nicht hätte alleine stemmen können. Ich möchte allen danken, die in den letzten Jahren durch Diskussionen, Denkanstöße, Motivation aber auch durch tatkräftige Unterstützung im Labor zum Gelingen dieser Arbeit beigetragen haben. Mein besonderer Dank gilt dabei:

Prof. Dr. Joost Wintterlin für die Möglichkeit meine Doktorarbeit in seinem Arbeitskreis durchführen zu können, für das große entgegengebrachte Vertrauen und die damit verbundenen Freiheiten, für das immer ansprechbar sein, und für die stete Bereitschaft bei großen und kleineren Problemen auszuhelfen.

Prof. Dr. Axel Groß für die Übernahme des Zweitgutachtens und die tolle Zusammenarbeit im Rahmen des Diffusions-Projekts.

Dr. Patrick Zeller für die exzellente Betreuung während meiner Bachelor- und Masterarbeit und das damit verbundene Wecken der Begeisterung für die Arbeit im und mit Ultrahochvakuum, für allerlei experimentelle Tricks und Kniffe, für eine stets heitere und freundschaftliche Arbeitsatmosphäre und schließlich auch für sein äußerst gründliches Korrekturlesen meiner Doktorarbeit.

Dr. Martin Ehrensperger für die Einarbeitung an der VT-STM Apparatur und für seine zahllosen erheiterten Geschichten während Mittags- und Kaffeepausen (die natürlich stets nur einem seiner Freunde passiert waren).

Regina Wyrwich, **Bernhard Böller**, **Katharina Durner** und **Paul Leidinger** für die freundliche und hilfsbereite Arbeitsatmosphäre in der Gruppe, die gegenseitige Unterstützung, für den morgendlichen Kaffee und den mittäglichen Espresso, für viele Abspüldienste und für die Vertiefung meiner Kenntnisse über die bayrische Sprache und Kultur.

Dem **AK Günther** für die Erweiterung und damit verbundene Bereicherung unseres Arbeitskreises, sowie für ihre starke Gruppen-Performance bei außeruniversitären Angelegenheiten.

Rita Römling-Engl und **Regina Huber** für die kompetente Hilfe in allen bürokratischen Angelegenheiten und die stellvertretende Austragung diverser Kämpfe mit der Reisekostenstelle.

Dem **AK de Vivie-Riedle** und seiner **„Chefin"** für meine quasi-Aufnahme in ihrem Arbeitskreis, für die vielen netten und hilfreichen Diskussionen von außer- und inner-universitären Angelegenheiten, die zahlreichen „Wochenend-Biere" und ihre tatkräftige Unterstützung am Nockherberg und auf der Wiesn.

Philipp Messer und **Prof. Dr. Don C. Lamb** für die Bereitstellung ihrer Expertise beim Erkennen und Verfolgen der kleinen hüpfenden Teilchen in den STM Videos.

Dr. Sung Sakong für die Theorie-Unterstützung zur Interpretation unserer Experimente, sowie die nette Zusammenarbeit.

Dr. Jochen Wiechers für seine Bereitschaft uns in seiner Freizeit mit seinen „elektronischen" Kenntnissen weiterzuhelfen.

Prof. Dr. Rolf Schuster für die unglaublich große Starthilfe bei der Entwicklung der Video-STM Software.

Den Feinmechanikern **Ralf Hiermaier**, **Thomas Gisicius** und **Fabian Kreuzer** für ihre kompetente Hilfe und ihre Ideen beim Planen neuer Aufbauten, sowie der zuverlässigen und akkuraten Umsetzung.

Den Elektronikern **Axel Gersdorf** und **Herbert Bachmeier** für das Pflegen unserer teilweise sehr „erfahrenen" elektronischen Komponenten, sowie für das Bereithalten verschiedenster Schmelzsicherungen, damit es schnell weitergehen konnte nachdem etwas „anders" als geplant verlaufen war.

Hannah Illner für die Weiterführung des Projekts im Rahmen ihrer Masterarbeit.

Kristian Jordan für die Unterstützung bei der schier endlosen Auswertung der STM Videos.